UNIVERSITEIT VAN PRETORIA
UNIVERSITY OF PRETORIA
YUNIBESITHI YA PRETORIA

OPTIMIZATION OF WIND BARRIERS FOR THE MINIMIZATION OF MIRROR SOILING IN A PARABOLIC TROUGH COLLECTOR PLANT

By Godswill Otukpa

Submitted in partial fulfilment of the requirements for the degree of

Master of Engineering (Mechanical Engineering)

DEPARTMENT OF MECHANICAL AND AERONAUTICAL ENGINEERING,
FACULTY OF ENGINEERING, BUILT ENVIRONMENT AND INFORMATION TECHNOLOGY
UNIVERSITY OF PRETORIA

December 2020.

Supervisor: Dr. Mohammad Moghimi Ardekani

Co-Supervisor: Prof. Josua P Meyer

EXECUTIVE SUMMARY

Optimization Of Wind Barriers For The Minimization Of Mirror Soiling In A Parabolic Trough Collector Plant

Author: Godswill Otukpa

Student Number: 12007872

Supervisor: Dr Mohammad Moghimi Ardekani

Co-Supervisor: Prof. Josua P Meyer

University: University of Pretoria

Department: Mechanical and Aeronautical Engineering

Degree: MEng (Mechanical Engineering)

Keywords: CSP, PTC, Solar, Radiation, DNI, Porous, Solid, Wind, CFD, Energy, Mirror, Soiling.

Concentrated Solar Power (CSP) also known as concentrated solar thermal is the systematic act of using mirrors and lenses to concentrate direct sunlight to a specific focal point so that solar radiation can be converted into useful electrical energy. The genesis of CSP technology dates back from the 1800s, when August Mouchout used a Parabolic Trough Collector (PTC) to produce steam. CSPs are known to have different types of collector technology which include the enclosed trough, solar power tower, fresnel reflectors, dish stirling, and parabolic trough collector.

It has been established that a Parabolic Trough collector (PTC) is the most developed form of technology that a concentrated solar power plant can utilize to harness the energy of the sun. PTCs are commonly used by large scale plants to collect a large amount of solar radiation and incorporate it into their many functions. PTCs are energy reactors which enables heat exchange between solar energy and a transport fluid medium. They are ‘parabolic’ in shape, consist of an absorption tube located at the focal concentrating point, a bearing structure, and a shiny reflector surface. PTCs can either have a one or two-axis tracking system. PTCs with a two-axis tracking system are more efficient because of their zero-incidence angle, however they are generally more costly to maintain and have higher thermal losses involved. It is highly imperative that the PTC reflector surface has constant good reflectance as this is where the Direct Normal Irradiance (DNI) is absorbed and emitted to the focal line of the PTC. Strict design requirements such as high UV reflectance, corrosion resistance and weather resistance are necessary. Past research has proven that aluminium is a good choice of material because of its low cost and high reflective properties.

A PTC system can be applied in different areas according temperature output requirements. For lower temperature requirement (100°C- 250°C) they are used for domestic heating, heat driven refrigeration systems and air conditioning units. For higher temperature requirement (300°C- 400°C), they are used in CSP plants arranged in array form with multiple PTC units connected together ultimately forming a PTC plant. Generally, all CSP plants are located in dessert arid regions where the exposure to sunlight is hardly hindered. Maximum exposure to sunlight is necessary for a CSP plant as the solar energy that reaches the earth is about 170 trillion kWH and the major aim of all CSP plants is to harness as much as possible effectively. In this regard, the reflectivity of mirror facets of a collector unit needs to be kept clean and free of any substance that reduces reflectivity. Due to CSP plant location, dessert storms and sandstorms occur frequently causing sand particles to be deposited on the surface of mirrors. Mirror soling is defined as the deposition of dust particles on mirror facets resulting from particle movement from one region to the mirror. Dust particles can absorb and deflect solar rays that hit the mirror facets limiting reflectivity and limiting the performance output of a CSP plant. Mirror soiling is phenomena that cannot be easily prevented 100% as there are different sizes to particles and one would have to stop the weather and climate altogether.

PTC plants as well as other CSP plants experience mirror soiling on a daily basis of their operation. In dealing with this problem, plants have employed cleaning methods that commonly utilize a large volume of water which gives favourable results in trying to maintain high reflectivity. However, for a location that is dry and arid, it is not economical to carry on using water where it is a considerable finite resource. To minimize water usage in handling this problem to a significant number or nil, researchers have tried automated novel methods, water saving methods and dust prevention methods. A dust prevention method that has proven to reduce mirror soiling to a significant number is the installation of a wind barrier. It has been numerically proven and validated that a wind barrier, placed in the prevailing wind direction, can deflect dust particles away from a defined mirror location.

The presented thesis and research aims to re-introduce porous barriers and non-porous barriers as a simple economical practical approach that can minimize mirror soiling and present it as an alternative solution that lessens the volume of water used to clean collector facets. The thesis is purely simulation-based and incorporates particle mechanics and computational fluid dynamic (CFD) to show results and performance of wind barriers ultimately deriving an optimum candidate that can be manufactured and used in CSP plants. The study used ANSYS 2019 packages as the simulation tool to perform simulations and optimization procedures. Results showed that an optimum porous barrier has the capability to increase a CSP plant efficiency by a significant percentage.

ACKNOWLEDGMENTS

I would like to thank God in heaven for the strength, courage, guidance, and provision for all this to happen. Could not have happen without him. I would like to thank my family, Joseph, Priscilla, Igbe, Victor, Emmanuel, and Faith Otukpa for their love, support, and unending prayers.

Special thanks go to the department of mechanical and aeronautical engineering of the University of Pretoria and especially to my supervisor, Dr Mohammad Moghimi Ardekani for his research in renewable energy field, leading me, being there and available.

I would also like to acknowledge that this dissertation is a form, continuation and part of the following conference paper, journal article and chapter publication respectively, principally authored by me:

- Numerical analysis of porous wind barrier for minimizing collector mirror soiling in a parabolic trough collector plant.
- Numerical analysis of porous and non-porous wind barriers for minimizing collector mirror soiling in a parabolic trough collector plant.
- A review on conventional and sustainable mirror cleaning technologies in Parabolic Trough Collector (PTC) plants.

TABLE OF CONTENTS

LIST OF FIGURES

LIST OF TABLES

NOMENCLATURE

po = porosity [m].

l_3 = Flap length [m].

θ = Flap angle [°].

l = length [m].

u_i^p = velocity vector of particle [m/s].

u_i = instantaneous velocity [m/s].

F_D = drag coefficient.

g_i = acceleration of gravity [m/s^2].

ρ_p = particle density [kg/m^3].

µ = viscosity of fluid [m^2/s].

ρ = density of fluid [kg/m^3].

$\boldsymbol{x}$ = position vector [m].

p = mean fluid pressure [Pa].

u = fluid velocity vector [m/s].

$\boldsymbol{u}'$ = fluctuating velocity vector [m/s].

k = turbulence kinetic energy [J].

ε = dissipation rate of turbulence energy [m^2/s^3].

C1 = function of mean strain and turbulence field.

Cµ = function of rotation rate, mean strain, the system rotation angular velocity and turbulence field

CHAPTER 1

INTRODUCTION

1.1. BACKGROUND

Global resource depletion appears to be a recurring phenomenon, with sustainable energy as a possible solution to counter it. Primary energy consumption grew at a rate of 2.9% last year (2019) and almost double its 10-year average of 1.5% per year and it is the fastest since 2010 (BP, 2019). Fossil fuel continues to be in high demand; however, there is a limited supply, and the implications of this excess usage are numerous on a national and international scale. Fossil fuels are the major considered factor as an energy resource in our world. Factually, burning fossil fuels leads to emission of carbon dioxide, carbon monoxide, NOx and other harmful gasses which leads to greenhouse effect, acid rain and other destructive environmental issues. Carbon emissions grew by 2.0%, this is the fastest rate in the last 30 years (BP, 2019). Turning our focus to clean renewable energy is a solution that will prove beneficial for the world in the near future and for generations to come.

Solar energy generation grew by $3.489 \times 10^{11} kWhr$ just below the increase in wind energy ($3.7216 \times 10^{11} kWhr$), and provided more than 40% of renewables growth in 2018 (BP, 2019). Amongst the alternative renewable energy resources, solar energy is the most recognized and the easiest form of energy that can be converted to electrical energy due to its availability and unlimited eco-friendly nature (Mohammad et al., 2017). The solar energy emitted by the sun is an exceptionally large amount. It has been recorded that if we convert only 0.1% of solar radiation that hits the earth the output power would be approximately 17300 GW, which was seven times higher than the global average consumption in 2012 (Gavez et al., 2009). There are two major ways solar energy can be harnessed. One way is by using photovoltaics, and the other is by solar thermal, which is also known as concentrated solar power (CSP). The useful power extracted from technology associated with CSP is reliable, environmentally friendly, and clean (Muhammad et al., 2016).

The design and implementation of concentrated solar power (CSP) plants appear to be a solution to harnessing solar energy at a lower cost compared to fuel-powered stations. CSP technology can be categorized into four major technology types, namely, parabolic trough collectors (PTCs), solar towers, linear Fresnel and parabolic dish. For large-scale utility power production, the PTCs are the most mature form of technology and have proven to be the most effective in regions with very dry and semi-arid environments (Boukelia et al., 2013). Regions like these are high in irradiance because they are highly exposed to sunlight. Direct normal irradiance (DNI) is one of the most important factors that contributes to the effective power generation sourced from the sun. It can be defined as the amount of solar energy falling per square meter per day at a specific location or region. DNI is directly proportional to the amount of electricity produced from a collector unit. Thus, the higher and uninterrupted the amount of DNI hitting a PTC collector unit is, the more electricity produced from that unit. It has been recorded (Suncyclopedia, 2020) that Africa has the most amount of DNI regions which is about 13 million km^2 in the world.

The PTC plant system comprises mainly of three important sub-systems: the PTC solar collector field, the storage system, and the power block. The solar collector acts as a boiler and consists of a solar receiver for the reflector mirror surfaces. For reliable operations, the average requirement of DNI must be more than 2000 kWh/m2 (Bhuiyan et al., 2019). A typical PTC concentrates sunlight on a single focal point by using several curved parallel mirrors and a heat transfer fluid (HTF) to convert sunlight into electricity. A single solar collector of a PTC plant (PTC module) consists of a solar receiver, a reflector surface, and a support structure base. The reflector surfaces are generally made up of a series of mirrors that concentrates the solar rays to the receiver. The amount of absorbed energy of a PTC technology is majorly dependent on the optical properties of the curved parallel mirrors and the absorber tube containing the HTF. In 2016, it was reported and analysed that an installed PTC plant had an operational capacity of 3.5GW from 4.2GW absorbed solar energy (Chaanaoui et al., 2016).

PTC technology usually experiences mirror soiling at plant sites due to their locations. Locations like these are dry, torrid, and rainless. The existence of precipitation is a foreign concept and, as such, the land is barren, enabling airborne dust particles to move freely and haphazardly. Four major characteristics of dust particles can be observed when they come in contact with surfaces: they can be reflected off the surface; they can stick to the surface (deposition); they can penetrate the surface and they can react with the surface. Particles that are typically less than 100 µm are generally a problem for PTC modules. It has been reported that sand particles between 2.5 µm and 10 µm diameter become airborne in gusts of 15–17 m/sec (Lee et al., 2009). When small sand particles of this nature collide with mirror reflector surfaces, there is an attractive force that occurs between the reflectors and the sand particles. This attractive force is a result of the surface energy present on the mirror facets, the electrostatic energy effects of particles creating a temporary suspension and filth on mirror facets. This is chiefly known as mirror soiling, and it continues to be a major dilemma for CSP plants.

Mirror soiling is defined as the deposition and suspension of dust particles on parallel mirror faces, which can reduce the instantaneous and average performance output of a CSP plant by 60% and 37%, respectively (Liang et al., 2015). The presence of dust particles on mirror surfaces reduces the shiny, lustrous effect of PTC modules, making it difficult to concentrate solar rays effectively. Majorly, commercial plants wash mirror facets regularly to get rid of mirror soiling. However, with any solution that involves the usage of water, it is not ideal to use water as water is considered a scarce resource in dry regions and the amount needed is large. The cleaning systems generally use about 0.2-1 litter of water per square meter of collector area (Moghimi et al., 2018). Researchers observed that an alternative solution is needed to be implemented and opted for novel water-saving cleaning and dust prevention methods which majorly include ultrasonic, electrostatic discharge and wind barriers.

With the use of Computational fluid dynamics (CFD) coupled with experimental validations, wind barriers can alter the number of deposited particles in a solar collector field. Wind barriers are structural component barriers placed in the direction of the prevailing wind used to redirect the flow of wind carrying dust particles over the solar collector field. By optimizing wind barriers one can ensure an economical approach in dealing with mirror soiling and increase the productivity of a CSP plant (Moghimi et al., 2018).

1.2. PROBLEM STATEMENT

The installation of any CSP plant with the potential use of PTC modules are generally likely to pose a series of problems for the environment and neighbouring communities. Although solar energy is a means to provide employment as at the end of 2019, the total workforce employed was 3.46 billion and out of the that number the solar PV accounted for 3.6 million, solar thermals accounted for 0.8 million and CSPs accounted for 0.03 million jobs (IRENA, 2020). One needs to take account of the factors that are involved in dealing with mirror facets. Evidently, mirror soiling is a considerable phenomenon that pose a major threat to the survivability of a PTC plant.

Soiling is a constant limiting factor on PTC plants that cannot be controlled, predicted, or collected. It sourced from dust storms, sandstorms and climate change, and its random nature makes it difficult for scientists and researchers to study. Its complex nature is due to the countless varying particle size involved in its occurrence. Plants have recorded a 1% to 25% power loss per week due to mirror soiling (Banke, 2018). As a result of mirror soiling, PTC plants have generally used cleaning methods which involve the usage of large amounts of water ultimately costing the plants financially and their respective environments economically.

According to Otieno et al., 2016, a total number of 17 risks associated with the development of a CSP plant have been identified and recorded. The results were obtained from a survey conducted. Based on the results shown in table 1, the number one risk factor associated with CSPs is the risk of depletion / disruption of local water resources.

Table 1.1. Risk ranking position before and after mitigation (Source: Otieno et al., 2016)

Reviewed Risk	**Position and Score Before Mitigation**	**Position and Score After Mitigation**
Risk of Depletion / Disruption of Local Water Resources	1	1
Risk to Worker Health and Safety	2	3
Risk to Avian Species	3	2
Risk of Production of Hazardous Materials and Waste	4	6
Risk due to Noise on Acoustic Environment	5	4
Risk of Disruption of Visual and Recreational Resources	6	5
Risk to Ecological Resources	7	11
Risk to Locational Social Economics	8	9
Risk to Public Health	9	8
Risk due to Glint and Glare	10	10
Risk of Withdrawal of Land for Other Uses	11	14
Risk to Archaeological Resources	12	13
Risk to other Animals and Plants	13	17
Risk to Land Traffic and Transportation	14	15
Risk to Cultural Resources	15	12
Risk to Air Quality	16	7
Risk to Geological Resources	17	16

In arid dessert regions that are exposed to high DNI amounts, water is scarce and high in local value and PTC plants are situated in these regions. For PTC plants water is used for the plant cooling system cleaning PTC mirrors and additional water demands for the steam cycle. Water consumption for cooling ranges from 80% to 97% of water requirements where evaporative wet cooling systems are used (US DOE, 2008, Turchi et al., 2010 and Hogan, 2009).

To summarize the problem at hand, PTC plants experience mirror soiling which decreases the productivity of plants. The continuous use of water to aid as a major cleaning agent is completely uneconomical for plants and environmentally detrimental as per table 1. The present study majorly aims to tackle this problem.

1.3. OBJECTIVES AND DOCUMENT OVERVIEW

The problem has been identified in the problem statement as an industrial problem that PTC plants experience continuously. Thus, to solve this problem the following objectives were top priority in this research:

- To analyse the problem statement and break it down into simpler problems in which these subproblems will be handled individually.
- To categorize the problem as a fluid flow problem and comprehend the essence of the problem as well as the sub-components of the problem.
- To research and understand dust particle phenomena and dynamics.
- To research and produce a literature review of the problem and understand what has been done with regards to the problem.
- To research and understand why computational fluid dynamics is applicable and fundamental to the problem.
- To use computational fluid dynamics (CFD) for various simulations and optimization procedures.
- To perform 25 simulations of geometrically altered form of two different wind barrier structures.
- To research and understand the process that occurs with ANYS CFD package.
- To produce and discuss results from simulations that are sensible and readable to users.
- To produce an optimum wind barrier with the use of ANSYS CFD package and research.
- To verify that a wind barrier has the potential to deflect and reduce mirror soiling from a certain direction of wind flow.
- To document findings of the proposed research study accurately and accordingly.

With these objectives in mind, the chapters were written in full consideration of the research objectives. Chapter 2 is the literature review which produces detailed information of what has been done and what is currently been done with regards to the cleaning procedure of PTC modules. The design and history of PTC modules was also incorporated to educate readers on the type of energy structure this research is concerned with. Chapter 3 is the geometry and mesh modelling chapter which provides readers with the way the problem was initially handled. Chapter 3 gives insight to how the CFD approach initially begin on the problem, providing readers with the problem broken down and converted into a visual form for the meshing process to occur.

Chapter 4 provides the detailed information of the numerical process that occurs within the CFD package that performs simulations and the optimization calculation. Chapter 5 shows the various settings used for the simulation cases involved in this study as well as their respective results. Chapter 5 also provides readers with validation for the support of the simulations that has been done. Optimization information with regards to the problem is located in chapter 6. The optimization results are also displayed and explained fully in this chapter. Chapter 7 is the final chapter of the dissertation which concludes the research study and explains any future work and recommendations that could occur with the proposed research topic.

CHAPTER 2

LITERATURE REVIEW

2.1. INTRODUCTION

This chapter introduces the current and past design concepts of PTC modules. The chapter also gives descriptive information on the types of cleaning procedures that are currently in use and have been implemented by CSP plants. All the information with regards to CSPs that were utilized for the completion of this study can be found in this chapter.

The chapter begins with a brief history of PTC modules and its origin. The mathematical design concepts of PTC module were also highlighted and addressed within the chapter.

2.2. THE HISTORY OF PTC MODULES

The idea of the parabolic trough collector revolved around its shape and mirrors. Initially, according to a semi-spherical shape, solar rays in the form of DNI would hit the focal point situated at half of the spherical section and above the vertex of the whole sphere. Researchers sought to use the derivative of the circular equation to examine and determine the focal point in the sphere’s inner surface ultimately leading to the premise that the rays of the sunlight would intersect at the focal point.

It was in 1870 that the first practical occurrence of a PTC module was introduced. John Ericsson, a Swedish engineer immigrant of the United States, designed and constructed a collector with an aperture area of 3.25m^2 for a small operational steam engine of 373W. He further constructed and built several similar systems with air as the working fluid from 1872 to 1875 (Pytilinski, 2018). Charles Greeley Abbot, and American astrophysicist, used PTC to convert solar energy into mechanical energy to operate a 0.37kW steam engine in 1936 and 2 years later he used it to generate a 0.15kW steam engine (Pytilinski, 2018). Using PTC, he proved that a system should have a theoretical overall efficiency of 15.5% and an actual efficiency of 11.7% to produce steam at 225°C (Spencer, 1989). The continuous research of PTC technology became redundant soon after.

A century later, in the 1970s, during the oil crisis when the prices of oil rose significantly, nations opted for an alternative energy source. The interest on PTC modules then re-surfaced. At this year, the US government designed their first two collectors operating below the temperature of 250 °C. In 1975, three PTC modules, equipped with a 4cm diameter chrome-coated carbon-steel receiver tube with a 1cm evacuated annulus were further designed and constructed with an aperture area of $7.8m^2$ and a 90° rim angle (Shaner et al., 1979). In 2010, the Southeast University and Sanle Electronic group of China designed the first PTC module with a Sanle-3 heat collecting element (HCE) receiver tube (Gong, et al., 2010).

2.3. THE DESIGN OF A PARABOLIC TROUGH COLLECTOR SYSTEM

Since the 1980s, PTC technology has attracted attention due to the oil crisis that arose (Milton, et al., 2009) and its functions. PTCs are generally classified into three major sub systems in the design stage. These subsystems include:

i. PTC geometric module

ii. Hydraulic and thermal subsystem

iii. Bearing Structure (PTC module Base).

2.3.1. PTC GEOMETRIC MODULE

A single PTC module, as shown in figure 2.1, consists of three fundamental components which are the reflector, the receiver, and the structural base. The reflector is parabolic in nature (parabolic trough). The mirror reflector is used to focus the DNI obtained from the sun to its focal line. The receiver, which is situated at the focal line, is used to absorb the heat produced by the sun.

The parabolic trough should have design requirements of light weightiness and shiny surface for high reflectivity. Due to the location of the receiver, the material used to coat the receiver should have high thermal absorptance. The coated material is usually surrounded by a tube made of glass and to decrease heat losses, a vacuum status is created between the tube and the receiver. A vacuum can cause four times higher heat loss (Ahmadi, et al., 2018).

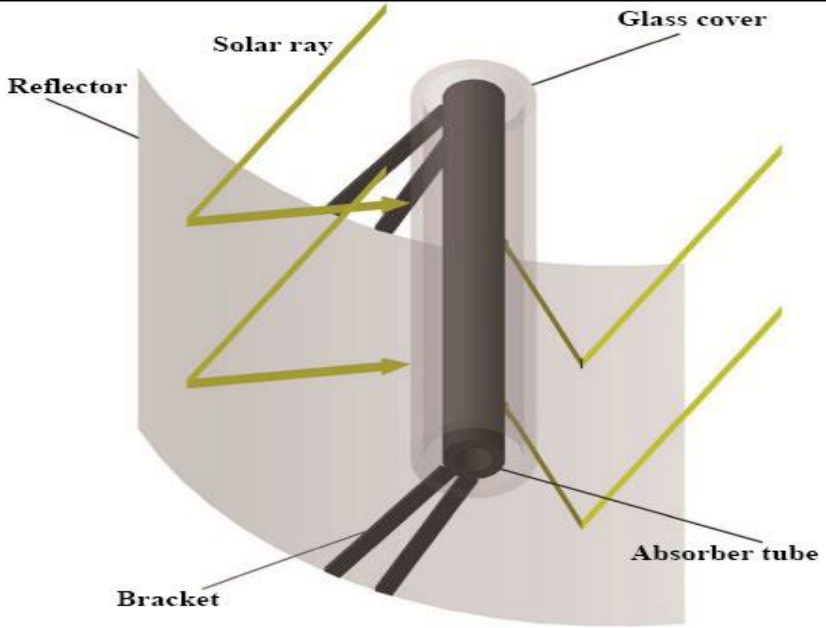

Figure 2.1. PTC module (Source: Ahmadi, et al., 2018)

A conventionnel PTC module is place with its axis in the North-South direction and it tracks the sun in the East-West Direction (Duffie, et al., 2006). This strategy of placement allows for optimum sun irradiation within desert regions. PTC modules are placed linearly and connected to each other in series. A series of many modular PTCs are then connected in a parallel configuration to form a solar field of PTC modules, as seen in figure 2.2.

Figure 2.2. Solar field of PTC modules (Source: 'Parabolic Trough', 2020)

To derive the mathematical modelling for a PTC module, the schematic shown in figure 2.3 is used.

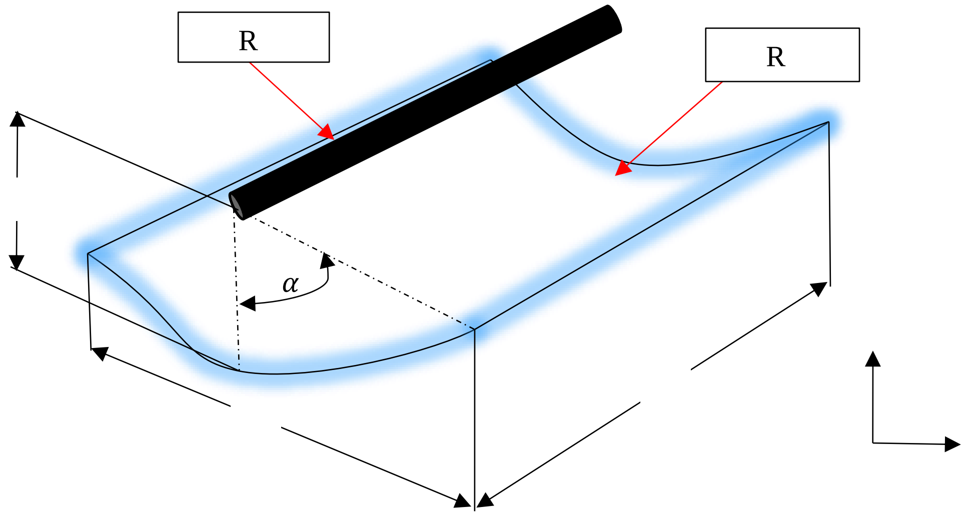

Figure 2.3. Geometrical modelling of a PTC module

Given the defined axis in figure 2.3, the parabolic shape is obtained by equation 2.1:

$$y = \frac{x^2}{4f} \tag{2.1}$$

Where f known as the focal distance, is the distance between the vertex of the parabola and its focal point. The rim angle, α, is defined as the angle between the mirror rim and focal point and can be calculated using w and f (Menrabi, et al., 2016, Price, et al., 2002, Sup et al., 2015, and Kaseian, et al., 2015).

$$\alpha = arctan\left[\frac{8\frac{f}{w}}{16\left(\frac{f}{w}\right)^2 - 1}\right] \tag{2.2}$$

The rim angles the sole ability to determine (Sup, et al., 2015) the shape of the cross-section of the PTC module.

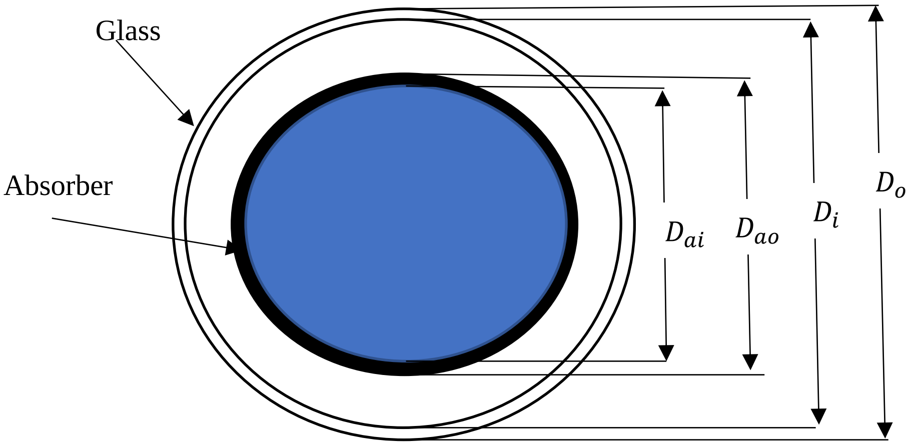

Figure 2.4. Cross section of the geometric model of the absorber tube

The total collector aperture area, A_c is thus given as the product of the aperture width and length.

$$A_c = wL \tag{2.3}$$

Figure 2.4 shows the modelling of the cross-sectional area of the receiver located at the focal point of the reflector. It is important to note the vacuum and coating present within this model.

The total absorber area is then given as equation 2.4

$$A_a = \pi D_{ao} L \tag{2.4}$$

Given the total absorber area and collector area, the total geometrical concentration ratio is thus given as equation 2.5:

$$C = \frac{A_c}{A_a} = \frac{w}{\pi D_{ao}} \tag{2.5}$$

Taking into consideration that the absorber tube is not only irradiated by the reflected radiation but also by the radiation that reaches the tube directly so that the whole absorber tube surface is irradiated (Günther, et al. 2010). Concentration ratios generally vary from values less than one to high values of 10^5 (Collares, et al., 1991, Good, et al., 2016, and Canavarro, et al., 2013).

The surface area of a PTC module is needed to determine the material requirements needed and thus is presented as follows in equation 2.6:

$$A_{sc} = \left(\frac{w}{2} \sqrt{1 + \frac{w^2}{16f^2}} + 2f \ ln \left(\frac{w}{4f} + \sqrt{1 + \frac{w^2}{16f^2}} \right) \right) L \tag{2.6}$$

2.3.2. HYDRAULIC AND THERMAL SUBSYSTEM

This subsystem addresses the nature, mechanics, and materials of the Heat Transfer Fluid (HTF). The major determining factor of the absorption of solar rays is the type of fluid used to collect energy emitted by the sun and transport it accordingly to the plant involved. The working temperature of PTC is wide, in range of 100 to 400°C, which makes it applicable for several applications. PTCs are categorized based on their working temperature. PTCs work in temperature range between 300 and 400°C are mainly applied for power generation while the ones operate in the range of 100-250°C are used for heating purposes. The energy reflected to the receiver is absorbed by forced convection (Gaul, et al., 1980).

2.3.2.1. Thermal Modelling

During energy flow within the receiver, there are optical and thermal losses that occur, and this affect the usable power. Optical losses occur at the glass tube section and the absorber tube has limited absorptivity, thus the radiation coming in at some parts of the tube is reflected away. The use of antireflective and clear transparent glass reduces optical losses to about 4 – 5%. The energy balance according to the absorber presented in figure 2.5 indicates that the absorbed solar irradiation, Q_{abs}, is separated into useful heat, Q_u, and thermal losses, Q_{loss}.

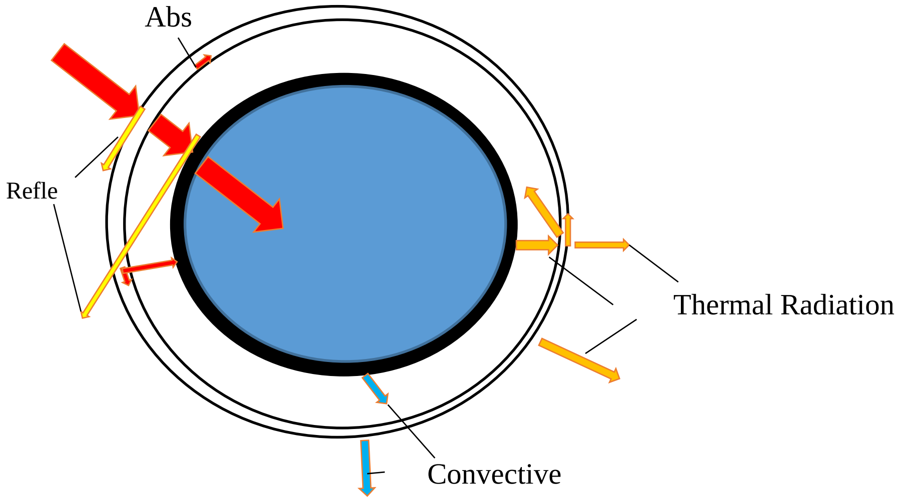

Figure 2.5. Energy flow at the receiver

The energy balance can be then defined as equation 2.7:

$$Q_{abs} = Q_u + Q_{loss} \tag{2.7}$$

The relationship between the solar irradiation, Q_{irr}, and absorbed energy can be written in terms of optical efficiency by equation 2.8.

$$\eta_{opt} = \frac{Q_{abs}}{Q_{irr}} \tag{2.8}$$

Now, the optical efficiency changes with incident angle and can be modelled with an incident angle modifier, K, and the maximum optical efficiency, $\eta_{opt,max}$ (Gaul, et al., 1980).

$$\eta_{opt}(\theta) = K(\theta)\,\eta_{opt,max} \tag{2.9}$$

The K modifier function is defined by the following equation 2.10:

$$K(\theta) = cos(\theta) - \frac{f}{L}\left(1 + \frac{w^2}{48f^2}\right) sin(\theta) \tag{2.10}$$

Given a tracking strategy with the PTC axis in North-South direction, the cosine of the incident angle is calculated as seen in equation 2.11 by Duffie et al., 2006.

$$cos(\theta) = \sqrt{cos^2(\theta_z) + cos^2(\delta) + sin^2(\omega)} \tag{2.11}$$

Where θ_z represents the zenith solar angle and is the complement of the altitude angle. δ is the solar declination angle and this is the angle between the rays of the sun and the plane of earth's equator. It varies between ± 23° 27' and (±23.45°). ω is the solar hour angle, which is the angular distance between the hour circle of the sun and the local meridian (Axaopoooulos, 2016).

The maximum optical efficiency is a product of parameters in which every parameter represents a different optical loss:

$$\eta_{opt,max} = \rho_{tot}\gamma\tau\alpha \tag{2.12}$$

Here, α represents the absorber absorbance and τ is the cover transmittance. Both these values take values close to 90-95%. γ is the intercept factor that usually takes values close to 1 for optimized commercial plants. ρ_{tot} is the total reflectance and includes various factors (Behar, et al., 2015) such as the concentrator reflectance, tracking errors, the shading factors, and the clearness factors. The reflectance takes about 90-93% approximately. The maximum optical efficiency of a typical PTC is around 75% (Bellos, et al., 2017).

The thermal losses involved are generated by thermal radiation, convection, and heat conduction (figure 2.5) and are dependent on the temperature difference between the absorber tube and surrounding air. As mentioned earlier, heat conduction and convection between the absorber tube and cooler glass tube is reduced significantly by the glass tube. The useful heat production can be calculated as follows by energy balance:

$$Q_u = Q_s - Q_{refl,glass} - Q_{ref,abs} - Q_{rad,glass} - Q_{conv,glass} \tag{2.13}$$

The total amount of available solar irradiation is given by the formula:

$$Q_s = A_c G_b \tag{2.14}$$

Here, G_b represents the direct solar irradiation beam hitting the absorber. $Q_{refl,glass}$ represents the energy loss due to the reflection on the glass tube and given as equation 2.15:

$$Q_{refl,glass} = \mathrm{A}_{ao} U_L (T_c - T_{ambient}) \tag{2.15}$$

Where U_L is the thermal loss coefficient and T_c is the mean glass temperature. $Q_{ref,abs}$ represents the energy loss due to reflection by radiation on the absorber tube (Bellos, et al., 2018) to the glass.

$$Q_{abs,glass} = \mathrm{A}_{ao}\sigma\left(\frac{T_a^4 - T_c^4}{\frac{1}{\varepsilon_a} + \frac{1-\varepsilon_c}{\varepsilon_c}\left(\frac{A_{ai}}{A_o}\right)}\right) \tag{2.16}$$

$Q_{rad,glass}$ is the energy loss to the ambient by radiation emittance from the glass cover and given by (Bellos, et al., 2018).

$$Q_{abs,glass} = \mathrm{A}_{co}\sigma\varepsilon_c\left(T_c^4 - T_{sky}^4\right) \tag{2.17}$$

The sky temperature can be calculated as follows (Swinbank, 1963):

$$T_{sky} = 0.0552(T_{ambient}^{1.5}) \tag{2.18}$$

$Q_{conv,glass}$ is the convective energy loss at the glass cover tube and given as follows:

$$Q_{conv,glass} = \mathrm{A}_{co} h_{out} (T_c - T_{ambient}) \tag{2.19}$$

h_{out} is the heat transfer coefficient between the glass cover and ambient and can be calculated using the following formula (Bhowmik, et al., 1985, and Qiu, et al., 2017):

$$h_{out} = 4\left(V_{wind}^{0.58}\right)(D_{co}^{-0.48}) \tag{2.20}$$

The thermal efficiency of the solar collector can then be obtained by equation 2.21:

$$\eta_{th} = \frac{Q_u}{Q_s} \tag{2.21}$$

Now the equation of heat transfer from the absorber to the fluid can be stated as follows:

$$Q_u = \mathrm{A}_{ao} h\left(T_a - T_{fm}\right) \tag{2.22}$$

Where the mean fluid temperature, T_{fm}, can be calculated according to equation 2.23:

$$T_{fm} = \frac{T_{in} + T_{out}}{2} \tag{2.23}$$

The heat transfer coefficient, h can then be calculated according to the following equation:

$$h = \frac{Nu(k)}{D_{ai}} \tag{2.24}$$

The flow inside the absorber tube of a PTC is turbulent and the Nusselt number can be calculates using Reynolds number and the Prandtl number (Leinhard, et al., 2012).

$$Nu = 0.023(Re^{0.8})(Pr^{0.4}) \tag{2.25}$$

2.3.2.2. *Hydraulic Modelling*

Given the cross sectional that is cut in the longitudinal axis, figure 2.6 is shown:

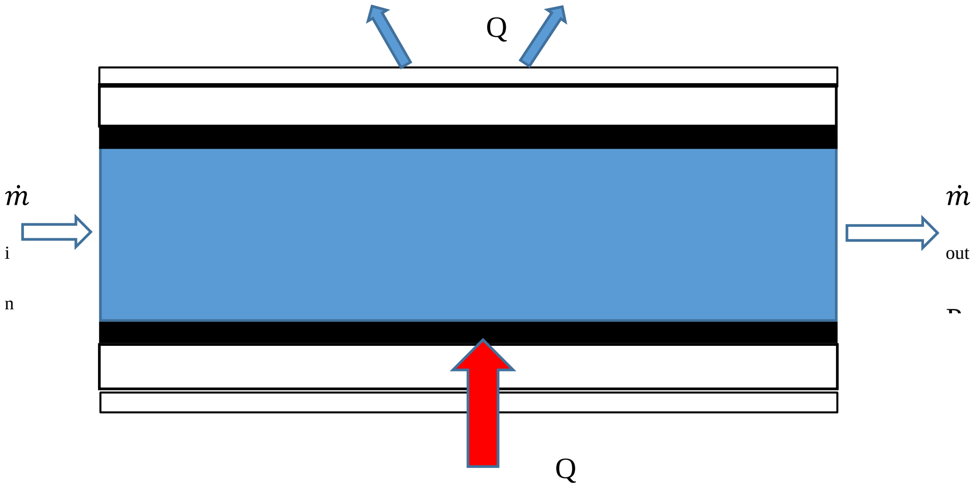

Figure 2.6. Cross sectional area of the absorber tube

Using the annotation from figure 2.3 and figure 2.6, the pressure drop equation is obtained by the following equation:

$$\Delta P = f_r \left(\frac{L}{D_{ai}}\right)\left(\frac{1}{2}\rho u^2\right) \tag{2.26}$$

Where the mean fluid velocity, u, is obtained by the following equation:

$$\mathrm{u} = \frac{\dot{m}}{\rho \frac{\pi}{4} D_{ai}^2} \tag{2.27}$$

The friction factor, f_r is calculated by the Moody equation for turbulent flow (Moody, 1994):

$$f_r = 0.184(Re)^{-0.2} \tag{2.28}$$

Thus, the pumping work demand of the fluid is given as:

$$W_p = \frac{\dot{m}}{\rho}\Delta P \tag{2.29}$$

2.3.3. BEARING STRUCTURE (PTC MODULE BASE)

The bearing structure of a typical PTC module consist of the main body which is usually a space frame or a tube structure and other elements. These elements include (Günther, et al., 2010):

- Mirror support points on the frame structure or on cantilever arms.
- Heat Collection Element (HCE) support.
- Structure for the mounting to the pylon.
- Pylons, and drive pylons.
- Foundation.

The functions of the bearing structure are to carry the mirror facets in the appropriate upright angular position, provide stability to the PTC module and to allow sun tracking. It is important to note that the material specification of the bearing structure must consist of a high stiffness component coupled with light weight construction. The reason is high stiffness requirements enable the parabolic trough to maintain high optical efficiency as any deviation from the ideal parabolic shape will lead to losses in optical efficiency. The high stiffness and light weight construction must be able to withstand the PTC module load and wind load due to its atmospheric exposure. Additionally, these requirements allow for longer troughs to be made so that the number of pylons and tracking units can be reduced which in turns reduces major costs. Examples of materials used for this construction are aluminium and steel.

Figure 2.7. Bearing structure of a PTC (Source: Günther, et al., 2010)

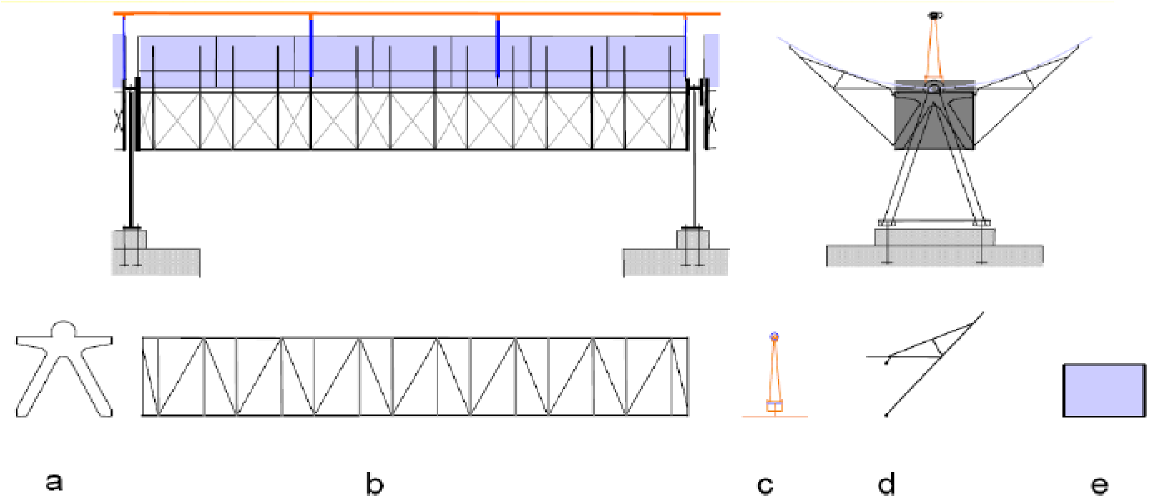

Figure 2.8. Bearing structure components. (a) front and rear endplates for mounting(b) space frame structure, (c) receiver supports, (d) cantilever arm, (e) mirror facet (Source: Günther, et al., 2010)

2.4. PTC POWER PLANT INTEGRATION AND CHALLENGES

Most CSP projects currently under construction or development are based on parabolic trough technology, as it is the most mature technology and shows the lowest development risk. Parabolic troughs and solar towers, when combined with thermal energy storage and a power block unit, can meet the requirements of utility-scale, schedulable power plants (Günther, et al., 2010). The process of a typical PTC plant is as follows: The energy supply of PTC modules is obtained from the sun by Direct Normal Irradiation (DNI) through a tracking and concentration process. The absorber converts radiation energy into thermal energy. The steam generator converts thermal energy into pressure energy of a gaseous medium. The steam turbine converts pressure energy into electrical energy which is then supplied to an electric field.

A PTC plant design is determined and built based upon a rated fixed design power. In the case were a designed plant can enlarge a solar field to harness thermal power above the needed criteria, it is necessary to have a thermal storage unit present. The excess thermal energy that was generated would be stored in the thermal storage unit, as the power block unit can no longer process the excess thermal energy due to its maximum load being reached. The excess thermal energy stored in the thermal storage unit can be later used in times when there is no or low irradiation from the sun and in times of demand. The solar field size is directly proportional to a thermal storage unit capacity. A design factor known as the “solar multiple” (SM) is used to find the ratio of thermal power of the solar field design to the required thermal power for the power block operated at full load (Günther, et al., 2010).

Figure 9 depicts a schematic of an indirect steam generator power plant. This type of design consists of two fluid cycles, which is the HTF cycle and the Rankine cycle. The thermal connection is realized in the Heat exchanger where the molten salt solution act as the HTF. Indirect steam generation is the most commercial way of PTC plant design due to its advantages which include a better control of the solar field as compared to that of Direct Steam Generator (DSG) and its thermal storage ability and capacity. Other examples of typical HTF liquids could be mineral oil, synth oil, silicon oil, nitride salt, carbonate salt and liquid sodium.

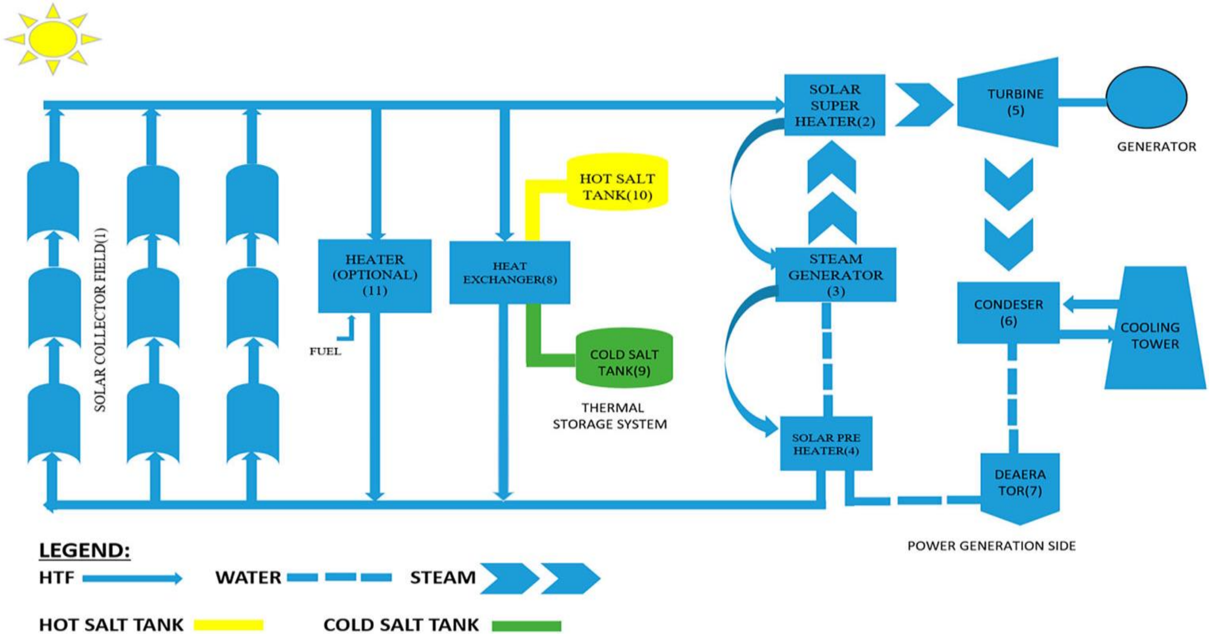

Figure 2.9. Schematic diagram of a PTC plants (Source: Bellos, et al., 2018)

2.4.1. PTC POWER PLANT PERFORMANCE AND EFFICIENCY

2.4.1.1. Major Plant Efficiency Parameter

Mathematical modelling enables the thermal efficiency of a PTC power plant to be produced effectively. By combining equation 5, 7, 8, 9, 14, 15, and 21, the following equation is given (Bellos, et al., 2018):

$$\eta_{th} = \eta_{opt,max} K(\theta) - U_L \left(\frac{T_c - T_{atmosphere}}{C G_b} \right) \tag{2.30}$$

The overall plant efficiency, η_{ovr}, assesses the pumping work demand as the equivalent primary energy consumption which is deducted from the useful heat production (Wirz, et al., 2013):

$$\eta_{ovr} = \frac{Q_u - \frac{w_p}{\eta_{el}}}{Q_s} \tag{2.31}$$

Where the η_{el} is the average electrical efficiency which is usually close to 35% (Wirz, et al., 2013).

2.4.1.2. PEC

A plant performance can be evaluated by the Performance Evaluation Criterion (PEC). This evaluates the heat transfer coefficient enhancement of an alternative design compared to the reference case. This index assesses the increase of the heat transfer coefficient under the equivalent conditions of “same pumping work demand” and represented as follows (Hasanpour, et al., 2014):

$$PEC = \frac{\left(\frac{Nu}{Nu_0}\right)}{\left(\frac{f_r}{f_{r,o}}\right)^{\frac{1}{3}}} \tag{2.32}$$

Nu_0 and $f_{r,o}$ represents the Nusselt number and friction factor at reference point respectively. If the PEC value is above 1, then there is heat enhancement in the flow which leads to an enhancement in the heat transfer coefficient. This ultimately leads to higher heat transfer rates and lower absorber temperatures. Thus, more useful heat production thereby minimising thermal losses.

2.4.2. PTC PLANT CHALLENGES

A PTC power plant experiences major challenges in harnessing solar irradiation. In dealing with the challenges of a PTC power plant, it is important to know the source of these challenges. One can start by analysing the efficiency structure of a plant to derive the major losses that affect the efficiency parameters. The major challenges can then be categorized according to the following:

i. Optical Losses: The optical losses affect the solar field efficiency and losses are caused by geometrical inaccuracies**,** beam incidence angle variance, shadowing losses, limited reflectivity, absorptance and transmittance.

ii. Thermal Losses: The thermal losses also affect the solar field efficiency and losses occur in the absorber tubes in the HTF pipes. Thermal losses of a system are generally dependent on temperature difference between the surrounding air and heat transfer medium.

iii. Power block losses: These losses affect the power block efficiency where thermal energy is converted to mechanical energy. They are caused by additional thermal losses from HTF to water/steam, thermal to mechanic conversion, pressure losses, friction losses and generator losses.

The presented thesis focused on the optical losses caused by limited reflectivity, transmittance and absorption in arid regions primarily caused by mirror soiling. Solutions and developing procedures thereafter will be discussed in the topics to come.

2.4.2.1. Optical Losses Caused by Limited reflectivity, Absorptance or Transmittance of Mirrors as a result of Dessert Location

According to equation 12, the major parameters that affect the maximum optical efficiency of a PTC module mirror facet are reflectivity, absorptance and transmittance. The process of energy conversion on a PTC collector starts off with the solar rays being reflected from the mirror then transmitted from the glass cover to the absorber and then finally absorbed as solar energy. The essence of an efficient PTC plant is strongly related to these parameters and the solar collector of a PTC module is usually designed taking these parameters into high priority design consideration.

There are external environmental factors that occur within an optimum location that limit these parameters. For optimum overall efficiency of PTC plants, a solar field of PTC modules is installed at regions with a high DNI; coincidentally, regions with high DNI are dry desert regions. Deserts and arid regions usually have low precipitation, little cloud formation, little to no vegetation and close to zero evapotranspiration. Due to these features, desert regions with high DNI values are suitable for the optimum performance of CSP plants, although with the penalty of exposure to frequent occurrences of desert sandstorms. Table 2.1 shows the potential location of CSP plant (high DNI regions) with massive fallen dust amounts.

Table 2.1. Fallen dust for various locations of interest to CSP Plant. (Source: Sansoma, et al., 2017)

Country	**Location**	**Fallen Dust (tons/km^2/year)**
Iraq	Khur Al-Zubir	75.92
Iraq	Um Qasir	193.47
Oman	Al-Fahal	89
Saudi Arabia	Riyadh	392
Palestine	Dead Sea	45
Chad	North Dianena	142
Nigeria	Kano	137-181
Greece	Crete	10-100
USA	Arizona	54
USA	Nevada	4.3-15.7

USA	California	6.8-33.9
Libya	Libya	155
Morocco	Tan Tan	175
Morocco	Boujdour	219
Mauritania	Dakhla	191
Mali	Niger river	913-10446
Australia	Namoi valley	16.9-58.2
China	Shapotou	372

Sand and dust storms are not only harmful to human beings, but they are also harmful to the performance of a PTC plant. They are considered lower atmosphere events that occur when strong winds pass over dry loose sand or soil. Known as a haboob (Arabic for strong wind), sandstorms are caused by airborne organic and inorganic debris, ranging from large sand particles to small dust particles, lifted from the surface of the land. Dust from storms can be carried by winds hundreds to thousands of miles and can reach elevations of 10,000 ft. Depending on weather conditions and particle size, dust can stay in the atmosphere for a few hours up to ten days (Gross, et al., 2018). As a steady wind begins to blow, fine particles lying on the exposed ground begin to vibrate. At greater wind speeds, some particles are lifted into the air stream. When they land, they strike other particles which may be jerked into the air in their turn, starting a chain reaction. Once ejected, these particles move in one of three possible ways, depending on their size, shape, and density; suspension, saltation, or creep. Suspension is only possible for particles less than 0.1 mm (0.004 in) in diameter (‘Desert’, 2020).

Suspended dust particles, sandstorms, dust storms and light rains are inevitable in dessert regions and they are the major cause of mirror soiling. Mirror soiling is the strongest factor that affects the reflectivity of mirror facets. Poor reflectivity results in poor transmittivity and therefore poor absorptance ultimately leading to a deficiency in plant optical performance and plant overall performance.

2.5. MIRROR SOILING

The deposition of dust particles on a reflector mirror facet of a PTC module is known as mirror soiling. Dust particles can deflect and absorb the solar incident rays projected from the sun and prevent DNI from reaching the reflector target.

A single dust particle is composed of discreet electric charges and when hit with the electromagnetic incident ray becomes excited and is set to move in an oscillatory manner. Excited electric charges radiate electromagnetic energy in all directions, this is known as elastic scattering and a percentage of the excited electromagnetic incident energy is converted to thermal energy by absorption. A combination of elastic scattering and absorption is known as extinction and this is the total energy loss of the incident ray from the sun (Bohren, et al., 1983). The elastic scattering of incident rays is dependent on size, shape and chemical composition of dust particles and the direction at which the light is scattered (Li, 2008). Figure 2.10 shows the explained phenomena of light rays hitting a single dust particle.

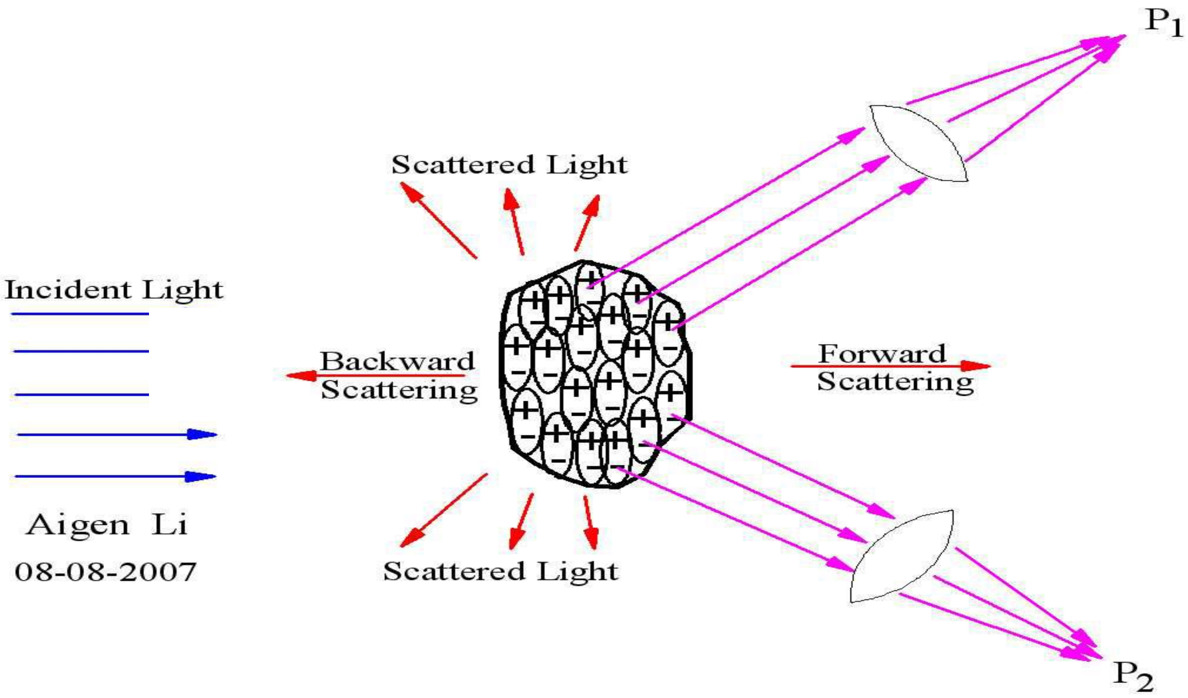

Figure 2.10. Concept of incident rays on a dust particle (Source: Li, 2008])

The nature and quantity of mirror soiling is site specific and measuring mirror soiling is recorded and reported over a significant amount of time ranging from 6 months to 12 months (Bouaddi, et al., 2017 and Griffith, et al., 2017). This is because reflectivity is analysed in this time span.

2.5.1. EFFECTS OF MIRROR SOILING

Mirror soiling is known to cause the following in PTC plants:

- Dirty mirror facets.
- Minimal mirror reflectivity.
- Reduced DNI absorption.
- Low optical performance.
- Low plant performance.
- High volume usage of water for cleaning.
- Reduced revenue for a CSP plant

Understanding these effects, like every problem life has to offer, is the first step to solving the problem. Scientists and researchers have certainly developed ideal solutions that address the needs of power plants in this regard; these include cleaning methods and mirror prevention techniques.

2.6. CONVENTIONAL AND NOVEL SUSTAINABLE TECHNIQUES IN CLEANING MIRRORS IN COMMERCIAL PLANTS

To deal with mirror soiling, PTC plants have employed cleaning strategies and minimisation plans to reduce or eliminate mirror soiling. The most common methods involve a large volume use of water whereas the dry methods are gaining more attraction as they are more compatible for PTC plants in dessert regions.

2.6.1. WATER-BASED WASHING METHODS

PTC plants in general are not considered sustainable if the impact of water is not analysed properly and accordingly (Hadian, et al., 2013). For conventional methods of cleaning, water is the major compound used either alone or in conjunction with other mechanical and non-mechanical devices.

Water-based methods can generally be classified into two categories namely: Contact and Non-contact cleaning.

2.6.1.1. Non-Contact Cleaning

When used alone, the cleaning effectiveness are determined by a high-pressure system, the nozzle characteristics, and the distance between the high-pressure system and the reflector surfaces. Although increasing the inlet pressure of water enhances the cleaning effectiveness (Anglani, et al., 2017), this solution is not advantageous because of its consumption of additional water volumes. The following techniques are described and are used as follows:

- **High-Pressure Spraying**

This method involves a high-pressure stream of water directed to reflectors and glass absorbers. According to this technique, applying water on both glass and acrylic mirrors can recover 98% of their initial reflectance, whereas acrylic mirrors restore just 92% reflectance (Roth, et al., 2017)

Figure 2.11. High-pressure cleaning with hand-held nozzle (Source: Cohen, et al., 1999)

Approximately 0.19 gallons of water per square meter of aperture area are used with this method, and this increases the reflectance by 3% (Cohen, et al., 1999). A high- pressure spraying machine usually consist of a surface cleaner, and the fluid is applied at a pressure ranging from 5–200 MPa. Figure 11 depicts a high-pressure system being used to clean PTC facets.

- **Deluge Spraying**

This method requires a large volume of water at a low pressure and the spray system delivers a ‘deluge-type’ of spray. Reflectivity increases by 1% and water consumption is 20% higher than the high-pressure spraying system (Cohen, et al., 1999).

Figure 2.12. Deluge valve (body) (Source: Rapidrop, 2020)

Figure 2.13. Simultaneous cleaning of the mirrors with a "deluge-type" stream (Source: Cohen, et al., 1999)

2.6.1.2. Contact Cleaning

This method is effective in restoring full reflectance after mirror soiling occurs. The method utilises brushing, scrubbing, or wiping on soiled surfaces. Contact methods generally achieve high cleaning effectiveness; however, they can cause harm or damage to reflectors by leaving scratches and delamination over time. It became known that using a soft brush with water was a key solution in preventing physical damage on reflectors (Sansom, et al., 2016). Thus, a combination of scrubbing and rinsing is effective for highly adhered dust particles; however, before applying any cleaning device, water spray should be first applied to remove loose dust (Begeron, et al., 1981)

The following techniques are applicable as a contact cleaning method:

- **Manual Cleaning**

This method is time-consuming and justified because of its effectiveness. It involves man labour that physically washes the mirrors with cleaning agents such as a soft brush and demineralized water (Cohen, et al., 1999). Due to the nature of the method, the method requires great effort and thus cheap labour.

Figure 2.14. Pressure washing device with hand spray nozzle accessory (1), water-fed natural horse-hair bristle brush accessory (2), steam cleaner (3), demineralized water tank (4), and additives tank (5). (Source: Raza, et al., 2016)

- **Semi – Autonomous Cleaning**

This is the most common option used currently (Burgaleta, et al., 2012, and Bouaddi, et al., 2018). The procedure combines man-labour with machine-labour to wash rows of reflectors sequentially and starting each time from a reference point of the adjacent rows that need washing. In the case where rows are facing each other, the man-controlled machine cleans simultaneously (figure 2.13).Generally, semi-autonomous cleaning vehicles used in CSP plants are trucks equipped with a tank and pump unit in addition to the necessary cleaning tools, that is nozzles for water jetting at a range between 30 bar and 200 bar and brushes, squeegee, or sponge for contact cleaning (Cohen, et al., 1999) Figure 2.13 and figure 2.15 shows a semi-autonomous cleaning of two distinct types.

From figure 2.13, two arms are needed for washing the upper and lower part of PTC modules. Depending on the CSP technology used, the cleaning tool can adopt different designs to satisfy cleaning requirements. In the case of figure 13, the adoption of two arms was necessary to carry out optimal cleaning functions due to its parabolic geometrical structure. Cleaning vehicles are evaluated according to their fuel consumption, water consumption, the time required for cleaning and the number of operators needed. To achieve optimal results with semi-autonomous cleaning, it is necessary to have a high pressure with high volumes of demineralised water applied on PTC modules.

By using these vehicles, the potential to sprinkle dust after cleaning surfaces is high due to the unpaved roads or the deterioration of paved roads. Also, operator error is a major possibility and can cause damage and corrosion to mirrors surfaces.

Figure 2.15. Semi-autonomous cleaning (Source: Bouaddi, et al., 2018)

- **Autonomous Cleaning**

This method of cleaning has no human involvement whatsoever and many procedures under this method is particularly used for flat mirror facets technology of CSPs. The robots designed are generally equipped with a navigation system and optical sensors. The most common commercial unmanned vehicles are Hector for the Heliostat technology and PARIS for parabolic troughs (Hardt, et al., 2011, and .

Figure 2.16. PARIS (Source: SENER, 2020)

The PARIS cleaning system is a 4x4 low weight vehicle which minimizes the impacts on the roads while improves its manoeuvrability. Its small size allows it is on-field parking, minimizing downtime deployment and collection of vehicles. The procedure incorporates a wet brush and performs a wet mechanical cleaning using rotary motion which can significantly raise the reflectivity factor of the mirrors in just one passing. This efficiency allows for reducing the cleaning frequency as well as minimizing the water and fuel consumption (SENER, 2020).

The use of drones, unmanned aerial vehicles (UAV) and counter balancing devices are in development phases and appear to be potential future automated solutions for CSP plants.

2.6.2. WATER-SAVING CLEANING METHODS

These methods are designed to use a low volume of water to address the water scarcity challenges faced by CSP plants. The technology used here employs a low water consuming feature and reports on the cost measure within utilization of the method. The following are considered suitable water-saving novel cleaning methods:

- **Ultrasonic Cleaning**

This is a non-contact form of cleaning and this method uses ultrasonic waves which generate a cavitation bubble into liquids. This method is achieved through the piezoelectric materials that changes their form under the effect of electric charge (Kohli, et al., 2011). When liquid is exposed to acoustic ultrasonic wave pressure caused by the piezoelectric material under a high frequency (above 20kHz), cavitation occurs. Then microbubbles implode releasing shock waves which delivers microscopic high velocity (100m/s max) jet stream to nearby surfaces (other microbubbles, solid walls, free surfaces) (figure 2.17). This removes deposited particles and eliminates mirror soiling.

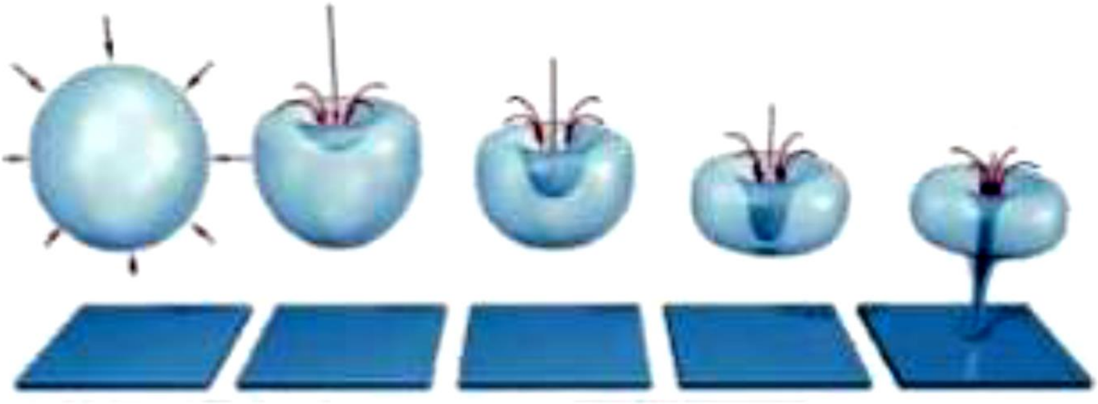

Figure 2.17. Bubbles implosion evolution when applying high ultrasonic waves (Source: Atlas Copco, 2018)

In comparison with other technologies such as pressurized water or brushing, this technology has the advantage of going in the deep imperfections of the material (cracks and pores) and as a result, provides better cleaning performance in comparison with the traditional ones (Verma, 2018). The water consumption is said to be 0.025 L/m^2 when horizontally orientated. Deionized water consumption can be regulated by means of nozzles and sweeping speed controlled by measuring the process cleaning process time (Bouaddi, et al., 2018). This method has proven to be one of the most effective cleaning methods in CSPs.

- **Automated Wiper Lip Cleaning Methods**

This cleaning method addresses the fact that due to climate and weather change; water-soluble particle is cemented onto mirror reflector surfaces over time. In dealing with these cemented particles, the effort and volume of water is significantly higher than that used on the usual mirror soiling phenomena caused by sand and dust storms. Thus, a simple cleaning method with low water consumption like a wiper system can be applied (Bouaddi, et al., 2018). To avoid high labour costs, automated systems can be installed.

Dew is a major source of water in arid regions where it could provide up to 40% of the annual water deposition (Lkouch, 2010). It is desirable for CSP plants to clean mirrors after every dew formation. Using a dew-based cleaning method was proposed where wipers, cleaning angles and surface wetting time were varied and tested. This study revealed that a 99.3% cleaning efficiency is obtained using normal single wiper, versus 98.9% results from applying industrial wiper (Farag, 2015).

2.6.2.1. Dry and Semi-Dry Cleaning

The cleaning techniques used here are completely independent of water usage and majorly dependent electro-mechanical means to eliminate mirror soiling. The cleaning method is presented as follows:

- **Electrostatic Method**

Here, a transparent conductor sheet is charged with a high voltage and by applying phased voltage pulses, the electrodes charge the dust particles which are then removed by a three-phase alternating electric field (Sayyah, et al., 2016). In order achieve this method, electro-dynamic screens which are designed by laminating a transparent dielectric film, containing parallel electrodes are fitted on reflectors of CSP technology as seen in figure 2.18.

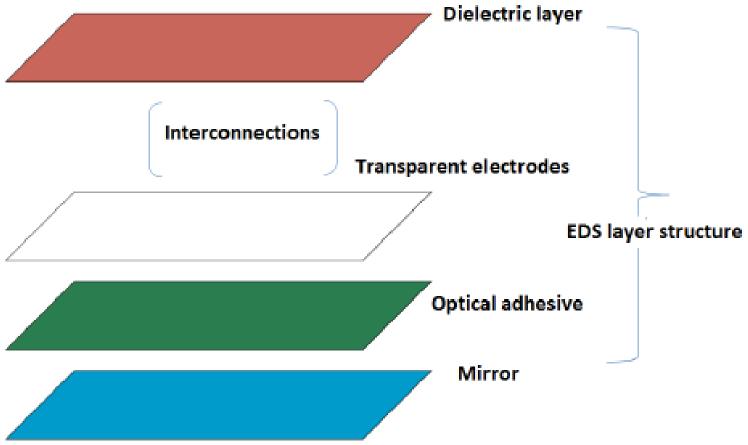

Figure 2.18. The components layers of EDS technology (Source: Sayyah, et al., 2016)

The electrostatic method consumes low energy, and its effectiveness has been reported to achieve mirror soiling reduction of 90% in 2 minutes. However, this performance is true for certain condition which are the humidity levels and the deposited size particle.

2.6.3. SOIL PREVENTION METHODS

The usage of mirror soiling prevention techniques is a way to reduce the frequent cleaning of reflectors. Researchers have developed anti-soiling coating and dust barriers to prevent mirror soiling and they are described as follows:

- **Anti-Soiling Coatings**

This preventive measure utilizes a form of surface coating on a chemical level applied on reflectors to minimize the deposition of dust particles. There are two major categories of coating that are available ad developed:

i. **Hydrophobic Coating**: This is a water-repellent surface coating that has been developed from the observation of the nature of lotus leaves (Lorenz, et al., 2014). The principal factors involved of this form of coating are namely the contact angle between water and surface, low surface energy and the roughness that creates an uneven surface where air bubbles are trapped. A superhydrophobic coating is considered when it achieves a high contact angle of 160° or above. With a high contact angle, low surface energy and a high surface roughness the friction on reflector surface is decreased. This enables water droplets to slip easily off the surface creating a self-cleaning feature on mirror surfaces removing dust particles (Aoukli, 2018). To prepare a superhydrophobic coating, there are different methods based on silica, combined with some fluoropolymers or polyurethane of polisiloxane binder applied using spin and spray technique, while other methods (Ennaceri, 2016) are based on Al_2O_3, TiO_2 and ZnO top coatings using the Ion Layer Gas Reaction (Spray-ILGAR) technique.

ii. **Hydrophilic Coating**: This is a water-attracting surface coating that enables the spread of water across the mirror reflectors (Gua, 2005). A superhydrophilic coating is considered when the contact angle is 10° or less. With a low contact angle, a high surface energy, and a low surface roughness there is a greater spread of water across reflector surfaces. The water spread across reflector surfaces enable the soiling to be washed away. To prepare super hydrophilic coatings, there are different materials such as WO_3 and TiO_2 used and the most common material used is TiO_2. These materials have photocatalytic ability which causes the decomposition of organic material under solar irradiation.

A major disadvantage to using anti-soiling coating is the low durability and subsequent loss of reflectance.

- **Wind Barriers**

Solid wind barriers placed in the prevailing wind direction could prevent and minimize mirror soiling that occur on mirror facets. An optimally designed wind barrier can deflect a huge number of particles over the solar field of about 86% and reduce the mirror soiling to an exceedingly small amount of about 0.8% (Moghimi, et al., 2018).

The use of wind barriers was further validated and simulated. According to Sansom, et al., 2018, the use of a porous barrier can redirect a more significant number of dust particles as compared to that of a solid barrier. The paper uses CFD and test procedures for validation. This solution is a different solution compared to security fences and wind breaks that are commonly used in CSPs.

Computational Fluid Dynamic (CFD) solutions have shown that mirror soiling is reduced effectively, and the use of wind barriers can reduce the costs of CSP plants (Moghimi, et al., 2018).

Not much literature on this method have been researched and made readily available.

Figure 2.19. A wind barrier structure (Source: Bouaddi, et al.,2018)

2.7. COMPARATIVE FEATURES

Table. 2.2. Comparative parameters of available Cleaning method

Features		**Water-Based Non-Contact Washing Methods**	**Water-Based Contact Washing Methods**	**Ultrasonic Cleaning**	**Electrostatic method**	**Anti-soiling Coating**	**Wind Barriers**
Cleaning Effectiveness	**Cleaning Capability**	Average	High	High	Average	Average	Average-High
	Cleaning operators	Average	Average	Low	Low	Not Applicable	Not Applicable
	Speed of Cleaning	Average	Low	Average	High	Not Applicable	Not Applicable
	Frequency of Cleaning	High	High	Average	Average	Low	Low
Environmental Impact	**Energy Consumption**	Average	Average - High	Average	Not Applicable	Not Applicable	Not Applicable
	Water Saving	Low	Low	High	Average	High	Not Applicable
Economic Implications	**Replacement of Components**	Average	Average	Low- Average	Low-Average	High	Low
	Investment Costs	Average	Average	High	High	High	Low

Table 3 shows a clear comparative table of the cleaning methods described in the previous topics. The cleaning methods explained in the table are majorly used by CSP plants. It is important to note each comparative advantage a cleaning method is over the another.

2.8. NUMERICAL STUDIES PERFORMED ON CSP PLANTS

Numerical studies have and always will be at the forefront of modern-day engineering. Researchers have used numerical modelling to understand different CSP phenomena and produce effective results accordingly for industrial use. The following sections give a review of the numerical cases that were done on CSPs.

2.8.1. GENERAL NUMERICAL STUDIES PERFORMED ON CSP PLANTS

According to the research publication by Yu, et al., 2016, a simulation and experimental investigation was utilized to increase the economic and safety performance of a 1MWe solar tower CSP plant located in China. The modelling methodology of this paper recorded that 100 heliostats each with 64 small square mirror elements that were 10 x 10 m in dimension was mounted on a 6.6m steel pillar. The rays of sunlight were concentrated by the heliostats and then reflected to a cavity receiver located 78m above a 118m high tower. The simulation system incorporated a multi-physical process, unsteady state, multivariable, strong non-linear and complicated coupled system (Yu, et al., 2016). Modelling was done with a simplified linear processing based on the lumped parameter method. The simulation platform used was STAR-90 and results showed that there were minimal errors between the simulation and experimental investigation. The paper concluded that it is possible to carry out a simulation process in this particular virtual environment to reduce the risk of a CSP.

Another numerical study conducted by Caranese, et al., 2017 investigated the simulation model for molten salt parabolic trough (MSPT) CSP parabolic trough. The need to have molten salt in a CSP plant stems from the requirement of a proper thermal logic management system as well as a freeze protection system for the heat transfer fluid settings during normal operation and non-normal operation. The simulation study utilized ASSALT, Ase software for SALT CSP plants for a 55 MWe Molten Salt Parabolic Trough CSP located in Tianjin Binhai. Modelling was done for every plant component and by defining the plant architecture as well as the procedures and the plant control strategies (Caranese, et al., 2017). The simulation platform was designed in a visual basic (VBA) environment which was specific to the MSPT plant. The logic for ASSALT software is shown by figure 2.20.

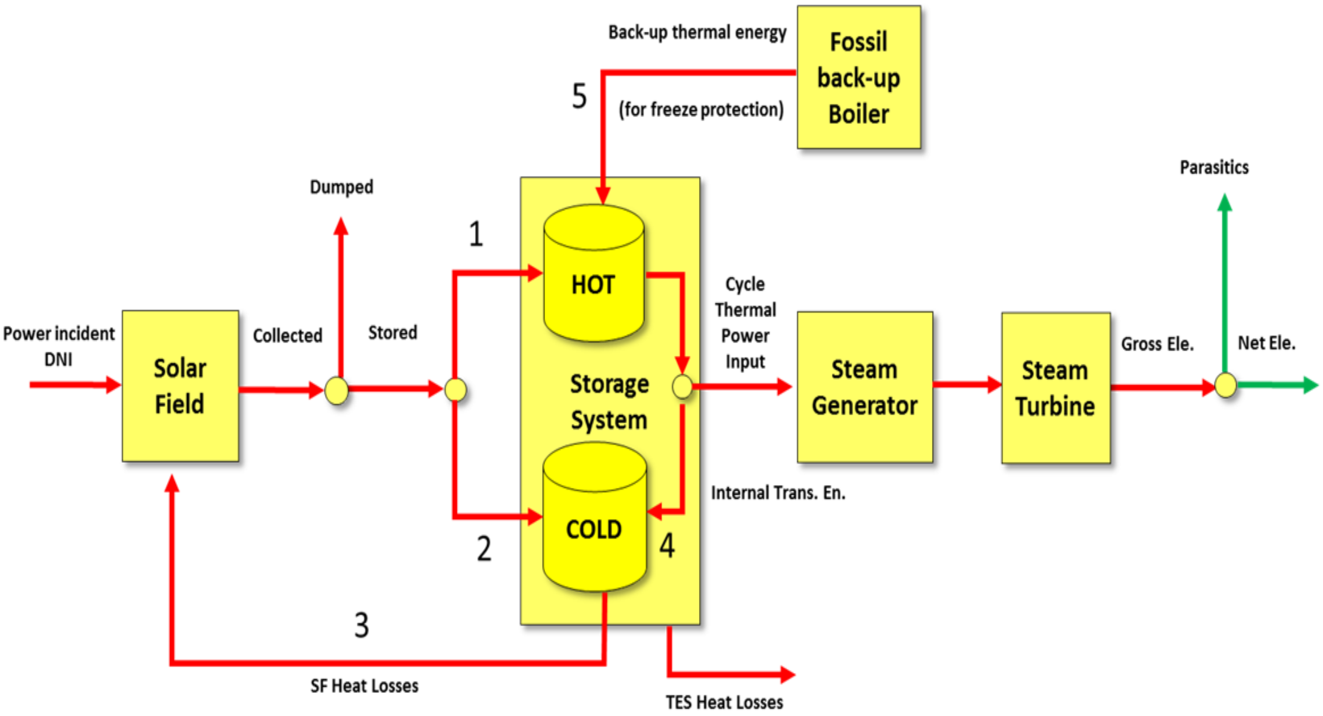

Figure 2.20. ASSALT procedure scheme (Source: Caranese, et al., 2017)

Results showed that the implementation of the ASSALT software produced an effective and realistic analysis for freeze protection and thermal storage as there is a lack of the on-purpose tool that deals with these CSP plant problems. This ultimately leads to higher plant efficiency.

A 100 MW CSP located near Nawabshah was designed, modelled, and simulated according to the research of Liaqat, et al.,2018. The establishment of this CSP was to increase supply of energy where a high DNI region was site selected based on research parameters. The design of this CSP incorporated a thermal storage to keep supply of energy operational when there is no solar irradiation. Modelling and simulation occurred with the use of SAM. SAM (systems advisory model), is a financial performance model developed by the national renewable energy laboratory (NREL). The results obtained from the simulation provided a sufficient amount of data in designing the power plant. It was concluded that further investigation was necessary in order to improve parameters such as the loop configuration of PTC and thermal capacity (Liaqat, et al.,2018).

A numerical study conducted by Merouni, et al., 2017 in Morroco, investigated the simulation for a 10MWe CSP plant using linear fresnel technology. The study was done in the north east region of Morroco in which the DNI was recorded to be 240 W/m^2 on a day average. A software package called Greenius was used to perform the simulations of the CSP plant. Greenius is a simulation software developed by the German Aerospace Centre (DLR) and it is majorly used for CSP plant simulations. The software takes in a one-year file of meteorological data with one-hour steps processing interval. According to the study, the meteorological data was obtained from a high meteorological station installed at the roof top. The modelling of the linear fresnel technology was done similarly to the system of PTC technology in which there was a system composed of row segments arranged in an array. Results of the study concluded that with DNI amounts, the plant can produce electricity for 9 hours with normal operations within that particular region in question.

2.8.2. NUMERICAL STUDIES PERFORMED RELATED TO MIRROR SOILING PREVENTION AND CLEANING

According to the publication presented by Anglani, F., et al. 2016, a numerical study was done on a high -pressure-water-spray cleaning for CSP reflectors. This investigation was done in order to optimize a cleaning strategy for the restoration of mirror reflectance after when mirror soiling has occurred. The paper identified water and air as the most conventional method for cleaning purposes and defined stationary water-jets as the cleaning structure used. Geometrical modelling of the nozzles, flat target surface and control volume was done in SolidWorks 2013. The nozzles selected were full cone types with 30x20mm section and 2mm diameter set up in an array with a 60mm distance between them. The model was then imported to ANSYS Workbench v.15 and processed with ANSYS CFX package. A computational domain of size 600x300mm was created around each nozzles' geometry and target flat surface to capture all surface characteristics. The fluid flow is not normal to boundaries on approach and thus a transformation of cartesian coordinates to polar coordinates occur during computational calculations.

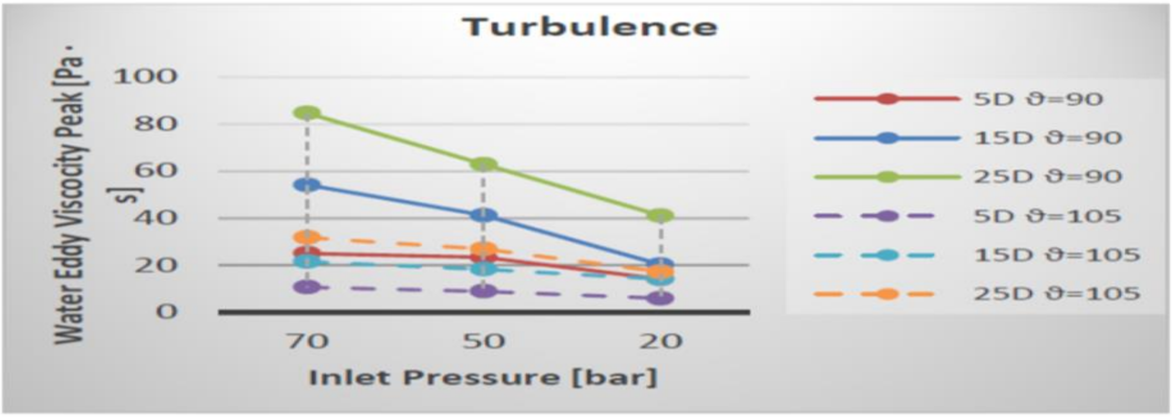

Figure 2.21. Turbulence peak at different inlet pressures and standoff distance and angle impingement (Source: Anglani, F., et al. 2016)

The SST turbulence model was used, and shear stress was generated after the jet impingement, at seven steps of pressure (5, 10, 15, 20, 30, 50, 70 [bar]), three levels of standoff distance (5D, 15D, 25D) and two angles of impingement (ϑ= 90° and ϑ=75°) (Anglani, F., et al. 2016). Results from this research showed that with a lower developed turbulence profile near the nozzle, the tilted scenarios are proven to clean mirror surfaces better as there were fewer surface vortices and possibilities for backflow to obstruct central jet flow.

According to research done by Sansom, et al., 2018, a numerical and experimental investigation was carried out on different forms of dust barriers to prevent mirror soiling. Dust barriers were modelled with different features to force dust particles to either be brought to rest near the barrier or to be deflected away from the solar field region. ANSYS-FLUENT was used for modelling and simulation of barrier various shapes and porosities ranging from 20-50%.

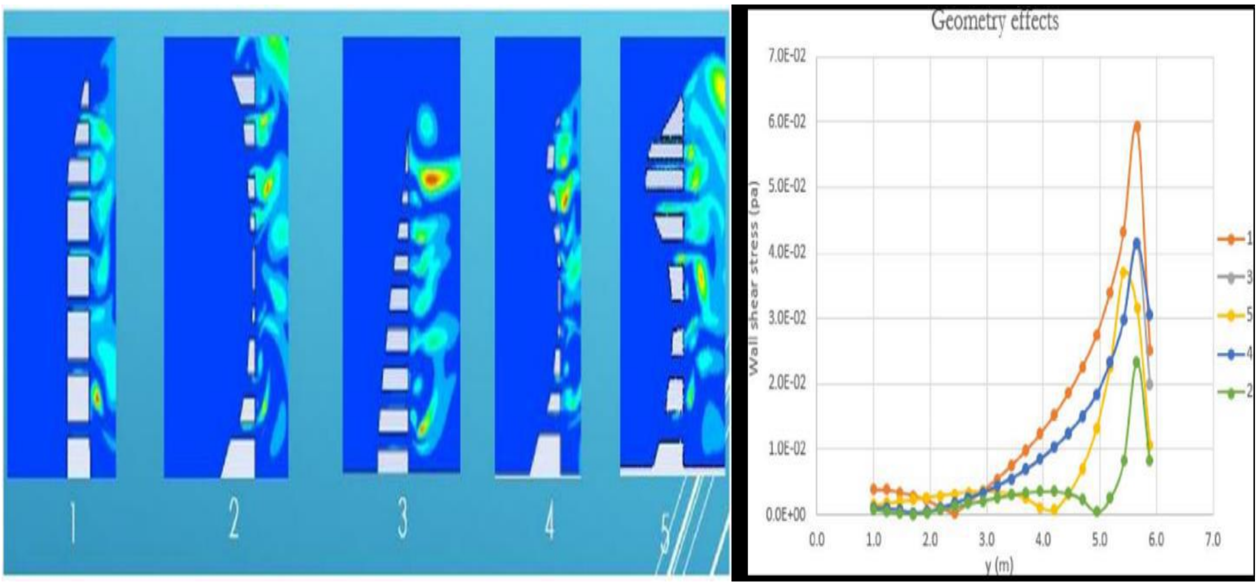

Figure 2.22. Five barrier shapes modelled (Source: Sansom, et al., 2018)

The turbulence model used for this investigation was the SST k-ω model which is known to have good predictions in adverse pressure gradients and separated flows. The 5 barrier structures with porosity of 30% and barrier height of 5.5m shown in figure 2.22 was ultimately selected after careful consideration of numerous simulations. STRAND7 was used to calculate the stress and mechanical analysis of the geometrical structure 5 in figure 2.22. STRAND 7 is a finite element analysis (FEA) software that generally provides users with stress and mechanical equilibrium.

The conclusion of the reported research yielded that a barrier with 35% porosity, curved beams, 6m high and 0.6m thick, 12m in length was a possible solution to minimizing mirror soiling in CSPs as shown in figure 2.23. A wind tunnel experiment was carried out for validation of the research report which was proven to be successful.

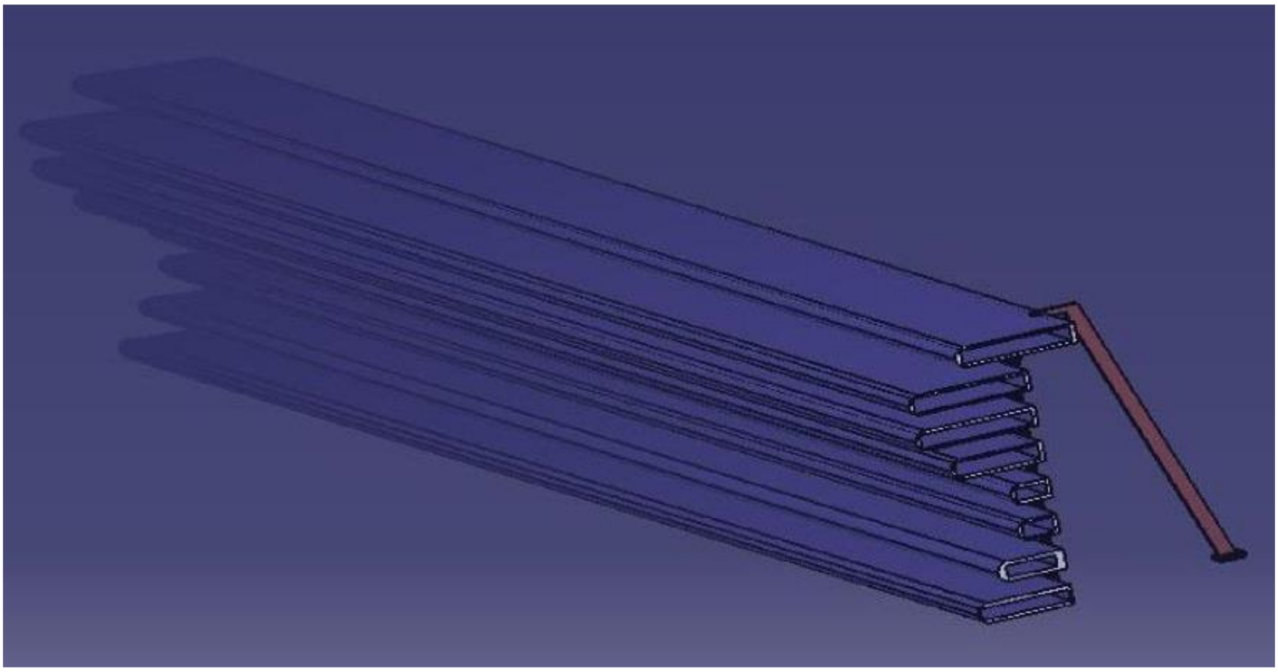

Figure 2.23. Proposed geometrical shape (Source: Sansom, et al., 2018)

2.9. CONCLUSION

This chapter was primarily focused on the design of PTC modules and cleaning methods utilised by CSP plants. The solar field of a PTC power plant consists of PTC modules that harnesses solar irradiation. During this process, there are major losses that occur within the PTC module and they must be accounted for in the accurate design of a typical PTC plant. The optical efficiency and thermal efficiency have adverse effect in the overall efficiency of a plant.

Due to the location of a CSP plant, which incorporates dust storm, dry weather, and sandstorms, CSP technologies are exposed to harmful conditions that can affect the performance of a CSP plant. Mirror soiling is an inevitable phenomenon that constantly occurs in dessert regions and is major contributor to the deficiency of optimum plant performance. The deposition and suspension of dust particles can limit the reflectivity of mirror facets thus causing a reduction in optical efficiency and a reduction in overall efficiency.

There are conventional and novel cleaning methods that are present to combat mirror soiling and increase mirror reflectivity. Some of the past and present methods used are known to have a cost, economic and environmental advantage over one another. The major aim of this dissertation is to expand on the wind barrier section by providing an optimized wind barrier using cases of CFD that proves the current validation.

There are numerical investigations that researchers have carried out for CSPs. Majority of the papers that are available have to do with increasing CSP productivity and efficiency. However, there is little research with regards to numerical investigations on wind barriers and generally on mirror soiling prevention and cleaning strategies. The proposed dissertation is necessary due to the fact that there is little research and serve as an alternative means to provide a faster solution compared to the current literature, effectively for the define mirror soiling problem.

CHAPTER 3

MODELLING AND MESH METHODOLOGY

3.1. INTRODUCTION

This chapter defines the basis of simulation and optimization. The chapter aims to introduce the problem statement as mathematical features readable for simulation and optimization process. Modelling and simulation are concrete cost-effective techniques used by researchers and scientists to bridge the gap between real-life situations and re-created digital scenarios of the real-life situations with the sole objective of overcoming a problem.

The genesis of modelling begins with the understanding of the problem. According to section 1.3 of chapter 1, the problem specified in the presented thesis has been defined and will be further broken down as dictated in this chapter. The figure 3.1 shows the flow chart of the modelling and simulation process used for this study.

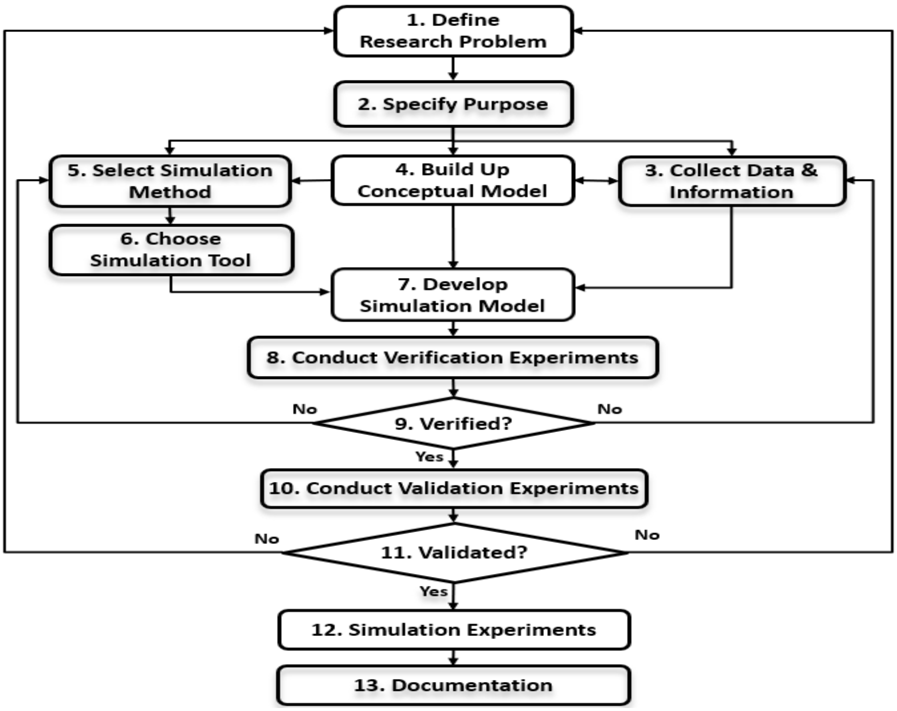

Figure 3.1. Modelling and Simulation Process (Source: Chenggang, et al., 2018)

3.2. PROBLEM LAYOUT

According to the section 1.2. of the problem statement, mirror soiling is the uncontrolled process of dust deposition on mirror facets on a PTC module in a plant. Further breakdown of this problem can be identified as follows:

i. The size, structure, number, and location of PTC modules within solar field.
ii. The size, structure, and location of the wind barrier to prevent mirror soiling.
iii. Definition of region parameters.
iv. The process of dust particles entering and exiting a specific location of a solar PTC field within a PTC plant.
v. The number of dust particles generally entering the region.
vi. The size of dust particles involved.
vii. The speed and direction of wind carrying dust particles exhibiting the dust storm

Solution development of the above sub-problems were done in a two-dimensional form. A 2D representation provides a simplified economic approach in modelling, in which the important necessary model features are still valued and considered during and after simulations. The problem will be considered infinitely in depth. By ultimately creating a solution form for the above listed breakdown topics, the model will be clearly defined.

3.2.1. THE SIZE, STRUCTURE, NUMBER, AND LOCATION OF PTC MODULES WITHIN SOLAR FIELD

The main shape of a PTC module is “parabolic” in design. For the stated problem, 6 parabolic trough collectors were considered. All PTC modules placed in space with each module placed equidistant (mirror pitch) in front of each other and having the same mirror aperture. The mirror pitch and aperture used were 2m long.

3.2.2. THE SIZE, STRUCTURE, AND LOCATION OF THE WIND BARRIER TO PREVENT MIRROR SOILING

A wind barrier defined by the flap length, a barrier height and a porosity feature were considered. The barrier height was kept constant at 1m, while the flap length, barrier height and porosity where variables. The overall solution of the stated problem is obtained when the variables are altered in the simulation process in such a way that mirror soiling is minimized producing an optimized barrier.

Depending on the type of barrier needed for the simulation case, the porosity feature would be completely neglected to produce a solid barrier case. Effectively, the wind barrier was placed in front of the first PTC module within the solar field region acting as an obstruction to the prevailing wind flow and direction. The distance between the wind barrier and the first PTC module was also kept constant at 1m.

3.2.3. DEFINITION OF REGION PARAMETERS

The region where the PTC modules and wind barrier were placed was defined as the domain. The domain is rectangular in shape with length and height of 62.5m and 20m respectively as it is a 2D model. With the assumption of the prevailing wind flowing from left to right, the inlet will be defined on the left side of the rectangular shape while the outlet will be located on the top and right side of the rectangular shape. The bottom side would then be defined as the ground wall of the domain.

The domain would then ultimately enclose the PTC modules and the wind barrier as defined. An atmospheric boundary layer (ABL) is imposed at the inlet of the domain to emphasize realistic conditions.

3.2.4. THE PROCESS OF DUST PARTICLES ENTERING AND EXITING A SPECIFIC LOCATION OF A SOLAR PTC FIELD WITHIN A PTC PLANT

This process was considered as the fluid dynamics of dust particles and modelled accordingly by the imposed ABL and fluid motion equation. Fluid dynamics have played a pivotal role in engineering. Given our domain, PTC modules and wind barrier we can use the flow chart in figure 3.2 to determine the basics of our governing equation.

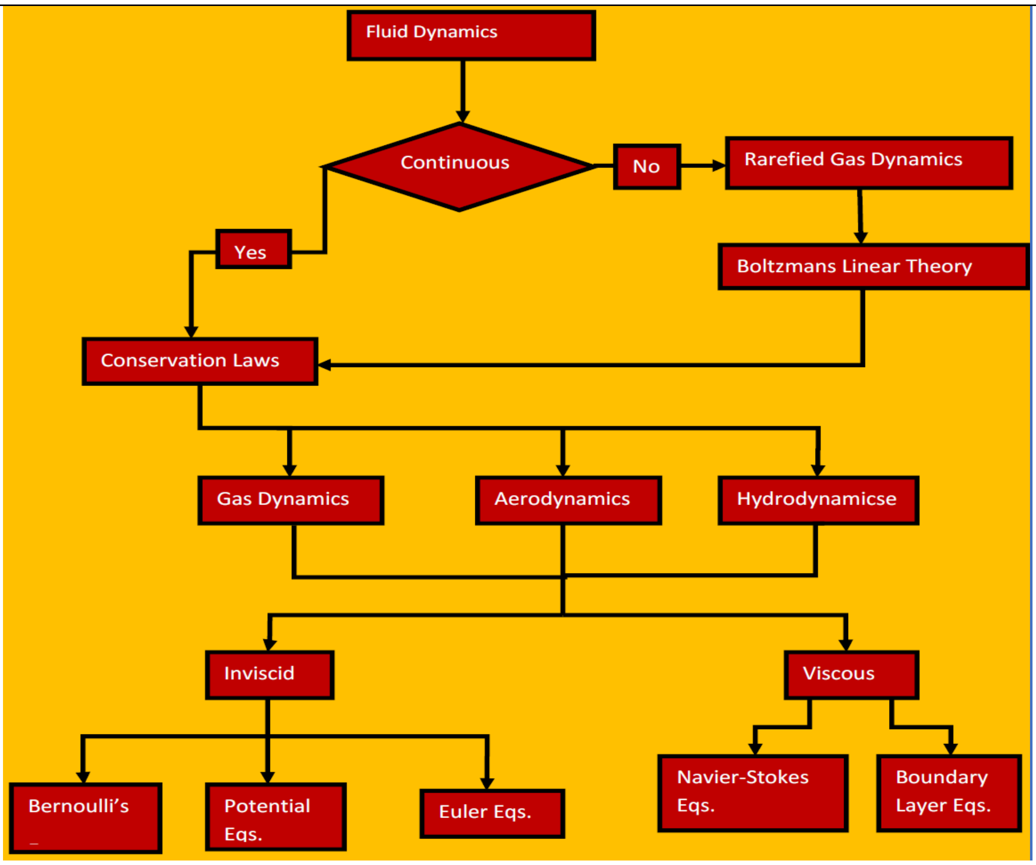

Figure 3.2. Basic fluid flow hierarchy. (Source: Sadrehaghighi, 2020)

The flow of dust particles was considered a viscous fluid according to figure 3.2 the governing equation that were used was the Reynolds Averaged Navier-Stokes (RANS) which is derived from the Navier-Stokes Equation, mass and momentum continuity equation which will be further explained in detail in the sections to come.

3.2.5. THE NUMBER OF DUST PARTICLES GENERALLY ENTERING THE REGION

Mirror soiling is a major parameter that needs to be measured. To do this, the number of dust particles are modelled with particle dynamics in a way that they can be tracked before and after the simulation process. Thus, the particle trajectory is governed by the Eulerian-Lagrangian method.

The Eulerian feature of this method attempts to tracks the fluid at a specific location in space (domain region) while Langranian feature looks at a dust particle as it goes through space and time. Dust particles are injected according to the number in the simulation case and were released at a height ranging from 0.5m to 3m at the inlet of the domain.

3.2.6. THE SIZE OF DUST PARTICLES INVOLVED

The study of dust particles is generally overly complex in nature because the realistic behaviour of dust particles in sandstorm is also a complex phenomenon. However, it has been reported and researched that particles ranging from 2.5 -10 µm are airborne with a wind velocity of 15-17m/s (Lee, at al., 2009) and particles ranging from 25-250 µm have a terminal velocity of 10m/s (Bagnold, 1965). There is generally little evidence of large particle deposition on PTC modules (> 250 µm) as reported in (Sansom, et al., 2018). Thus, for the current study, dust particles ranging from 25-250 µm were considered based on the assumption shown on table 3.1. The sand particles were chosen as inert particles with density of 1350 Kg/m^3.

The particle size distribution was defined based on Rosin-Rammeler diameter distribution method. The Rosin-Rammeler distribution employs a semi-empirical technique that explains particle distribution using two parameters. The mathematical function is based on the assumption that an exponential relationship correlates with the dust particle diameter and mass fraction of the dust particle provided that the diameter is greater. Figure 3.3 shows the sample collected at a specific CSP site. The size of dust particles was modelled according to the sample.

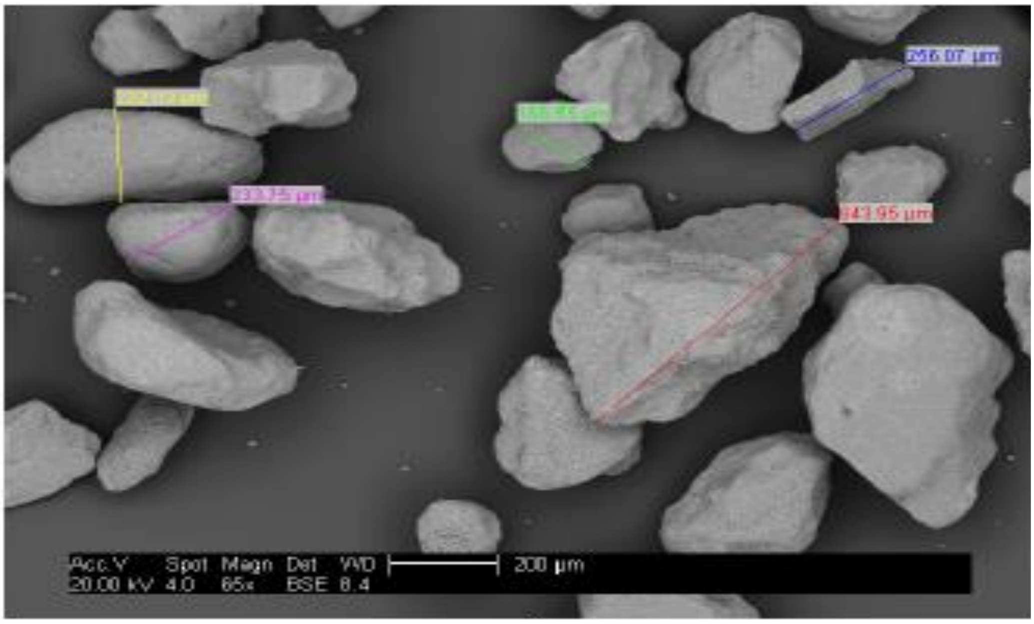

Figure 3.3. Particle collected from particle pole collector in Iran CSP plant at Ground level (Source: Moghimi, et al., 2018)

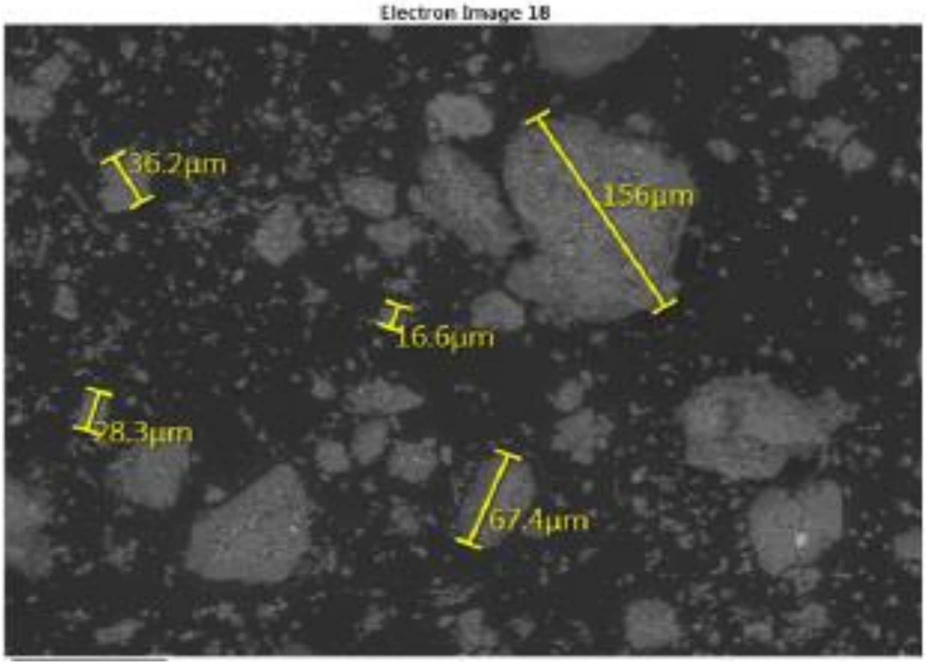

Figure 3.4. Particle collected from particle pole collector in Iran CSP plant above ground level (Source: Moghimi, et al., 2018)

3.2.7. THE SPEED AND DIRECTION OF WIND CARRYING DUST PARTICLES EXHIBITING THE DUST STORM

It was already assumed that the direction of the prevailing wind will flow from left to right in section 3.2.3. The wind speed was considered as 10m/s at the inlet of the domain. According to research (Klinkov, et al. 2005) the following assumptions in table 3.1 are considered as a rule of thumb:

Table 3.1. Assumptions of particle fate

Assumption	**Impact Velocity [m/s]**	**Particle Size[µm]**	**Particle Fate on PTC Module**
1	Less than 10	Greater than 250	Reflected from Surface
2	10	Smaller than 250	Sticks on Surface
3	10	Greater than 250	Erodes the surface

These assumptions were developed considering the figure 3.3 and 3.4.

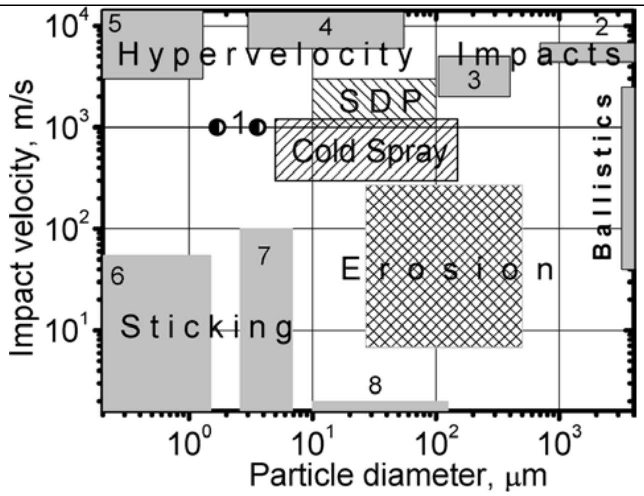

Figure 3.5. Classification of particle impact on solid surface (Source: Klinkov, et al. 2005)

3.2.8. MODEL REPRESENTATION AND SCHEMATICS

By combining all the geometrical requirements stated in from section 3.2.1-3.2.7, the problem can be represented as a schematic drawing in figure 3.6 and then represented as a model shown in figure 3.8.

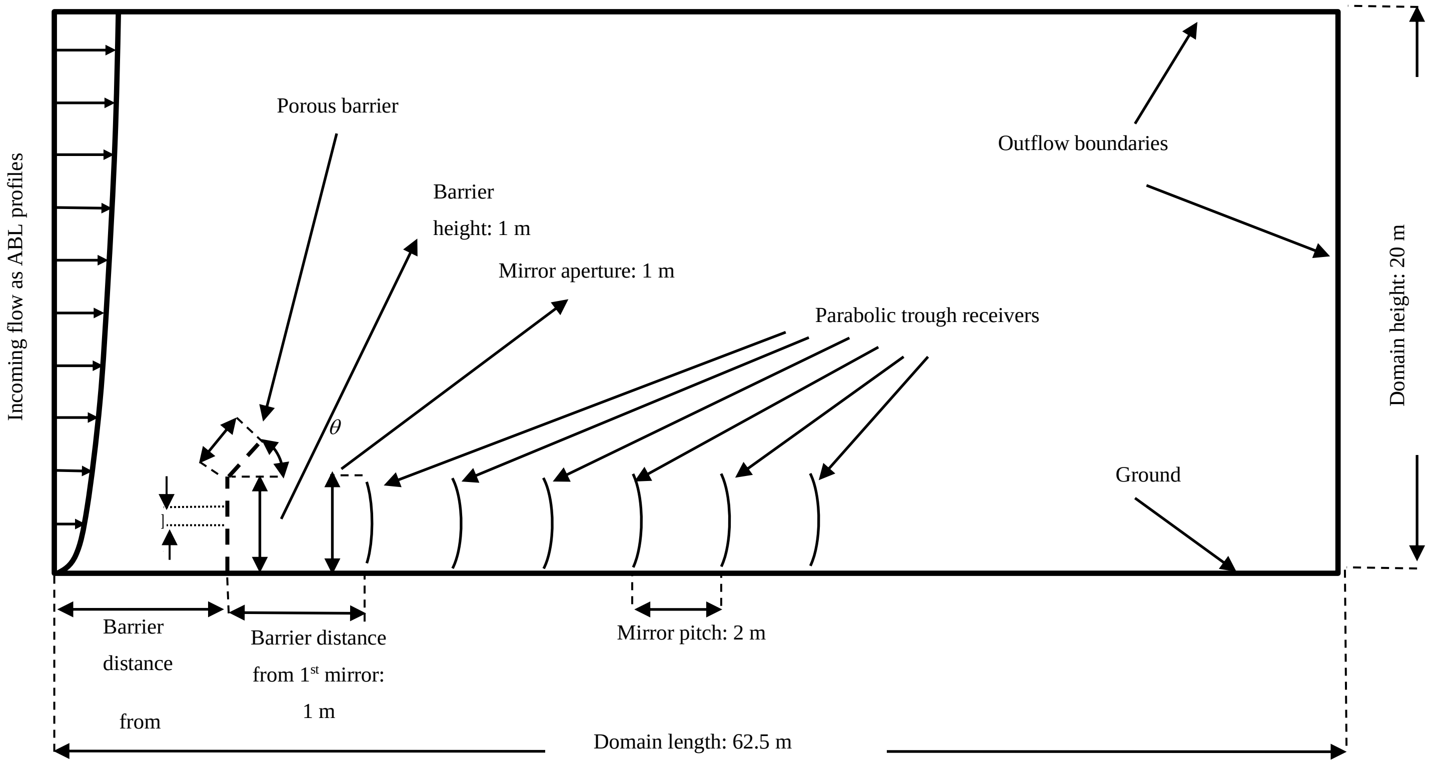

Figure 3.6. Schematic sketch of the domain with a porous barrier

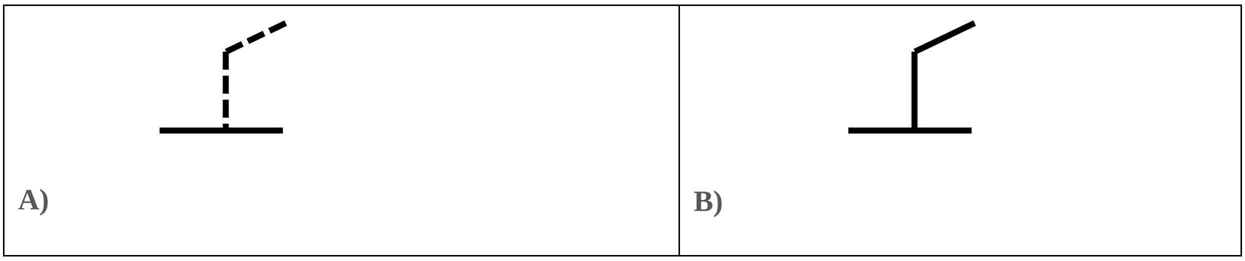

Figure 3.7. A(left)-schematic porous barrier and B(right)-non-porous barrier

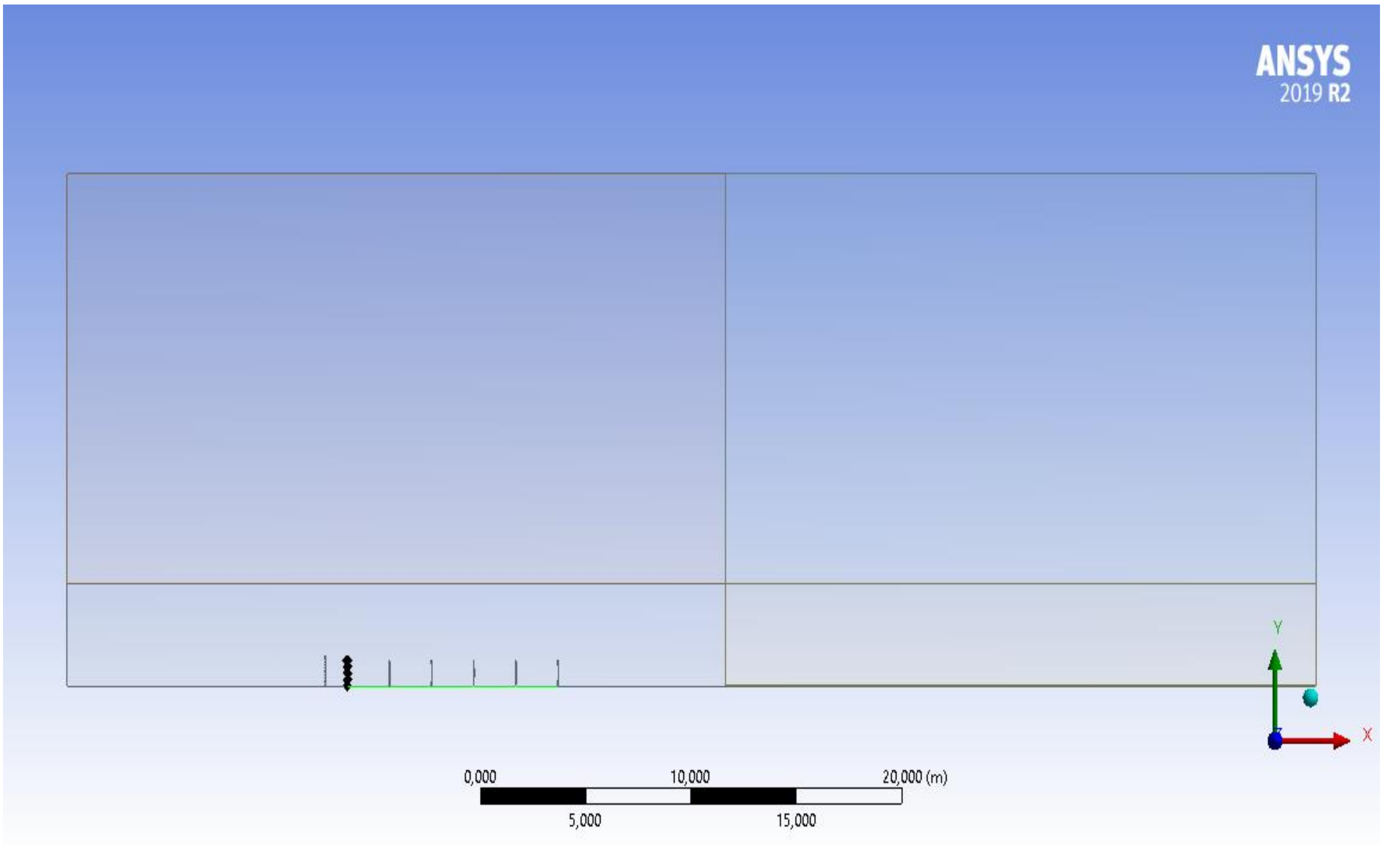

Figure 3.8. Model view of the problem in Ansys design modeler

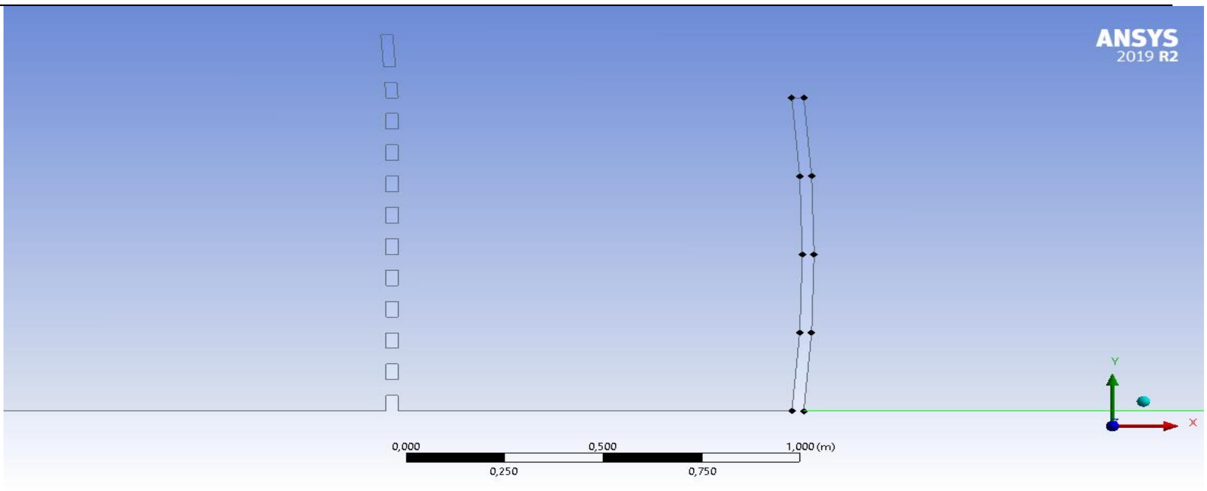

Figure 3.9. Zoomed in view of the porous barrier shown in model geometry

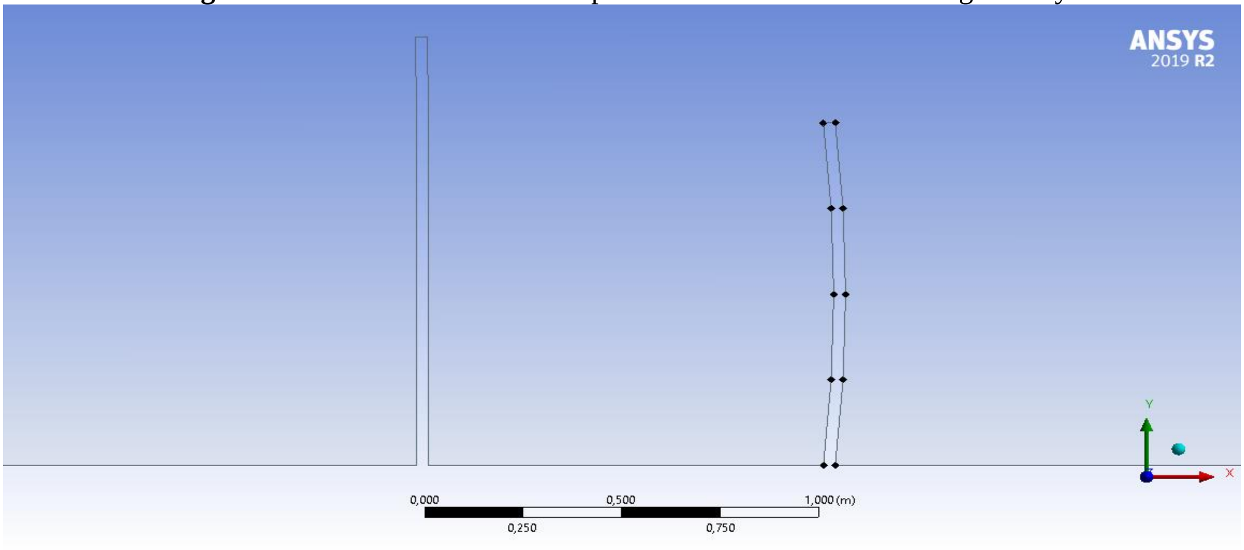

Figure 3.10. Zoomed in view of a solid barrier shown as model geometry

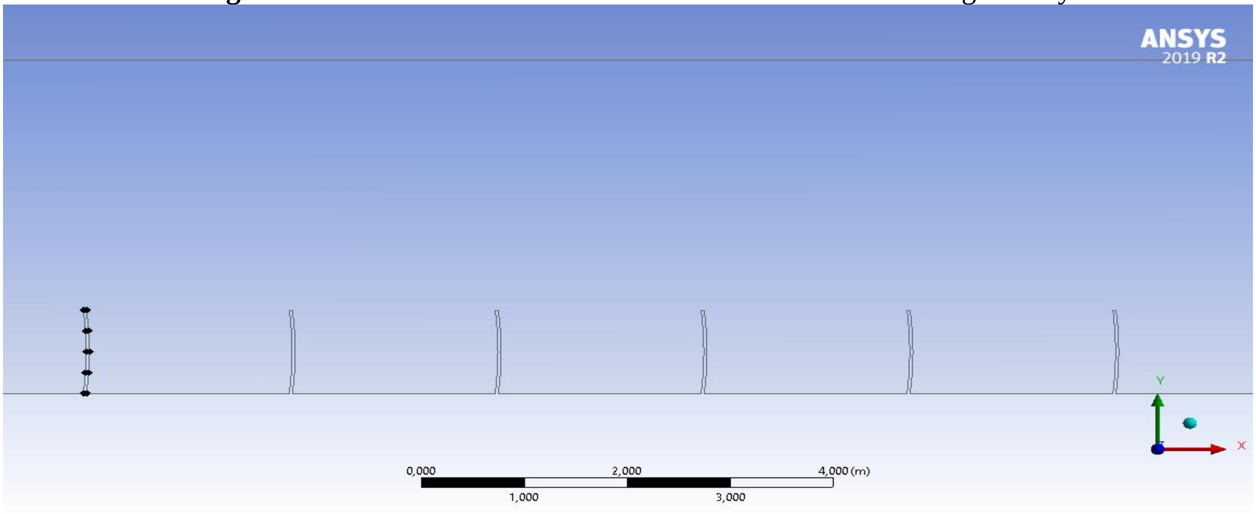

Figure 3.11. Zoomed in view of parabolic trough collector region

ANSYS 2019R2 Design Modeler was used to create the model schematic shown in figure 3.6 and shown in figure 3.8. It is shown in figure 3.8 that the domain is divided into 4 rectangular bodies to ensure a smooth meshing process. Depending on the simulation cases, both barriers will be alternated.

3.3. GOVERNING EQUATIONS AND PRINCIPLES

3.3.1. MIRROR SOILING CALCULATION

Mirror soiling has already been defined as the accumulation of dust particles on mirror facets. Thus, the mathematical expression to quantify mirror soiling based on our modelling of dust particles and particles tracked will be given as equation 3.1.

$$soiling = \sum particles\ trapped\ at\ the\ front\ sruface\ of\ mirrors \tag{3.1}$$

3.3.2. ATMOSPHERIC BOUNDARY LAYER (ABL) INLET PROFILE AND INCIDENT PROFILE

Prandtl in 1994 introduced the concept of boundary layer which changed the idea of fluid flow completely. Referring to Section 3.2.3, an atmospheric boundary layer was imposed on the inlet profile. The use of a boundary layer profile provides a direct link between simulated fluid flow and real-life fluid flow. Thus, a fully developed ABL profile was considered and imposed at the inlet, top and right sides of the domain as shown in figure 3.6. Here, we will consider a no slip condition at all solid surfaces (inlet wall, ground, outflow boundaries and PTC receivers) and there should be little to no difference between the inlet profile and the incident profile of the domain. The incident profile is the profile that exist in an empty domain without the features present within the domain. It has been researched (Richards, et al., 2011) that minor changes between these two profiles in the simulation environment would cause a major difference in a realistic environment, thus affecting the result. The ABL profile equation is given as (Richards, et al., 2011):

$$U(y) = \frac{u^*_{ABL}}{\kappa} \ln\left(\frac{y}{y_0}\right) \tag{3.2}$$

$$\kappa = \frac{{u^*_{ABL}}^2}{\sqrt{C_\mu}} \tag{3.3}$$

$$\varepsilon = \frac{{u^*_{ABL}}^3}{\kappa y} \tag{3.4}$$

$$u^*_{ABL} = \frac{U_{ref}}{\kappa} \ln\left(\frac{y_{ref}}{y_0}\right) \tag{3.5}$$

Equation 3.3 and 3.4 are the κ and ε feature velocity profiles, respectively. To ensure horizontal homogeneity between the incident profile and the ABL profile equation 3.6-3.7 were used:

$$\tau_w = \rho(u^*_{ABL})^2 \tag{3.6}$$

$$I_u(y) = \frac{\sqrt{\frac{2}{3}k}}{U(y)} \tag{3.7}$$

During simulation, equation 3.6 is imposed on the outflow boundaries and ground features in figure 3.6 while equation 3.7 is checked at inlet and the point of incidence to provide proof of horizontal homogeneity.

3.3.3. AIR (WIND) FLUID DYNAMICS

Having established that the prevailing wind will flow from left to right at 10m/s carrying dust particles, the fluid transportation equations must follow. In other words, airflow(wind) is two dimensional, incompressible and under steady state conditions flowing from left to right (figure 3.6) at 10 m/s and at constant properties of air at 300K. Majorly, all fluid problems obey the law of conservation of mass, momentum and as it is a continuous fluid, the same conservation laws were applied here (figure 3.2). Thus, the mass continuity equation is shown in equation 3.8:

$$\frac{\partial}{\partial x_i}(\rho u_i) = 0 \tag{3.8}$$

Due to the matter nature of fluids, it is more appropriate to study its velocity profile instead of its position. In this regard, the Reynolds Averaged Navier Stokes (RANS) equation is implemented:

$$\frac{\partial}{\partial x_i}\left(\rho u_i u_j\right) = -\frac{\partial p}{\partial x_i} + \frac{\partial}{\partial x_j}\left[\mu\left(\frac{\partial u_i}{\partial x_j} + \frac{\partial u_j}{\partial x_i} - \frac{2}{3}\delta_{ij}\frac{\partial u_l}{\partial x_l}\right)\right] + \frac{\partial}{\partial x_j}\left(-\rho\overline{u_i' u_j'}\right) \tag{3.9}$$

Equation 3.9 provides time-averaged fluctuating variables of instantaneous quantities of fluid motion for linear systems.

Now combining equation 3.2 and 3.3 with equation 3.8 to account for wind flow turbulence, will give the $\kappa - \varepsilon$ turbulent model respectively:

$$\frac{\partial}{\partial x_i}\left(\rho k u_j\right) = \frac{\partial}{\partial x_j}\left[\left(\mu + \rho C_\mu \frac{k^2}{\varepsilon}\right)\frac{\partial k}{\partial x_j}\right] - \rho\varepsilon - \rho\overline{u_i' u_j'}\frac{\partial u_i}{\partial x_j} \tag{3.10}$$

$$\frac{\partial}{\partial x_i}\left(\rho \varepsilon u_j\right) = \frac{\partial}{\partial x_j}\left[\left(\mu + \rho C_\mu \frac{k^2}{1.2\varepsilon}\right)\frac{\partial \varepsilon}{\partial x_j}\right] + \rho\varepsilon C_1\left(\frac{\partial u_i}{\partial x_j} + \frac{\partial u_j}{\partial x_i}\right) - 1.2\,\rho\frac{\varepsilon^2}{k + \sqrt{\nu\varepsilon}} \tag{3.11}$$

The k-ε model is a two-variable model that accounts for turbulent kinetic energy with the first transported variable and then dissipation with second transported variable.

3.3.4. DUST PARTICLE DYNAMICS

Referring to section 3.2.5, the particles were tracked and governed by the Eulerian-Lagrangian model. The equation is given as equation 3.12:

$$\frac{du_i^p}{dt} = F_D\left(u_i - u_i^p\right) - g_i\left(\rho_p - \rho\right)/\rho_p \tag{3.12}$$

The particle trajectory is calculated by integrating the particle force balance equation 3.12.

Now, given the typical forces that act on a single particle as shown in figure 3.12, a particle (or any matter) moves if the forces that promote movement is greater than forces that hinder movement. Thus, the three opposition forces that act on spherical particle is the drag force, lift and gravitational force. Now, given the definition of each term of equation 3.12, where u_i^p, u_i, F_D, g_i, ρ_p and ρ, are velocity vector of particle, instantaneous velocity vector of the fluid, drag coefficient, acceleration of gravity, particle density and the fluid density, respectively. One can see the correlation between the hinderance forces and equation 3.12.

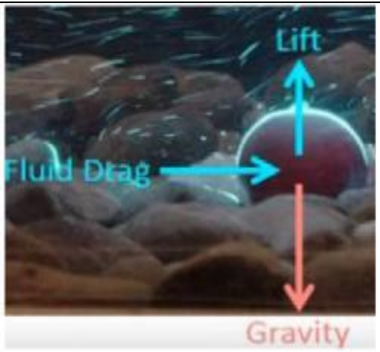

Figure 3.12. Forces acting on a particle (Source: Sansom, et al., 2018)

Turbulent dispersion of dust particles is determined by inconsistent velocity fluctuations and need to be accounted for in simulation procedure. Therefore, the stochastic discrete random walk model was used to govern the turbulent dispersion of dust particles within the domain (Lu, et al., 2019). This particular model describes the succession of random steps in a mathematical space. Realistically speaking, the motion of dust particles is generally haphazard and unpredictable in nature in any sandstorm or dust storm. Thus, the stochastic discrete random walk is a befitting model for turbulent dispersion.

3.4. MESH MODELLING AND REPRESENTATION

The pre-process whereby the domain of a CAD environment is discretized before it is simulated is known as mesh generation. Mesh generation can be generally categorised into two forms which are namely the structured mesh generation and the unstructured mesh generation. A structured mesh generation is a time-consuming procedure for complex geometries that uses a set of hexahedral elements with a tacit connectivity between points within the mesh. The domain of a structured mesh can be further broken down into blocks/regions manually depending on the complexity of the geometry for more accuracy. While the unstructured mesh generation involves a set of elements that are connected explicitly. This type of mesh generation is a two-step process that first, takes in point creation and then secondly, connectivity definition between these points. Although it is a faster method which makes it more appealing to many, it is less accurate due to its flexibility and its automation on sensitive regions that need a more detail attention like the boundary layer for fluids. The mesh general category can be shown in figure 3.13.

When one wishes to take full advantage of both types of meshing, the mesh generation process becomes a hybrid mesh generation. ANSYS 2019 R2 Mesh Component was used to generate the mesh for this study. A hybrid form of mesh generation was used to generate the geometry of figure 3.8. The domain was sliced into 4 rectangular faces (figure 3.8) by two planes. A vertical plane was placed 22m from the inlet and horizontal plane was placed 4m above ground ultimately slicing the domain into four blocks creating these 4 rectangular faces. The top (left and right) rectangular face, and bottom right are regions that are without any interior wall features while the bottom right is a region where the walls of the mirror facets and barrier are located.

Mesh generation process began with inflation. The inflation setting provides the ABL feature that was previously discussed in section 3.3.1. The figure 3.14 shows exactly where the setting was placed.

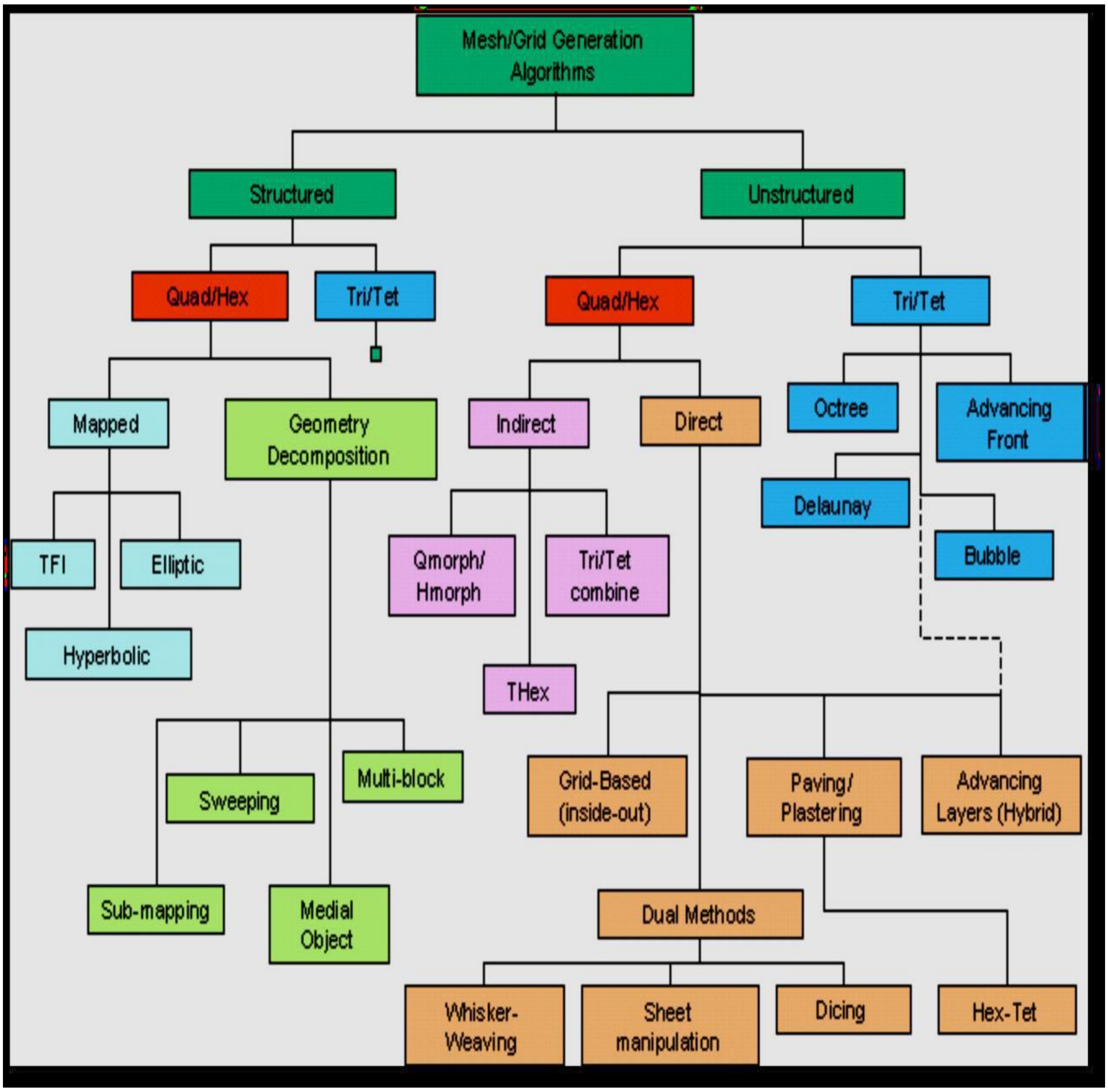

Figure 3.13. Mesh algorithm classification (Source: Sadrehaghighi, 2020)

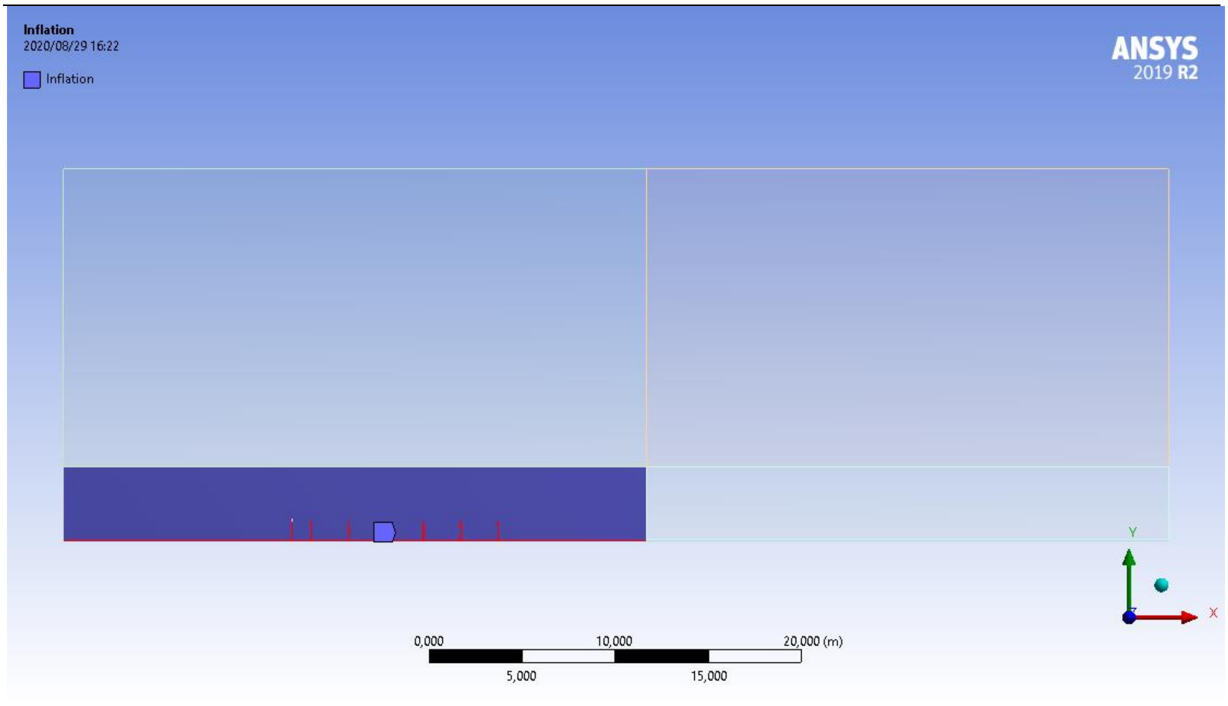

Figure 3.14. Inflation on mirror region

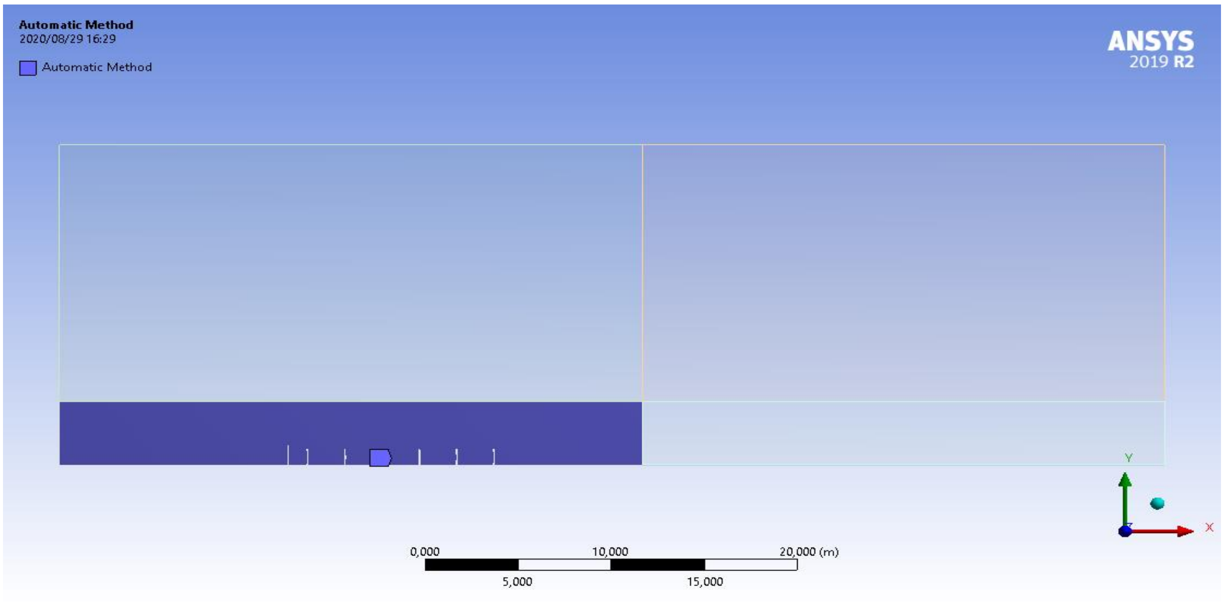

Figure 3.15. Automatic method placed at the mirror facet region

The rectangular face concerned with the mirrors was swept with the automatic method (figure 3.15). In this regard, the element midside nodes were kept at the program-controlled default settings. The element midside nodes are directly related to the number of degrees of freedom. Thus, reducing the number of midside nodes reduces the number of degrees of freedom available. Face sizing was then applied at the mirror face region of the domain. Sizing control accurately captures the resolution of a geometry and resolves high gradient areas that may have flow separation or recirculation (figure 3.16).

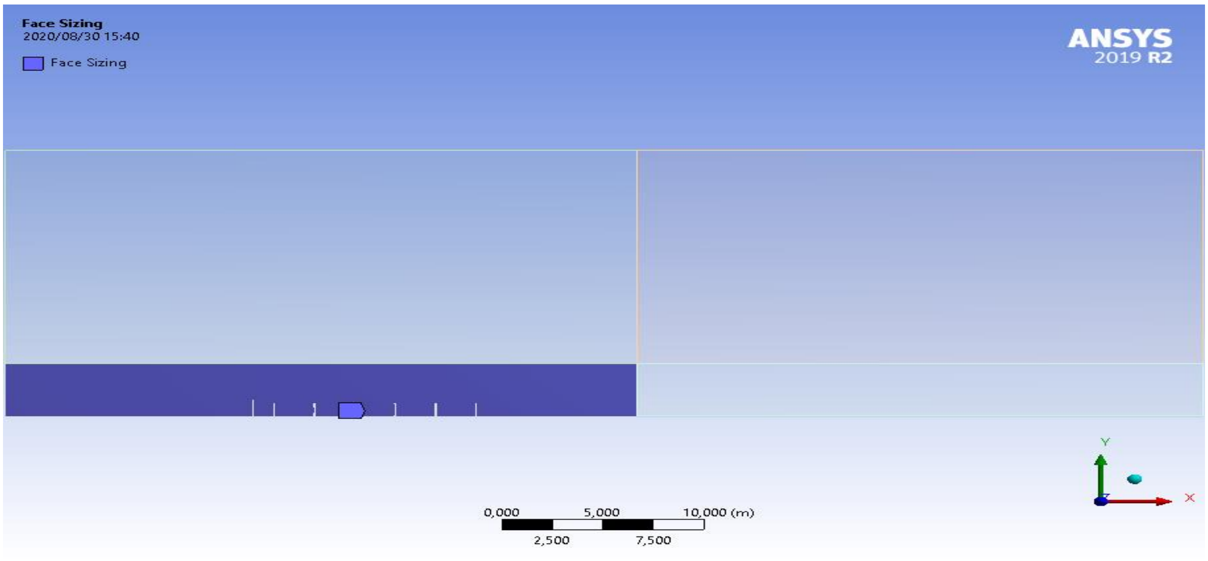

Figure 3.16. Face sizing on mirror facets region

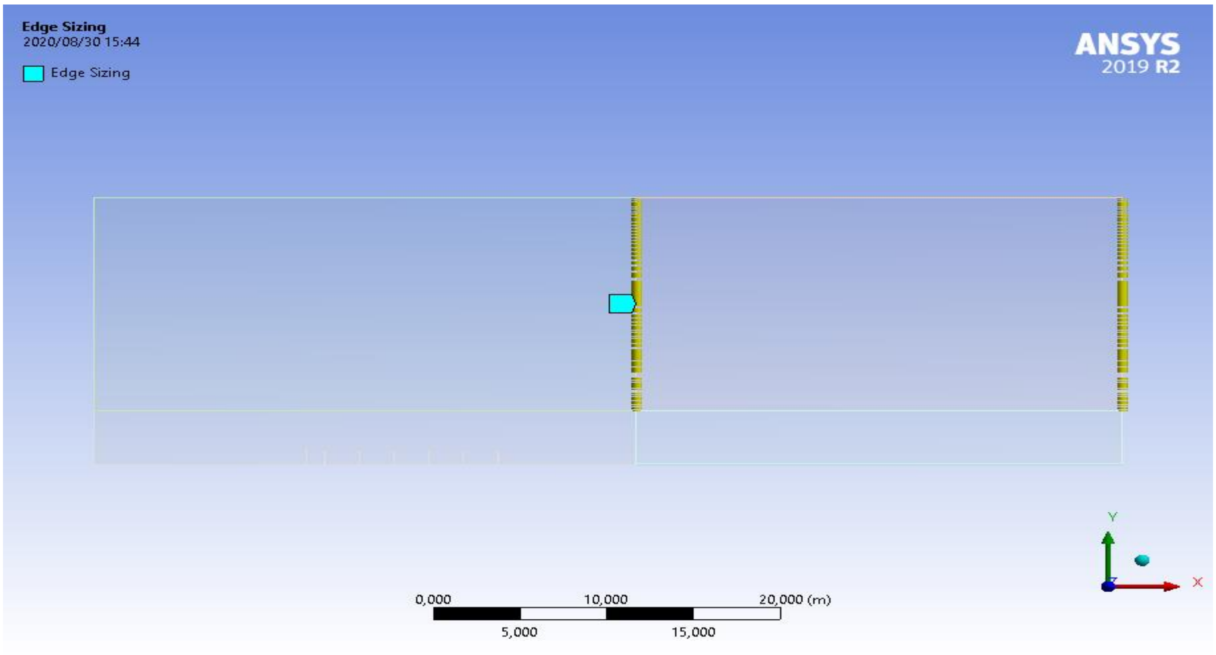

Figure 3.17. Edge sizing at top vertical edges outflow regions

Edge sizing can be applied to a single edge to allow for a bias control where the mesh size varies along that single edge. Edge sizing function was applied to the edges shown in figure 3.17 -3.19 to enable a biased mapped mesh towards various walls region such as the ground, and outflow wall.

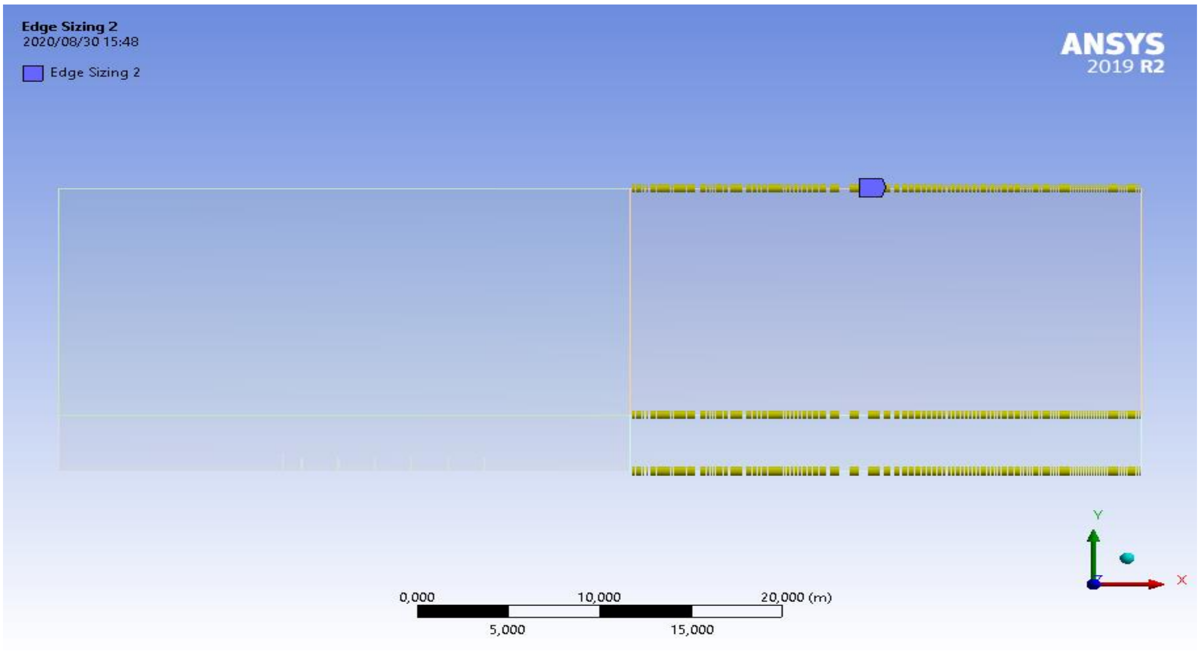

Figure 3.18. Edge sizing at horizontal edges at the outflow region

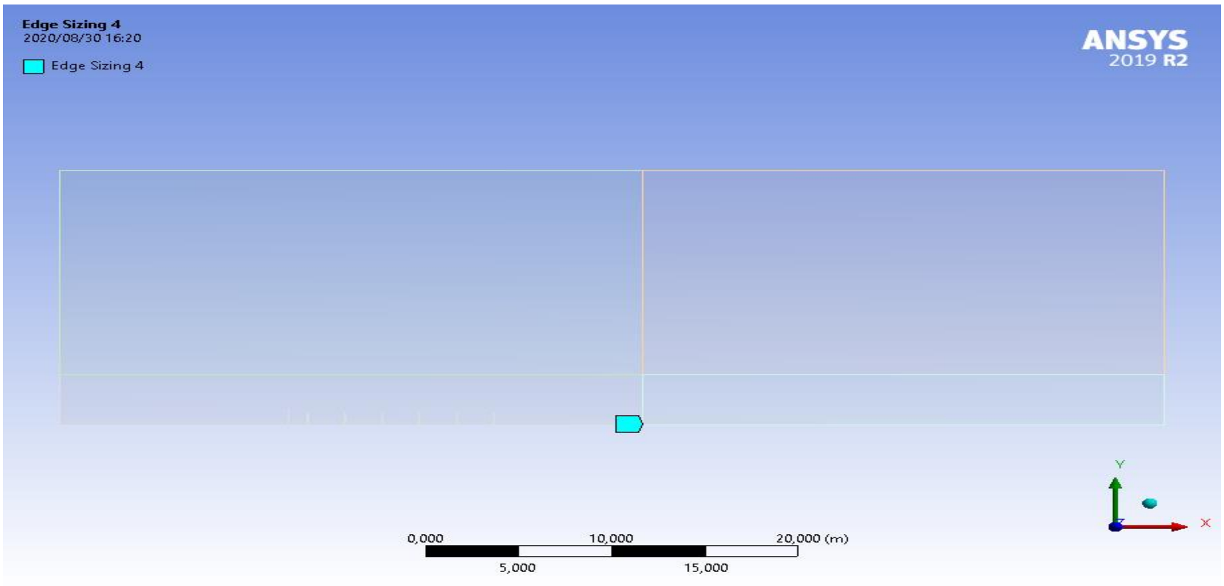

Figure 3.19. Edge sizing at edges of bottom right rectangular face

A smooth transition bias-controlled edge sizing was applied to the edges of the rectangular face at bottom right as shown in figure 3.19. This is was done to transform the mesh from the inflation layer (ABL bottom-left rectangular face) region to the domain core mesh (bottom-right rectangular face).

The final mesh setting was the mapped face mesh setting that was applied to all the rectangular faces that did not have the mirror facets within them (top left and right, bottom right). The mapped face mesh has uniform elements without distortion and less nodes which provides mapping for the rectangular split faces.

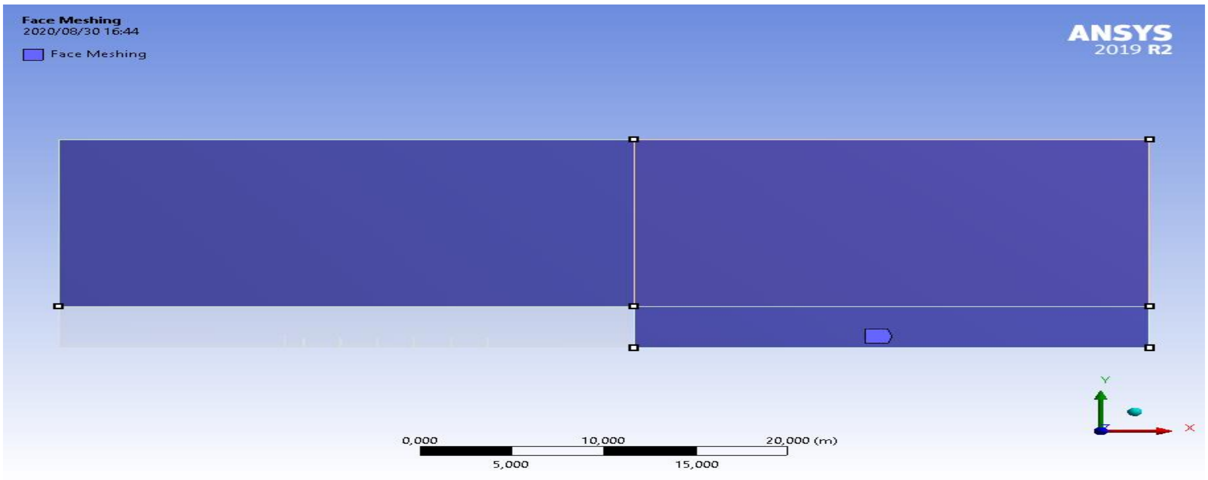

Figure 3.20. Face meshing on rectangular faces

Finally, the mesh that was generated with the explained setting that can be shown in figure 3.21-3.23.

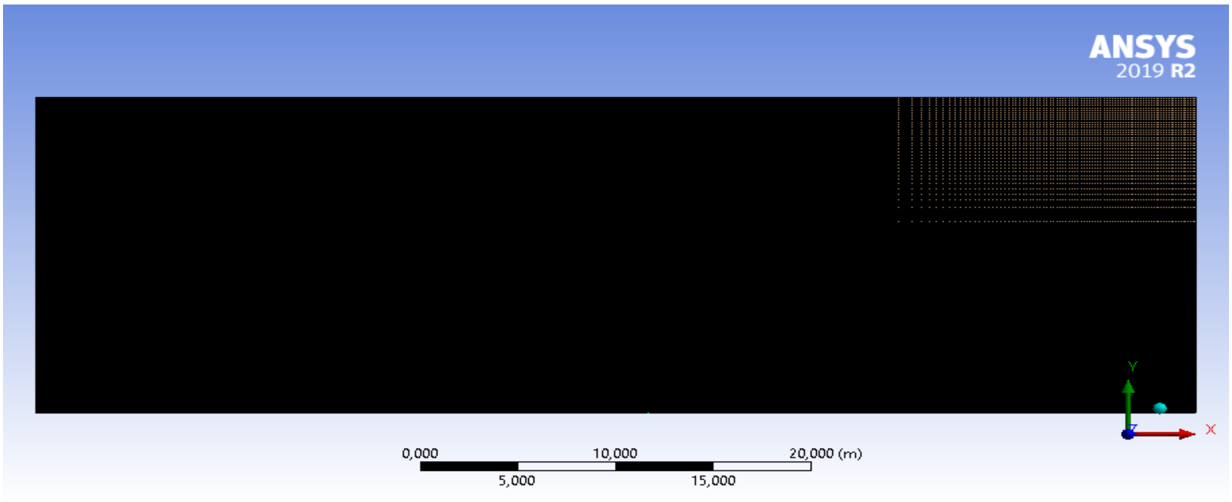

Figure 3.21. Generated mesh of the domain

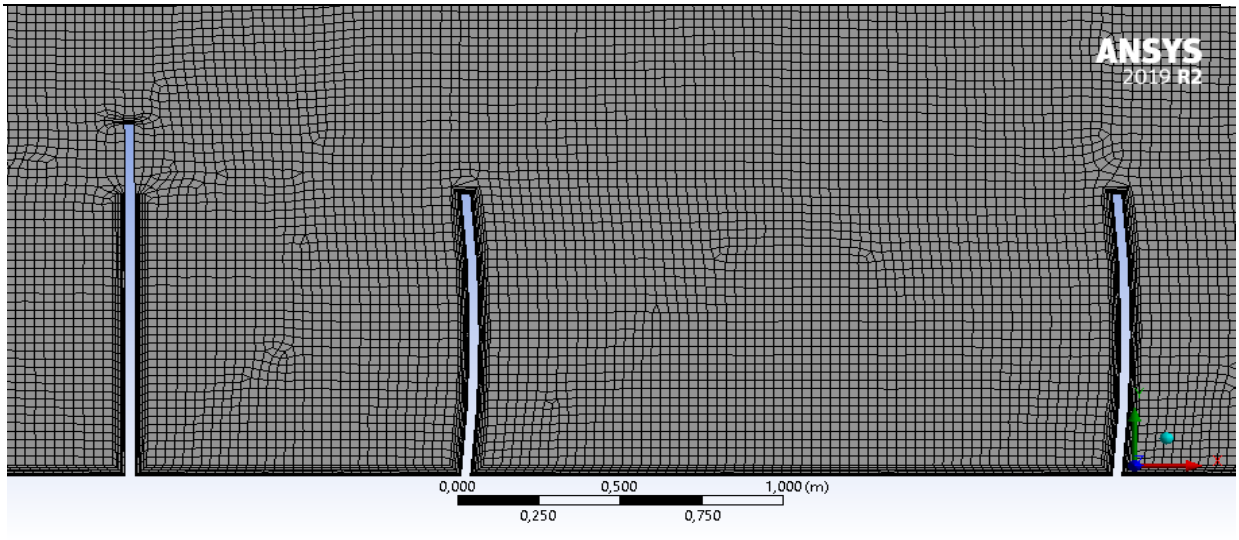

Figure 3.22. Zoomed in view of bottom right mirror facet region with wind barrier

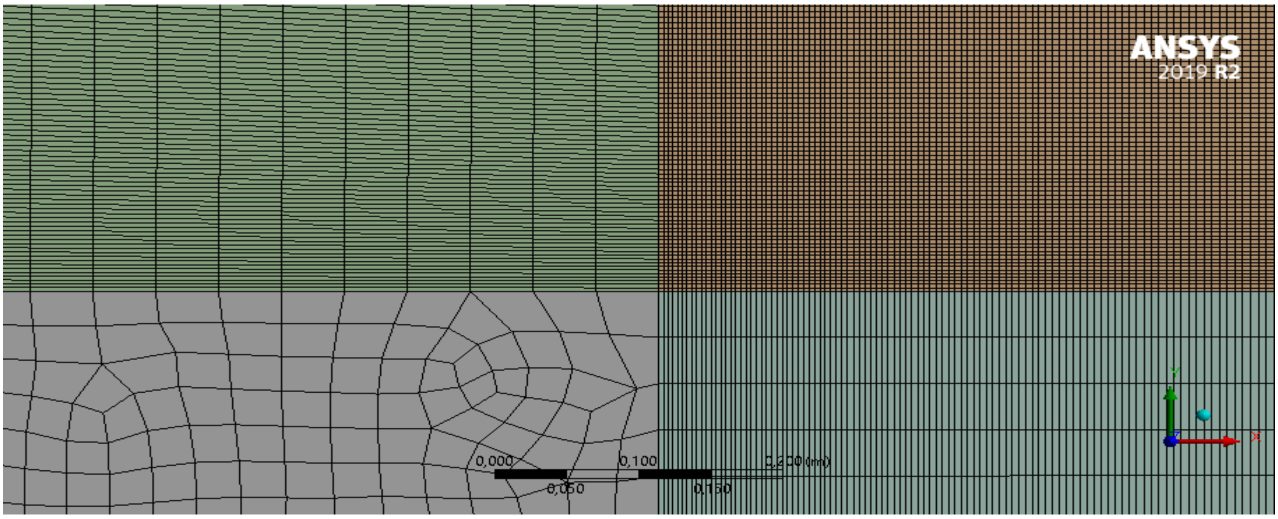

Figure 3.23. Zoomed in view of 4 Rectangular Faces at Point of Intersection

3.5. MESH INDEPENDENT STUDY

A mesh independence study was done after establishing the mesh settings and parameters in ANSYS. A mesh independence study is necessary to validate the mesh of any given geometrical profile. The process of grid study majorly aims to validate accuracy of this study and to determine the most refine mesh for the geometrical problem. In refining the mesh, the following will be taken as top priority (Godderidge, et al., 2006):

- Spacing: The mesh needs to be sufficiently fine to compute the governing equations at an accurate level. It is well known that a decrease in grid size for refinement will increase computational cost and memory requirement. The dissertation incorporated a balance in this regard.
- Resolution: The grid spacing needs to be sufficiently small to resolve the flow in all regions of the computational domain (Godderidge, et al., 2006). Given a coarse mesh, flow features such as pressure, velocity and temperature are not clear and will appear insensible.

3.5.1. MESH GRIDS USED

The process to obtain mesh independence occurred between three types of different mesh structures used on the same simulation case in which the finest mesh was chosen by size reduction of a factor scale. Taking the first case of the simulation cases performed (discussed in later chapters), the mesh grids used were:

I. **Coarse Mesh:** The coarse mesh used contained 957 nodes and 863 elements as shown in figure 3.24.

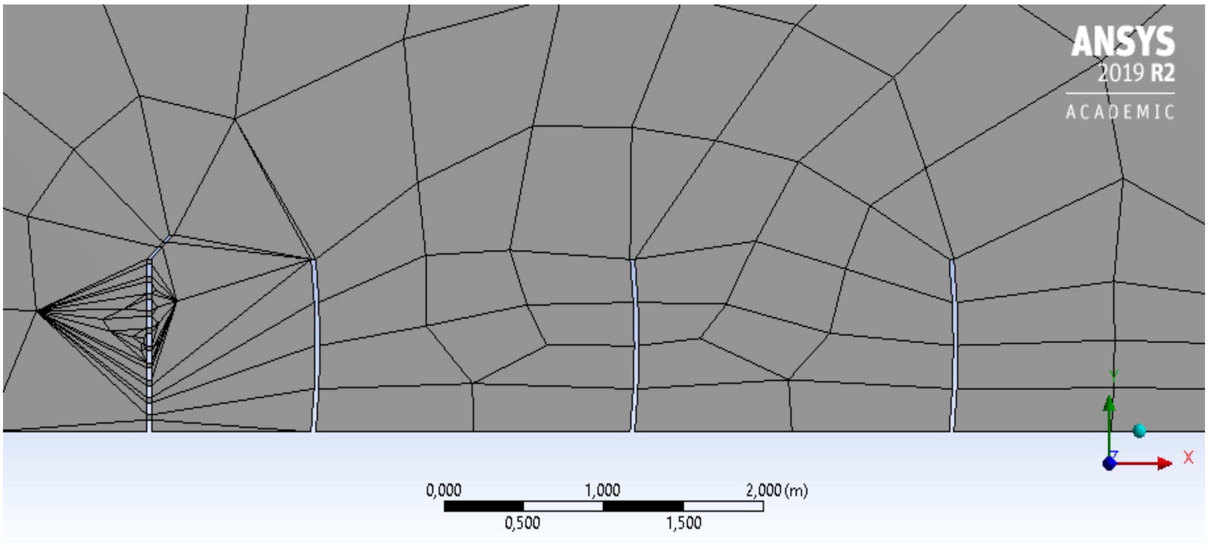

Figure 3.24. Coarse mesh structure

Figure 3.24 shows high resolution and large spacing. The extreme coarse cells will provide equation solutions at a fast rate.

Convergence was achieved after 1350 iteration and the results are shown by figure 3.25-3.27

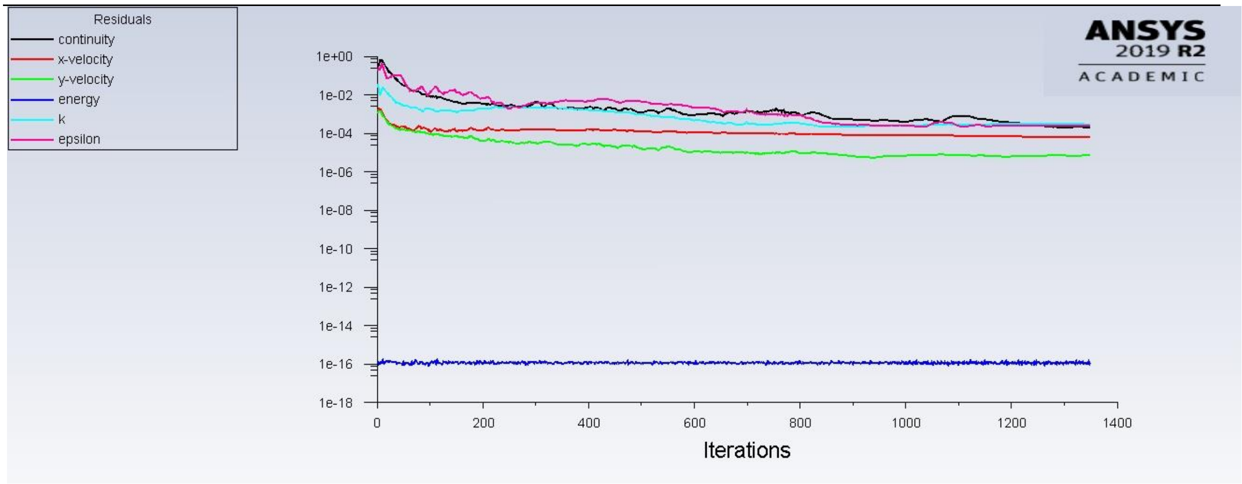

Figure 3.25. Scaled residuals of coarse mesh simulation

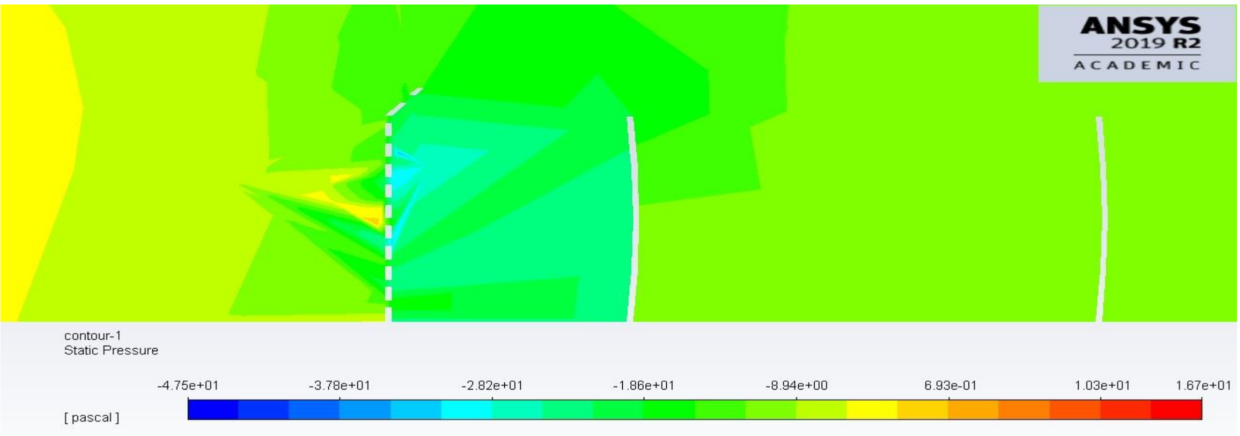

Figure 3.26. Pressure contour of coarse mesh simulation

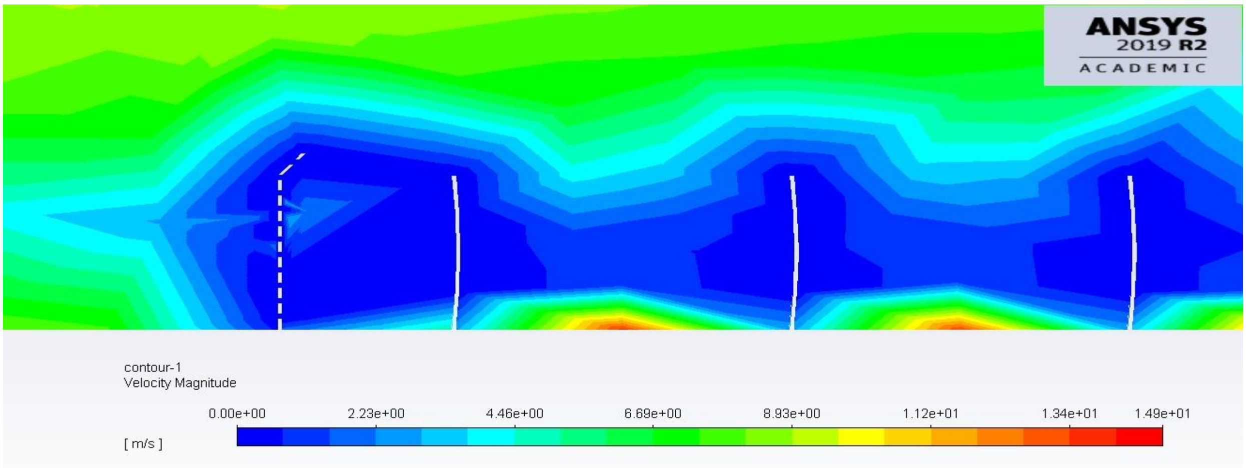

Figure 3.27. Velocity contour of coarse mesh simulation

Although convergence was achieved according to the results displayed by the scaled residuals shown in figure 3.25, the results shown by the contour in figure 3.26 which shows an inconsistent pressure drop in different regions cannot be explained. Also, the shape present in 3.27 seems to assume much of the coarse mesh instead of the contour of fluid flow represented by velocity.

II. **Medium Mesh:** The coarse mesh size was reduced by a factor of 10 producing a medium mesh structure containing 11987 nodes and 11707 elements as seen in figure 3.28.

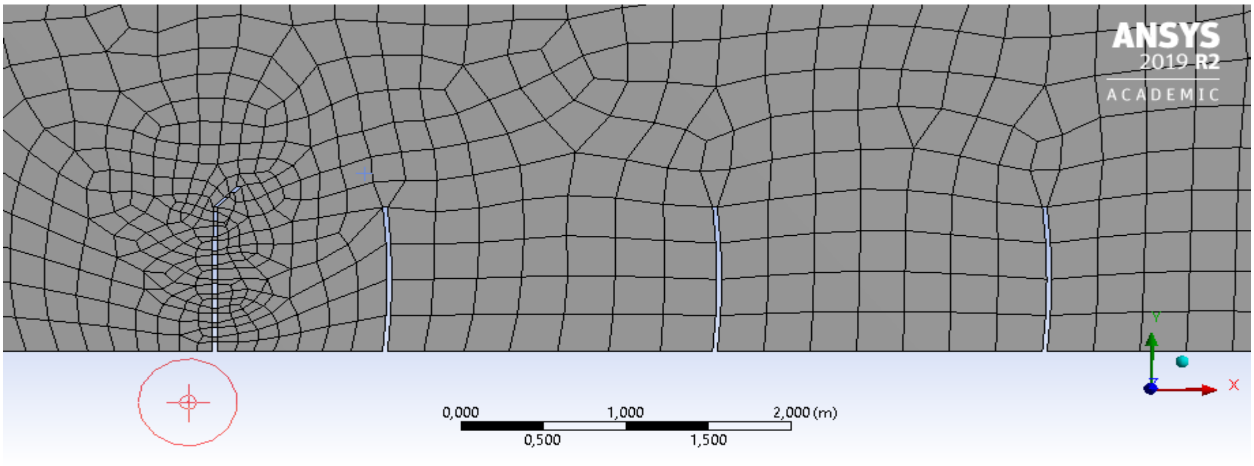

Figure 3.28. Medium mesh structure

Figure 3.28 shows a better resolution and better spacing of elements. The mesh structure provided a solution at slower rate compared to the coarse mesh structure which is understandable and expected of this structure.

Convergence was achieved after 1500 iteration and the results are shown by figure 3.29-3.31

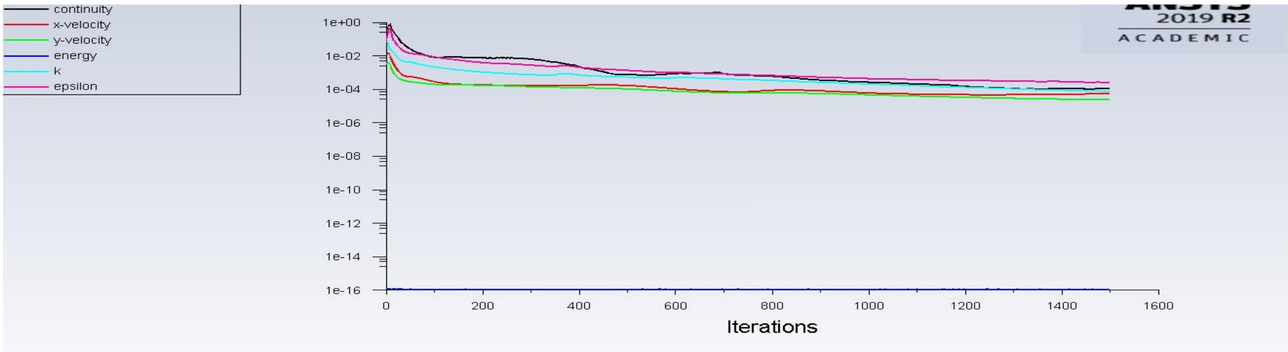

Figure 3.29. Scaled residuals of medium mesh simulation

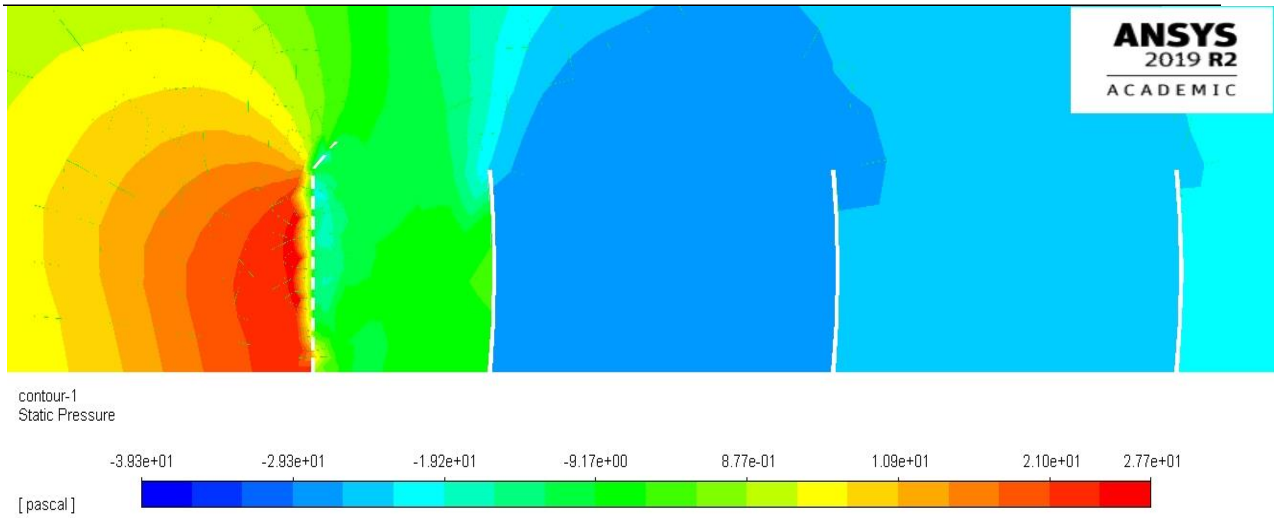

Figure 3.30. Pressure contour of medium mesh simulation

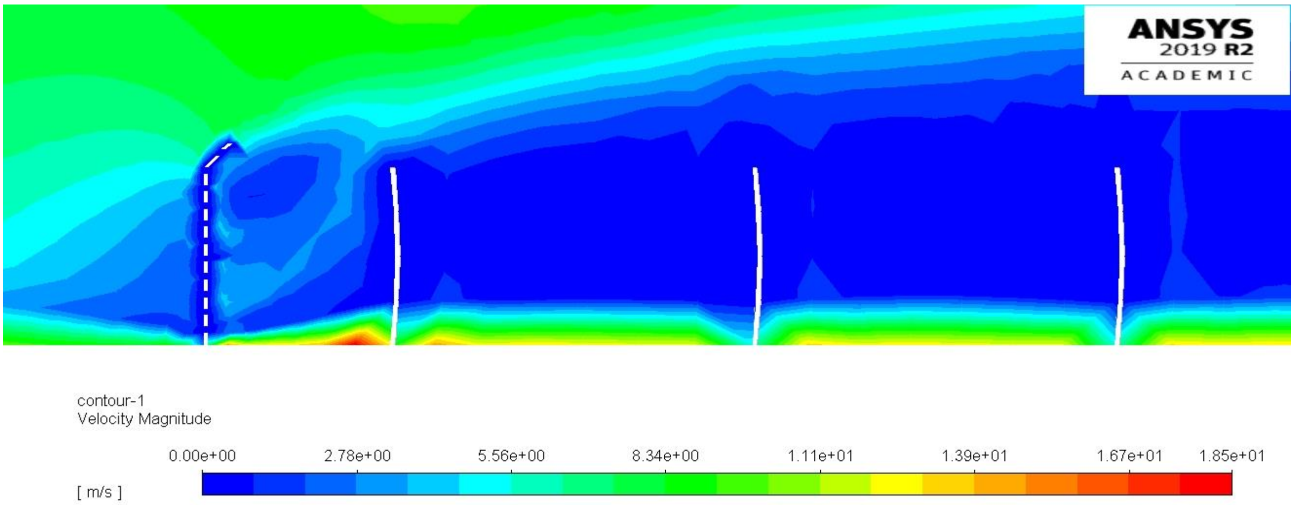

Figure 3.31. Velocity contour of medium mesh simulation

Figure 3.30 shows an explainable phenomenon as there is a pressure drop from one side of the domain as fluid hits the wind barrier and the mirror facets regions experience low pressure. Figure 3.31 also further provides some more detail to the velocity of the fluid entering the domain. Although there are some regions that lack accurate information such as the downstream region of the mirror facets, it is still possible to visualize and see the fluid flow occurrence of the simulation.

III. **Fine Mesh:** The medium mesh size was reduced by a factor of 100 to obtain a fine structured mesh. The fine structured mesh contained 875822 nodes and 873401 elements. Figure 3.32 shows the refined mesh structure used for the simulation cases.

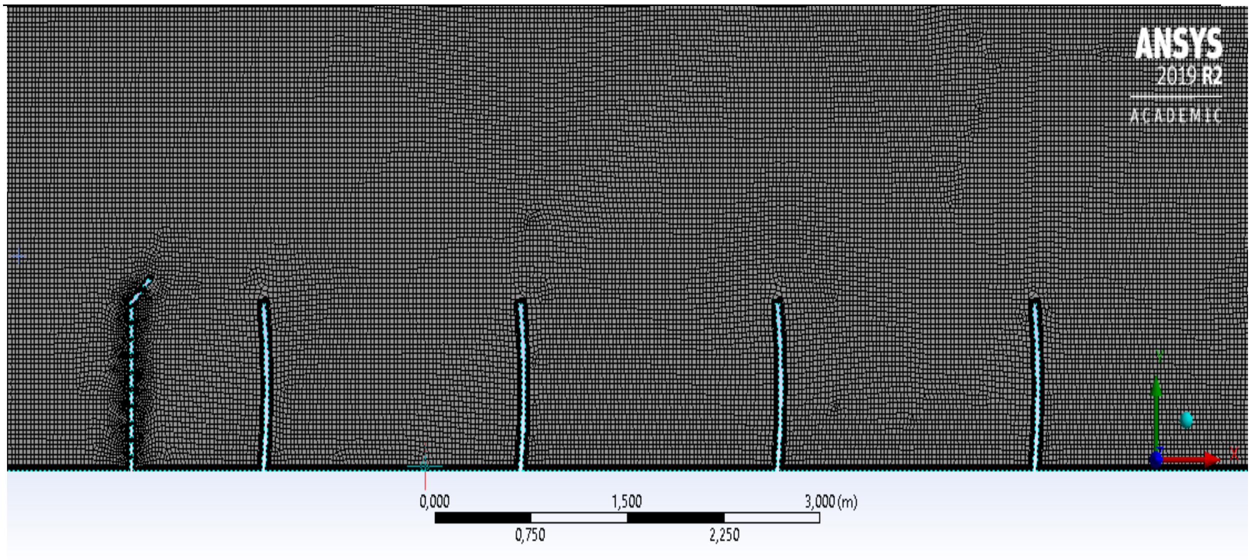

Figure 3.32. Fine mesh structure

It is clear from figure 3.32 that the mesh structure produced is proportionally spaced out in a fine grid and the resolution was made on the intent of capturing flow features in each region. Unlike the medium and coarse grid, the solution appeared different and was clear as shown in figure 3.33-3.35.

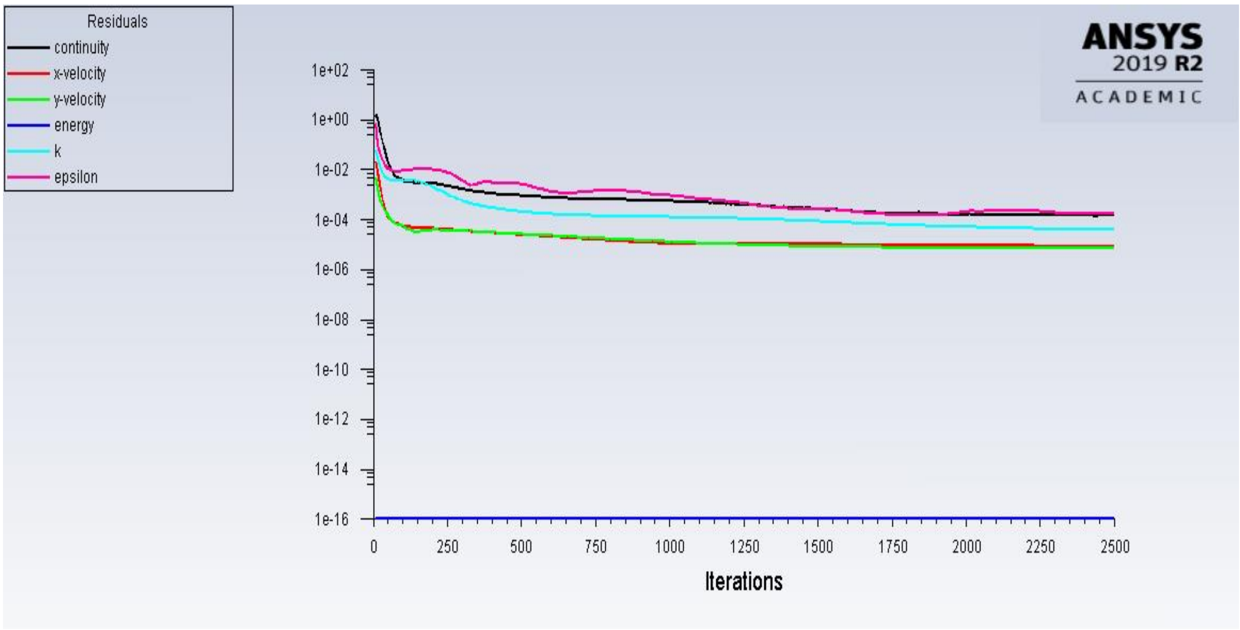

Figure 3.33. Scaled residuals of fine mesh structure

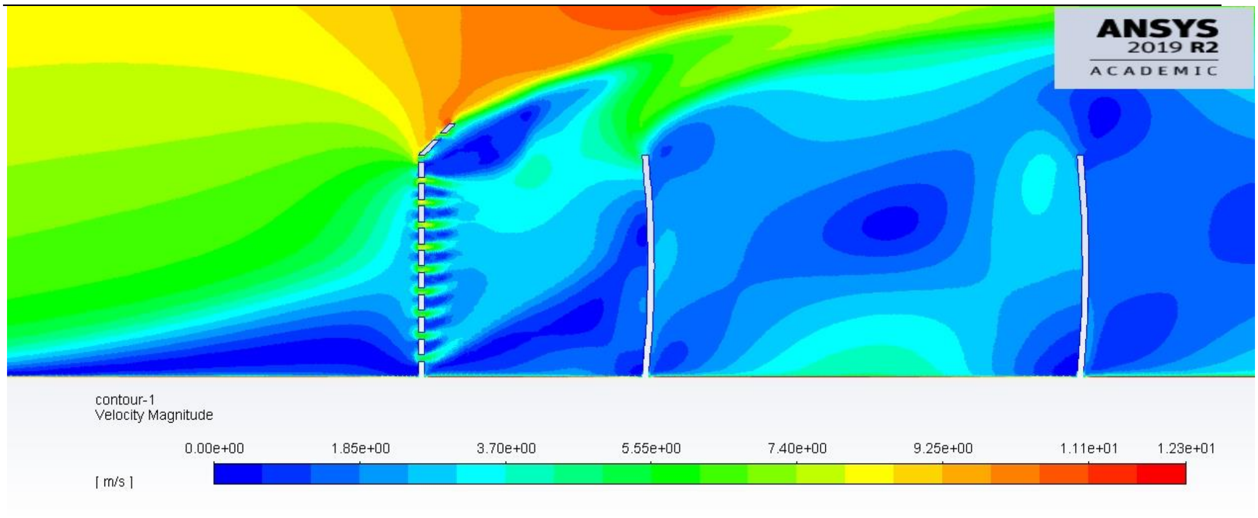

Figure 3.34. Velocity contour of fine mesh simulation

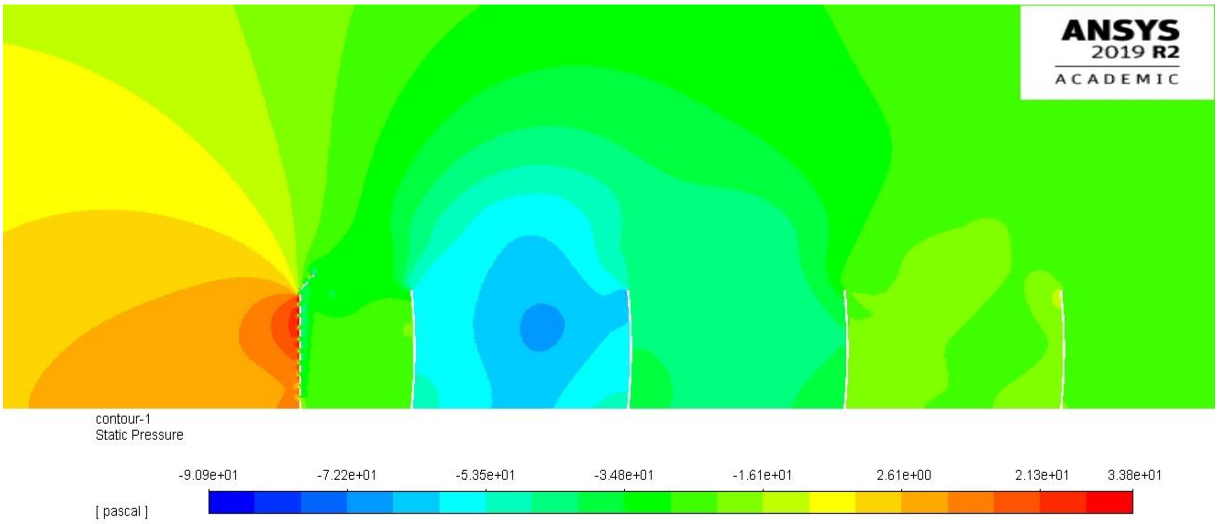

Figure 3.35. Pressure contour of fine mesh simulation

Comparing velocity and pressure contour of medium mesh to the fine mesh, the flow visualisation of the geometry is more accurate and more visible in figure 3.34 and figure 3.35. The pressure drop is as the colour changes dictates a sensible manner in which the left side of the barrier experiences high pressure and the right side of the barrier experiences a lower pressure. The velocity contour displays the flow velocity more accurately as even in between the porous regions of the barrier the change of colour is also shown. The results of this simulation case will be discussed in detail in chapter 5.

3.6. CONCLUSION

All simulation procedure starts with the geometric model (figure 3.8) which is then transformed into a mesh representation (figure 3.21- 3.23). To obtain a geometric model for simulation, it is important to derive the problem and its sub-problems accurately. This was done in the beginning of the chapter. The geometrical representation was then discretized accordingly.

To finalize the type of mesh needed, a mesh independent study was conducted. The mesh independent study utilized a scaling factor to determine a coarse mesh, a medium mesh, and a fine mesh. The first simulation case was simulated with these three mesh structures in which the results were obtained and observed. It was clear with a fine mesh that results were more sensible and accurate as this should be the case with a fine mesh due to the refined spacing and small resolution size of elements.

The mesh representation is where the solving of equations begins. This is where numerical study of CFD is first applied in obtaining and validating the mesh structure, simulation of cases can then commence. The fine mesh structure was chosen for simulation cases.

CHAPTER 4

NUMERICAL PROCEDURE AND OPTIMIZATION METHODOLOGY

4.1. INTRODUCTION

In developing the problem into a model geometry that could be understood mathematically by the computer, it is important to highlight the numerical events that occur with this problem. Numerical analysis of a fluid body has many industrial applications and has proven to be the fore front of optimum engineering design with minimal cost. The history of CFD dates back to the 1970s and at that time, the need for CFD was jumpstarted with the availability of an increasing number of powerful mainframes.

Computational fluid dynamics (CFD) is concerned with the numerical analysis of fluid mechanics using computer science to solve the governing equations and principles of a given discretised domain. The final result is a visual representation of the fluid flow displaying a form of mimicked reality. Ultimately, the presented research revolves around optimization of a wind barrier structure. Thus, the essence of numerical optimization lies in the key idea that a design can reach a state where the variables can be represented mathematically, and the solution can be obtained by iteration to achieve a common design objective. Mathematically speaking, optimization is the minimization or maximization of a function subject to constraints on its variables (Nocdeal, et al., 2006).

This chapter introduces and discusses the CFD numerical procedure and highlights the major differences of a numerical analysis versus the analytical analysis. This chapter is also concerned with the types of numerical methods performed in conjunction with the simulation case scenarios performed and the optimization methodology utilized after simulations. ANSYS FLUENT and ANSYS DX was the simulation and optimization tool respectively used for this research.

4.2. NUMERICAL VERSUS ANALYTICAL ANALYSIS

It is possible to solve a solution analytically however the course of engineering has always presented problems that our complex in nature. With problems proven difficult to generate solutions for, it is then recommended that numerical analysis be used to generate solutions. Table 4.1 shows a difference between the numerical analysis and analytical analysis.

Table 4.1. Differences between numerical analysis and analytical analysis.

Numerical Analysis	**Analytical Analysis**
This type of analysis can be used for moderate and high-level complex functions. Additional constrains are easily inclusive.	This type of analysis can be used for simple problems. However, with more constraint, the functions become more complex.
There is more time involved with this analysis because iterations are needed to generate a solution.	There is generally less time involved during solution generation.
The solution is not a direct solution to a given problem	An exact solution to the given problem is given.

Due to the complex nature of the problem identified in this thesis, the numerical procedure incorporated in a CFD package was used to obtain various solutions.

4.3. CFD AND ITS STRATEGY

A Computational fluid dynamic problem is generally determined by a numerical algorithm that handles the modelled fluid problem. The need for CFD is relevant because given the engineering governing equations (equation 3.8- 3.11), it is not possible to solve it analytically majority of the time due to certain reasons such as danger, and time. In the past and currently, this technique has been proven to be powerful in the development of engineering technology. Some of which include aerodynamics of aircrafts and vehicles, internal combustion of engines and turbines, the distribution of pollutants and effluents in each environment. etc. The major advantages that CFD has over experiment-based research are indicated as follows:

- CFD approach can deliver practically limitless level of detail of desired results.

- CFD enable systems to be studied within dangerous harmful conditions beyond their standard operating capacity.
- CFD enables controlled experiments of systems that are otherwise impossible to perform.
- CFD provides cost-effective less time-consuming approach in generating new engineering designs.

A CFD code is structured by numerical analysis to solve a given problem which takes account of engineering equations and principles. CFD codes can produce a massive amount of results without any additional expense. The strategy of CFD employed on any fluid problem majorly replaces a continuous domain with a discrete domain. For a continuous domain, each variable is defined at every point of the domain whereas for a discreet domain, each variable is defined at grid points. For instance, given a pressure variable in 1D one can show in figure 43 a clear difference between continuous and discreet domain.

$$p_i = p(x_i), \quad i = 1, 2, \ldots, N$$

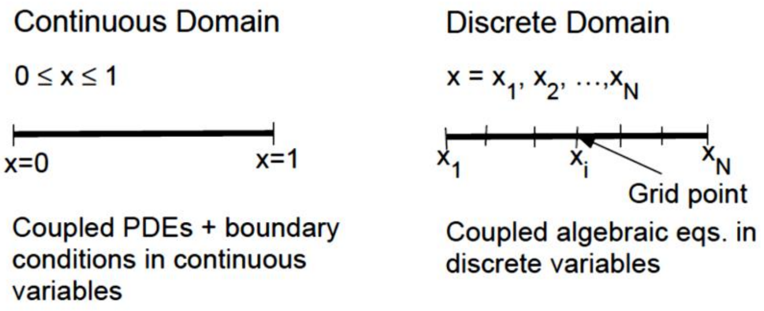

Figure 4.1. Continuous and discrete variable. (Source: Bhaskaran, et al., 2003)

Now a CFD package generally comprises of three main elements which were implemented in this study. The three elements are stated as follows:

1. The pre-processor
2. The Solver
3. The post-processor

The CFD approach already began with chapter 3 and will be explained in the subsequent sections.

4.3.1. THE PRE-PROCESSOR

This initial CFD element is the input features of the CFD problem. Here, the problem coupled with the geometry is defined, stated, and created (chapter 3, section 3.2). The domain is then discretised into smaller grids by means of a mesh generation of the domain (chapter 3, section 3.4). With smaller grids (discrete domain), miniature control volumes are formed, and it is easier to calculate flow over a smaller surface area as opposed to calculating flow over a larger surface area (the continuous domain). Thus, flow properties such as pressure, temperature and velocity are readily defined at the nodes of grid cells. In discretizing the domain, it is incredibly important to note that there is a potential for errors being introduced. However, due to the correlated refinement of the mesh, the risk of having these errors could be adversely low.

Given a discretised domain, there is always need to define a mathematical model that is best suited for the discretised domain and can be applied to the domain to accurately govern and assess fluid flow. With defined boundary conditions, governing equations were specified (chapter 3 section 3.3) and defined for the present study. Governing equations and principles are based on the problem at hand. If there are no equations that can govern a specific fluid problem, then the equation must be created from a theoretical point of view. It is important to note that errors can be introduced by the user during equation selection/creation and any untrue assumptions depending on the problem. The boundary conditions discussed in chapter 3 section 3.3 are referred to as the Dirichlet or direct boundary conditions. The Dirichlet boundary condition incorporates specific values on the unknown variables. For instance, it was stated that inflow wind velocity was 10m/s entering the domain. The other forms of boundary conditions namely the Neuman boundary condition and Mixed type boundary conditions were unnecessary as they both create extra equations that do not abide by our rule of thumb (table 3.1).

4.3.2. THE SOLVER

When the pre-processing is done and errors are at a minimum with the discretised domain (mesh), the solver of the equation is then employed. The solver is the heart of a CFD code package. It utilizes different streams of numerical solutions technique to find solutions for a given set of equations. There are different types of numerical solution techniques involved in problem-solving and these include the finite difference method (FDM), finite element method (FEM), and finite volume method (FVM). The method directly involved with this study is the finite volume method incorporated into the CFD package which is quite similar to the finite difference method on a one-dimensional level.

The solver feature begins with the control volume integration. This utilizes the FVM distinctly from all other methods of the CFD technique. The FVM was first used by McDonald in the beginning of the seventies for the simulation of two-dimensional inviscid flows (Blazek, 2001). With the control volume integrated, the governing equations are expressed exactly as conservation statements for each finite size cell. The FVM does this by discretising the integrated governing equations in which the physical space is divided into several arbitrary polyhedral control volumes and then the surface integral is approximated with fluxes crossing individual faces of the control volume. This is numerical method is generally known to be the most flexible compared to FDM and FEM. Thus, it can easily be implemented on structured and unstructured grids, it can therefore handle any type of mesh. Also, since it is based off a direct discretisation of the governing equations, it is also capable to produce weak solutions of the governing equations correctly (Blazek, 2001)

It is important to note that the application of FVM can occur as two different grid forms namely the cell centred and cell-vertex schemes. The cell-centred scheme enables flow properties such as velocity and pressure to be stored at centroids of the grid cells making the subdivided control volume identical to grid cells. While the cell-vertex scheme enables flow variables to be associated at grid points. This makes the control volume to have a union where a grid point can be shared at one point. ANSYS FLUENT package uses the cell-centred scheme for numerical procedures. Figure 44 a and b shows an image of both type of schemes.

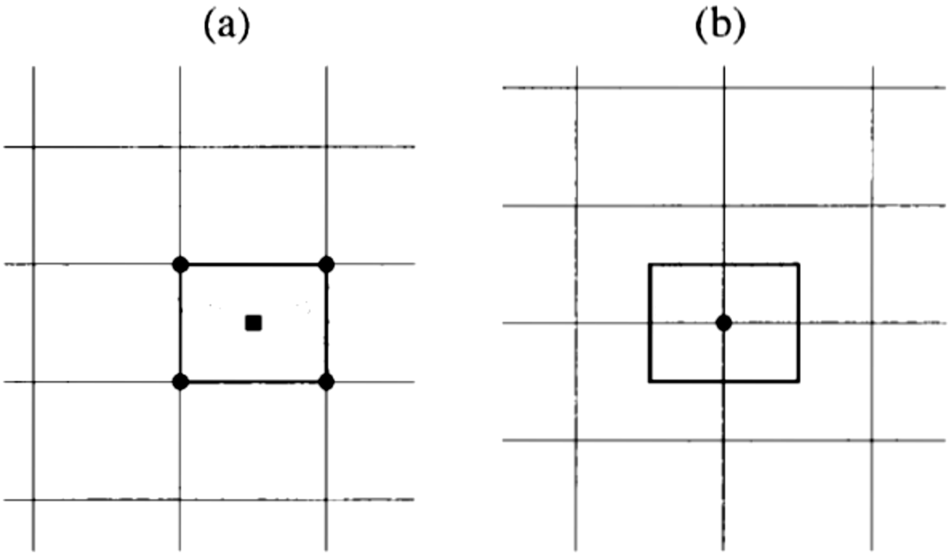

Figure 4.2. a) Cell-centred scheme and b) Cell-vertex scheme (Source: Blazek, 2001)

After when equations have been integrated and discretised accordingly by the FVM, an iterative procedure is utilized to obtain solutions at grid point of the domain. The presented research is majorly concerned with the correct linkage between pressure and velocity of the various dust particles carried by wind. Thus, the SIMPLE algorithm was used as the iterative procedure to obtain solutions.

4.3.3. THE POST-PROCESSOR

A typical CFD package is equipped with a post-processor to display multiple visual forms of the simulated case problem as results. This is the final process of simulation and it involves taking output files for flow properties (velocity, pressure, energy etc.) at each node area at a time step and displaying results visually. The CFD post processor translates simulation solutions of the domain into viewable results for engineering assessment. For this study, ANSYS post processor was used, and the following are the output formats generally used in ANSYS post processing:

- Iso-surfaces
- Vector Plots
- Contour Plots
- Streamlines and particle track
- XY Plotting
- Animation creation

4.4. NUMERICAL OPTIMIZATION

The key idea behind optimization lies in the fact that one can design and produce an object that is optimally suitable to its pre-designed specifications and design requirements. We are already aware of the fact that numerical solutions are an approximate form of the solution in which the CFD package delivers to users but in order to derive the best of solutions of a stated problem, numerical optimization is used. Optimization is an important procedure for scientists and engineers and used in various industries like the manufacturing, transportation, finance, and marketing.

Numerical optimization can occur in one of two ways namely with constraints and unconstrained equations. As there are objective functions involved, variables play a major role in the determination of a specific function. Thus, constrained equations put limits on how variables are used in each function while the unconstrained uses an infinitely amount of values assigned to variables. Variable can be either discreet or continuous.

The process of numerical optimization begins by formulating the problem and then modelling the problem accordingly. An optimization algorithm is then used to solve the model. There is no general algorithm used to solve models. The presented dissertation and research define a wind barrier structure for the purpose of reducing the number of particles entering the mirror field domain. With this stated objective we can formulate the numerical optimization problem in a mathematical format. The optimization algorithm used was based on speed of solve and accuracy likely to be achieved by the CFD package.

4.4.1. MATHEMATICAL FORMULATION OF THE OPTIMIZATION PROBLEM

Referring to figure 3.6, the flap length (l_3), flap angle (θ) and porosity (po) feature was considered as the geometrical constraints involved. Table 4.2 shows the input constraints variables for our optimization problem.

Table 4.2. Constrained variables of the wind barrier

Porous Wall Barrier		
Independent Parameter	**Lower Bound**	**Upper Bound**
po	0.02	0.05
l3	0	0.20
θ	5	175
Non-Porous Wall Barrier		
po	0	0
l3	0.05	0.25
θ	5	175

To optimize a wind barrier, a combination of the optimum candidates of constrained variables (table 6) must produce the most minimum amount of soiling out of all the possible solutions. Thus, an optimized wind barrier structure would be ultimately presented when we have optimum candidates that can reduce mirror soiling. With that being states the problem is formulated as follows:

$$Optimization\ problem$$
$$\rightarrow Minimize\ Mirror\ soiling\{Number\ of\ tracked\ particles\ in\ mirror\ field\ domain\ (\tilde{x})\},$$

$$\therefore \tilde{x} = (l_3, \theta, po) \tag{4.1}$$

4.5. CONCLUSION

The chapter began with presenting the various forms of solution finding for a CFD problem. Numerical study is an effective approach with advantages over analytical approach when dealing with industrial application problems. In this case, numerical procedures incorporated into the ANSYS package was key to the presented simulation cases that would be discussed in the next chapter.

When the domain has been meshed (pre-processor) for a CFD package solver (ANSY FLUENT). The numerical method involves solving with the FVM iterations to find an approximate solution. FVM was used here due to its flexibility with structured and unstructured mesh, which have been identified in the domain.

Using ANSYS DX, the wind barrier structured was optimized according to the constrained variables used in ANSYS Fluent simulations. The simulation cases will be discussed accordingly in the next chapter and the optimization of simulation cases will then follow.

CHAPTER 5

SIMULATION CASES

5.1. INTRODUCTION

In the previous chapter we defined the numerical procedure that occurs in a CFD package and the numerical optimization that occurs thereafter. This chapter introduces the simulation cases of the wind barrier that occurred with full utilization of the numerical procedure involved. The settings will be described for each simulation case. There are 25 cases that were performed, and the optimization of these cases followed immediately after. 16 cases were simulated for a porous barrier and 9 cases were simulated for a non-porous barrier.

As mentioned in the previous chapter, ANSYS-FLUENT was the simulation package used to perform these simulations. The simulation performed took account of the CPU processor and time. The validation of this simulation process is also discussed. This chapter will give details to each case simulated and corresponding settings and results of these cases.

5.2. ANSYS-FLUENT SETTINGS (SOLVER)

The settings that were applied in the solver were used for all the cases that are discussed within this chapter. The following modelling features were activated based on our problem definition, governing equations, and numerical solutions preference already discussed (chapter 2, 3 and 4):

- Energy- factoring in governing equations for solving.
- Viscous Realizable k-ε- factoring turbulence equations for solving.
- Discreet Phase- factoring in particle dynamics, density, and number of induced particles in the domain.

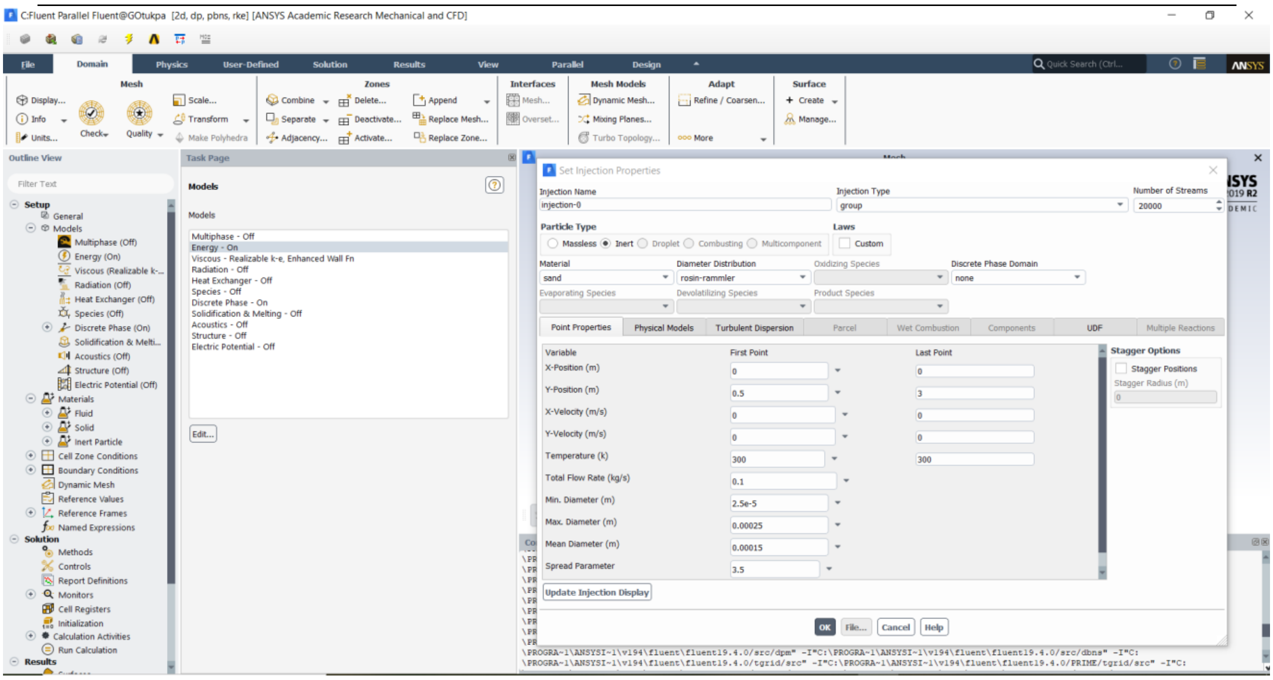

C:Fluent Parallel Fluent@GOtukpa [2d, dp, pbns, rke] [ANSYS Academic Research Mechanical and CFD]

Models

Models

Multiphase - Off
Energy - On
Viscous - Realizable k-e, Enhanced Wall Fn
Radiation - Off
Heat Exchanger - Off
Species - Off
Discrete Phase - On
Solidification & Melting - Off
Acoustics - Off
Structure - Off
Electric Potential - Off

Set Injection Properties

Injection Name: injection-0
Injection Type: group
Number of Streams: 20000

Particle Type: ○ Massless ● Inert ○ Droplet ○ Combusting ○ Multicomponent

Laws: ☐ Custom

Material: sand
Diameter Distribution: rosin-rammler
Discrete Phase Domain: none

Point Properties

Variable	First Point	Last Point
X-Position (m)	0	0
Y-Position (m)	0.5	3
X-Velocity (m/s)	0	0
Y-Velocity (m/s)	0	0
Temperature (k)	300	300
Total Flow Rate (kg/s)	0.1	
Min. Diameter (m)	2.5e-5	
Max. Diameter (m)	0.00025	
Mean Diameter (m)	0.00015	
Spread Parameter	3.5	

Stagger Options: ☐ Stagger Positions; Stagger Radius (m): 0

```
\PROGRA~1\ANSYSI~1\v194\fluent\fluent19.4.0/src/dpm" -I"C:\PROGRA~1\ANSYSI~1\v194\fluent\fluent19.4.0/src/dbns" -I"C:
\PROGRA~1\ANSYSI~1\v194\fluent\fluent19.4.0/tgrid/src" -I"C:\PROGRA~1\ANSYSI~1\v194\fluent\fluent19.4.0/PRIME/tgrid/src" -I"C:
```

Figure 5.1. Modelling settings in Ansys-fluent

The following materials were selected for simulation:

- Air- factoring in the features of the wind in the simulation.
- Sand - factoring the features of dust particles in the simulation.
- Aluminium- factoring the features of the solid walls of the domain.

The boundary conditions were assigned to the respective walls according to our geometrical definition and this is also derived from the mesh generated entering the FLUENT environment.

For the solution method settings, the SIMPLE scheme was selected for the pressure-velocity coupling. As stated in chapter 5, the SIMPLE scheme (a default setting) is an iterative approach in solving for equations. The SIMPLE scheme uses the relationship between velocity and pressure corrections to obtain a pressure field by enforcing mass conservation.

The Least Square Cell Based gradient was selected for the Spatial Discretization Scheme. This is the default setting for the gradient spatial discretization scheme. This method is more accurate compared to the node-based gradient and cell-based gradient when dealing with irregular unstructured mesh and more economical to compute.

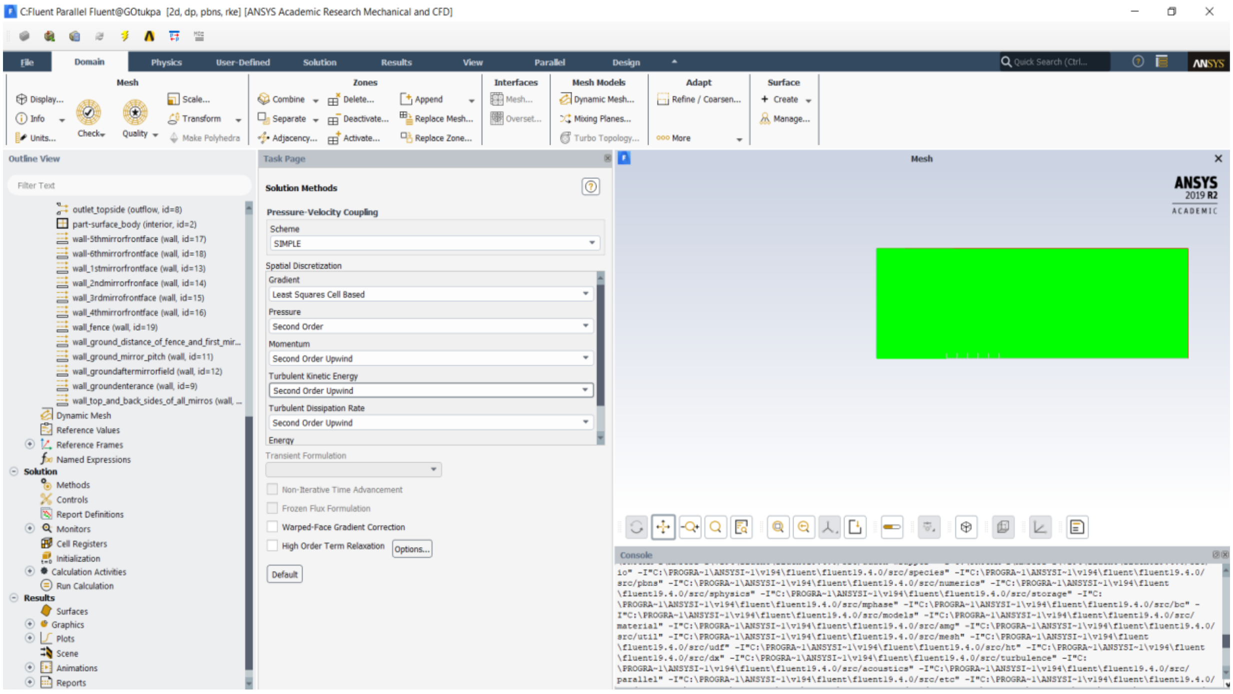

Solution Methods

Pressure-Velocity Coupling

Scheme: SIMPLE

Spatial Discretization

Gradient: Least Squares Cell Based

Pressure: Second Order

Momentum: Second Order Upwind

Turbulent Kinetic Energy: Second Order Upwind

Turbulent Dissipation Rate: Second Order Upwind

Energy

Transient Formulation

☐ Non-Iterative Time Advancement

☐ Frozen Flux Formulation

☐ Warped-Face Gradient Correction

☐ High Order Term Relaxation

```
io" -I"C:\PROGRA~1\ANSYSI~1\v194\fluent\fluent19.4.0/src/species" -I"C:\PROGRA~1\ANSYSI~1\v194\fluent\fluent19.4.0/
src/pbns" -I"C:\PROGRA~1\ANSYSI~1\v194\fluent\fluent19.4.0/src/numerics" -I"C:\PROGRA~1\ANSYSI~1\v194\fluent
\fluent19.4.0/src/sphysics" -I"C:\PROGRA~1\ANSYSI~1\v194\fluent\fluent19.4.0/src/storage" -I"C:
\PROGRA~1\ANSYSI~1\v194\fluent\fluent19.4.0/src/mphase" -I"C:\PROGRA~1\ANSYSI~1\v194\fluent\fluent19.4.0/src/bc" -
I"C:\PROGRA~1\ANSYSI~1\v194\fluent\fluent19.4.0/src/models" -I"C:\PROGRA~1\ANSYSI~1\v194\fluent\fluent19.4.0/src/
material" -I"C:\PROGRA~1\ANSYSI~1\v194\fluent\fluent19.4.0/src/amg" -I"C:\PROGRA~1\ANSYSI~1\v194\fluent\fluent19.4.0/
src/util" -I"C:\PROGRA~1\ANSYSI~1\v194\fluent\fluent19.4.0/src/mesh" -I"C:\PROGRA~1\ANSYSI~1\v194\fluent
\fluent19.4.0/src/udf" -I"C:\PROGRA~1\ANSYSI~1\v194\fluent\fluent19.4.0/src/ht" -I"C:\PROGRA~1\ANSYSI~1\v194\fluent
\fluent19.4.0/src/dx" -I"C:\PROGRA~1\ANSYSI~1\v194\fluent\fluent19.4.0/src/turbulence" -I"C:
\PROGRA~1\ANSYSI~1\v194\fluent\fluent19.4.0/src/acoustics" -I"C:\PROGRA~1\ANSYSI~1\v194\fluent\fluent19.4.0/src/
parallel" -I"C:\PROGRA~1\ANSYSI~1\v194\fluent\fluent19.4.0/src/etc" -I"C:\PROGRA~1\ANSYSI~1\v194\fluent\fluent19.4.0/
```

Figure 5.2. Solutions method settings

In addition to the Spatial Discretization Scheme, the second order was selected for pressure and second order upwind was selected for momentum, turbulent kinetic energy, and turbulent dissipation rate. The second order pressure scheme remakes the face pressures and provides improvement over standard linear schemes. The use of second-order upwind enables quantities at cell faces to be computed using multidimensional linear reconstruction approach and, in this approach, the taylor series expansion is used to achieve a higher-order accuracy of cell faces. Cell-centred solutions about the cell centroid are produced from this expansion. The default first-order upwind scheme was selected for the energy quantity. Results are discussed in the subsequent sections for a simulation case.

5.3. SIMULATION CASES AND THEIR RESPECTIVE SOILING RESULTS

All cases assume the general geometrical and form of figure 3.6 and mesh settings from chapter 3. Thus, with our constrained variables defined in table 4.2, variables shown in figure 3.6 were defined based on those constrained limits and assigned a case to it. 16 cases of the porous barrier were defined, and 9 cases of the non-porous barrier were also defined. Table 5.1 and 5.2 shows all the cases that were simulated with their respective variables along with soiling results for both porous and non-porous wind barrier.

Table 5.1. Simulated porous case

Case Number	**l_3 [m]**	**θ [°]**	**po [m]**	**Soiling (Particles)**
1	0.2	45	0.03	59537
2	0.15	90	0.035	51952
3	0.05	90	0.035	53880
4	0.25	90	0.035	46816
5	0.15	5	0.035	66858
6	0.15	175	0.035	67112
7	0.15	90	0.02	49410
8	0.15	90	0.05	42126
9	0.068696605	20.89211421	0.022804491	71120
10	0.231303395	20.89211421	0.022804491	75076
11	0.068696605	159.1078858	0.022804491	71886
12	0.231303395	159.1078858	0.022804491	80599
13	0.068696605	20.89211421	0.047195509	61870
14	0.231303395	20.89211421	0.047195509	53537
15	0.068696605	159.1078858	0.047195509	57570
16	0.231303395	159.1078858	0.047195509	51228

Table 5.2. Simulated non-porous cases

Case Number	**l_3 [m]**	**θ [°]**	**po [m]**	**Soiling (Particles)**
1	0.15	90	0	78562
2	0.05	90	0	74884
3	0.25	90	0	74427
4	0.15	5	0	78244
5	0.15	175	0	76702
6	0.05	5	0	82379
7	0.25	5	0	86959

8	0.05	175	0	74482
9	0.25	175	0	74442

The simulation case 1 is presented in 5.4. The results of all the other cases are presented in Appendix B of the dissertation and their respective soiling parameters is presented in table 5.1 and 5.2.

5.4. SIMULATED POROUS CASE 1

5.4.1. GEOMETRICAL SETTINGS

According to table 7, the first case assumes values as shown:

Table 5.3. Porous Case 1 Variables

Case Number	l_3 [m]	θ [°]	po [m]
1	0.2	45	0.03

In ANSYS the geometrical settings were defined as shown in figure 47 and table 10:

Table 5.4. Porous Case 1 ANSYS Geometrical Settings

Case Number	L6 [m]	A7 [°]	V10 [m]
1	0.2	45	0.03

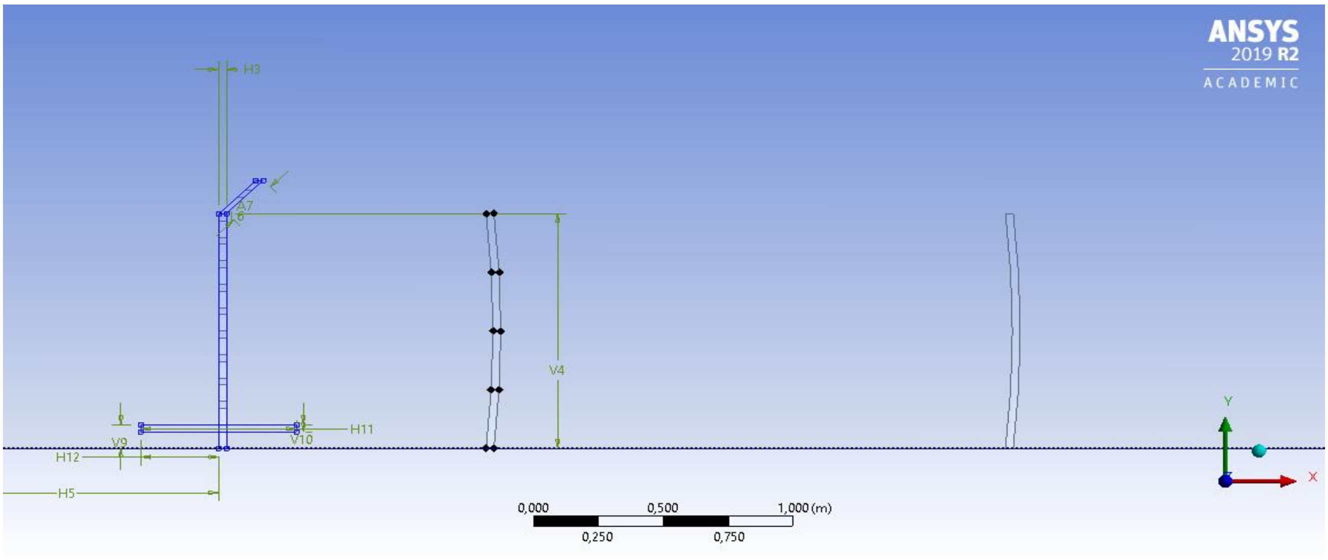

Figure 5.3. Porous Case 1 geometrical Settings

ANSYS design modeller was used to obtain figure 5.3. The use of the modeller offers a sketch and extrude approach to producing models. The modeller provides unique modelling functions for simulation that include parametric geometry creation, concept model creation, CAD geometry modification, automated cleanup and repair, and several custom tools designed for fluid flow, structural and other types of analyses (Ozen Engineering, 2020).

5.4.2. MESH SETTING

The mesh of this case was generated as explained in chapter 2 and the mesh information and quality can be shown in table 5.5 and displayed in figure 5.4.

Table 5.5. Porous Case 1 mesh statistics

Nodes	875822
Elements	873401
Mesh Metric Min -Element Quality	1,9711e-002
Mesh Metric Max-Element Quality	0,99947
Mesh Metric Average-Element Quality	0,7204

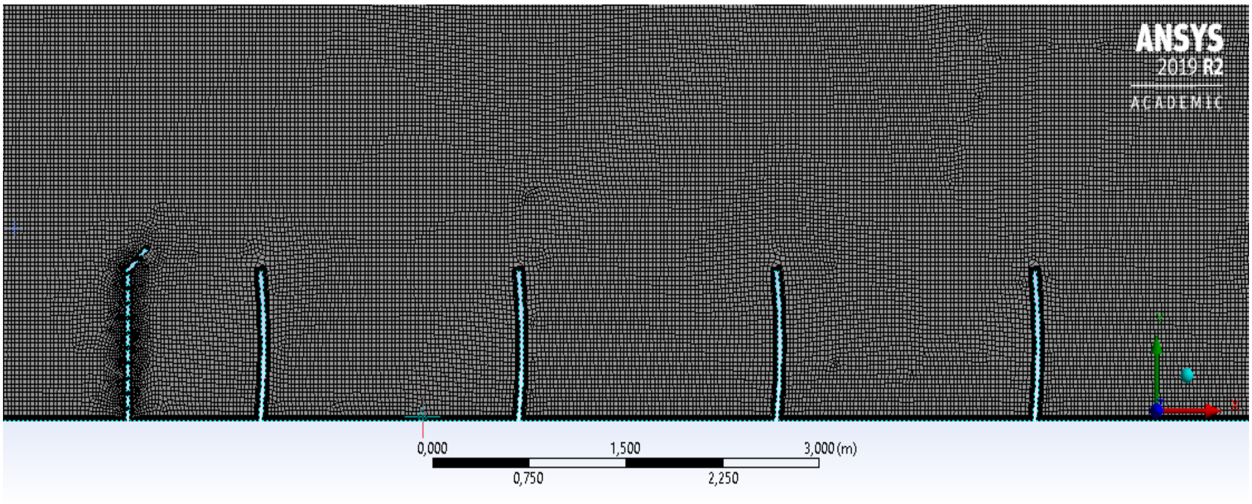

Figure 5.4. Porous case 1 mesh

With the mesh statistics displayed in figure 5.4 and table 5.5, the upcoming results will be seated at a fine level accuracy.

5.4.3. ANSYS-FLUENT SIMUALTION RESULTS

The ANSYS FLUENT settings were applied, and the following results were obtained after solving for 2500 iterations:

i. Scaled Residuals: Convergence was achieved after 2500 iterations. The convergence is shown by the levelling off of the residuals in which there is no change in values.

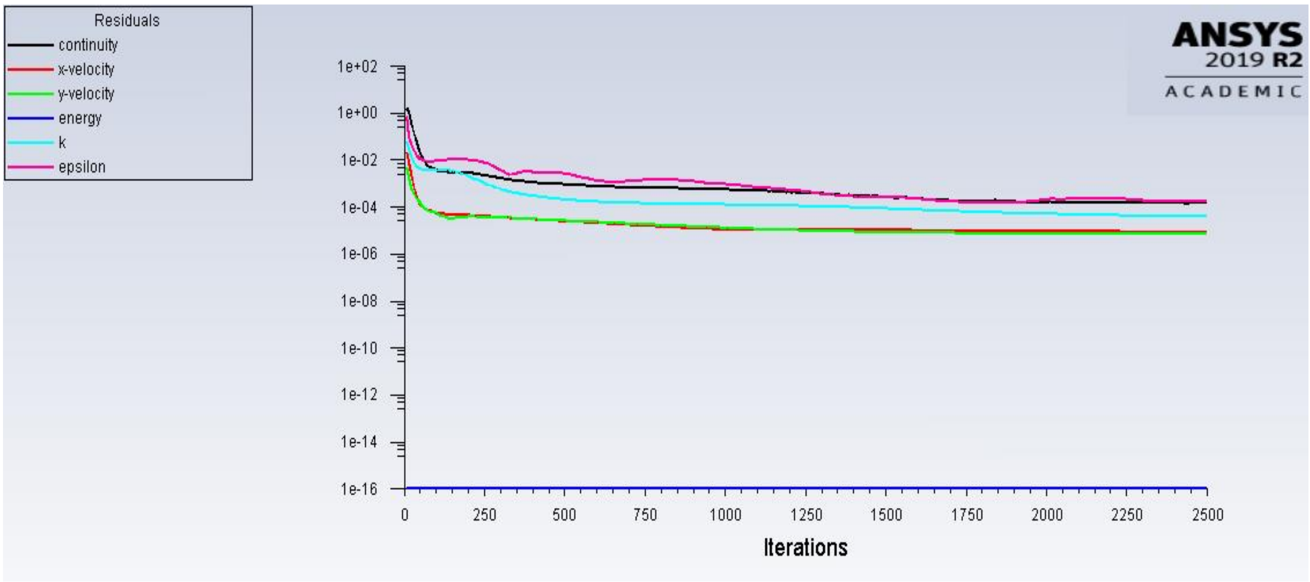

Figure 5.5. Porous Case 1 Scaled Residuals

ii. Particles tracked: 1 250 000 particles tracked

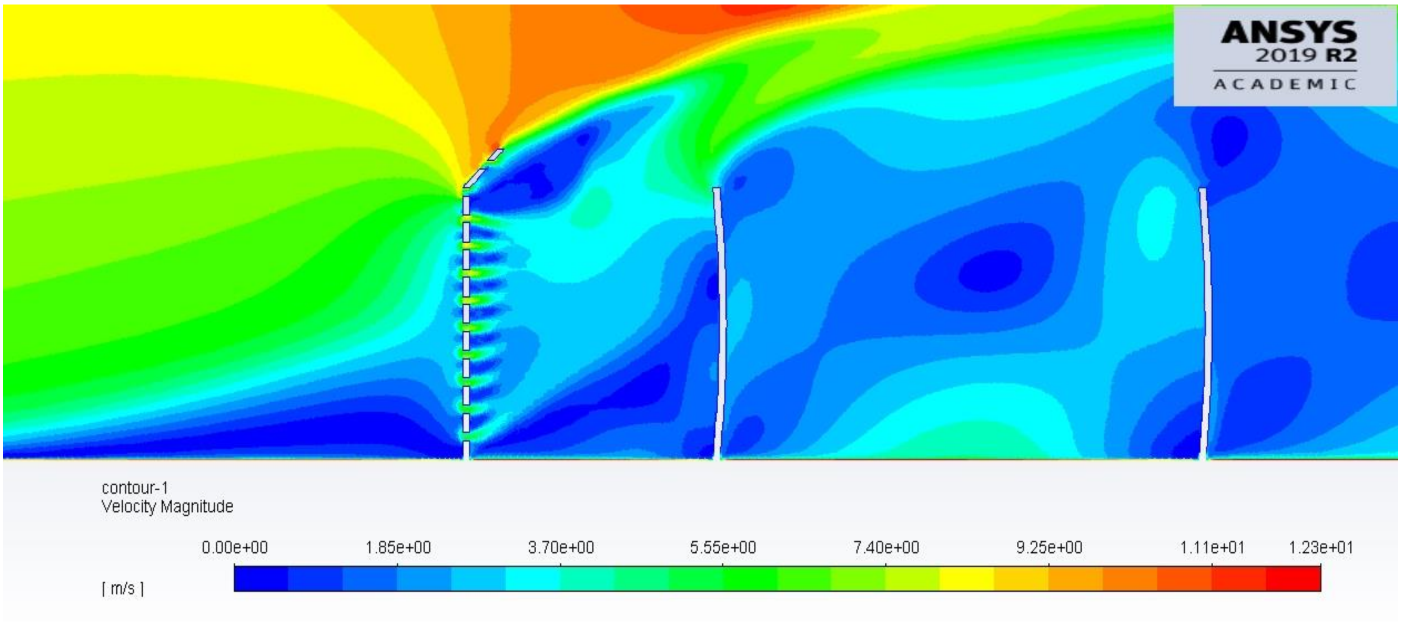

Figure 5.6. Porous Case 1 velocity contour magnitude

The velocity contour of the flow is displayed in figure 5.6. It is observed in figure 5.6 that the velocity close to the maximum velocity (12.3m/s) is seen to occur at flap region. This is definitely possible due to the fact that flap feature acts as deflection rod at the wind barrier upper region. Thus, there was a sudden change of velocity as dust particles collided with the angular surface of the flap causing an angular displacement of particles over mirror field. Flow velocity is generally reduced as dust particles enter mirror region to 3.7m/s. The wind barrier was generally essential in reducing velocity flow from wind carrying dust particles.

Table 5.6. Porous case 1 particle fate

ANSY labelled Wall- ID zone	**Geometric Definition**	**Particles Trapped**	**Particles Escaped**
7	Outlet end side		364217
10	Ground distance between fence and 1st mirror	14	
11	Ground distance of mirror pitch	47097	
12	Ground distance after mirror field	758722	
13	1st mirror front face	29	
14	2nd mirror front face	78	
15	3rd mirror front face	781	
16	4th mirror front face	9124	
17	5th mirror front face	22269	
18	6th mirror front face	27256	
19	Wind Barrier front	11700	
20	Top and back sides of all mirrors	8666	
Soiling [Particles] (Equation 3.1)		59537	

5.5. SIMULATION VALIDATION

It is important to note that verification of features for this study was done. To verify the 2D numerical model done approach in this study, the experimental set up presented by Paetzold, et al., 2014. The experimental set up had dimensions of 500mm, 150mm, 40mm and 40mm, respectively, for aperture, focal length, tube absorber diameter and rotating tube diameter as shown in figure 5.8. According the experimental set up a slight negative pitch of the trough of 1–2° was observed, due to the non-rigid turntable of the wind tunnel. Therefore, a 2D trough with a pitch angle of -2° was set up in the computational domain displayed in figure 5.9.

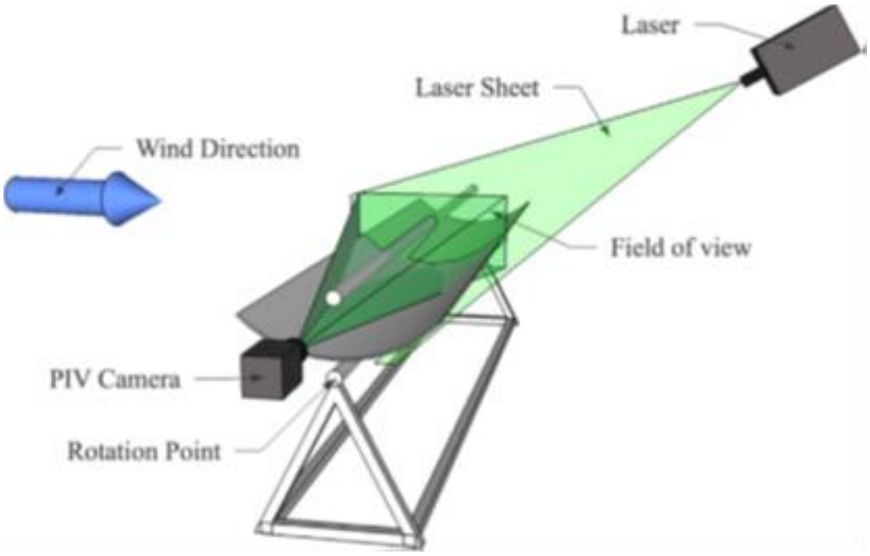

Figure 5.7. Schematic of the PTC experimental PIV set-up in the wind tunnel (Source: Paetzold, et al., 2014)

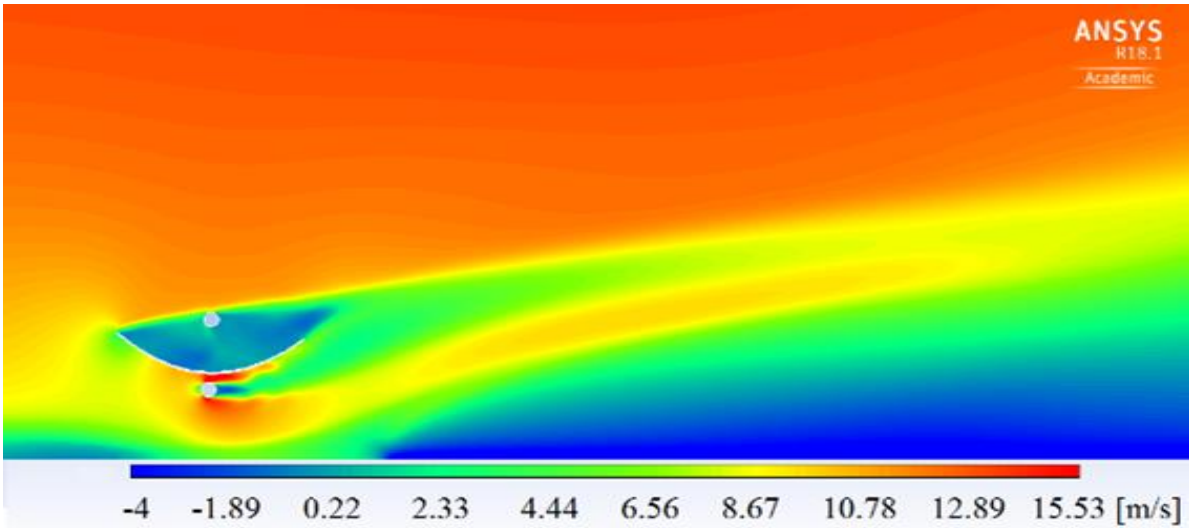

Figure 5.8. The CFD simulation at pitch angle= -2°. (Source: Paetzold, et al., 2014)

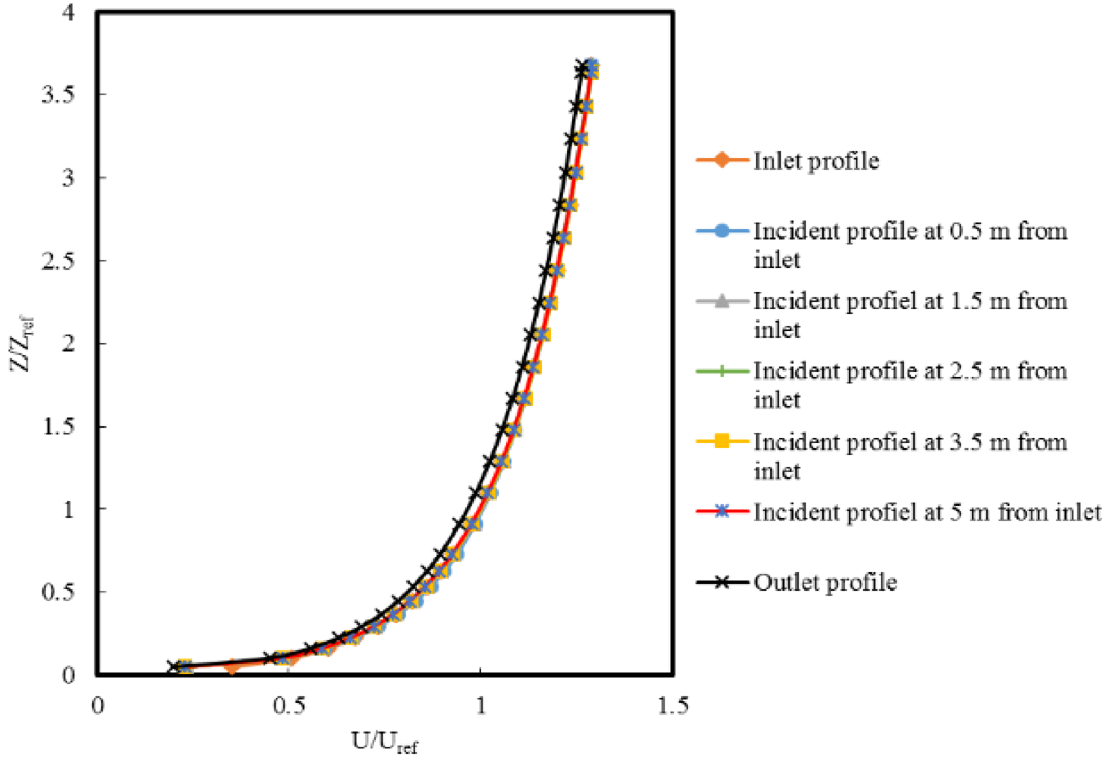

Figure 5.9. Dimensionless velocity profile (Source: Paetzold, et al., 2014)

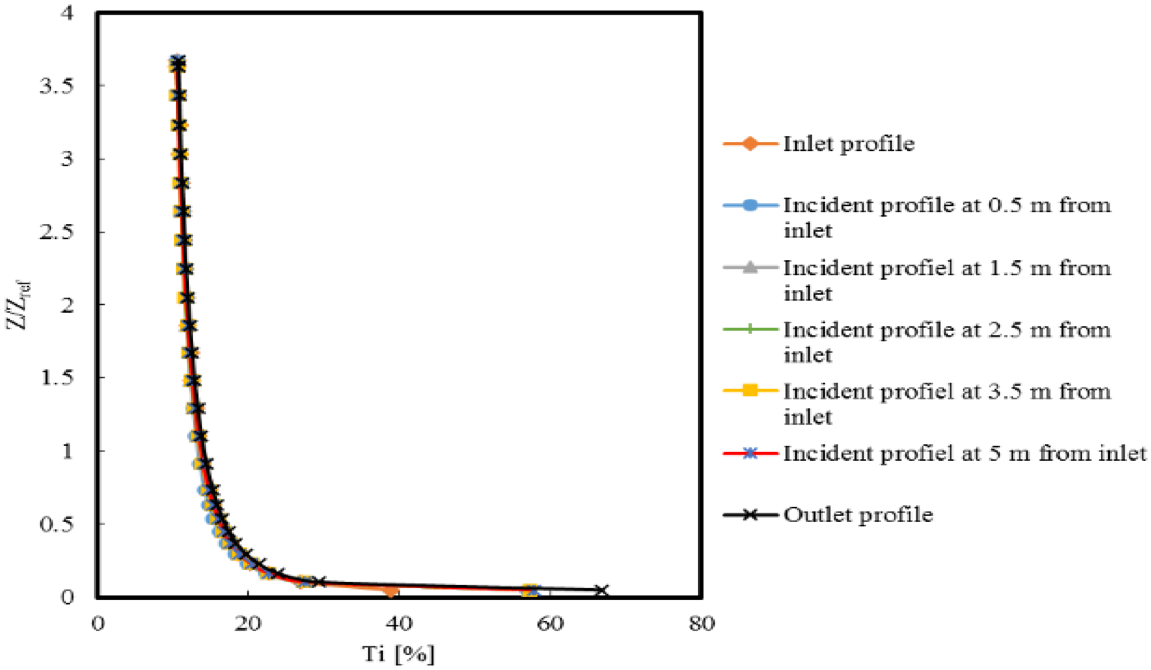

Figure 5.10. Dimensionless velocity profile (Source: Paetzold, et al., 2014)

Also, one of the most important features to verify in this investigation was to make sure to determine if the atmospheric boundary layer (ABL) is horizontally homogeneous for both models. According to Moghimi, et al., 2018, the horizontal homogeneity of an ABL verifies that the incident profile seen by both wind barrier structures in this investigation is the same as the one generated at the inlet. In observing figure 5.10 and figure 5.11, the shape and order were preserved from inlet to outlet. With both profiles having the same inlet and outlet values for each profile, one can consider the ABL profile to be horizontally homogenous with a slight decay across both domains.

5.6. CONCLUSION

There were 25 simulation cases that were performed. 16 porous cases and 9 non-porous cases. The chapter showed the geometrical, mesh and ANSYS-FLUENT settings of all cases. The chapter also provided readers with the particle fate of the induced particles within the domain. For all cases 12500000 were tracked and the particles stats entering the domain was recorded. The number of particles being deposited on all parabolic troughs were recorded and reported as soiling.

It is already apparent that mirror soiling occurs more with a non-porous (table 5.2) solid barrier as opposed to that of the porous barrier (table 5.1). The soiling for the porous cases was never above 81000 particles while for that of the non-porous case the soiling for majority of the cases were above 70000 particles. Therefore, one can conclude that the introduction of the porosity feature is a limiting factor for mirror soiling based on the simulation case results obtained from ANSYS-FLUENT. The next chapter will provide an optimum candidate based solely on the porous cases due to our conclusion and simulated cases performed.

CHAPTER 6

OPTIMIZATION OF SIMULATED POROUS CASES

6.1. INTRODUCTION

Numerical optimization is a technique used by everyone to determine the best possible design for any given scenario. Recollecting the information about optimization techniques performed in chapter 4, this chapter implements that information to determine an optimum candidate of the simulated cases.

Based on the conclusion in our previous chapter, the results of an optimum candidate of a porous wind barrier will be determined and explained to readers. As stated previously, ANSYS DX was the simulated tool used for this study.

6.2. SIMUTLATION TO OPTIMIZATION ALGORITHM PROCEDURE

During the optimization process, ANSYS DX was used to generate design points based on variation of the independent parameter. ANSYS DX uses mathematical optimization which is based on the Response Surface Method. The response surface method aims to visualize the relationship between the input and output parameters (Ansys, 2011). The optimization problem is given as equation 45 in chapter 4.

In order to create response surfaces, a Design of Experiments (DOE) was done to generate design points. In this case, 25 auto-defined different design points were defined for 2 independent input parameters for the non-porous barrier and 3 independent input parameters for a porous (porosity parameter) barrier (Chapter 5). This was done by a mathematical algorithm using the specified value of each parameter. For the output parameters, a 2nd order polynomial response surface with variable variation type was made and combined together. The 2nd order model was used because of its flexible nature, easy-to-estimate output parameters feature, and it is majorly used to solve real response surface problems practically (Ansys, 2011). The model is given by equation 6.1:

$$\eta = \beta_0 - \sum_{j=1}^{k} \beta_j x_j + \sum_{j=1}^{k} \beta_{jj} x_j^2 + \sum_{i<} \sum_{j=2}^{k} \beta_{ij} x_i x_j \qquad (6.1)$$

The first 16 cases were cases that had the porous wind barrier and the final 9 cases were cases that had a non-porous barrier. In total, 25 design points were then simulated using ANSYS-Fluent individually to determine the corresponding soiling for each individual design points. The wanted outcome for each simulation performed was the mirror soiling parameter quantified for each 25 cases.

Having established that the non-porous simulated cases provided soiling that was generally more than that of the porous cases (Chapter 5), the optimization process was only done on the 16 simulated porous cases. Mirror soiling is the total sum of tracked particles deposited on each mirror surface caused by the adhesion of particle assumption. Each mirror surface with its corresponding tracked particle number of the domain was identified by their respective zones which is assigned by ANSYS-FLUENT automatically (Chapter 5).

The results of the simulated porous 16 cases were then re-fed back into ANSYS DX as an input for a response surface-based optimization. ANSYS DX constructed a response surface for the porous wind barrier and an optimum case based on the constructed surfaces were obtained.

6.3. OPTIMIZATION RESULTS AND DISCUSSION

6.3.1. OPTIMUM CANDIDATES

After optimization with ANSYS DX was completed, table 109 shows the optimum candidate that was produced from the constrained limit.

Table 6.1. Optimum candidate porous wall barrier

Porous Wall Barrier			
Independent Parameter	**Lower Bound**	**Upper Bound**	**Optimum Candidate**
Po	0.02	0.05	**0.050**
l3	0	0.20	**0.201**
θ	5	175	**93.762**

6.3.2. GOODNESS OF FIT

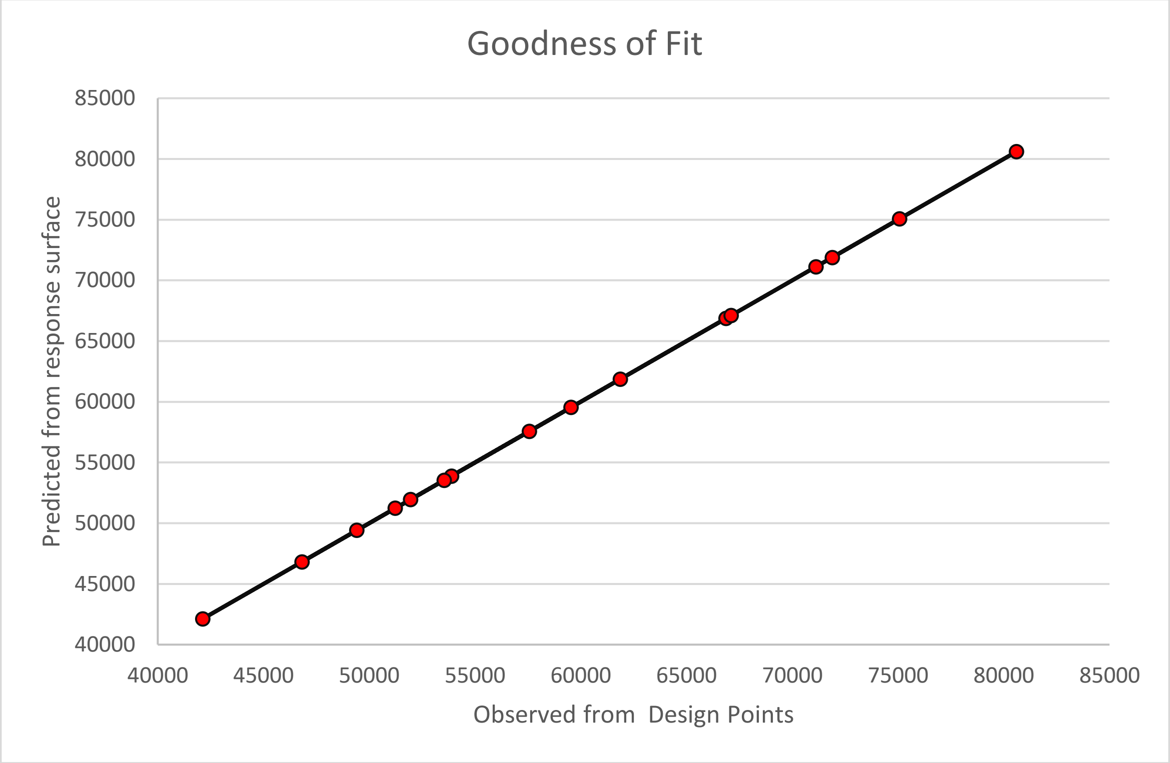

Figure 6.1. Goodness of fit for 16 simulated porous cases

Most of the points of figure 6.1 fit well within the straight line which indicates a high-level of accuracy.

6.3.3. SURFACE RESPONSE

The surface response is given by figure 6.2 and figure 6.3. It is observed from the surface response that mirror soiling decreases with increasing flap length, reaches a minimum value of soiling and then increases with a continuous increase of flap length. This occurrence is particularly true as increasing the flap length to a certain point deflects incoming high-altitude dust particles that have the chance to enter the domain from higher a region. Also, in addition to that point, an increase in flap length leads to deflecting most of the particle outside the mirror field. with a general increase in porous size there would be a decrease in mirror soiling. Increasing the porous gaps decrease the turbulence effect at the downstream therefore enabling flow that creates less vortices within the domain.

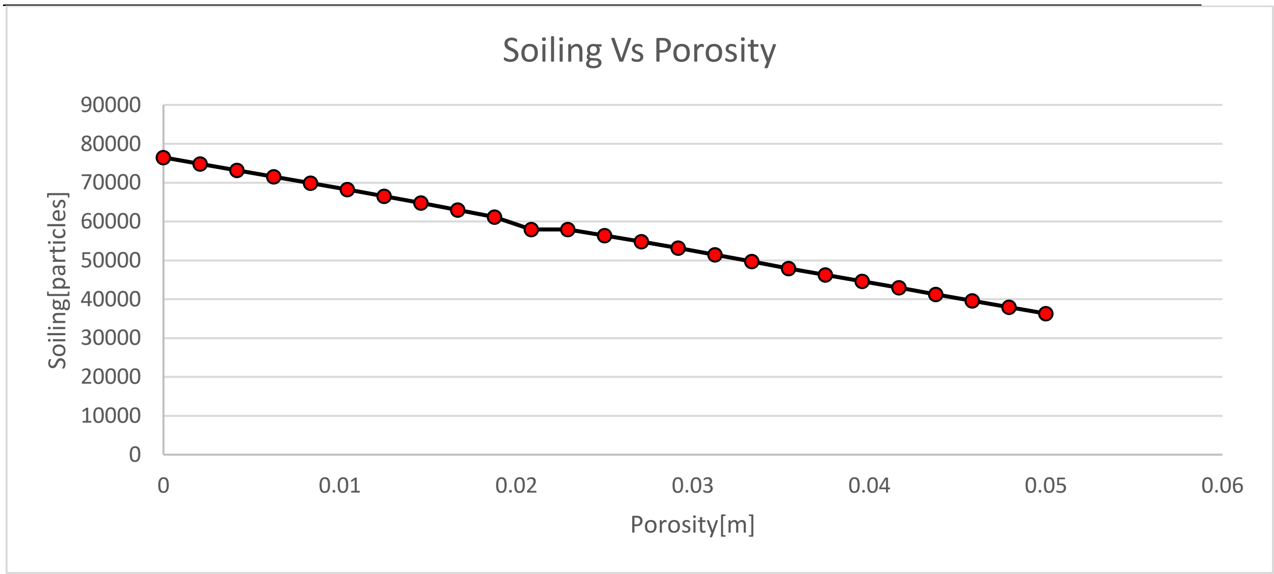

Figure 6.2. 2D response surface soiling vs. porosity

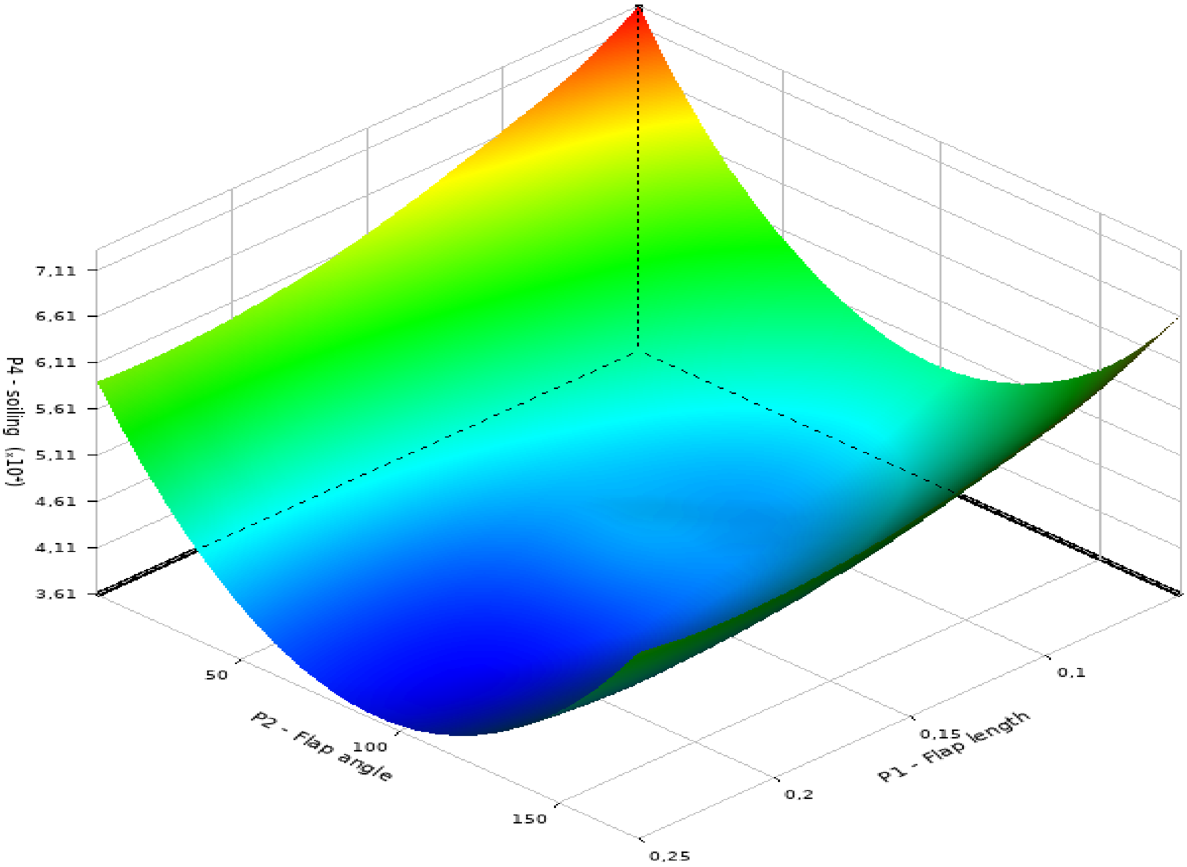

Figure 6.3. 3D Surface response flap length (x label), flap angle (y label) vs soiling on z axis

Downstream turbulence intensity controls the magnitude and number of formed vortices in the mirror field. By introducing a porous barrier, one can limit these vortices within a domain as it acts like a filter in reducing the velocity of the prevailing wind and thus the size of particles that passes through the barrier. This is also similar to the conclusion that was made about the non-porous barrier at the end of chapter 5.

6.3.4. LOCALITY SENSOR

Further proof of why the porosity feature on a wind barrier affects particle deposition is indicated by the local sensitivity displayed in figure 6.4. It is observed that porosity holds the highest percentage that contributes to the minimum particle deposition. This is true as the mirror soiling was higher with performed simulation cases with no porous feature.

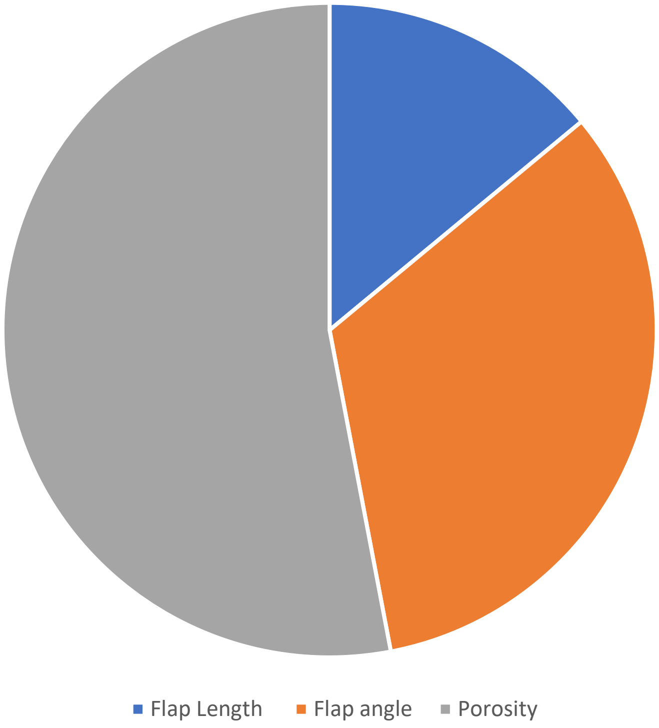

Figure 6.4. Locality sensor

6.4. VALIDATION OF THE OPTIMUM CANDIDATES AND RESULTS THEREOF

To validate the optimum candidates in shown in table 6.1. The values were adjusted in the geometrical settings and the fine mesh was derived accordingly (Chapter 3) and then simulated in ANSYS Fluent with the setting discussed in Chapter 5, ultimately producing the following results.

i. Velocity Streamline:

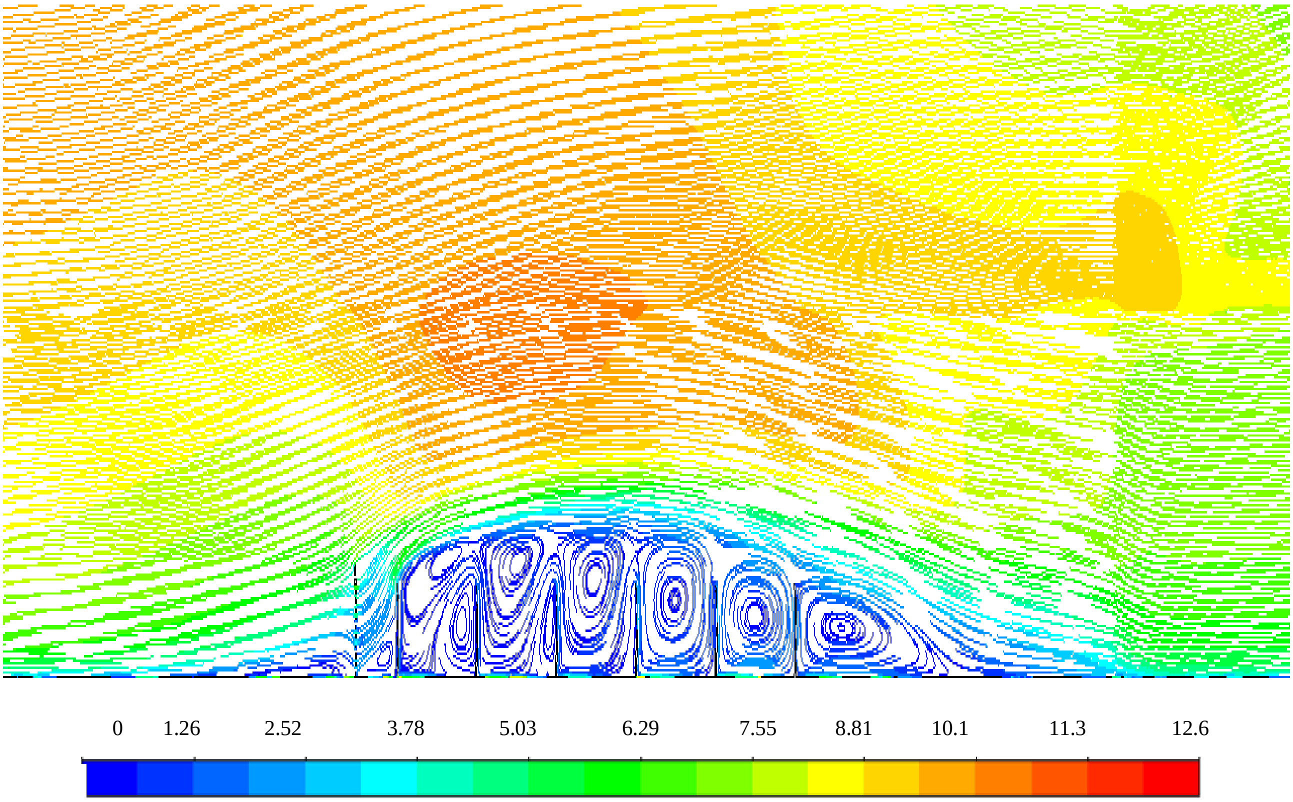

Figure 6.5. Velocity streamline of the optimum wind barrier

In observing the particle streamline, the porous barrier plays a significant role in reducing the velocity of the airflow and deflecting the stream at a fast magnitude over the mirror facets. The velocity of the stream was incoming at a value of 5 m/s (light blue) hitting the barrier and then deflected at the barrier flap at approximately 8 m/s. This high velocity defection is due to the barrier flap length as well as the barrier flap angle which enables the streamline to be passed over the domain region of mirror facets. It is important to note that the region containing the mirror facets have the least amount of streamline velocity (dark blue) magnitude as although the barrier is porous, it still maintains the ability to resist incoming airflow velocity accordingly.

Generally, there are vortices present between mirror facets in which the magnitude is close to 0 m/s (dark blue). A normal vortex occurs at a particular point in a fluid region indicating the rotation at that point in time and in this case, it is between mirror facets. The cause is due to low turbulence at a minimum temperature and low viscosity with a slight increase in velocity producing the vortices between mirror fields. With fewer particles present, the fluid flow in mirror facets regions shows that there is low viscosity, thus producing the vortices.

ii. Static Pressure Contour:

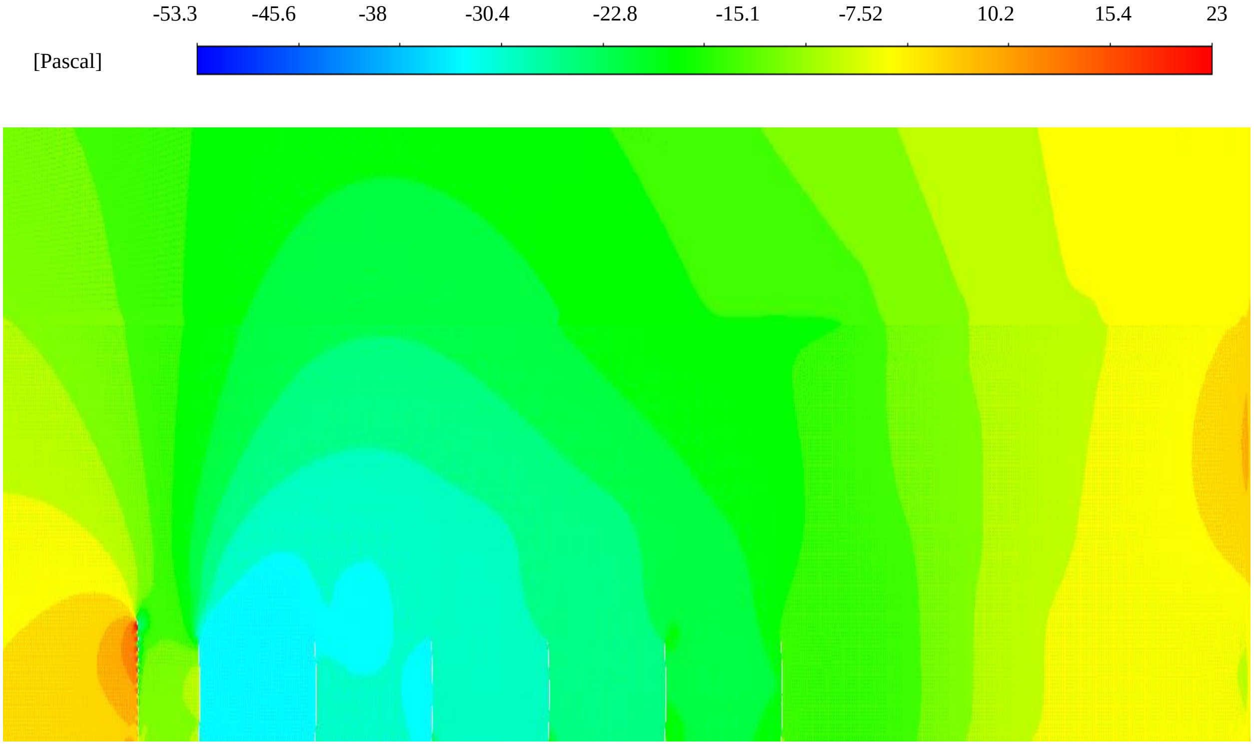

Figure 6.6. Optimal porous wind barrier static pressure contour

The streamline shown in figure 6.5 generally reduces in pressure which is visible in figure 6.6. It is seen that the pressure of the flow is reduced significantly when the airflow hits the porous wind barrier as the colour gradually changed from orange-yellow which indicates a value of about 10.2Pa (above atmospheric pressure) to a blue and green colour indicating a range of values between 7.52 Pa to 38 Pa (below atmospheric pressure). One can also see that between the 1st, 2nd, 3rd, and 4th there is a general constant pressure region (light blue) value of 30.4 Pa (below atmospheric pressure). After the 4^{th} mirror the pressure values gradually as the contour colour changes from light blue to green gradually between the 4th and 6th mirror. The cause of this could be due to the location of mirrors (1st to 4th) which are situated close to the wind barrier enabling a reduction of the turbulence effect formed by vortices.

iii. Turbulence Contour:

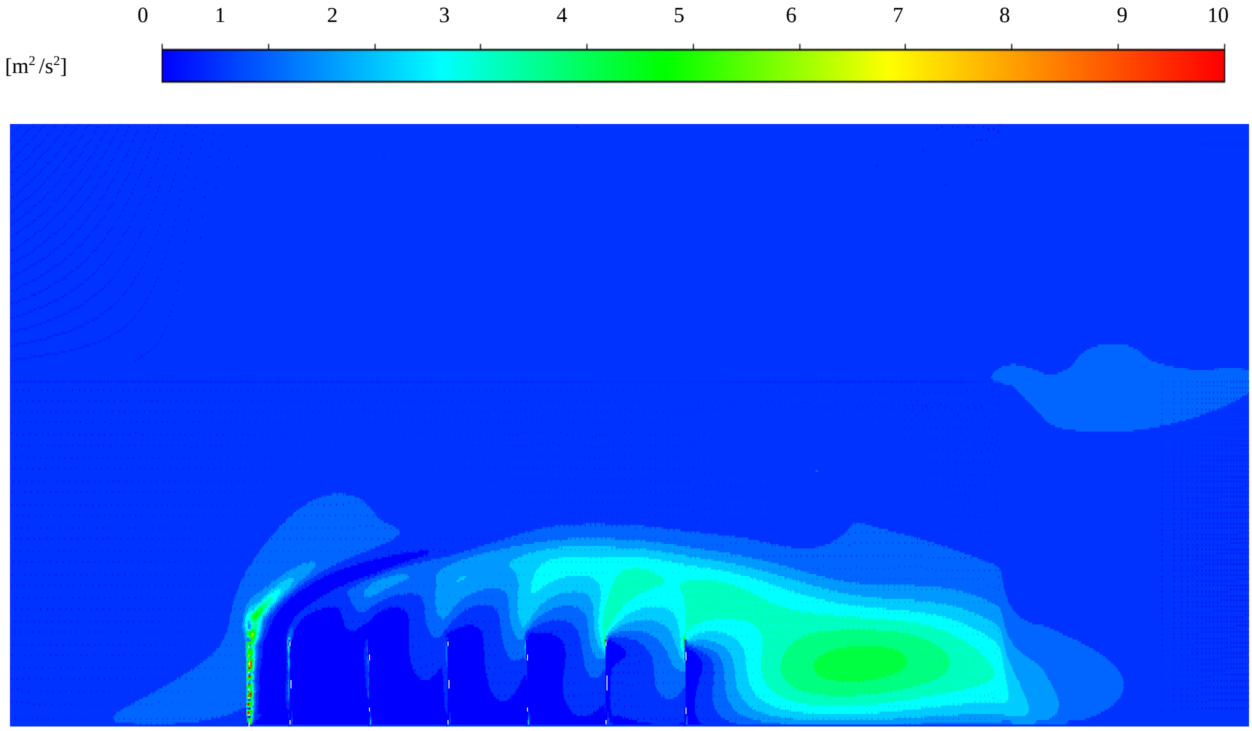

Figure 6.7. Optimal porous wind barrier turbulent kinetic energy contour

The velocity streamlines and pressure figures are further validated by figure 6.7. Figure 6.7 displays the contour of the turbulent kinetic energy that occurs over the domain. From the graph it is observed that there is generally little to no turbulent kinetic energy within the region of mirror facets. However, there is a colour change from dark blue to light blue containing a light green vortex that occurs at the back of the 6th mirror.

The flap feature present on the barrier, enables a massive deflection of particles over the field shown in figure 6.5 with high velocity coupled with a low-pressure difference enabling that turbulence kinetic energy change at that region. The evidence of a low- pressure change is the slight change of colour within that region. There is a change of turbulence that happens at the porous holes of the barrier as seen in figure 6.7 upon close observation. This occurs because porosity reduces the wind speed upon impact (also shown by figure 6.5) creating eddy sizes as large as the porous holes. This proves that the porous wind barrier has the ability to drastically reduce incoming airflow at high pressures keeping mirror facets region free from incoming high-pressured airflow dust particles.

iv. Particle Size distribution:

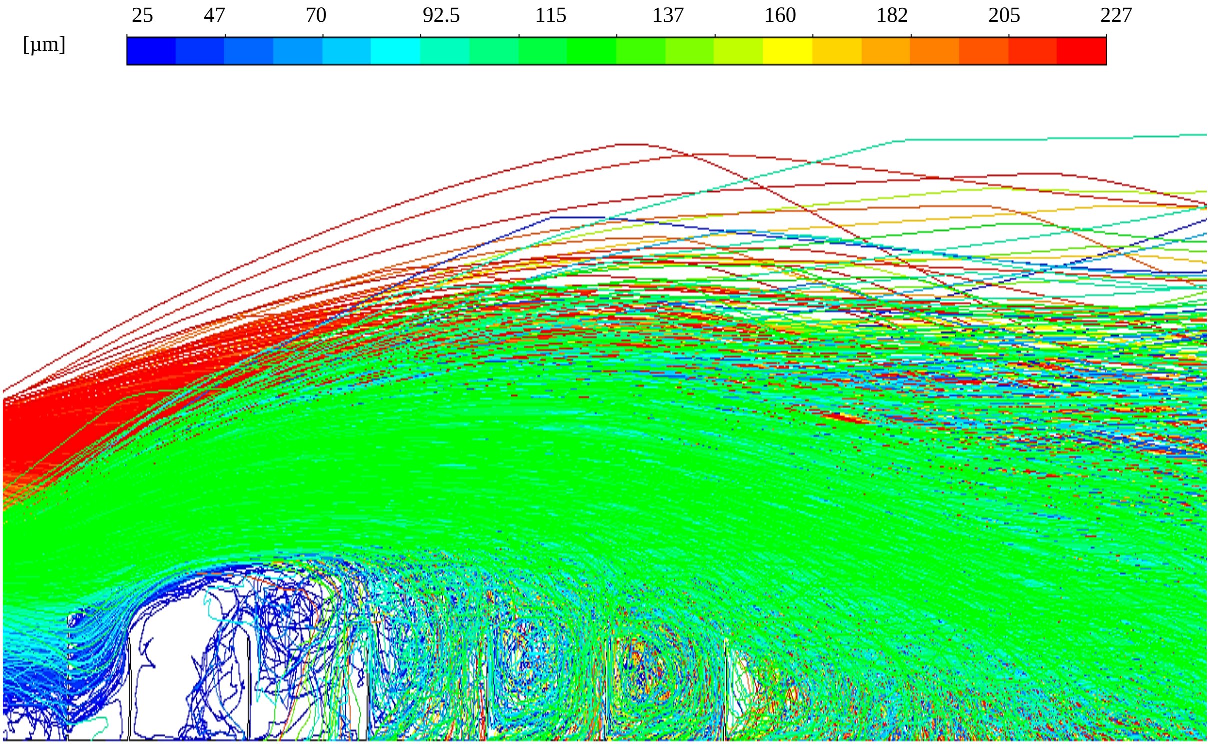

Figure 6.8. Optimal porous wind barrier particle size

It is shown in figure 6.7 that the diameter of larger size of the particles is either deflected over the domain or settled on the floor of the mirror region. The particle size ranging from 100µm(green) above (red) were generally deflected. This is certain phenomena due to flap feature attached to the barrier and structure. Thus, the size that is less than 100µm are more visible in the mirror regions creating recirculation and vortex regions between mirrors. As stated previously, with low viscosity from less dense particle regions will form the visible vortex regions formed at a low pressure.

6.5. DISCUSSION OF OPTIMIZATION RESULTS

The premise of this research dissertation indicates that wind barriers are capable of limiting mirror soiling of PTC plants. Optimization effectively decides the best features for the wind barrier structure to minimize mirror soiling to its lowest level through mathematical means and numerical accuracy.

This was done by means of ANSYS DX which takes data from the simulations performed as input in the previous chapter.

Both wind barriers share two major parameters in design (l3 and θ). In comparing the little difference and the constant range of θ between both wind barrier structure signifies the type of effect it had in determining the optimum candidates for both structures. It is evident that porosity is a key feature that limits soiling within a given PTC domain as shown by the presented results (table 5.1-5.2 and figure 6.5-6.8). Porosity is indicated as the void space feature in which the optimum candidate recorded it at its upper bound, 0.05m. It is possible that due to the massive effect caused by porosity on the wind barrier, an increase in porosity will further minimize mirror soiling depending on the barrier structure present and observing the trend presented in figure 6.2. With both structures being different, its sensible for any of the barrier to alter deflections of the wind particle with a longer flap length as the flap length is the only physical variable parameter that majorly affects the deflection (figure 6.5-6.8) while porosity can be considered as the feature that contributes to deflection as well as turbulence reduction within the domain figure 6.7.

The presented results can be summarised as the particle fate shown by table 6.2. The results shown by table 6.2 describes the particle conditions of the optimum candidate. As the wind barrier acted as a limiting factor to the incoming velocity, there were fewer large particles deposited on the mirror surfaces. This is because if the wind velocity is decreased below 1 m/s, particles bigger than 100 μm would fall to the ground (Sansom, et al., 2018) as there is not sufficient lift for these particles due to the wind velocity and particle density. Thus, there were more particles of the tracked particles that fell to the ground as compared to the other type of particles shown in table 6.2.

6.6. CONCLUSION

The optimization procedure performed yielded a case that brought to attention that porosity is indeed a major factor that must be considered in the design of a wind barrier. The optimum candidate was re-simulated for validation and the displayed results provided data in which the optimum candidate showed favourable results. In concluding the performance of the optimum candidate of the wind barrier, the particle fate table 6.2 can ultimately deduce its importance.

Table 6.2. Particle fate

ANSYS		**Optimum Porous Barrier**
ID Zone	Walls (names)	
13	wall_1stmirrorfrontface	1086
14	wall_2ndmirrorfronface	273
15	wall_3rdmirrofrontface	932
16	wall_4thmirrorfrontface	3352
17	wall-5thmirrorfrontface	7716
18	wall-6thmirrorfrontface	19634
Soiling (particle)		32993
number of particles tracked (particles)		1250000
number of particles escaped (particles)		281479
% particles soiling		2.64

It is observed from table 6.2 that the soiling of the optimum candidate is the minimum compared to the case results showed in the appendix and chapter 5.

CHAPTER 7

CONCLUSION AND FUTURE RECCOMENDATIONS

7.1. CONCLUSION

The presented dissertation and research focused on the numerical optimization of wind barriers for the minimization of mirror soiling in a PTC plant. A PTC plant has been proven to be the most developed type of CSP plant that uses PTC technology to harness solar energy and convert it to maximum usable energy for the masses of a given geographical location. Usually, PTC plants are located in dry arid regions where sunlight is easily accessible. However, dry regions are usually dessert regions where the atmosphere is disrupted by sandstorms and dust clouds ultimately causing the air to be filled with dust particles.

The deposition of dust particles from the atmosphere onto the mirror facets of PTC technology (and CSP technology) is mirror soiling. Mirror soiling majorly causes limited reflectivity on mirror facets and therefore causes a significant reduction of productivity of useful output energy. This is indicated by PTC plants as a major industrial problem. There are cleaning methods that have been developed to help with mirror soiling. Majority of them need water to be implemented. However, the use of water in dry regions where water is scarce and difficult to obtain is neither economical nor sustainable for a given region. Thus, mirror soiling reduction techniques were developed by researchers and engineers. One of these techniques involve the use of a wind barrier. The essence of the presented dissertation utilizes the wind barrier method with the hopes to combat mirror soiling.

The research incorporates numerical study with a CFD approach to produce a solution. Numerical studies are used commonly by researchers and engineers especially when problems are complex. The need to break down a problem into simpler problems become imperative. Thus, the research first broke down the problem into simpler problems. By identifying and understanding the occurrences of the sub problems in relation to the parent problem, it was easier to deduce and research the principles involved with the simpler problem. When using numerical study within a CFD approach it is necessary to accurately formulate the problem and sub problems at hand as a start. It is known that numerical study does not provide an exact solution to the problem however it provides and accurate approximation of the solution. Therefore, with optimization one can get extremely close to the solution with a given mathematical goal in hand to work practically and not just theoretically.

The presented dissertation utilized numerical optimization to obtain an optimum wind barrier candidate and according to the presented results the following can be concluded:

1. An optimum candidate that can be installed in a PTC plant needs to have a flap length **0.201m** at an angle of **93.7°** placed at the top of a unit length of a wind barrier with a porous feature of **0.050m** (table 6.1).
2. Porosity in a wind barrier structure is needed in order to effectively minimize mirror soiling.
3. The use of the porous barrier minimized mirror soiling by **2.64%.**
4. Wind Barriers with a longer flap length can deflect more airflow particles out of the domain.

The use of ANSYS simulation and optimization tool for the purpose of this study were particularly useful to the completion of this research. All the objectives stated in chapter 1 were completed successfully and with that being said there is always room for innovation and development on the proposed optimum candidate. Therefore, one can conclude that based on this dissertation, porous wind barriers with a flap can effectively deflect a significant amount of dust particles from the domain of a given PTC region ultimately increasing the productivity of a PTC plant limiting the use of water as a cleaning agent.

7.2. FUTURE RECOMMENDATION

As mentioned previously, there is always need for innovation for any developed engineered product. In terms of innovating the wind barrier, a more realistic scenario can be used with a 3D scenario where the geometrical model can be built as likely as possible of a given geographical region. In doing this one must use an immensely powerful CPU to achieve good result and generate results. Also, the use of other turbulent models such as the k-ω models can be implemented in the 3D model.

The introduction of different geometrical features on the wind barrier is also a recommendation. As proven in the dissertation the use of the porosity feature had a major effect in the number of particles entering the domain. Thus, change of geometrical features on a barrier can affect the number of particles. Alterations of the structure in general, alteration of the number of erected wind barrier structures and alterations of the features on the structure is a possibility for the future.

REFERENCES

‘Desert’. (2020). Wikipedia. Available at https://en.wikipedia.org/wiki/Desert#cite_note-Uwe20-38. Accessed: 14 July 2020.

‘Parabolic Trough’. (2020). Wikipedia. Available at https://en.wikipedia.org/wiki/Parabolic_trough#/media/File:Solar_Array.jpg. Accessed: 19 June 2020.

Ahmadi, M.H., Ghazvini, M., Nazari, M.S.M.A., Kumar, R., Naeimi, A., and Ming, T. (2018). Solar Power Technology For Electricity Generation A Critical Review. *Energy Sci Eng*. 6: 340–361.

Anglani, F., Barry, J., Dekkers, W. (2016). A Numerical Study On High-Pressure Water Spray Cleaning Forj CSP Reflectors. *AIP Conference Proceedings 1734, 160001*; https://doi.org/10.1063/1.4949242.

Anglani, F., Barry, J., Dekkers, W. (2017). Development and Validation of a Stationary Water-Spray Cleaning System for Concentrated Solar Thermal (CST) Reflectors. *Sol. Energy*. 155, 574–583.

Ansys. (2011). Design Exploration Brochure. *ANSYS INC.*

Aoukli I. (2018). Anti-Soiling Protective Coating for CSP Reflectors. *Akhawayn University.*

Atlas Copco. (2018). Power Blog. Atlas Copco. Viewed 19 July 2020. http://atlascopcopower.tech/dicas-de-manutencao-e servicos/index.php.

Axaopoulos, P. (2016). Basic principles of solar geometry. *TEI*. Chapter 3.

Bagnold, R. (1965). The Physics Of Blown Sand And Desert Dust. *Methuen and Co. Ltd. London*.

Banke, R. (2018). CSP Plant Operations & Maintenance. *Fraunhofer Institute for Solar Energy Systems ISE*. 2nd MENA CS P KIP Workshop.

Behar, O., Khellaf, A., and Mohammedi, K. (2015). A Novel Parabolic Trough Solar Collector Model – Validation With Experimental Data And Comparison To Engineering Equation Solver (EES). *Energy Conversion and Management* ;106:268-281.

Bellos, E., and Tzivanidis, C. (2018). Alternative Parabolic Trough Solar Collectors – A Review. *Progress in Energy and Combustion Elsevier;* 11:1129.

Bellos, E., and Tzivanidis, C. (2018). Enhancing The Performance Of Evacuated And Non-Evacuated Parabolic Trough Collectors Using Twisted Tape Inserts, Perforated Plate Inserts And Internally Finned Absorber. *Energies* 2018;11:1129.

Bellos, E., Tzivanidis, C., and Tsimpoukis, D. (2017). Multi-Criteria Evaluation Of Parabolic Trough Collector With Internally Finned Absorbers. *Applied Energy*; 205:540-561.

Bergeron, K.D., and Freese JM. (1981). Cleaning Strategies for Parabolic-Trough Solar-Collector Fields; Guidelines for Decisions. *Technical Report; Sandia National Labs.* Albuquerque, NM, USA.

Bhaskaran, R., and Collins, L. (2003). Introduction to CFD. Lecture notes accessed at http://courses.cit.cornell.edu/fluent/cfd/.

Bhowmik, N.C., and Mullick, S.C. (1985). Calculation Of Tubular Absorber Heat Loss Factor. *Solar Energy*; 35(3):219-225.

Bhuiyan, N., Ullah, W., Islam, R., Ahmed, T., and Mohammad, N. (2019). Performance Optimisation Of Parabolic Trough Solar Thermal A Case Study Inpower Plants – A Case Study In Bangladesh. *International Journal of Sustainable Energy*, DOI: 10.1080/14786451.2019.164926.

Blazek, J. (2001). Computational Fluid Dynamics: Principles and Applications. *Elsevier*, ISBN:0080430090.

Bohren, C.F., and Human, D.R. (1983). Absorption and Scattering of Light by Small Particles. *New York: Wiley*.

Bouaddi, S., Fernández-García A., Sansom G., Sarasua, J.A., Wolfertstetter, F., Bouzekri, H., Sutter, F., and Azpitarte, I. (2018). A Review Of Conventional And Innovative-Sustainable Methods For Cleaning Reflectors In Concentrating Solar Power Plants. *Sustainability*. doi:10.3390/su10113937.

Bouaddi, S., Ihlal, A., and Fernandez-García, A. (2017). Comparative Analysis Of Soiling Of CSP Mirror Materials In Arid Zones. *Renewable Energy*:101 437-449.

Boukelia, E.T., and Mecibah M.S. (2013). Parabolic Trough Solar Thermal Power Plant: Potential, and Projects Development in Algeria. *Renewable and Sustainable Energy Reviews*. doi:10.1016/j.rser.2012.11.074.

BP. (2019). BP Statistical Review of World Energy. British *Petroleum.* Available at https://www.bp.com/content/dam/bp/businesssites/en/global/corporate/pdfs/energy-economics/statistical-review/bp-stats-review-2019-full-report.pdf.

Burgaleta, J., Ternero, A., Vindel, D., Salbidegoitia, I., and Azcarrraga, G. (2012). Gemasolar, Key Points For The Operation Of The Plant. *SolarPACES Symposium Proceedings*. Marrakech, Morocco.

Canavarro, D., Chaves, J., and Collares-Pereira, M. (2013). New Second-Stage Concentrators (XXSMS) For Parabolic Primaries; Comparison With Conventional Parabolic Trough Concentrators. *Sol Energy* 2013;92:98–105. http://dx.doi.org/10.1016/j.solener.2013.02.011.

Caranese, C., Matino, F., and Maccari, A. (2017). On Purpose Simulation Model For Molten Salt CSP parabolic Trough. *AIP Conference Proceedings 1850, 160002*. https://doi.org/10.1063/1.4984536

Chaanaoui, M., Vaudreuil, S., and Bounahmidi, T. (2016). Benchmark of Concentrating Solar Power Plants: Historical, Current and Future Technical and Economic Development. *Procedia Computer Science*; 83: 782-89.

Chenggang, Y., and Alison, M. (2018). Introduction to Modelling and Simulation Techniques. In: Proceedings of ISCIIA 2018 and ITCA 2018. *The 8th International Symposium on Computational Intelligence and Industrial Applications and The 12th China-Japan International Workshop on Information Technology and Control Applications.* Tengzhou, China.

Cohen, G.E., Kearney, D.W., and Kolb, G.J. (1999). Final Report On The Operation And Maintenance Improvement program For Concentrating Solar Power Plants. *KJC Operating Company & Sandia National Laboratories. R*eport Number: SAND99-1290.

Collares, M., Gordon, J.M., Rabl, A., and Winston, R. (1991). High Concentration Two-Stage Optics For Parabolic Trough Solar Collector With Tubular Absorber And Large Rim Angle. *Sol Energy* 1991;47:457–66.

Duffie, J.A., and Beckman, W.A. (2006). Solar Engineering of Thermal Processes. *Wiley, Hoboken, third ed.*, NJ, USA.

Ennaceri, H. (2016). Nano-Coating Of CSP Reflectors: A Step Towards The Creation Of A Self-Cleaning Effect. *Ph.D Thesis*, *Mohammed V University*. Rabat, Morocco. Available online: https://toubkal.imist.ma/handle/123456789/10415.

Farag, Z. (2015). Development, Test and Optimization of Concept for Mirror Cleaning System for Solar Concentrators Using Dew. *Master's Thesis Kassel University*. Kassel, Germany.

Gaul, H., and Rabl, A. (1980). Incidence-Angle Modifier and Average Optical Efficiency of Parabolic Trough Collectors. *ASME. J. Sol. Energy Eng*. ;102(1):16-21 (doi:10.1115/1.3266115).

Gavez, J.B., and Rodriguez, S.M. (2009). Solar Energy Conversion And Photoenergy Systems. *Vol. I; Encyclopedia of Life Support Systems. Oxford United Kingdom: Eolss Publishers*.

Gong, G., Huang, X., Wang, J., and Hao, M. (2010). An Optimized Model And Test Of The China's First High Temperature Parabolic Trough Solar Receiver. *Sol Energy* 2010;84:2230–45. http://dx.doi.org/10.1016/j.solener.2010.08.003.

Godderidge, B., Tan M., Turnock S., and Earl C. (2006). A Verification and Validation Study of the Application of Computational Fluid Dynamics to the Modelling of Lateral Sloshing. *University of Southampton Fluid Structure Interaction Research Group Ship Science*. Report No 140

Good, P., Ambrosetti, G., Pedretti, A., and Steinfeld, A. (2016). A 1.2mwth Solar Parabolic Trough System Based On Air As Heat Transfer Fluid At 500°C — Engineering Design, Modelling, Construction, And Testing. *Sol Energy* 2016;139:398–411. http://dx.doi.org/10.1016/j.solener.2016.10.002.

Griffith, D.J., Vhengani, L., and Maliage, M. (2014). Measurements Of Mirror Soiling At A Candidate CSP Site. *Energy Procedia 49*:1371 – 1378.

Gross, J.E., Carlos, W.G., Cruz, C.S.D., Harber, P., and Jamil, S. (2018). Sand And Dust Storms: Acute Exposure And Threats To Respiratory Health. *American Thoracic Society.* Am J Respir Crit Care Med Vol. 198, 13–14.

Gua, K. (2005). Relationship Between Photocatalytic Activity, Hydrophilicity And Self-Cleaning Effect Of Tio2/Sio2 Films. *Surface and Coatings Technology.* vol. 191, no. 2-3, pp. 155–160.

Günther, M., Joemann, M., Csambor, S. (2010). Parabolic Trough Technology. *Advanced CSP Teaching Materials*. Chapter 5: 1 – 106.

Hadian, S., and Madani, K. (2013). The Water Demand Of Energy: Implications For Sustainable Energy Policy Development. *Sustainability*: 5, 4674–4687.

Hardt, M., Martınez, D., González, A., Garrido, C., Aladren, S., Villa, J.R., and Saenz, J. (2011). HECTOR—Heliostat Cleaning Team-Oriented Robot. In *Proceedings of the Solar-PACES Conference.* Granada, Spain, 20–23; pp. 20–23.

Hasanpour, A., Farhadi, M., and Sedighi, K. (2014). A review study on twisted tape inserts on turbulent flow heat exchangers: The overall enhancement ratio criteria. *International Communications in Heat and Mass Transfer*; 55:53-62.

Hogan, M. (2009). “The secret to low-water-use, high-efficiency concentrating solar power.” [Online]. Available: http://thinkprogress.org/climate/2009/04/29/204025/csp-concentrating-solar-power-heller-wateruse/.

IRENA. (2020). Renewable Energy Employment by Country. IRENA. Viewed 18 May 2020 https://www.irena.org/Statistics/View-Data-by-Topic/Benefits/Renewable-Energy-Employment-by-Country.

Kasaeian, A., Daviran, S., Azarian, R.D., and Rashidi, A. (2015). Performance Evaluation And Nanofluid Using Capability Study Of A Solar Parabolic Trough Collector. *Energy ConversManag* 2015;89:368–75. http://dx.doi.org/10.1016/j.enconman.2014.09.056.

Klinkov, S.V., Kosarev, V.F., and Rein, M. (2005). Cold spray deposition: Significance of particle impact phenomena. *Aerosopace Science and Technology*; 9: 582-91.

Kohli, R., and Mittal, K.L. (2011). Developments in Surface Contamination and Cleaning. *Volume 1: Fundamentals and Applied Aspects*. MA, USA.

Lee, J., Gill, T.E., Mulligan, K.R., Acosta, M.D., and Perez, A.E. (2009). Land Use/Land Cover And Point Sources Of The 15 December 2003 Dust Storm In Southwestern North America. *Geomorphology*. 105, 18–27.

Leinhard, J IV., and Leinhard, J V. (2012). A Heat Transfer Textbook. *Philogiston Press* fourth ed, USA.

Li, A. (2008). Optical properties of dust, in Small Bodies in Planetary Sciences. *Springer* 167–188.

Liang, H., and You, S. (2015). Comparison Of Different Heat Transfer Models For Parabolic Trough Solar Collectors. *Appl Energy*; 148:105–114.

Liaqat, K., Anss, M., Ali, and Mengal, A.N. (2018). Modelling And Simulation Of A 100MW Concentrated Solar Thermal Power Plant Using Parabolic Trough Collectors In Pakistan. *IOP Conf. Series: Materials Science and Engineering* 414 (2018) 012032 doi:10.1088/1757-899X/414/1/012032.

Lkouch, I. (2010). Production D’eau Potable par Condensation Passive de L’humidité Atmosphérique (Rosée). *Ph.D Thesis*, Ibn Zohr University, Agadir, Morocco.

Lorenz, T., Klimm, E., and Weiss, K.A. (2014). Soiling And Anti-Soiling Coatings On Surfaces Of Solar Thermal Systems – Featuring An Economic Feasibility Analysis. *Energy Procedia*, vol. 48, pp. 749–756.

Lu, H., and Zhang L. (2019). Particle Deposition Characteristics And Efficiency In Duct Air Flow Over A Backward-Facing Step: Analysis Of Influencing Factors. *Sustainability*, vol 11, 751; doi:10.3390/su11030751.

Menbari, A., Alemrajabi, A.A., and Rezaei, A. (2016). Experimental Investigation Of Thermal Performance For Direct Absorption Solar Parabolic Trough Collector (DASPTC) Based On Binary Nanofluids. *Exp Therm Fluid Sci* 2017;80:218–27.

Merrouni, A.A., Amrani, A-I., Lahoussine Ouali, H.A., Moussaoui, M.A., and Mezrhab A. (2017). Numerical Simulation Of Linear Fresnel Solar Power Plants Performance Under Moroccan Climate. *J. Mater. Environ. Sci.,* 2017; Volume 8, Issue 12, 4226-4233.

Milton, M.R.C.T., and Fraidenraich, N. (2009). Analytic Modeling Of A Solar Power Plant With Parabolic Linear Collectors.” *Sol Energy* 2009; 83(1):126-133.

Moghimi, M.A., and Ahmadi, G. (2018). Wind Barriers Optimization for Minimizing Collector Mirror Soiling in A Parabolic Trough Collector Plant. *Appl Energy*; 225: 413–423.Donald R. Solar energy. New Jersey: Prentice Hall; 1981.

Mohammad, N., and Mishra, Y. (2017). Transactive Market Clearing Model with Coordinated Integration of Large-Scale Solar PV Farms and Demand Response Capable Loads. *In Proceedings of* *the 2017 Australasian Universities Power Engineering Conference*, AUPEC, Melbourne. doi:10.1109/AUPEC.2017.8282496.

Moody, L.F. (1944). Friction Factors For Pipe Flow. *Trans. ASME* 1944;66:671-84.

Muhammad Q., Mohammad N., Matin, M.A., and Alam, M.R. (2016). Highly Efficient Maximum Power Point Tracking Using DC-DC Coupled Inductor Single-Ended Primary Inductance Converter for Photovoltaic Power Systems. *International Journal of Sustainable Energy* 35 (9), doi:10.1080/14786451.2014.961922.

Nocdeal, J., and Wright, S.J. (2006). Numerical Optimization. *Springer Science+Business Media*, LLC. ISBN-10: 0-387-30303-0.

Otieno, G.A., and Loosen, A.E. (2016). An Analysis Of Key Environmental And Social Risks In The Development Of Concentrated Solar Power Projects. *AIP Conference Proceedings* 1734, 160012; https://doi.org/10.1063/1.4949253.

Ozen Engineering. (2020). Automation With The Flexibility To Customize. *Ozen Engineering Inc.* Viewed 20 June 2020. https://www.ozeninc.com/automation-wth-the-flexibility/.

Paetzold, J., Cochard, S.,Vassallo, A., and Fletcher, D.F. (2014). Wind Engineering Analysis Of Parabolic Trough Solar Collectors: The Effects Of Varying The Trough Depth. *Journal of Wind Engineering and Industrial Aerodynamics*; 135: 118-28.

Price, H., Lüpfert, E., Kearney, D., Zarza, E., Cohen, G., Gee, R., and Mahoney, R. (2002). Advances In Parabolic Trough Solar Power Technology. *J Sol Energy Eng* 2002;124:109. http://dx.doi.org/10.1115/1.1467922.

Pytilinski, J.T. (2018). Solar Energy Installations For Pumping Irrigation Water. *Sol Energy 1978;21:255–62*.

Yu, Q., Wang, Z., and Xu, E. (2016). Simulation And Experimental Research Of 1MWe Solar Tower Power Plant In China. *AIP Conference Proceedings* 1734, 070032 (2016); https://doi.org/10.1063/1.4949179.

Qiu, Y., Li, M-J., He, Y-L., and Tao, W-Q. (2017). Thermal Performance Analysis Of A Parabolic Trough Solar Collector Using Supercritical Co2 As Heat Transfer Fluid Under Non-Uniform Solar Flux. *Applied Thermal Engineering*;115:1255-1265.

Rapidrop. (2020). Model A Deluge Valve. Rapidrop. Viewed 14 June 2020. https://www.rapidrop.com/model-a-deluge-valve.

Raza, A., Higgo, A.R., Alobaidli, A., and Zhang, T. (2016). Water recovery in a concentrated solar power plant. *AIP Conf. Proc*. 1734, 160014.

Richards, P.J., and Norris, S.E. (2011). Appropriate boundary conditions for computational wind engineering models revisited. *Journal of Wind Engineering and Industrial Aerodynamics.*

Roth, E., and Pettit, R. (1980). The Effect Of Soiling On Solar Mirrors And Techniques Used To Maintain High Reflectivity. In Solar Materials Science. *Academic Press: New York, NY, USA*; pp. 199–227.

Sadrehaghighi, I. (2020). Elements Of Fluid Dynamics. *CFD Open Series.*

Sadrehaghighi, I. (2020). Mesh Generation In CFD. *CFD Open Series*.

Sansom, C., Fernadez-Garcia, A., Sutter, F., and Rachidi, S. (2018). The design of dust barriers to reduce collector mirror soiling in CSP plants. *AIP Conference Proceedings 2033, 030017 (2018); https://doi.org/10.1063/1.5067033*.

Sansom, C., Fernández-García, A., Sutter, F., Almond, H., and King, P. (2016). Contact cleaning of polymer film solar reflectors. *AIP Conf. Proc*. 1734, 020022.

Sansoma, C., Comleya, P., Kinga, P., Almonda, H., Atkinsona, C., and Endayab, E. (2015). Predicting The Effects Of Sand Erosion On Collector Surfaces In CSP Plants. *Energy Procedia* 2015; 69 : 198-207.

Sayyah, A., Horenstein, M.N., Mazumder, M.K., and Ahmadi, G. (2016). Electrostatic Force Distribution On An Electrodynamic Screen. *J. Electrostatics*, Vol. 81, pp. 24-36.

SENER. (2020). SENER. PARIS - Autonomous Cleaning System for Parabolic Troughs. Available online:http://www.sener-aerospace.com/EPORTAL_DOCS/GENERAL/SENERV2/DOCcw509b9bf804082/paris-parabolic-trough-cleaning-system.pdf. Viewed on 10 March 2020.

Shaner, W.W., and Duff, W.S. (1979). Solar Thermal Electric Power Systems: Comparison Of Line Focus Collectors. *Sol Energy* 1979;22:49–61.

Spencer, L.C. (1989). A Comprehensive Review Of Small Solar-Powered Heat Engines: Part I. Ahistory Of Solar-Powered Devices Up To 1950. Sol Energy 1989;43:191–6. http://dx.doi.org/10.1016/0038-092X(89)90019-4.

Suncyclopedia. (2020). DNI-Direct Normal Irradiance. Suncyclopedia. Viewed 13 May 2020. http://www.suncyclopedia.com/en/dni-direct-normal-irradiance/.

Sup, B.A., Zainudin, M.F., Ali, T.Z.S., Bakar, R.A., and Ming, G.L. (2015). Effect Of Rim Angle To The Flux Distribution Diameter In Solar Parabolic Dish Collector. *EnergyProc* 2015;68:45–52. http://dx.doi.org/10.1016/j.egypro.2015.03.231.

Swinbank, W.C. (1963). Long-Wave Radiation From Clear Skies. *QJR Meteorol Soc*; 89:339–40.

Tian, L., and Ahmadi G. (2007). Particle Deposition In Turbulent Duct Flows Comparisons Of Different Model Predictions. *Journal of Aerosol Science* 2; 38: 377-97.

Turchi, C.S., Wagner, M.J., and Kutscher C.F. (2010). Water Use in Parabolic Trough Power Plants: Summary Results from WorleyParsons' Analyes. *NREL*. NREL/TP-5500-49468.

US DOE. (2008). Concentrating Solar Power Commercial Application Study: Reducing Water Consumption of Concentrating Solar Power Electricity Generation Report to Congress. *US Department of Energy*.

Verma, P. (2018). Water Saving Comparison Study Between Innovative And Conventional Cleaning Systems For CSP Technologies. *Masters Thesis European Solar Engineering School*. No. 247.

Wirz, M., Roesle, M., and Steinfeld, A. (2013). Design Point for Predicting Year-Round Performance of Solar Parabolic Trough Concentrator Systems. *ASME. J. Sol. Energy* Eng;136(2):021019-021019-7 (doi:10.1115/1.4025709)

APPENDIX

APPENDIX A: DERIVATION OF REYNOLDS AVERAGED NAVIER STOKES (RANS) EQUATIONS

Given figure A1:

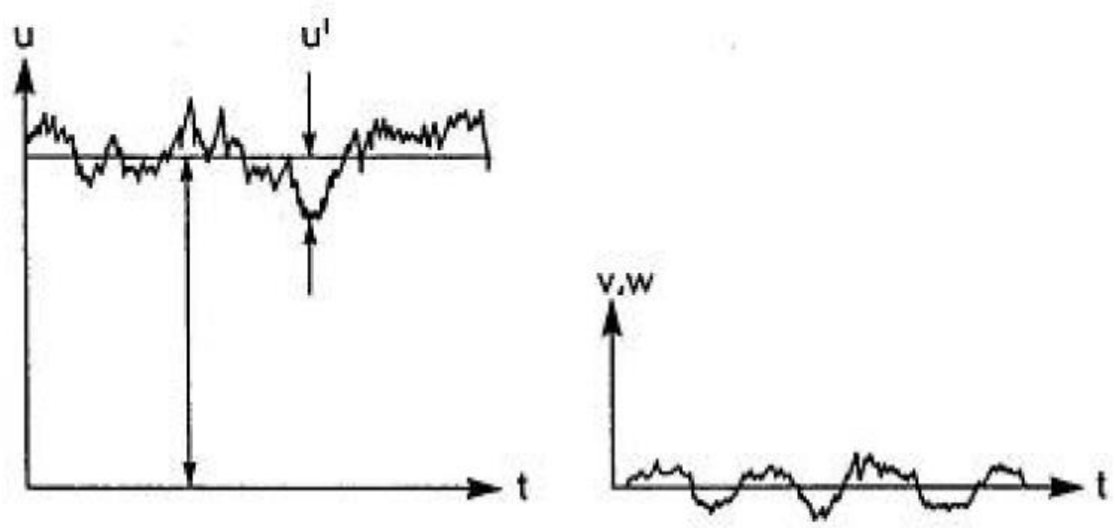

Figure A.1. Turbulent Velocity Fluctuation As A Function OF Time

Decomposition for quantities can occur

$$u = \bar{u} + u', \qquad v = \bar{v} + v', \qquad w = \bar{w} + w', \qquad p = \bar{p} + p', \qquad \rho = \bar{\rho} + \rho', \qquad T = \bar{T} + T'$$

Where the time average values are given as $\bar{u}, \bar{v}, \bar{w}, \bar{p}, \bar{\rho}$ and $\bar{T}$.

$$\therefore \bar{u} = \frac{1}{\Delta t}\int_{t_0}^{t_0+t_1} u dt$$

$$\therefore \frac{\partial \bar{u}}{\partial x} = \frac{1}{\Delta t}\int_{t_0}^{t_0+t_1} \frac{\partial u}{\partial x} dt = \overline{\frac{\partial \bar{u}}{\partial x}}$$

$$\therefore \overline{\frac{\partial u'}{\partial x}} = \frac{1}{\Delta t}\int_{t_0}^{t_0+t_1} \frac{\partial u'}{\partial x} dt = 0$$

Thus, from continuity equation:

$$\frac{\partial u}{\partial x}+\frac{\partial v}{\partial y}+\frac{\partial w}{\partial z}=0$$

- Substitute decomposition to get:

$$\frac{\partial(\bar{u}+u')}{\partial x}+\frac{\partial(\bar{v}+v')}{\partial y}+\frac{\partial(\bar{w}+w')}{\partial z}=0$$

- Time averaged of continuity decomposed:

$$\overline{\frac{\partial(\bar{u}+u')}{\partial x}+\frac{\partial(\bar{v}+v')}{\partial y}+\frac{\partial(\bar{w}+w')}{\partial z}}=0$$

$$\therefore\frac{\partial\bar{u}}{\partial x}+\frac{\partial\bar{v}}{\partial y}+\frac{\partial\bar{w}}{\partial z}=0 \qquad \text{(A.1)}$$

Navier stokes in x direction and continuity:

$$u\frac{\partial u}{\partial x}+v\frac{\partial v}{\partial y}+w\frac{\partial w}{\partial z}=\frac{\partial(u^2)}{\partial x}+\frac{\partial(uv)}{\partial y}+\frac{\partial(uw)}{\partial z}-u\underbrace{\left(\frac{\partial\bar{u}}{\partial x}+\frac{\partial\bar{v}}{\partial y}+\frac{\partial\bar{w}}{\partial z}\right)}_{Continuity\ (A.1)}=\frac{\partial(u^2)}{\partial x}+\frac{\partial(uv)}{\partial y}+\frac{\partial(uw)}{\partial z}$$

Time-averaged Navier stokes in x direction and continuity with decomposition:

$$\overline{\rho\left[\frac{\partial(\bar{u}+u')}{\partial t}+\frac{\partial(\bar{u}+u')^2}{\partial x}+\frac{\partial(\bar{u}+u')(\bar{v}+v')}{\partial y}+\frac{\partial(\bar{u}+u')(\bar{w}+w')}{\partial z}\right]}$$
$$=\overline{F_x-\frac{\partial(\bar{p}+p')}{\partial x}+\mu\left(\frac{\partial^2(\bar{u}+u')}{\partial x^2}+\frac{\partial^2(\bar{u}+u')}{\partial y^2}+\frac{\partial^2(\bar{u}+u')}{\partial z^2}\right)}$$

Thus, can be transformed into:

$$\rho\left[\frac{\partial\bar{u}}{\partial t}+\frac{\partial\bar{u}\bar{u}}{\partial x}+\frac{\partial\overline{u'u'}}{\partial x}+\frac{\partial\bar{u}\bar{v}}{\partial y}+\frac{\partial\overline{u'v'}}{\partial y}+\frac{\partial\overline{u'w'}}{\partial z}+\frac{\partial\bar{u}\bar{w}}{\partial z}\right]=F_x-\frac{\partial\bar{p}}{\partial x}+\mu\left(\frac{\partial^2\bar{u}}{\partial x^2}+\frac{\partial^2\bar{u}}{\partial y^2}+\frac{\partial^2\bar{u}}{\partial z^2}\right)$$

Finally, in Tensor form:

$$\rho\frac{D\bar{u}_i}{Dt}=F_i-\frac{\partial\bar{p}}{\partial x_i}+\mu\Delta\bar{u}_i-\ \rho\ \underbrace{\left(\frac{\partial\overline{u_i'u_j'}}{\partial x_j}\right)}_{Reyolds\ Stress} \qquad \text{(A.2)}$$

APPENDIX B: SIMULATION RESULTS

B.1. SIMULATED POROUS CASE 2

B.1.1. GEOMETRICAL SETTINGS

The second case assumes values as shown:

Table B.1. Porous case 2 variables

Case Number	**l_3 [m]**	**θ [°]**	**po [m]**
2	0.15	90	0.03

In ANSYS the geometrical settings were defined as shown in figure B.1 and table B.2:

Table B.2. Porous case 2 ANSYS geometrical settings

Case Number	**L6 [m]**	**A7 [°]**	**V10 [m]**
2	0.15	90	0.03

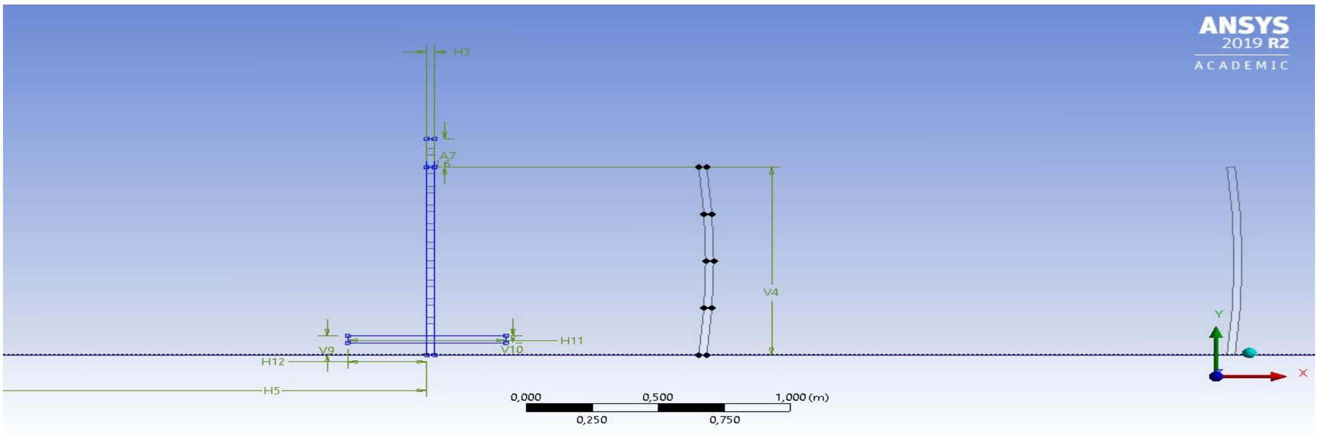

Figure B.1. Porous case 2 geometrical settings

B.1.2. MESH SETTING

The mesh of this case was generated as explained in chapter 2 and the mesh information and quality can be shown in table B.3 and displayed in figure B.2.

Table B.3. Porous case 2 mesh statistics

Nodes	875269
Elements	872927
Mesh Metric Min -Element Quality	2,0255e-002
Mesh Metric Max-Element Quality	0,99992
Mesh Metric Average-Element Quality	0,71855

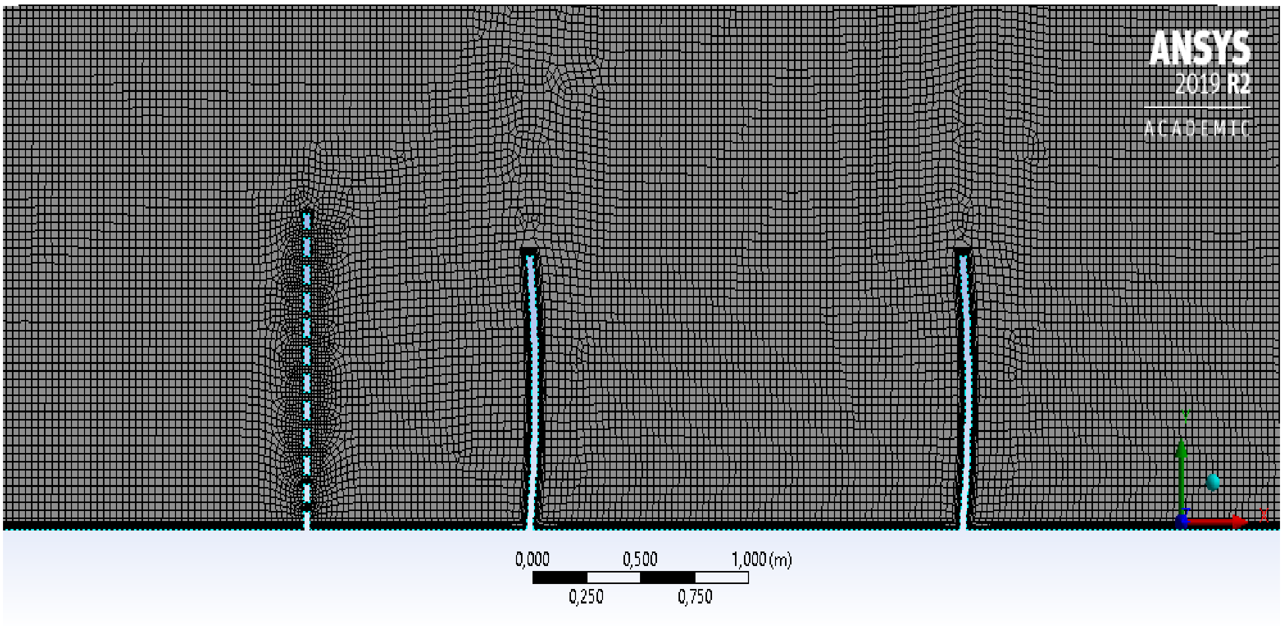

Figure B.2. Porous case 2 mesh settings

B.1.3. ANSYS-FLUENT SIMUALTION RESULTS

The ANSYS FLUENT settings were applied and the following results were obtained after solving for 2700 iterations:

i. Scaled Residuals: Convergence was achieved after 2700 iterations:

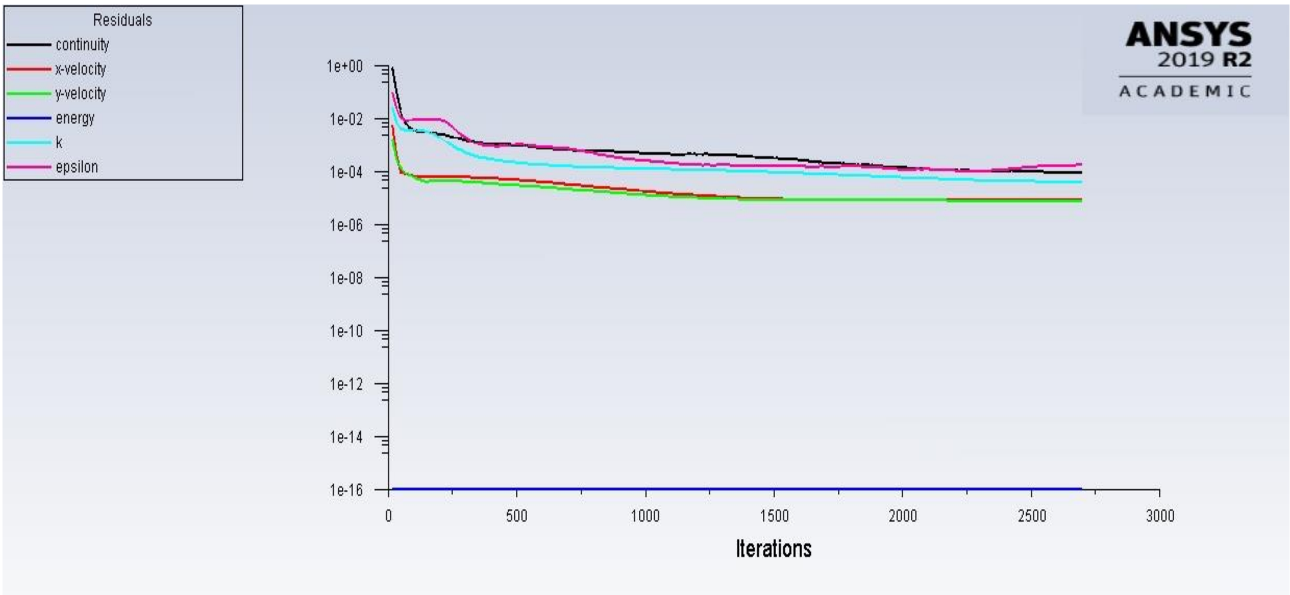

Figure B.3. Porous case 2 scaled residuals

ii. Particles tracked: 1 250 000 particles tracked

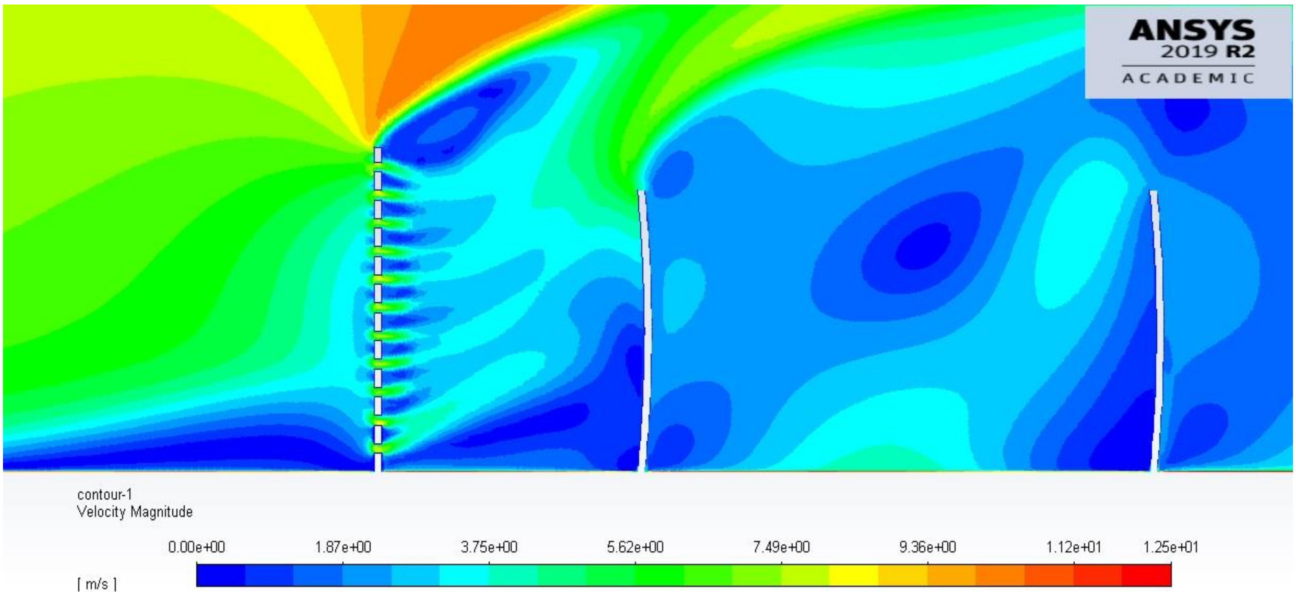

Figure B.4. Porous case 2 velocity contour magnitude

Table B.4. Porous case 2 particle fate

ANSY labelled Wall- ID zone	Geometric Definition	Particles Trapped	Particles Escaped
7	Outlet end side		360262
11	Ground distance of mirror pitch	47097	
12	Ground distance after mirror field	758722	
13	1st mirror front face	29	
14	2nd mirror front face	78	
15	3rd mirror front face	954	
16	4th mirror front face	7952	
17	5th mirror front face	14949	
18	6th mirror front face	27990	
19	Wind Barrier front	27036	
20	Top and back sides of all mirrors	9224	
Soiling [Particles]		51952	

B.2. SIMULATED POROUS CASE 3

B.2.1. GEOMETRICAL SETTINGS

The third case assumes values as shown:

Table B.5. Porous case 3 variables

Case Number	l_3 [m]	θ [°]	po [m]
3	0.05	90	0.035

In ANSYS the geometrical settings were defined as shown in figure B.5 and table B.6:

Table B.6. Porous case 3 ANSYS geometrical settings

Case Number	L6 [m]	A7 [°]	V10 [m]
3	0.05	90	0.035

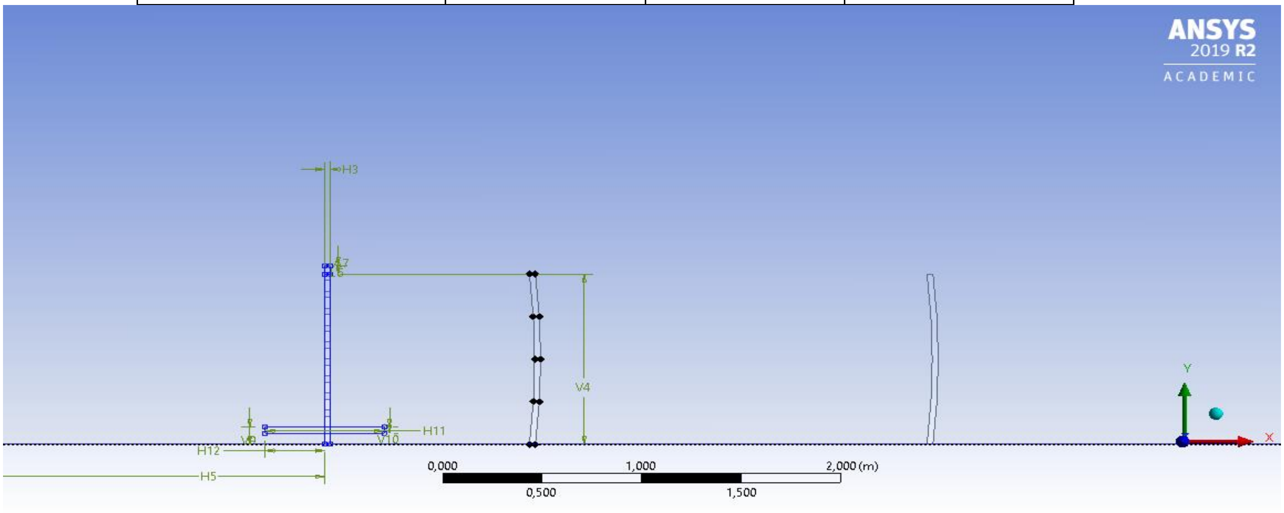

Figure B.5. Porous case 3 geometrical settings

B.2.2. MESH SETTING

The mesh of this case was generated as explained in chapter 2 and the mesh information and quality can be shown in table B.7 and displayed in figure B.6.

Table B.7. Porous case 3 mesh statistics

Nodes	870966
Elements	868574
Mesh Metric Min -Element Quality	2,0255e-002
Mesh Metric Max-Element Quality	0,99947
Mesh Metric Average-Element Quality	0,71408

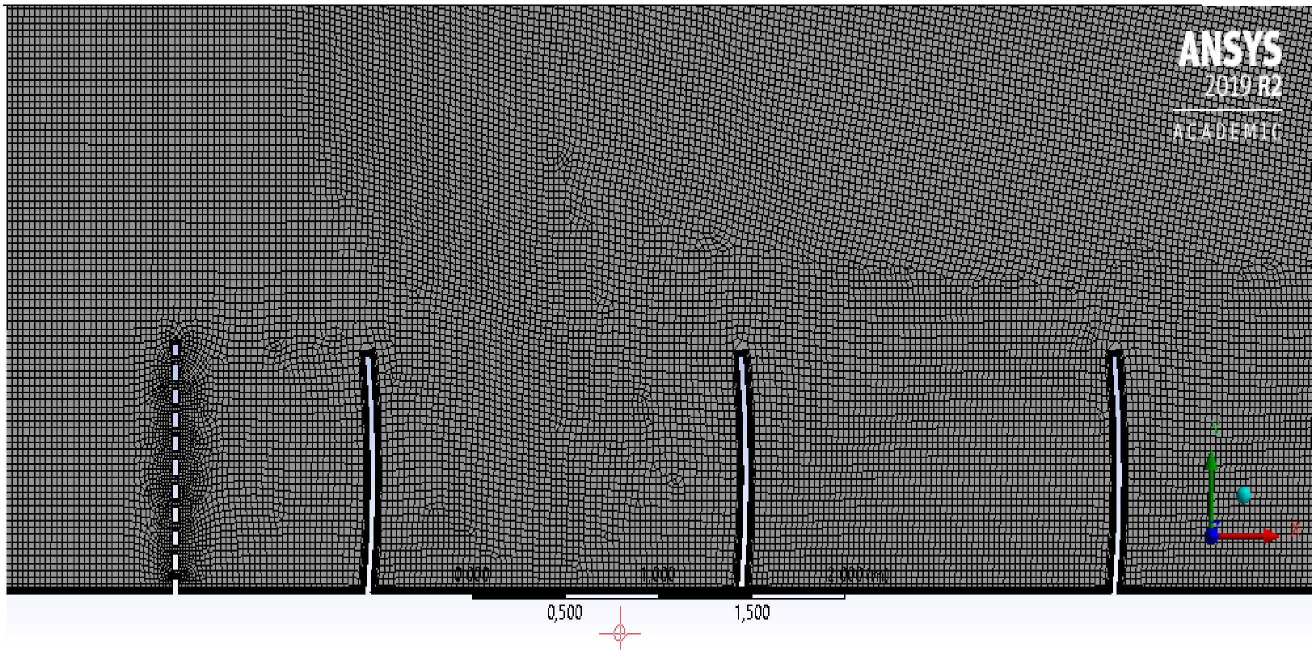

Figure B.6. Porous case 3 mesh settings

B.2.1. ANSYS-FLUENT SIMUALTION RESULTS

The ANSYS FLUENT settings were applied and the following results were obtained after solving for 2700 iterations:

i. Scaled Residuals: Convergence was achieved after 2600 iterations.

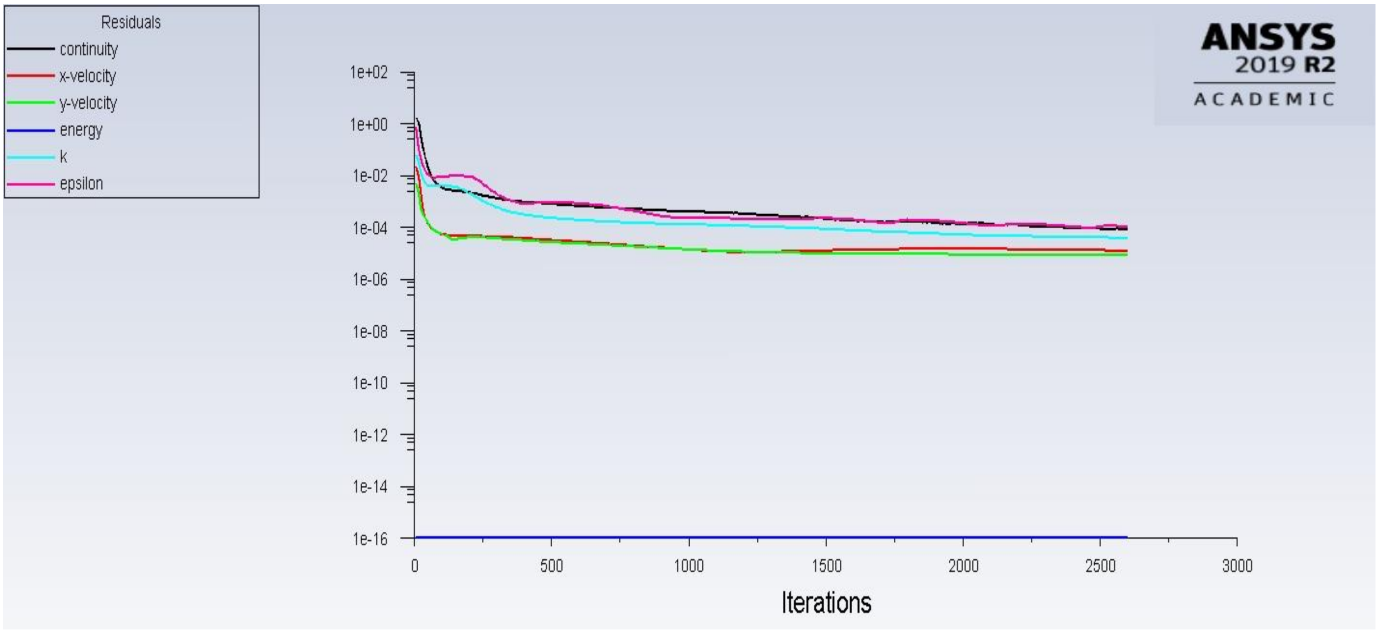

Figure B.7. Porous case 3 scaled residuals

ii. Particles tracked: 1 250 000 particles tracked

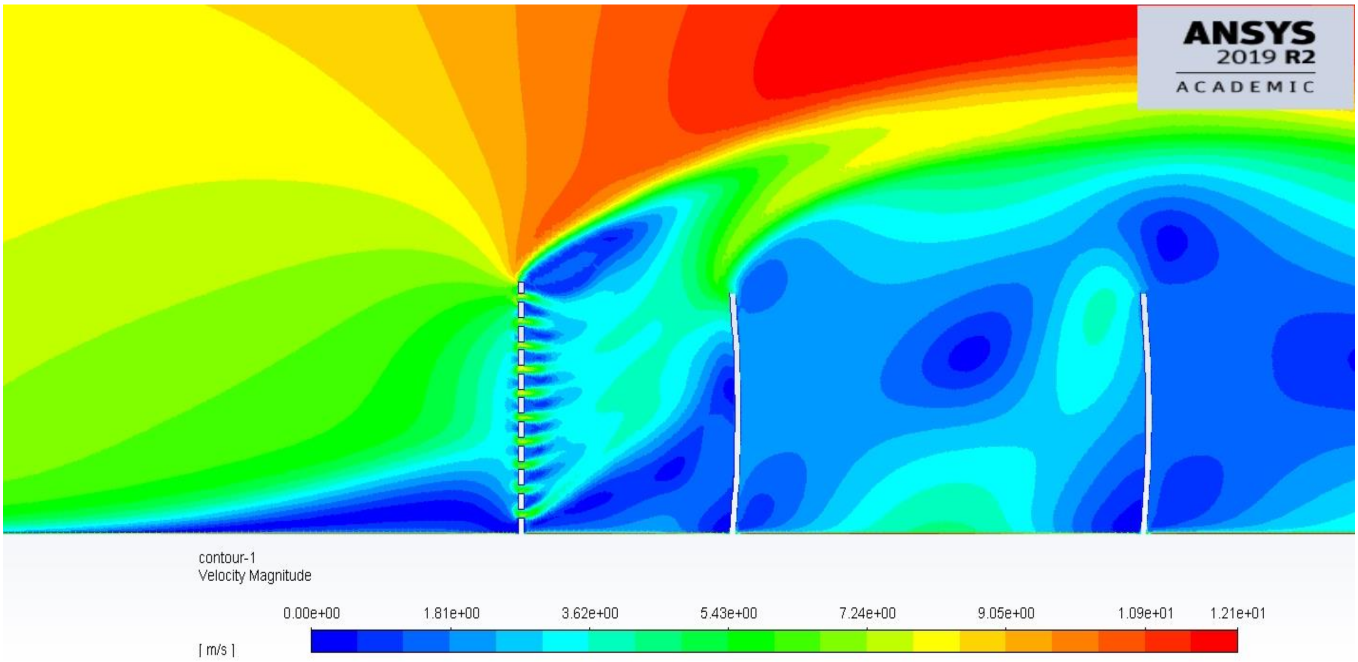

Figure B.8. Porous case 3 velocity contour magnitude

Table B.8. Porous case 3 particle fate

ANSY labelled Wall-ID zone	Geometric Definition	Particles Trapped	Particles Escaped
7	Outlet end side		366412
11	Ground distance of mirror pitch	37214	
12	Ground distance after mirror field	769084	
13	1st mirror front face	32	
14	2nd mirror front face	95	
15	3rd mirror front face	636	
16	4th mirror front face	6679	
17	5th mirror front face	16858	
18	6th mirror front face	29580	
19	Wind Barrier front	14631	
20	Top and back sides of all mirrors	8906	
Soiling [Particles]		53880	

B.3. SIMULATED POROUS CASE 3

B.3.1. GEOMETRICAL SETTINGS

The fourth case assumes values as shown:

Table B.9. Porous case 4 variables

Case Number	l₃ [m]	θ [°]	po [m]
4	0.25	90	0.035

In ANSYS the geometrical settings were defined as shown in figure B.9 and table B.10:

Table B.10. Porous case 4 ANSYS geometrical settings

Case Number	L6 [m]	A7 [°]	V10 [m]
4	0.25	90	0.035

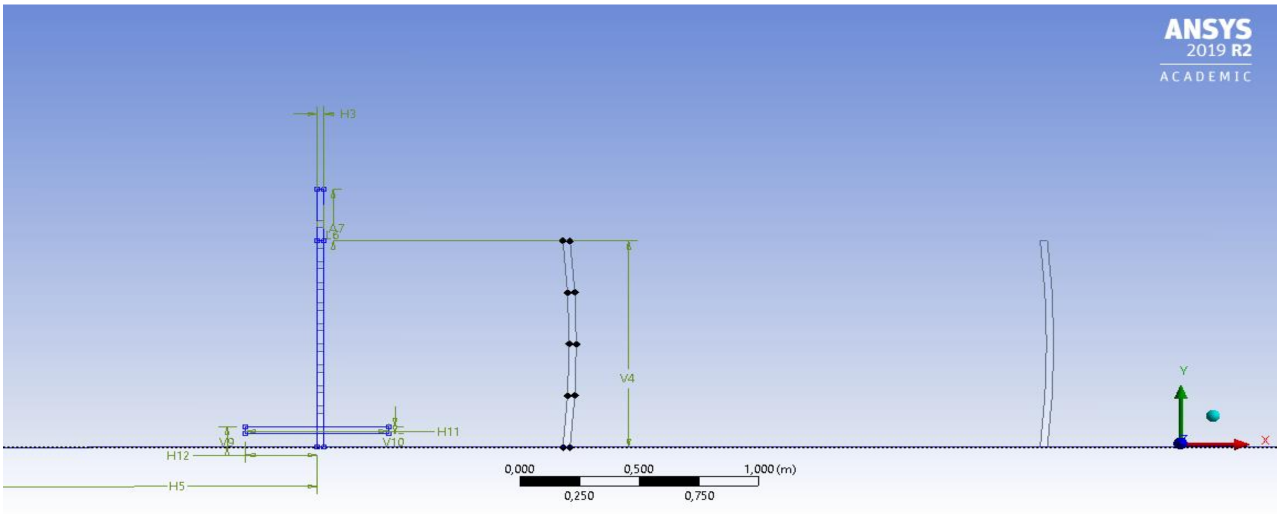

Figure B.9. Porous case 4 geometrical Settings

B.3.2. MESH SETTING

The mesh of this case was generated as explained in chapter 2 and the mesh information and quality can be shown in table B.11 and displayed in figure B.10.

Table B.11. Porous case 4 mesh statistics

Nodes	873942
Elements	871558
Mesh Metric Min -Element Quality	2,0255e-002
Mesh Metric Max-Element Quality	0,99947
Mesh Metric Average-Element Quality	0,71675

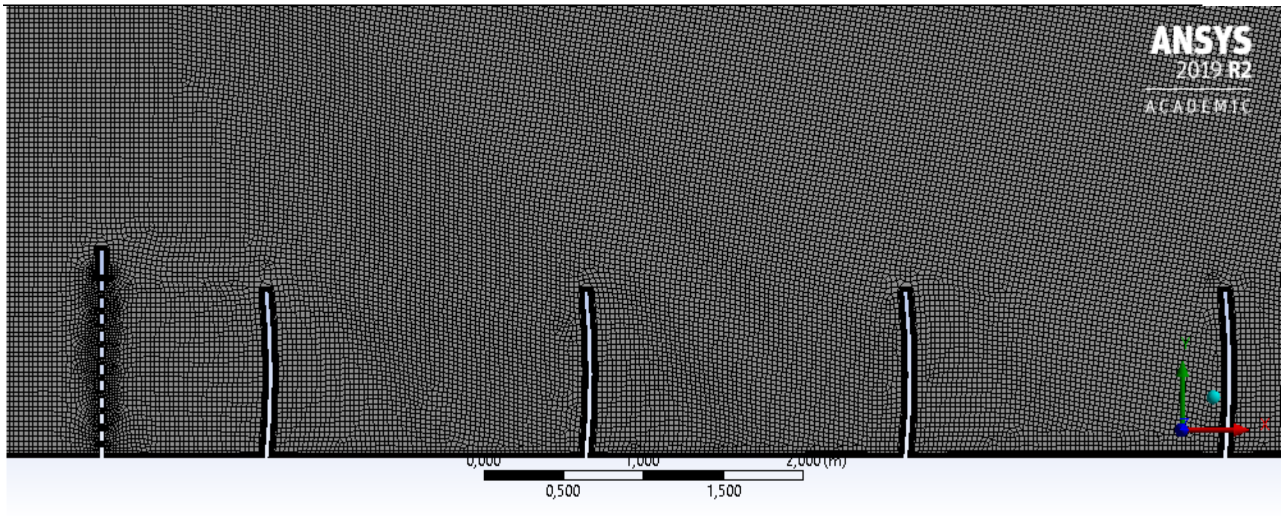

Figure B.10. Porous case 4 mesh settings

B.3.3. ANSYS-FLUENT SIMUALTION RESULTS

The ANSYS FLUENT settings were applied and the following results were obtained after solving for 2700 iterations:

i. Scaled Residuals: Convergence was achieved after 2700 iterations.

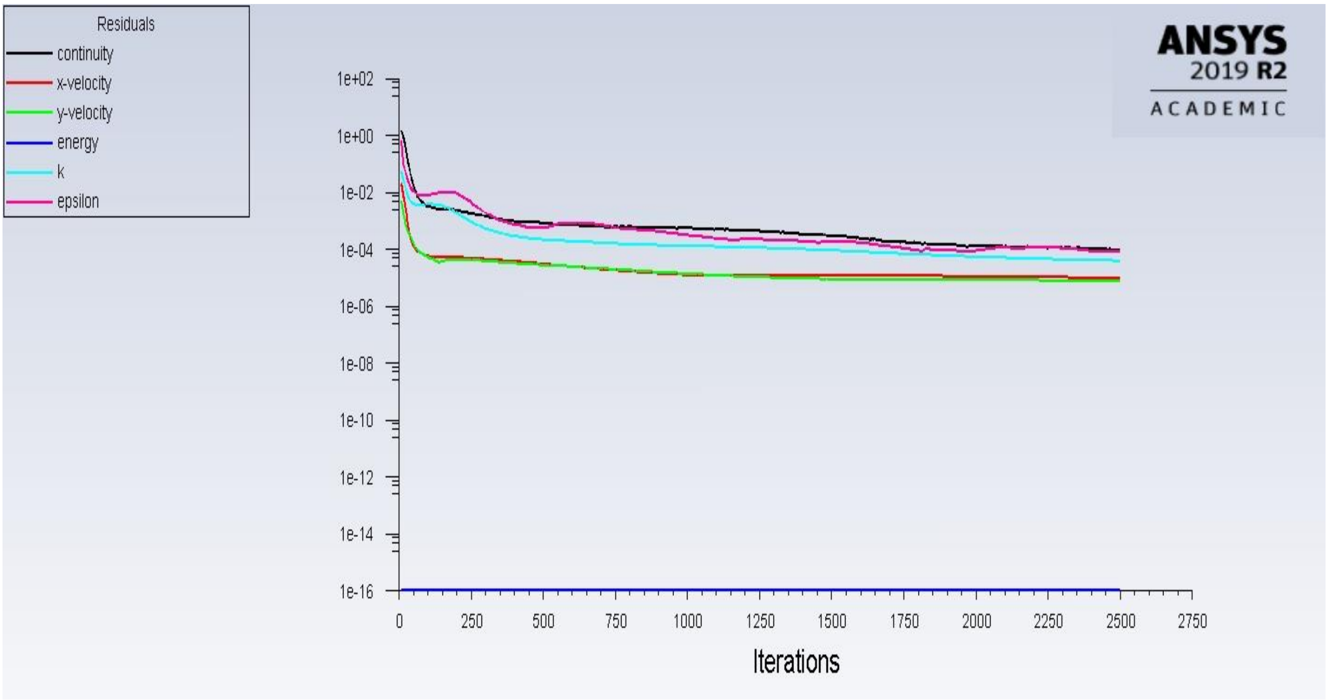

Figure B.11. Porous case 4 scaled residuals

ii. Particles tracked: 1 250 000 particles tracked:

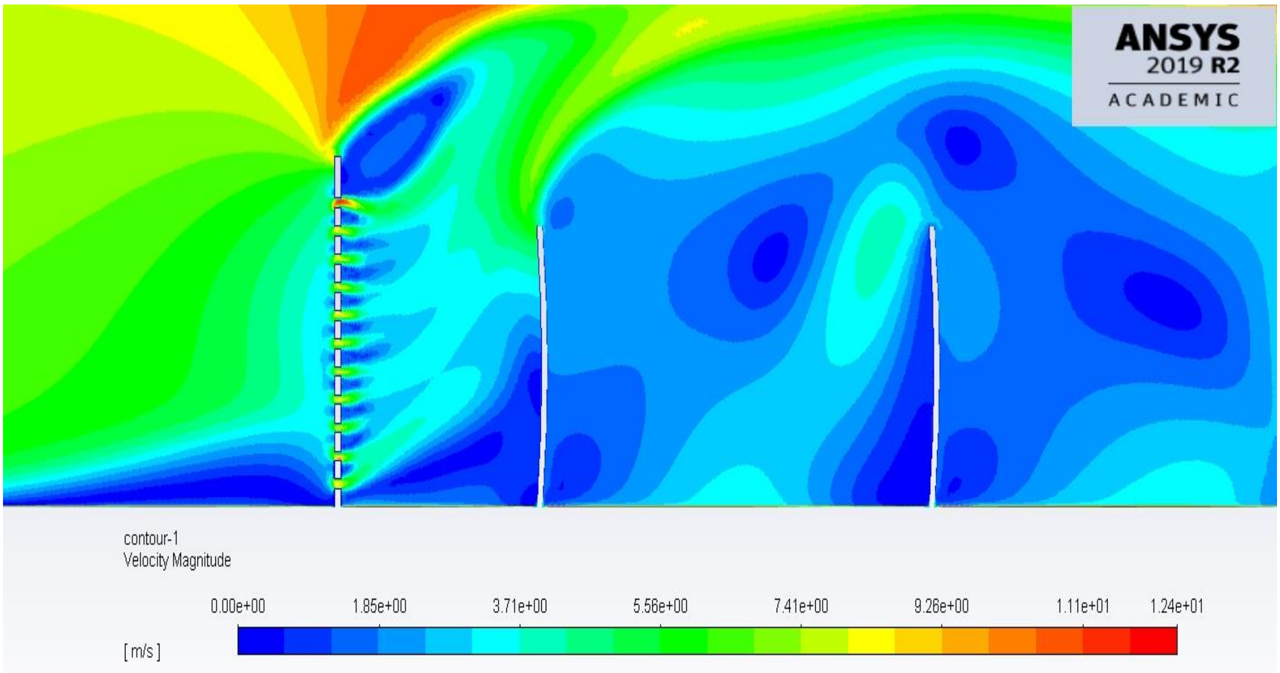

Figure B.12. Porous case 4 velocity contour magnitude

Table B.12. Porous case 4 particle fate

ANSY labelled Wall- ID zone	**Geometric Definition**	**Particles Trapped**	**Particles Escaped**
7	Outlet end side		366412
11	Ground distance of mirror pitch	38804	
12	Ground distance after mirror field	757634	
13	1st mirror front face	29	
14	2nd mirror front face	32	
15	3rd mirror front face	318	
16	4th mirror front face	5089	
17	5th mirror front face	13995	
18	6th mirror front face	27354	
19	Wind Barrier front	28944	
20	Top and back sides of all mirrors	6679	
Soiling [Particles]		46816	

B.4. SIMULATED POROUS CASE 5

B.4.1. GEOMETRICAL SETTINGS

The fifth case assumes values as shown:

Table B.13. Porous case 5 variables

Case Number	l_3 [m]	θ [°]	po [m]
5	0.15	5	0.035

In ANSYS the geometrical settings were defined as shown in figure B.13 and table B.14:

Table B.14. Porous case 5 ANSYS geometrical settings

Case Number	L6 [m]	A7 [°]	V10 [m]
5	0.15	5	0.035

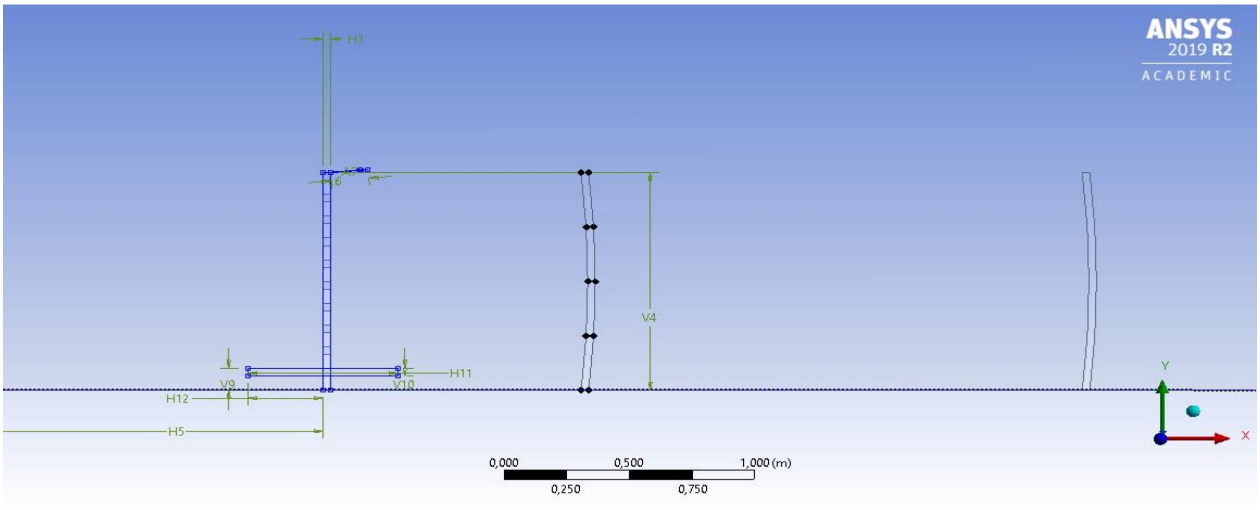

Figure B.13. Porous case 5 geometrical settings

B.4.2. MESH SETTING

The mesh of this case was generated as explained in chapter 2 and the mesh information and quality can be shown in table B.15 and displayed in figure B.14.

Table B.15. Porous case 4 mesh statistics

Nodes	875251
Elements	872845
Mesh Metric Min -Element Quality	2,0255e-002
Mesh Metric Max-Element Quality	0,99982
Mesh Metric Average-Element Quality	0,72028

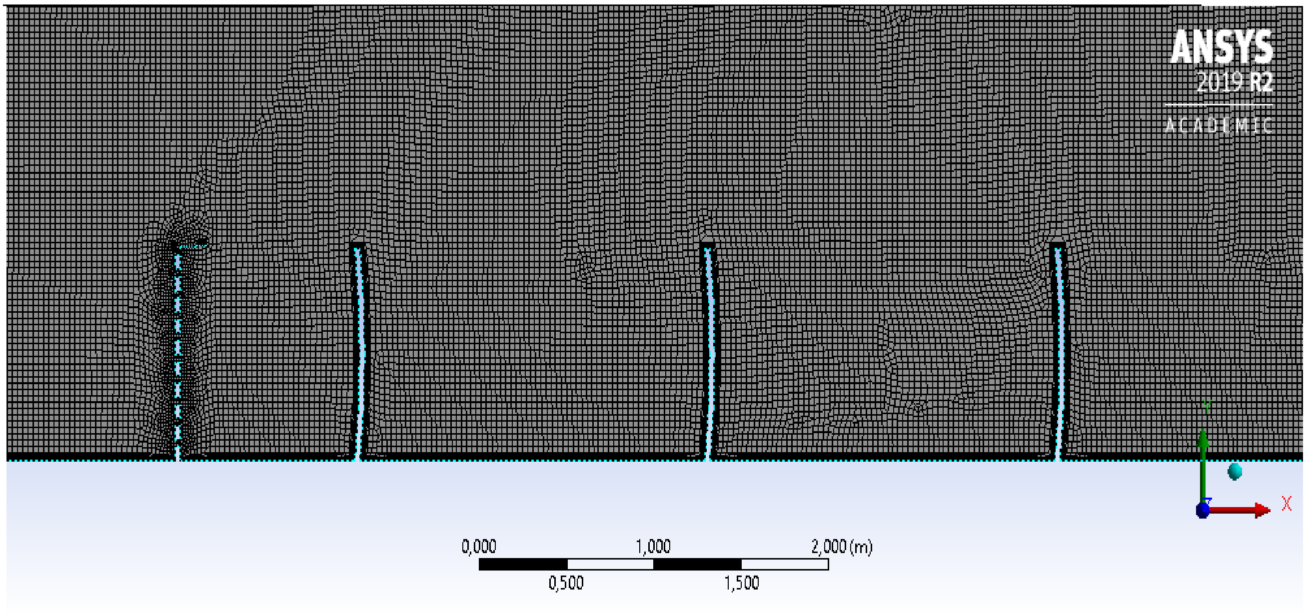

Figure B.14. Porous case 5 mesh settings

B.4.3. ANSYS-FLUENT SIMUALTION RESULTS

The ANSYS FLUENT settings were applied and the following results were obtained after solving for 2600 iterations:

i. Scaled Residuals: Convergence was achieved after 2600 iterations.

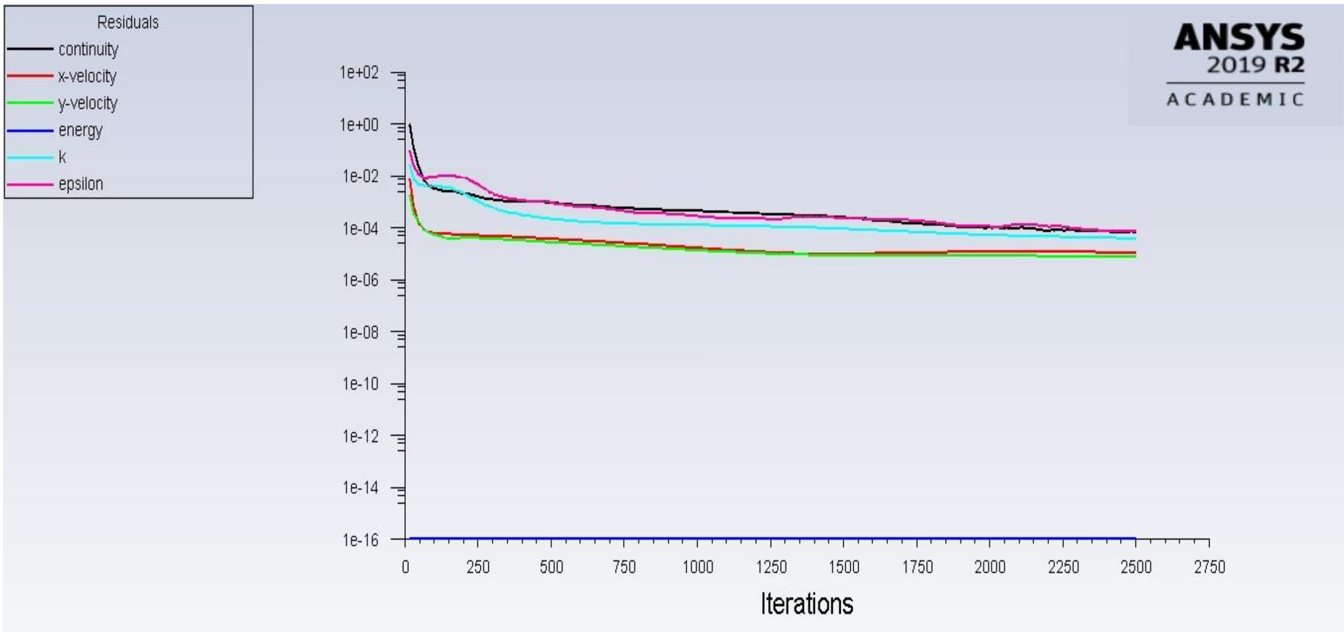

Figure B.15. Porous case 5 scaled residuals

ii. Particles tracked: 1 250 000 particles tracked:

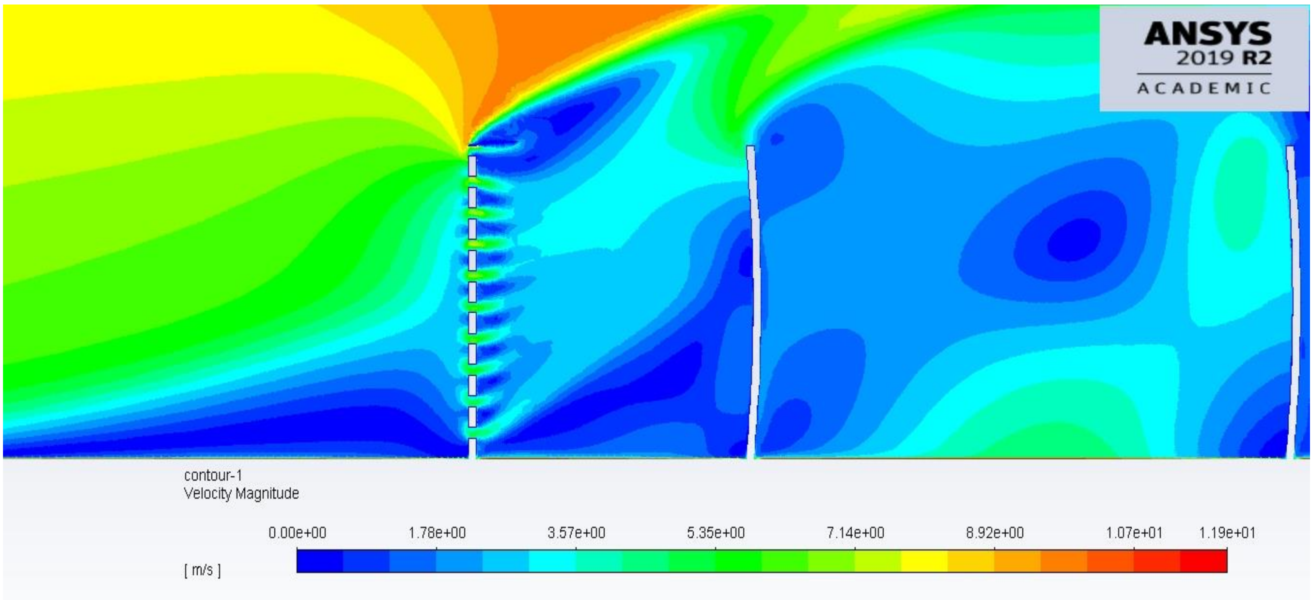

Figure B.16. Porous case 5 velocity contour magnitude

Table B.16. Porous case 5 particle fate

ANSY labelled Wall- ID zone	Geometric Definition	Particles Trapped	Particles Escaped
7	Outlet end side		360051
11	Ground distance of mirror pitch	38804	
12	Ground distance after mirror field	757634	
13	1st mirror front face	382	
14	2nd mirror front face	636	
15	3rd mirror front face	2863	
16	4th mirror front face	9224	
17	5th mirror front face	23537	
18	6th mirror front face	30216	
19	Wind Barrier front	10814	
20	Top and back sides of all mirrors	8906	
Soiling [Particles]		66858	

B.5. SIMULATED POROUS CASE 6

B.5.1. GEOMETRICAL SETTINGS

The sixth case assumes values as shown:

Table B.17. Porous case 6 variables

Case Number	**l_3 [m]**	**θ [°]**	**po [m]**
6	0.15	175	0.035

In ANSYS the geometrical settings were defined as shown in figure 67and table 30:

Table B.18. Porous case 6 ANSYS geometrical settings

Case Number	**L6 [m]**	**A7 [°]**	**V10 [m]**
6	0.15	175	0.035

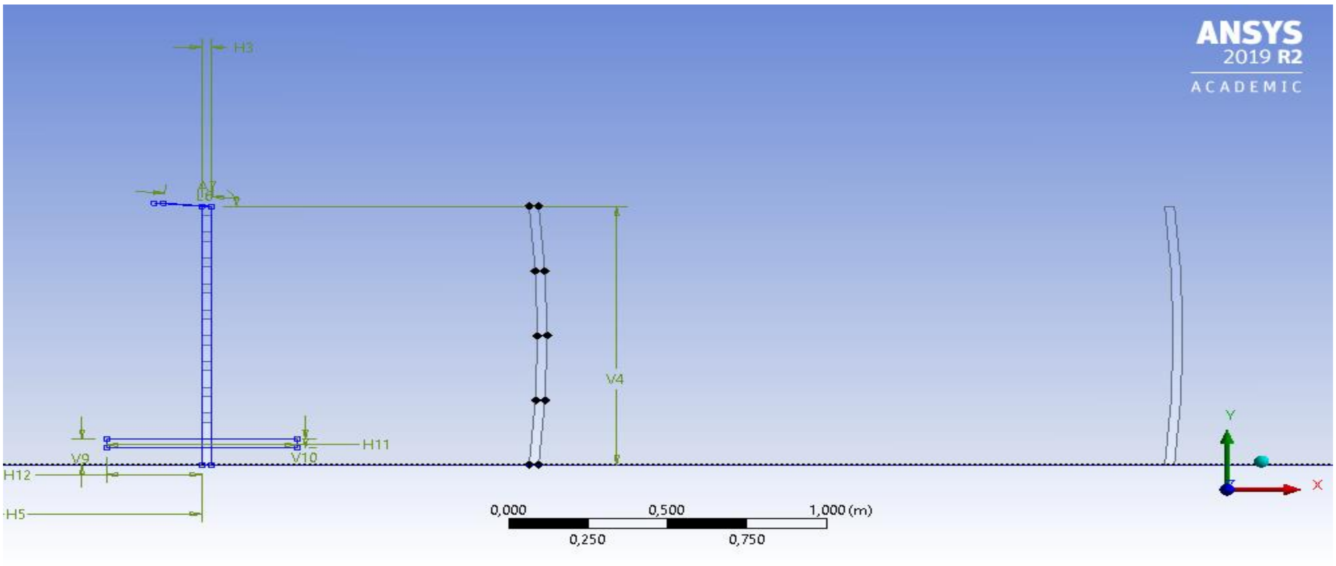

Figure B.17. Porous case 6 geometrical settings

B.5.1. MESH SETTING

The mesh of this case was generated as explained in chapter 2 and the mesh information and quality can be shown in table B.19 and displayed in figure B.18.

Table B.19. Porous case 6 mesh statistics

Nodes	875529
Elements	873190
Mesh Metric Min -Element Quality	2,0255e-002
Mesh Metric Max-Element Quality	0,99987
Mesh Metric Average-Element Quality	0,71895

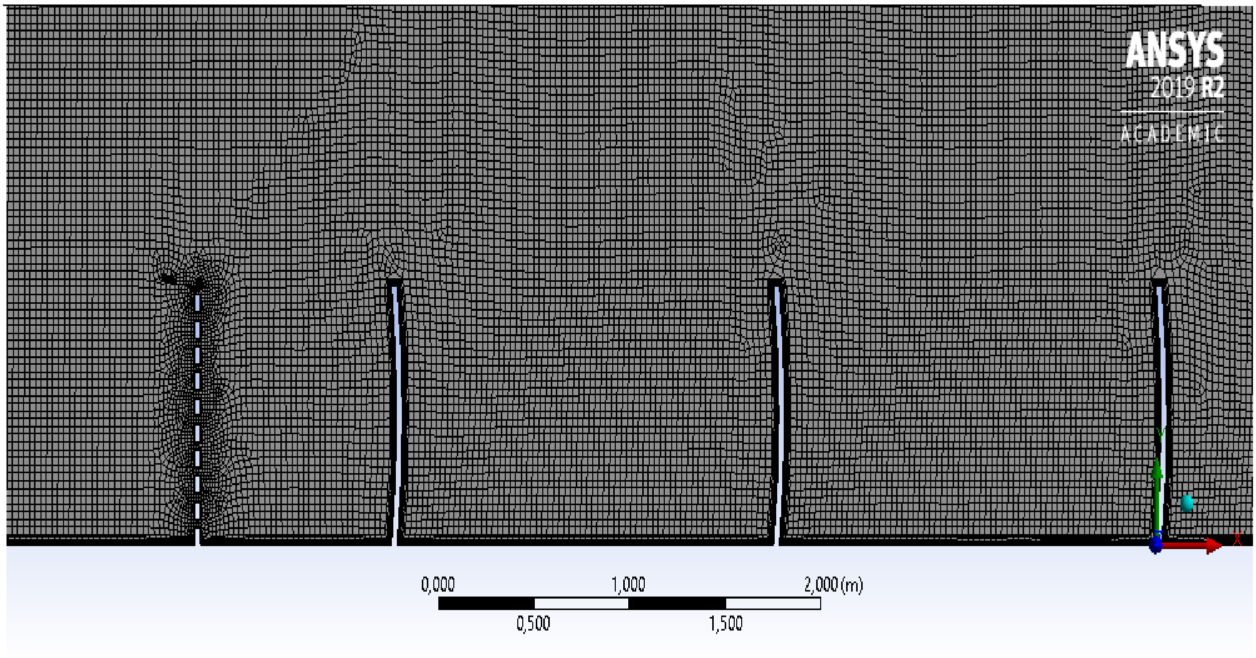

Figure B.18. Porous case 5 mesh settings

B.5.2. ANSYS-FLUENT SIMUALTION RESULTS

The ANSYS FLUENT settings were applied and the following results were obtained after solving for 2500 iterations:

i. Scaled Residuals: Convergence was achieved after 2500 iterations.

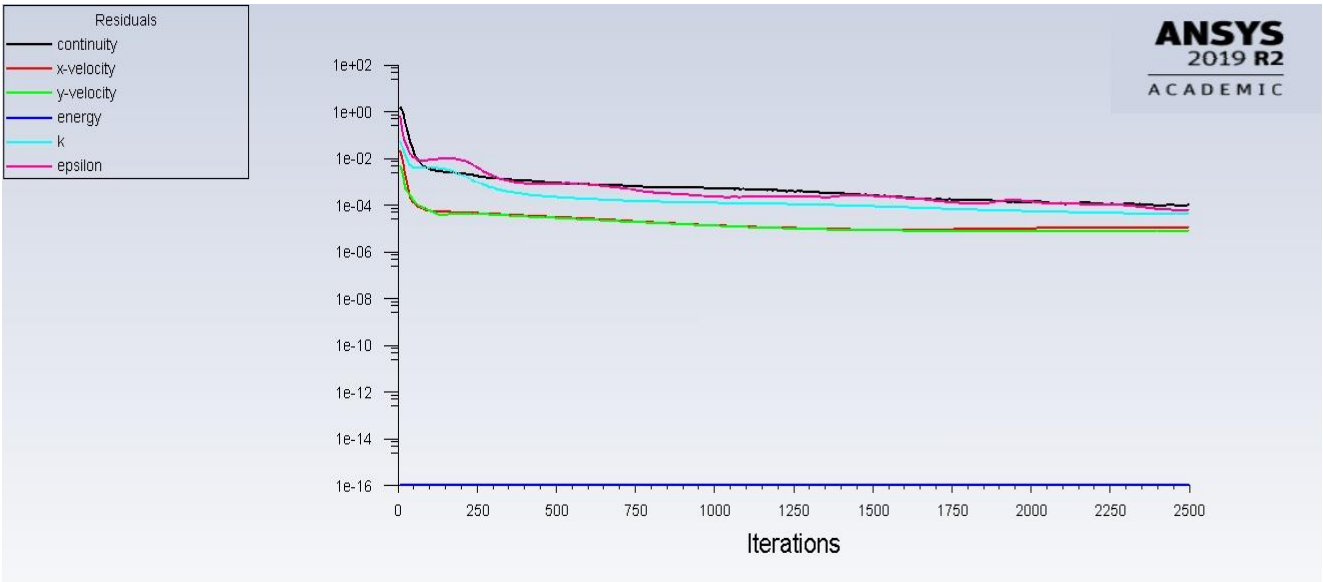

Figure B.19. Porous case 6 scaled residuals

ii. Particles tracked: 1 250 000 particles tracked:

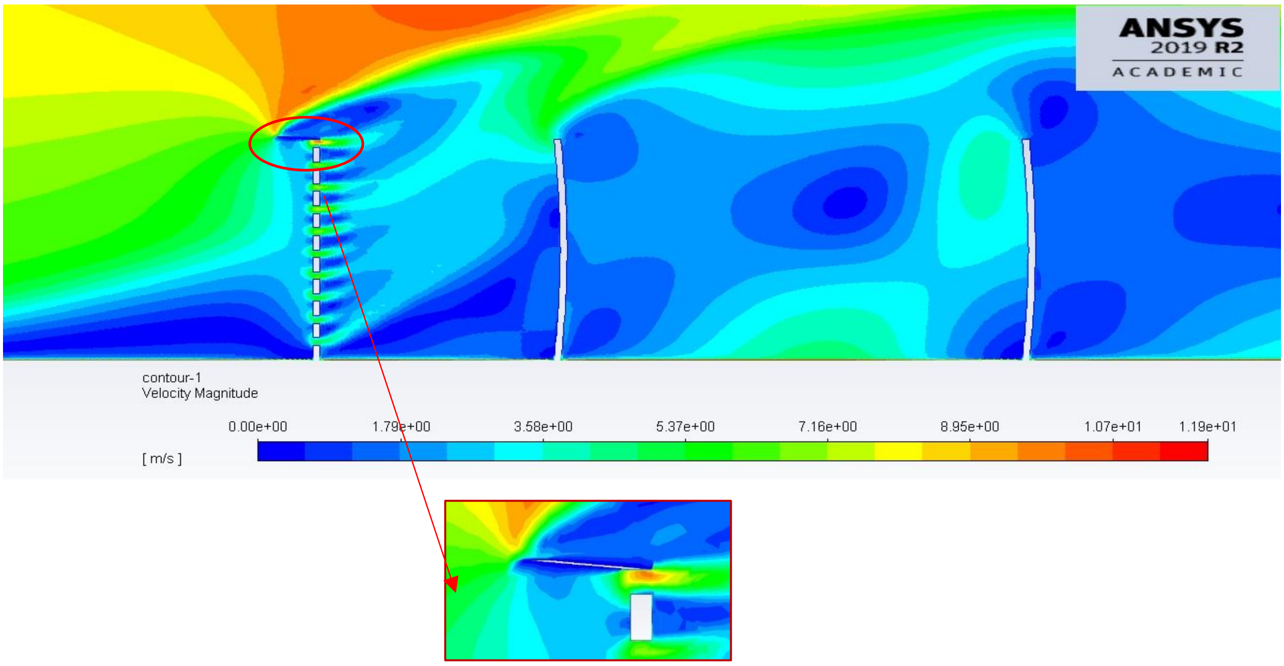

Figure B.20. Porous case 6 velocity contour magnitude

Table B.20. Porous case 6 particle fate

ANSY labelled Wall- ID zone	Geometric Definition	Particles Trapped	Particles Escaped
7	Outlet end side		347964
11	Ground distance of mirror pitch	44211	
12	Ground distance after mirror field	765585	
13	1st mirror front face	318	
14	2nd mirror front face	636	
15	3rd mirror front face	3181	
16	4th mirror front face	8906	
17	5th mirror front face	20674	
18	6th mirror front face	33397	
19	Wind Barrier front	12405	
20	Top and back sides of all mirrors	12723	
Soiling [Particles]		67112	

B.6. SIMULATED POROUS CASE 7

B.6.1. GEOMETRICAL SETTINGS

The seventh case assumes values as shown:

Table B.21. Porous case 7 variables

Case Number	l_3 [m]	θ [°]	po [m]
7	0.15	90	0.02

In ANSYS the geometrical settings were defined as shown in figure B.21 and table B.22:

Table B.22. Porous case 7 ANSYS geometrical settings

Case Number	L6 [m]	A7 [°]	V10 [m]
7	0.15	90	0.02

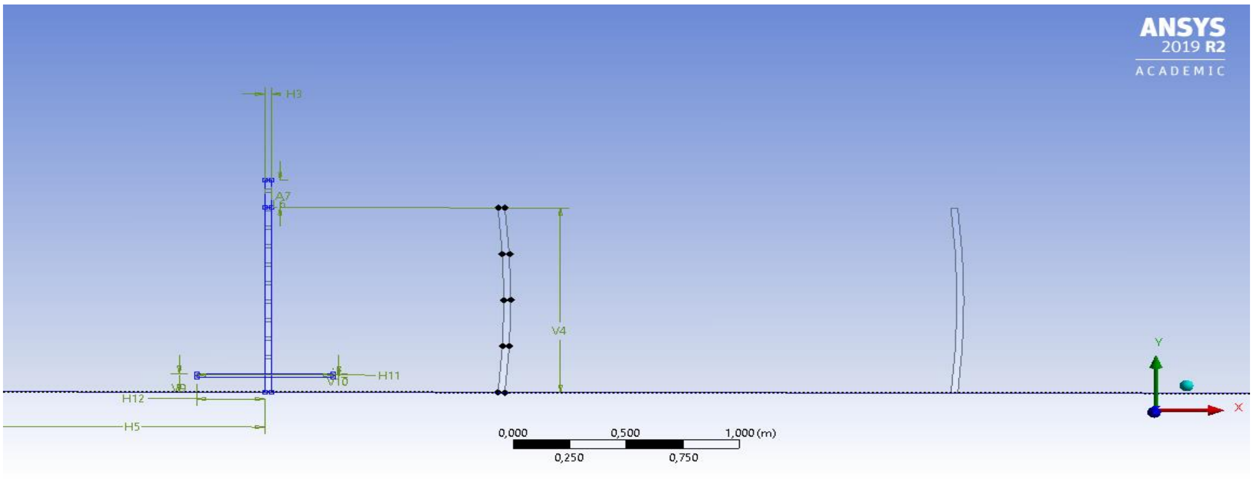

Figure B.21. Porous case 7 geometrical settings

B.6.1. MESH SETTING

The mesh of this case was generated as explained in chapter 2 and the mesh information and quality can be shown in table B.23 and displayed in figure B.22.

Table B.23. Porous case 7 mesh statistics

Nodes	877115
Elements	874657
Mesh Metric Min -Element Quality	8,1059e-003
Mesh Metric Max-Element Quality	0,99947
Mesh Metric Average-Element Quality	0,72055

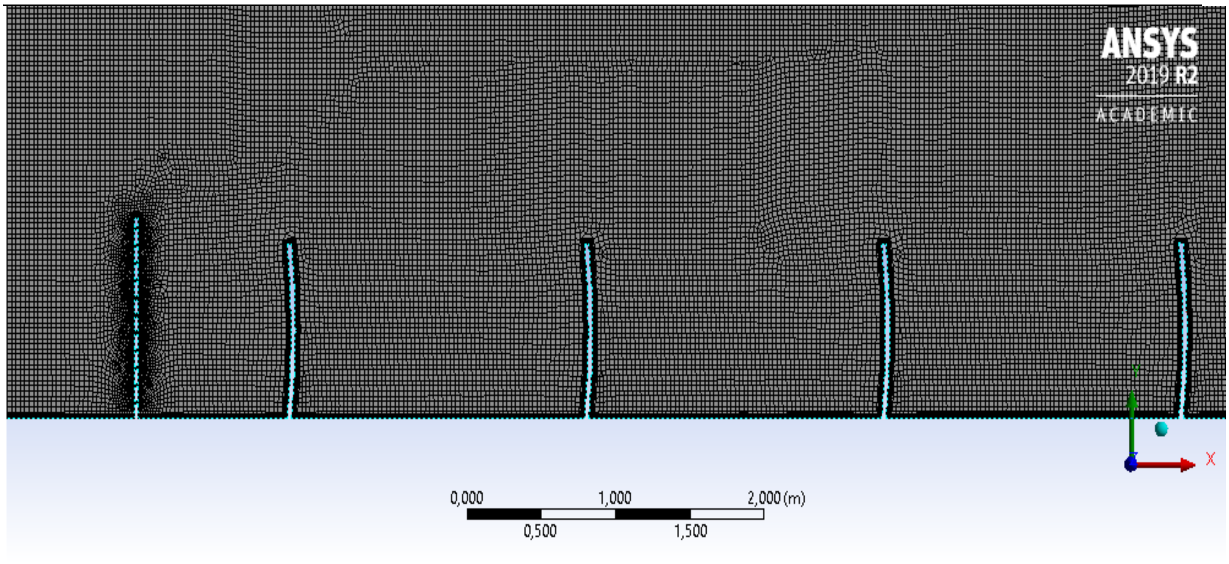

Figure B.22. Porous case 7 mesh settings

B.6.2. ANSYS-FLUENT SIMUALTION RESULTS

The ANSYS FLUENT settings were applied and the following results were obtained after solving for 2700 iterations:

i. Scaled Residuals: Convergence was achieved after 2700 iterations

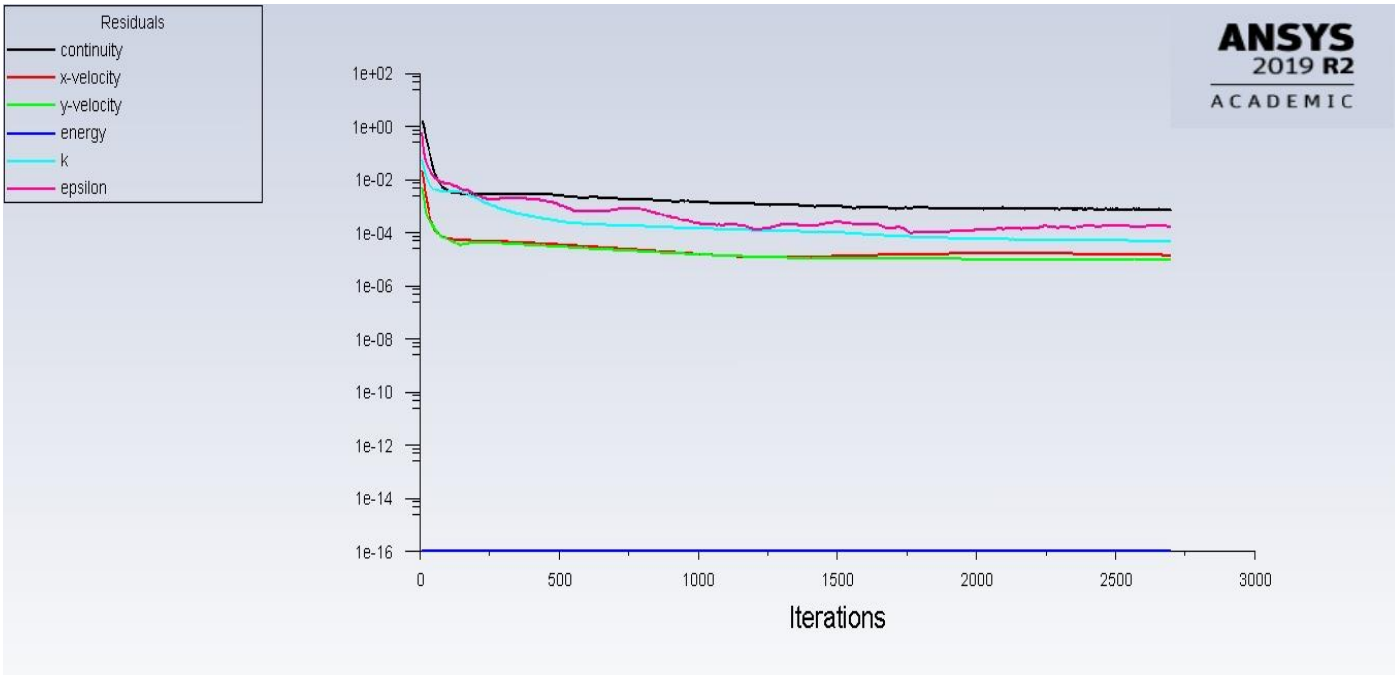

Figure B.23. Porous case 7 scaled residuals

ii. Particles tracked: 1 250 000 particles tracked:

n

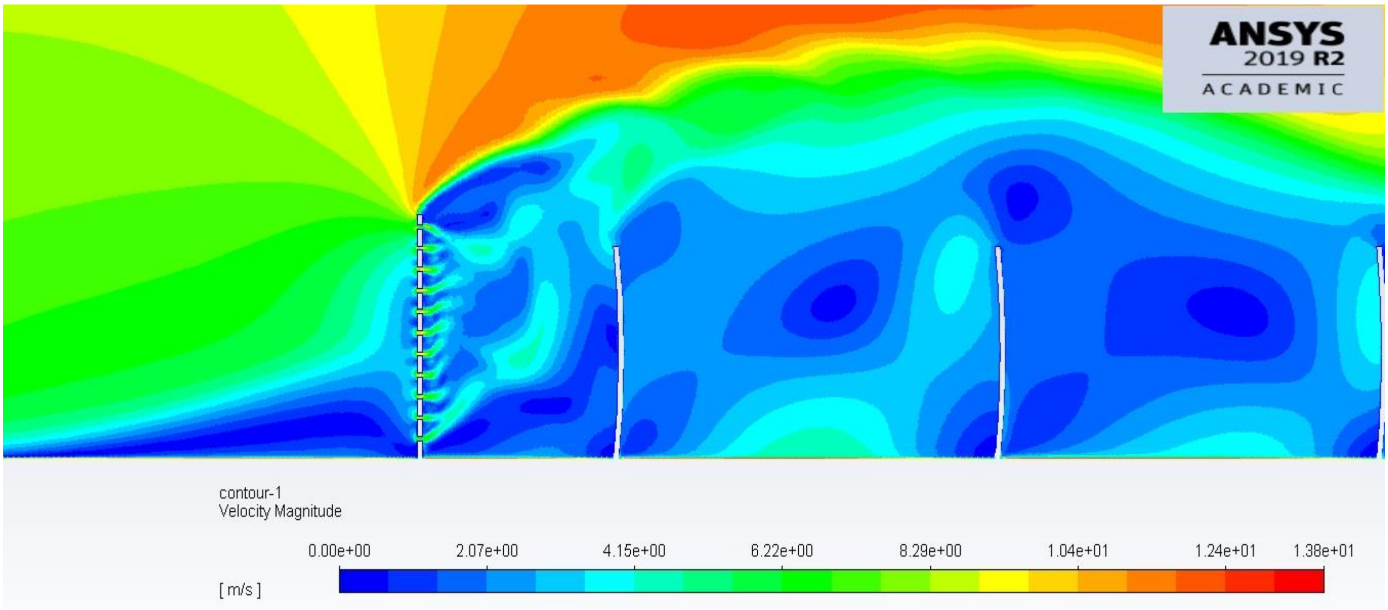

Figure B.24. Porous case 7 velocity contour magnitude

Table B.24. Porous case 7 particle fate

ANSY labelled Wall-ID zone	Geometric Definition	Particles Trapped	Particles Escaped
7	Outlet end side		372456
11	Ground distance of mirror pitch	48982	
12	Ground distance after mirror field	768130	
13	1st mirror front face	32	
14	2nd mirror front face	78	
15	3rd mirror front face	636	
16	4th mirror front face	8270	
17	5th mirror front face	15585	
18	6th mirror front face	24809	
19	Wind Barrier front	12405	
20	Top and back sides of all mirrors	10814	
Soiling [Particles]		49410	

B.7. SIMULATED POROUS CASE 8

B.7.1. GEOMETRICAL SETTINGS

The eighth case assumes values as shown:

Table B.25. Porous case 8 variables

Case Number	**l_3 [m]**	**θ [°]**	**po [m]**
8	0.15	90	0.05

In ANSYS the geometrical settings were defined as shown in figure B.25 and table B.26:

Table B.26. Porous case 8 ANSYS geometrical settings

Case Number	**L6 [m]**	**A7 [°]**	**V10 [m]**
8	0.15	90	0.05

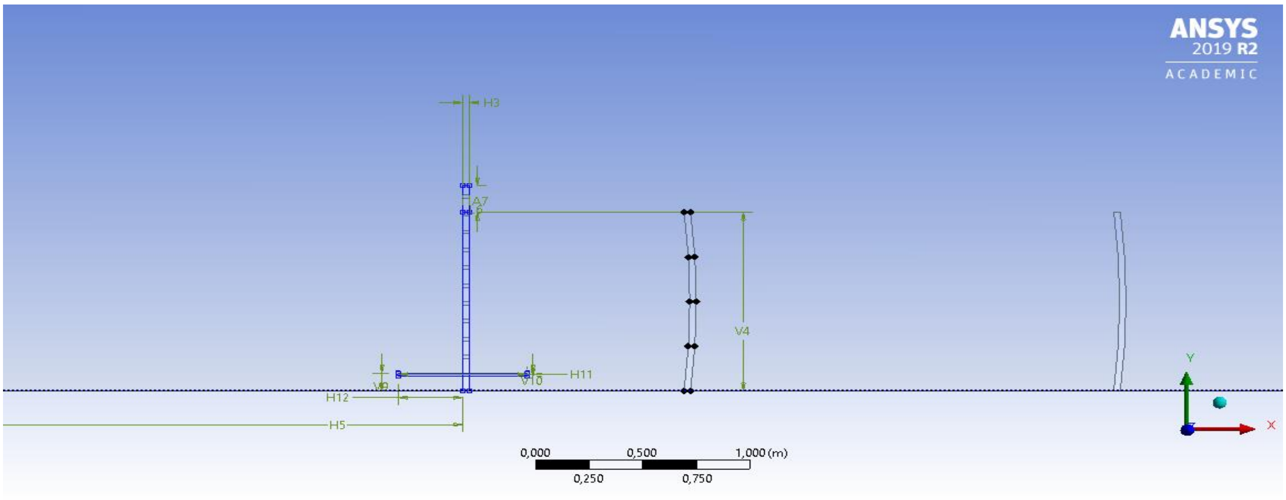

Figure B.25. Porous case 8 geometrical settings

B.7.1. MESH SETTING

The mesh of this case was generated as explained in chapter 2 and the mesh information and quality can be shown in table B.27 and displayed in figure B.26.

Table B.27. Porous case 8 mesh statistics

Nodes	877115
Elements	874657
Mesh Metric Min -Element Quality	8,1059e-003
Mesh Metric Max-Element Quality	0,99947
Mesh Metric Average-Element Quality	0,72055

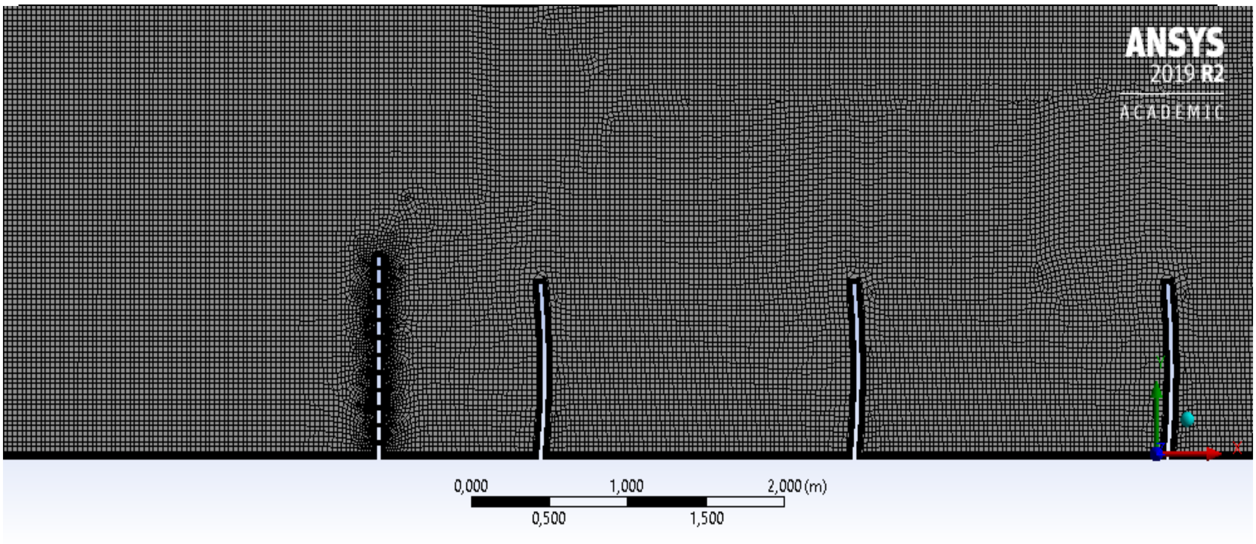

Figure B.26. Porous case 8 mesh settings

B.7.1. ANSYS-FLUENT SIMUALTION RESULTS

The ANSYS FLUENT settings were applied and the following results were obtained after solving for 2600 iterations:

i. Scaled Residuals: Convergence was achieved after 2600 iterations

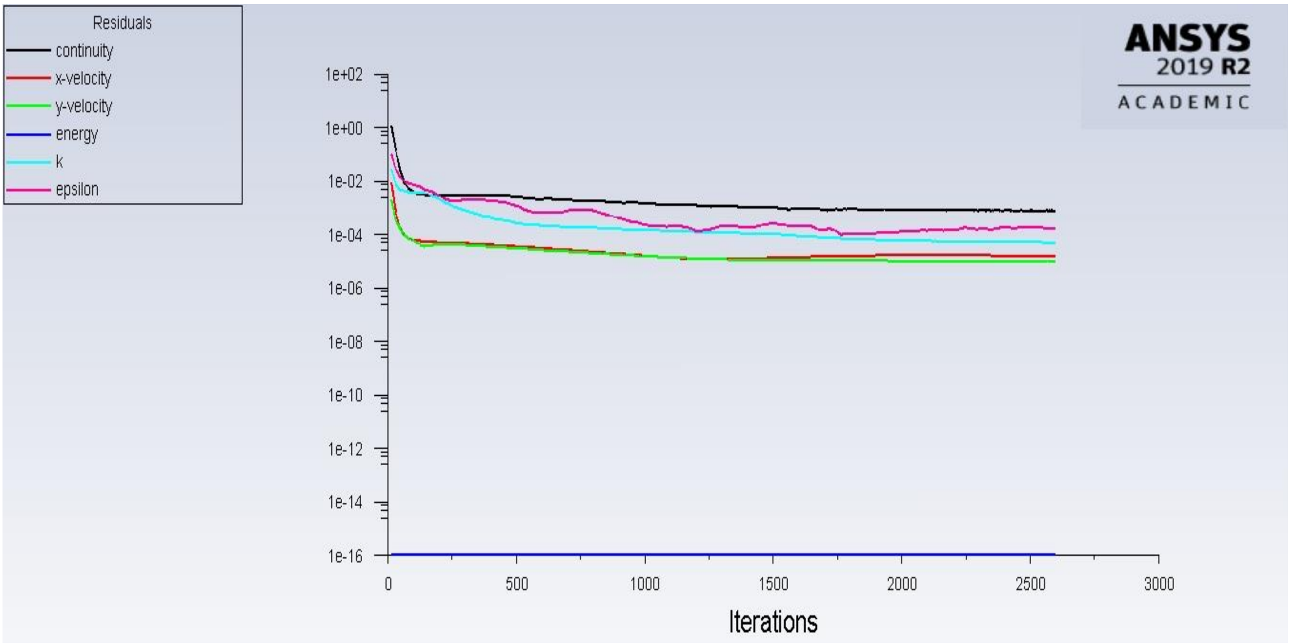

Figure B.27. Porous case 8 scaled residuals

ii. Particles tracked: 1 250 000 particles tracked:

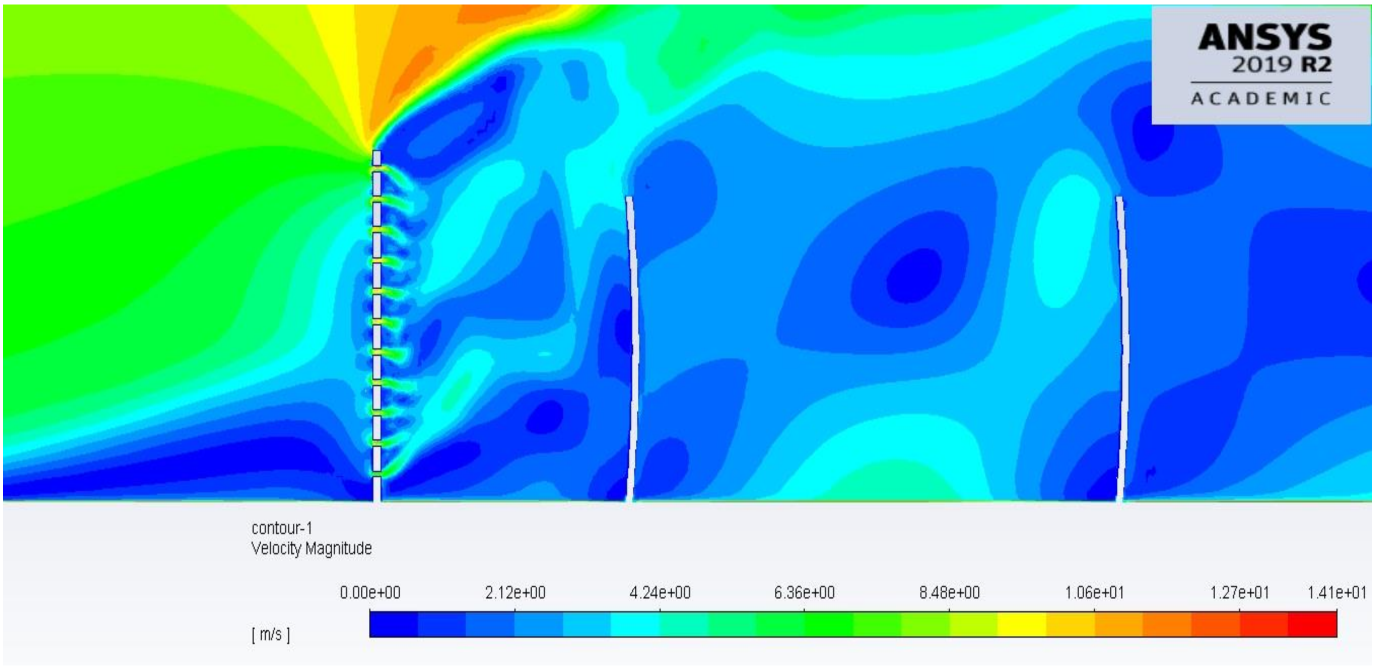

Figure B.28. Porous case 8 velocity contour magnitude

Table B.28. Porous case 8 particle fate

ANSY labelled Wall- ID zone	**Geometric Definition**	**Particles Trapped**	**Particles Escaped**
7	Outlet end side		360369
11	Ground distance of mirror pitch	29898	
12	Ground distance after mirror field	773537	
13	1st mirror front face	14	
14	2nd mirror front face	191	
15	3rd mirror front face	254	
16	4th mirror front face	2226	
17	5th mirror front face	13995	
18	6th mirror front face	25445	
19	Wind Barrier front	35941	
20	Top and back sides of all mirrors	8588	
Soiling [Particles]		42126	

B.8. SIMULATED POROUS CASE 9

B.8.1. GEOMETRICAL SETTINGS

The ninth case assumes values as shown:

Table B.29. Porous case 8 variables

Case Number	l_3 [m]	θ [°]	po [m]
9	0.068696605	20.89211421	0.022804491

In ANSYS the geometrical settings were defined as shown in figure B.29 and table B.30:

Table B.30. Porous case 8 ANSYS geometrical settings

Case Number	L6 [m]	A7 [°]	V10 [m]
9	0.068696605	20.89211421	0.022804491

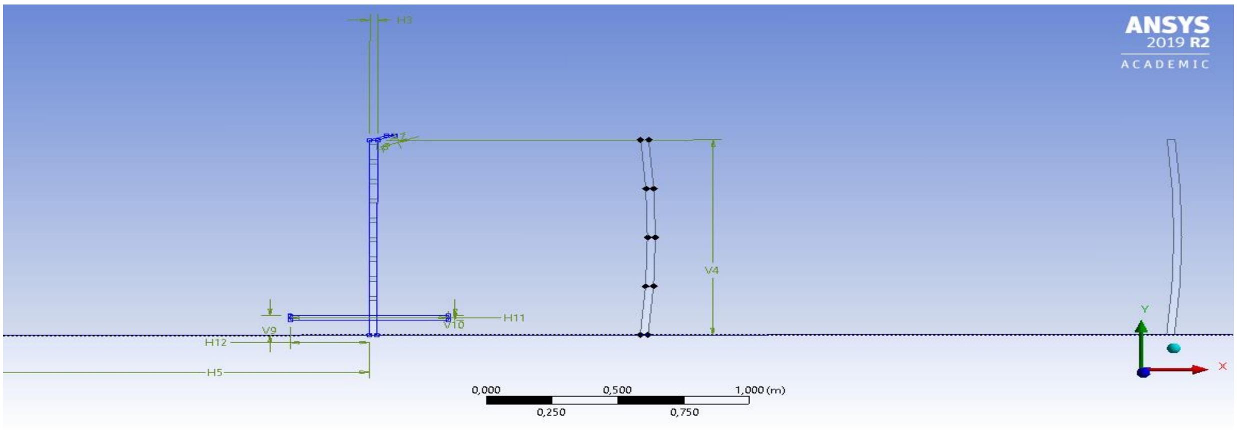

Figure B.29. Porous case 9 geometrical settings

B.8.1. MESH SETTING

The mesh of this case was generated as explained in chapter 2 and the mesh information and quality can be shown in table B.31 and displayed in figure B.30.

Table B.31. Porous case 9 mesh statistics

Nodes	876973
Elements	874590
Mesh Metric Min -Element Quality	1,1392e-002
Mesh Metric Max-Element Quality	0,99981
Mesh Metric Average-Element Quality	0,72055

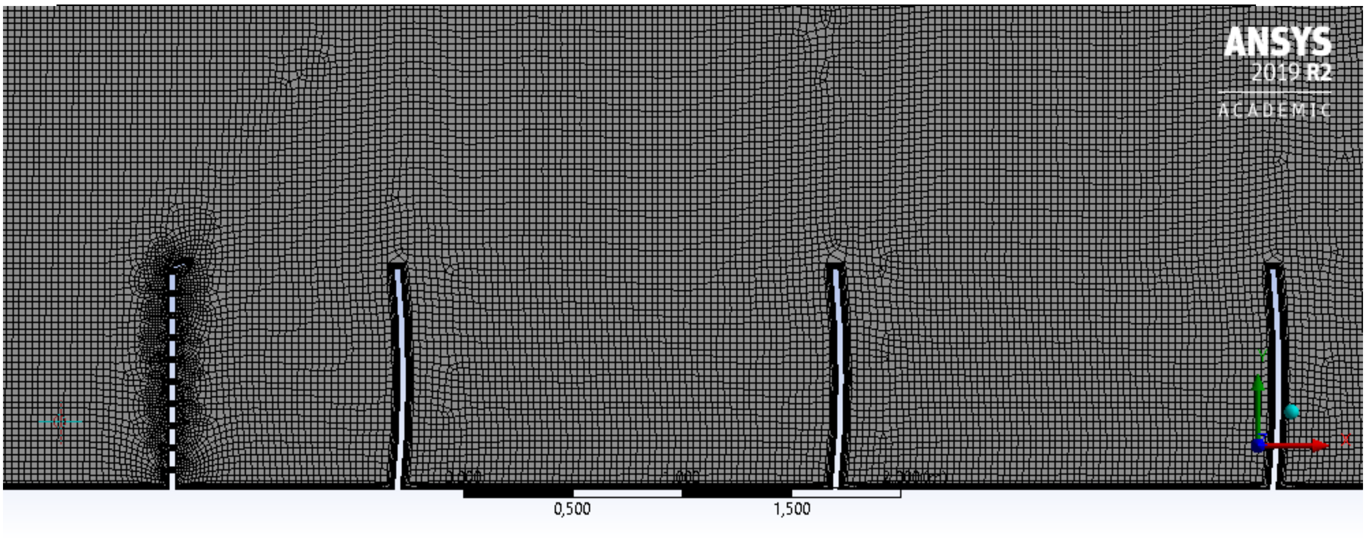

Figure B.30. Porous case 9 mesh settings

B.8.2. ANSYS-FLUENT SIMUALTION RESULTS

The ANSYS FLUENT settings were applied and the following results were obtained after solving for 2600 iterations:

i. Scaled Residuals: Convergence was achieved after 2600 iterations

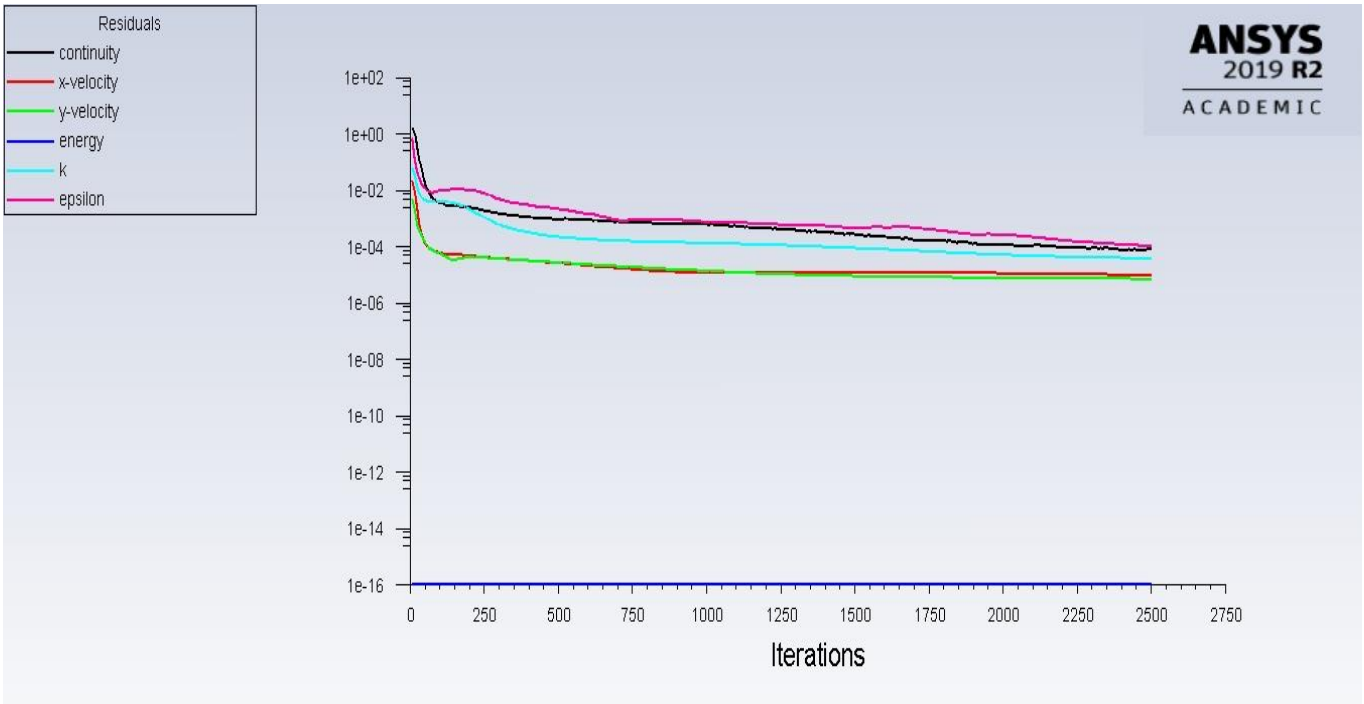

Figure B.31. Porous case 9 scaled residuals

ii. Particles tracked: 1 250 000 particles tracked.

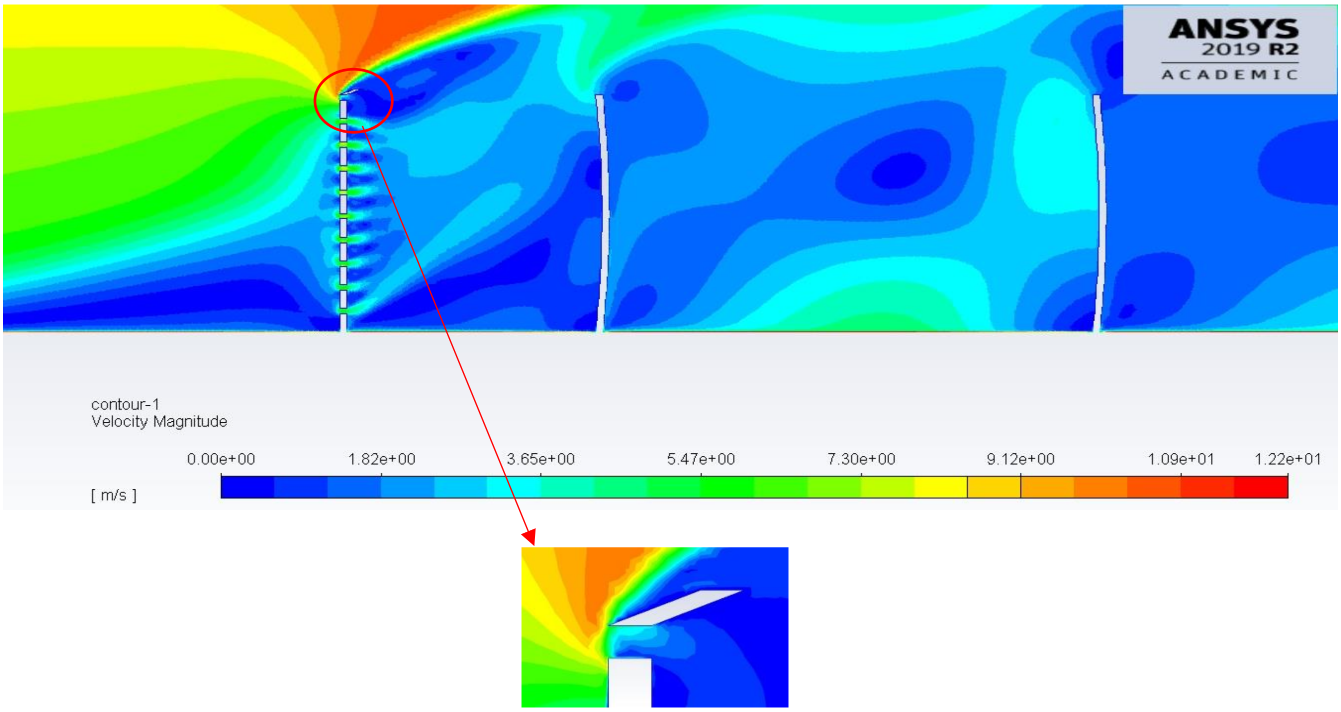

Figure B.32. Porous case 9 velocity contour magnitude

Table B.32. Porous case 9 particle fate

ANSY labelled Wall-ID zone	**Geometric Definition**	**Particles Trapped**	**Particles Escaped**
7	Outlet end side		361641
11	Ground distance of mirror pitch	50573	
12	Ground distance after mirror field	750954	
13	1st mirror front face	318	
14	2nd mirror front face	191	
15	3rd mirror front face	2863	
16	4th mirror front face	13359	
17	5th mirror front face	23219	
18	6th mirror front face	31170	
19	Wind Barrier front	35941	
20	Top and back sides of all mirrors	8588	
Soiling [Particles]		71120	

B.9. SIMULATED POROUS CASE 10

B.9.1. GEOMETRICAL SETTINGS

The tenth case assumes values as shown:

Table B.33. Porous case 10 variables

Case Number	**l_3 [m]**	**θ [°]**	**po [m]**
10	0.231303395	20.89211421	0.022804491

In ANSYS the geometrical settings were defined as shown in figure B.33 and table B.34:

Table B.34. Porous case 10 ANSYS geometrical settings

Case Number	**L6 [m]**	**A7 [°]**	**V10 [m]**
10	0.231303395	20.89211421	0.022804491

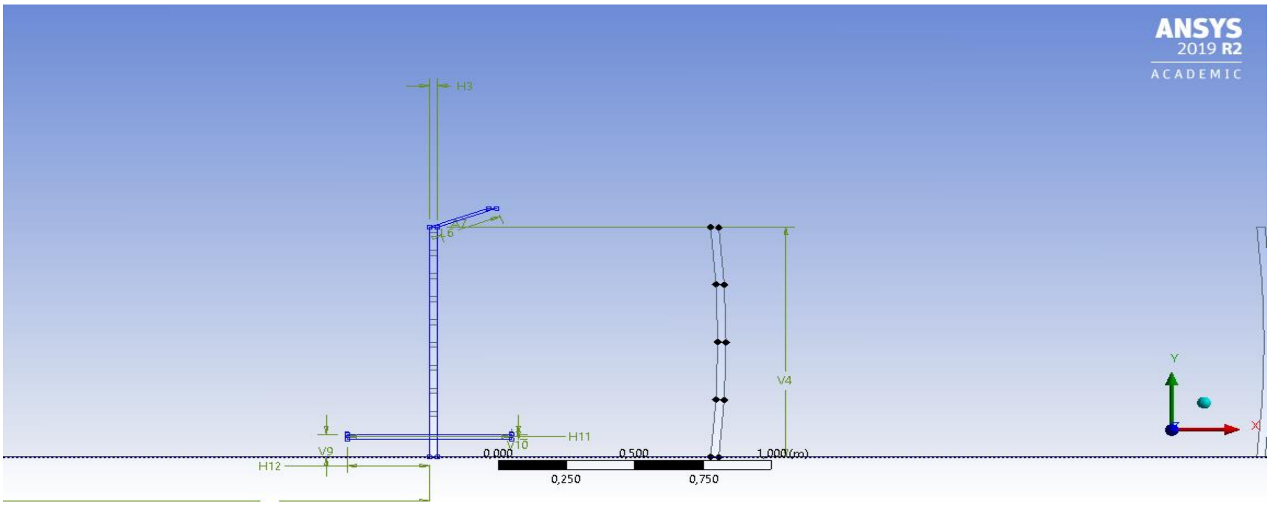

Figure B.33. Porous case 10 geometrical settings

B.9.1. MESH SETTING

The mesh of this case was generated as explained in chapter 2 and the mesh information and quality can be shown in table B.35 and displayed in figure B.34.

Table B.35. Porous case 10 mesh statistics

Nodes	873646
Elements	871194
Mesh Metric Min -Element Quality	2,2485e-002
Mesh Metric Max-Element Quality	0,99965
Mesh Metric Average-Element Quality	0,71506

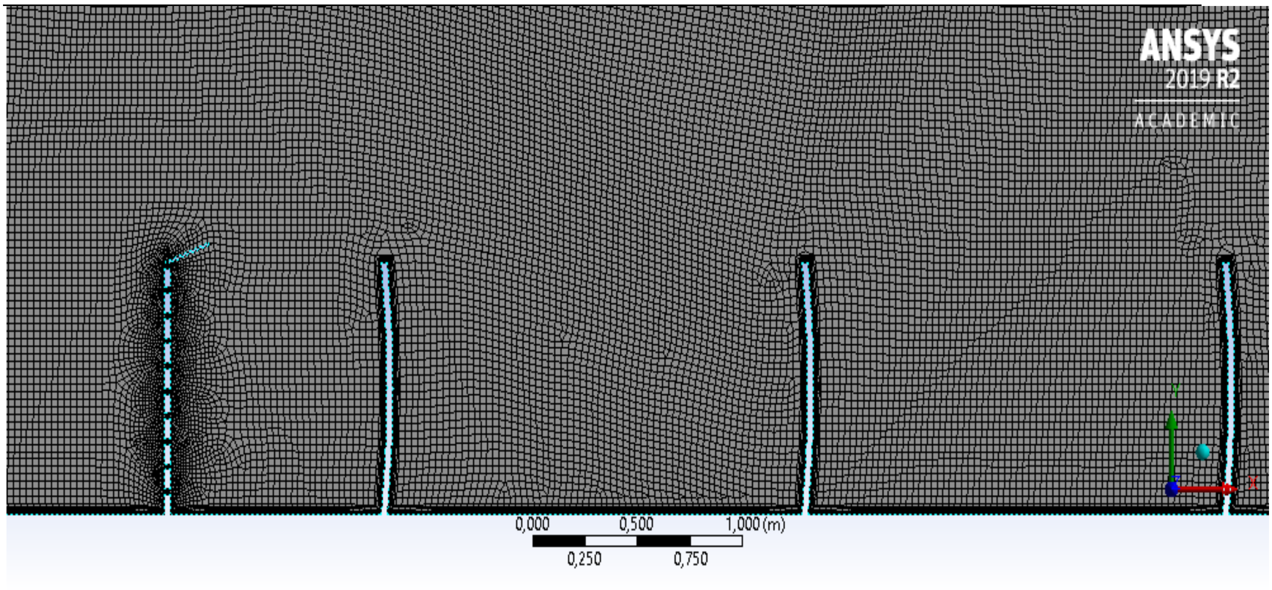

Figure B.34. Porous case 10 mesh settings

B.9.2. ANSYS-FLUENT SIMUALTION RESULTS

The ANSYS FLUENT settings were applied and the following results were obtained after solving for 2500 iterations:

i. Scaled Residuals: Convergence was achieved after 2500 iterations.

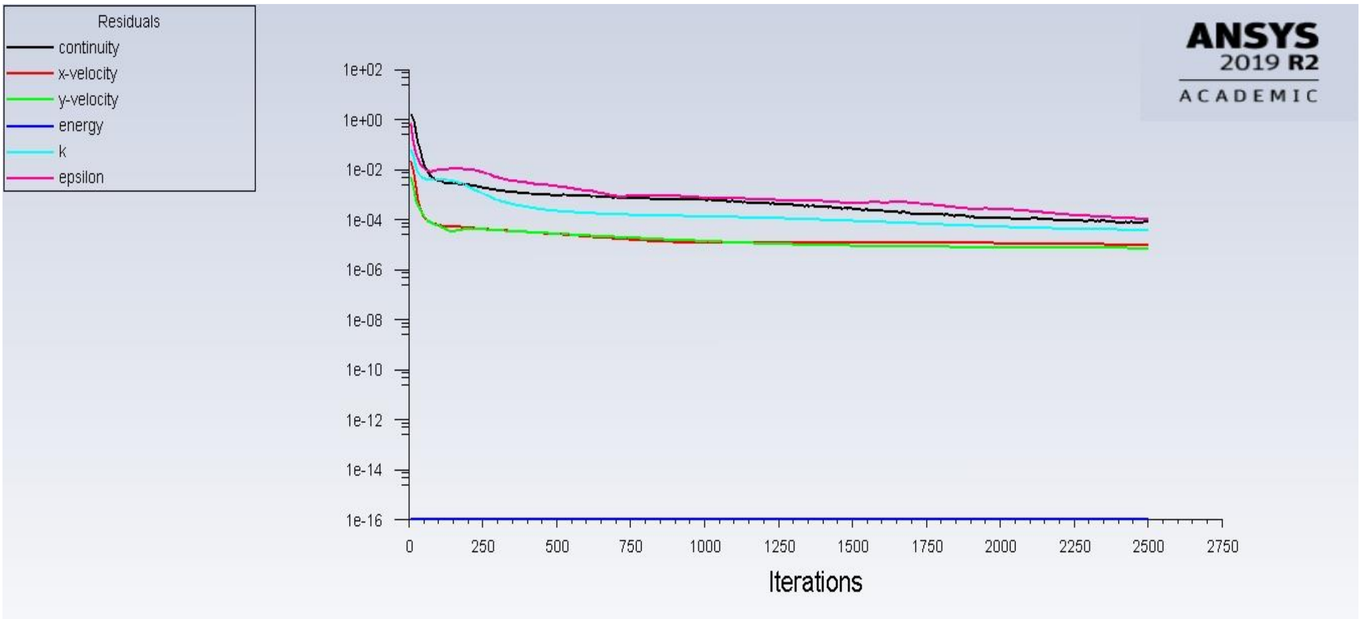

Figure B.35. Porous case 10 scaled residuals

ii. Particles tracked: 1 250 000 particles tracked.

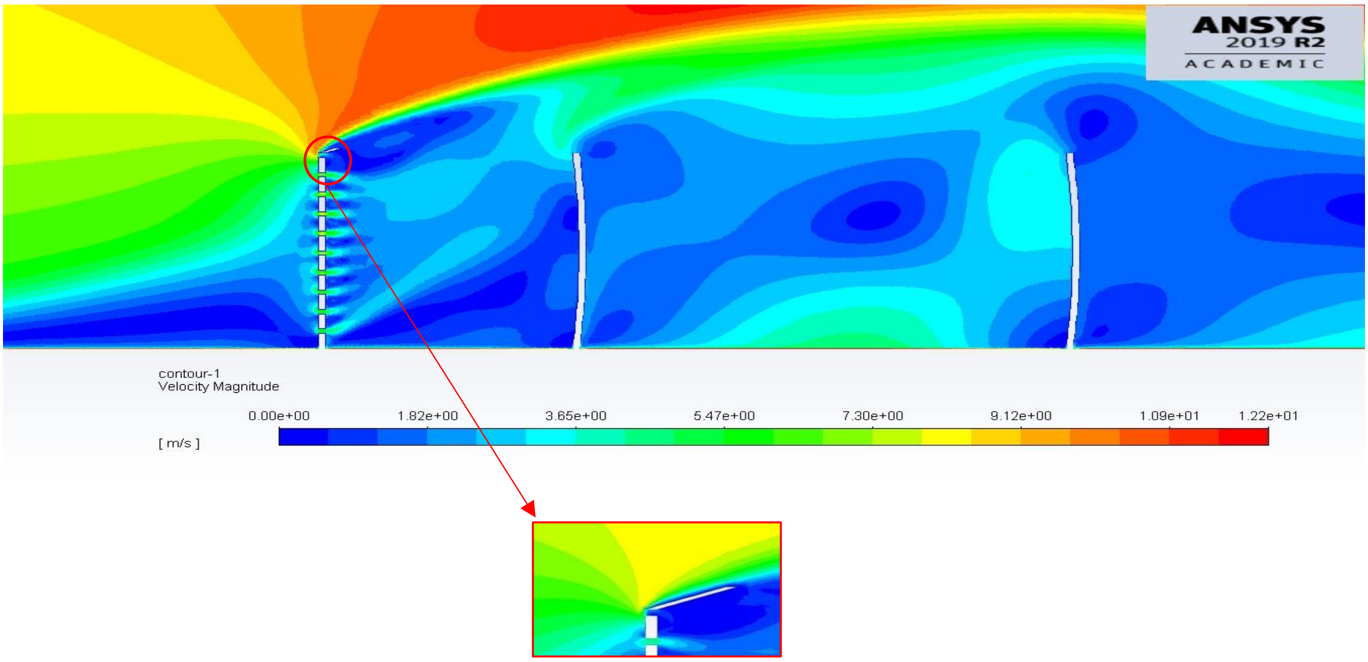

Figure B.36. Porous case 10 velocity contour magnitude

Table B.36. Porous case 10 particle fate

ANSY labelled Wall- ID zone	**Geometric Definition**	**Particles Trapped**	**Particles Escaped**
7	Outlet end side		358779
11	Ground distance of mirror pitch	47074	
12	Ground distance after mirror field	753181	
13	1st mirror front face	13	
14	2nd mirror front face	954	
15	3rd mirror front face	2226	
16	4th mirror front face	13359	
17	5th mirror front face	25127	
18	6th mirror front face	33397	
19	Wind Barrier front	5725	
20	Top and back sides of all mirrors	10178	
Soiling [Particles]		75076	

B.10. SIMULATED POROUS CASE 11

B.10.1. GEOMETRICAL SETTINGS

The eleventh case assumes values as shown:

Table B.37. Porous case 11 variables

Case Number	l_3 [m]	θ [°]	po [m]
11	0.068696605	159.1078858	0.022804491

In ANSYS the geometrical settings were defined as shown in figure B.37 and table B.38:

Table B.38. Porous case 11 ANSYS geometrical settings

Case Number	L6 [m]	A7 [°]	V10 [m]
11	0.068696605	159.1078858	0.022804491

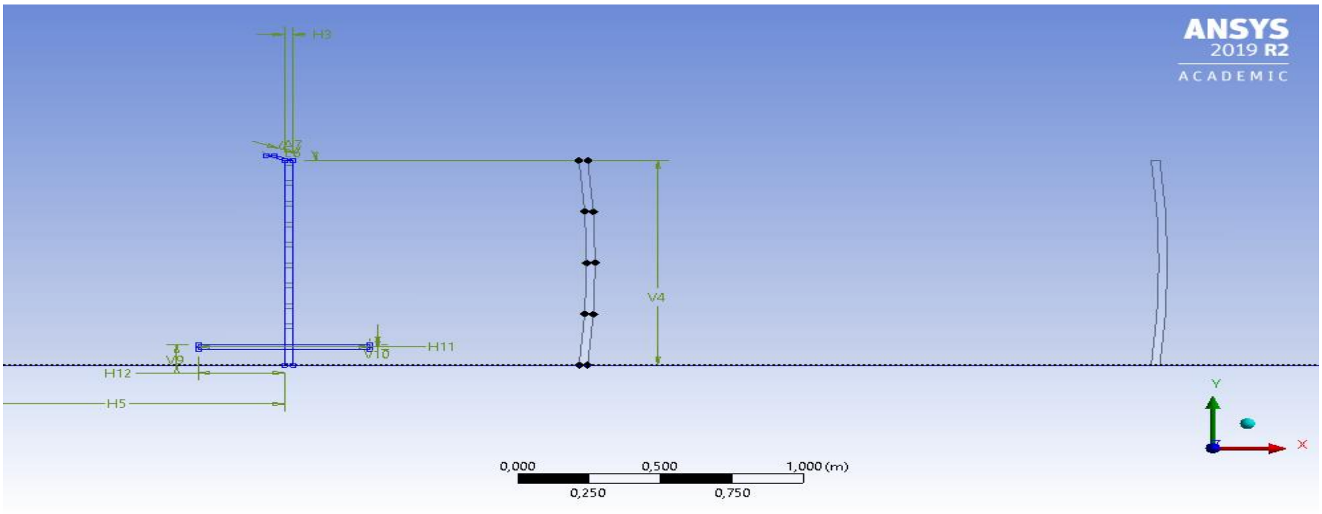

Figure B.37. Porous case 11 geometrical settings

B.10.2. MESH SETTING

The mesh of this case was generated as explained in chapter 2 and the mesh information and quality can be shown in table B.39 and displayed in figure B.38.

Table B.39. Porous case 11 mesh statistics

Nodes	876519
Elements	874140
Mesh Metric Min -Element Quality	2,3382e-002
Mesh Metric Max-Element Quality	0,99994
Mesh Metric Average-Element Quality	0,72004

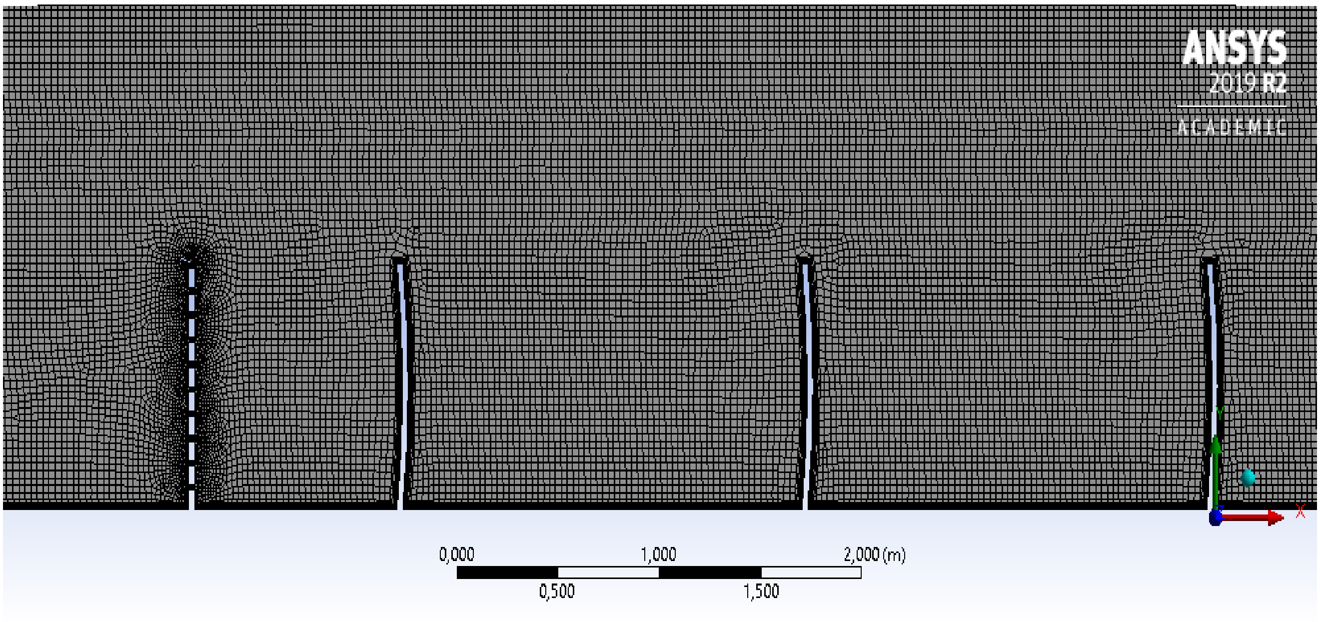

Figure B.38. Porous case 11 mesh settings

B.10.3. ANSYS-FLUENT SIMUALTION RESULTS

The ANSYS FLUENT settings were applied and the following results were obtained after solving for 2500 iterations:

i. Scaled Residuals: Convergence was achieved after 2500 iterations.

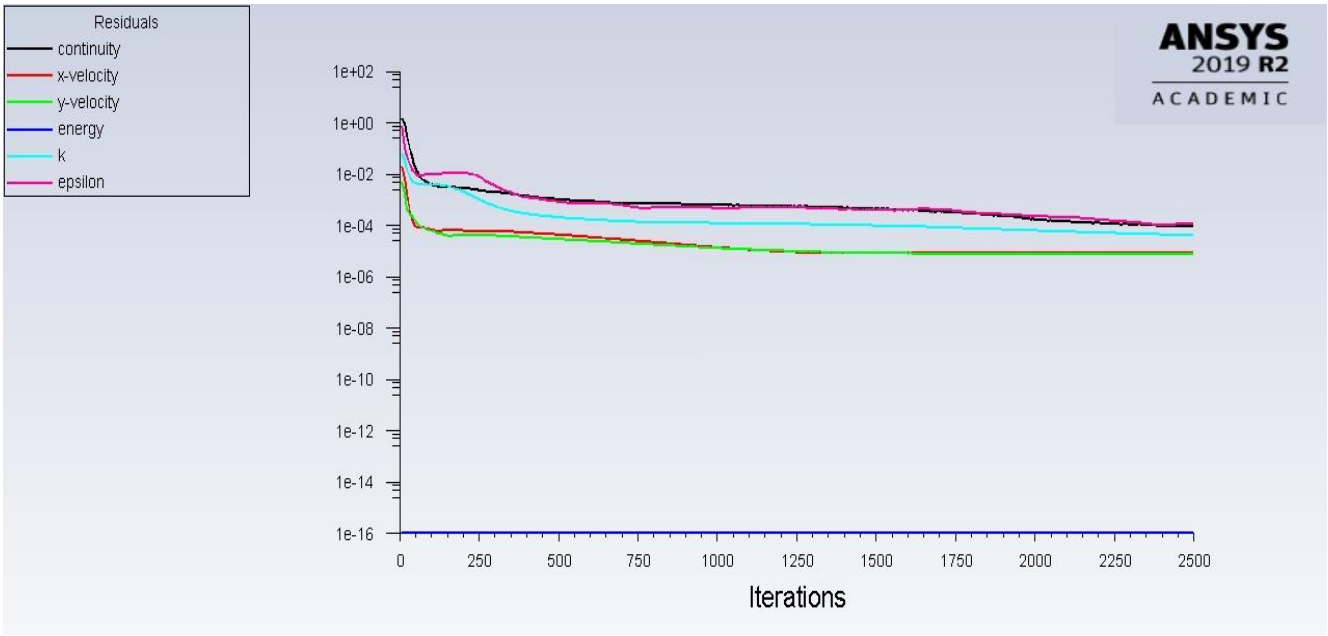

Figure B.39. Porous case 11 scaled residuals

ii. Particles tracked: 1 250 000 particles tracked.

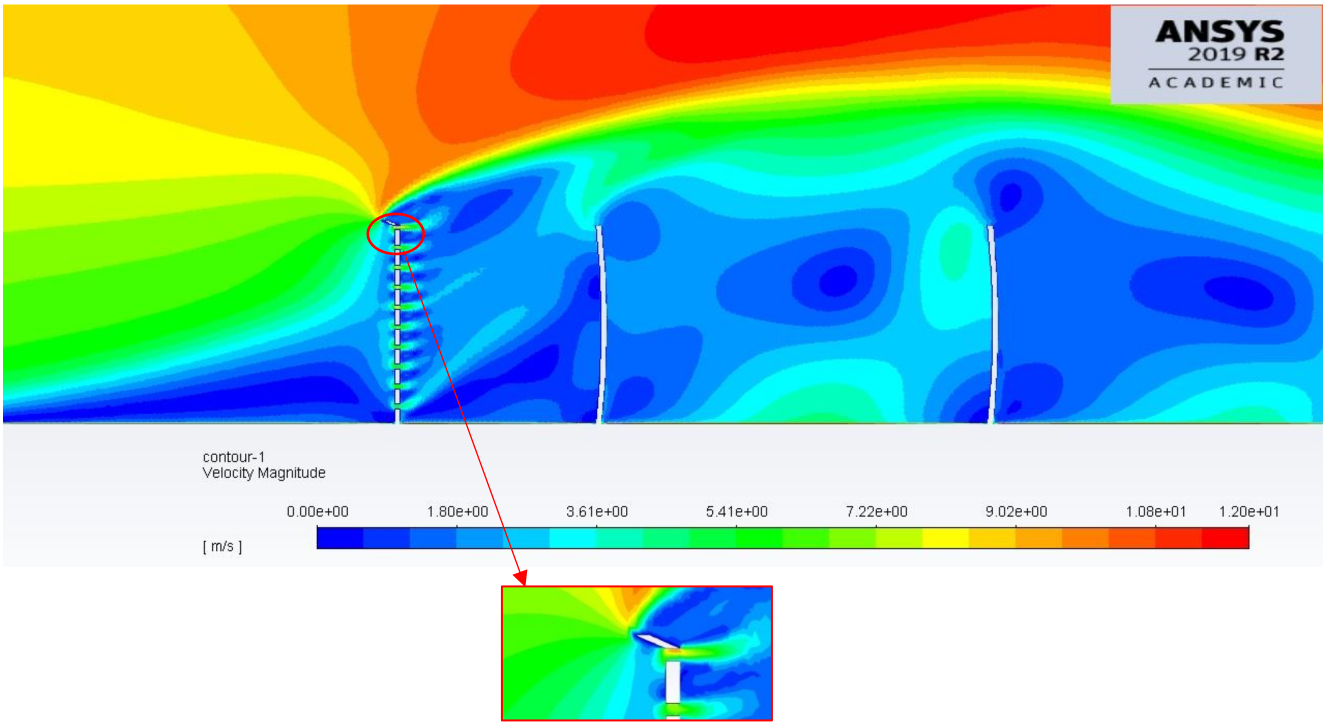

Figure B.40. Porous case 11 velocity contour magnitude

Table B.40. Porous case 11 particle fate

ANSY labelled Wall-ID zone	Geometric Definition	Particles Trapped	Particles Escaped
7	Outlet end side		328562
11	Ground distance of mirror pitch	61387	
12	Ground distance after mirror field	771311	
13	1st mirror front face	3	
14	2nd mirror front face	954	
15	3rd mirror front face	6043	
16	4th mirror front face	12087	
17	5th mirror front face	20992	
18	6th mirror front face	31807	
19	Wind Barrier front	6361	
20	Top and back sides of all mirrors	10178	
Soiling [Particles]		71886	

B.11. SIMULATED POROUS CASE 12

B.12.1. GEOMETRICAL SETTINGS

The twelfth case assumes values as shown:

Table B.41. Porous case 12 variables

Case Number	**l_3 [m]**	**θ [°]**	**po [m]**
12	0.231303395	159.1078858	0.022804491

In ANSYS the geometrical settings were defined as shown in figure B.42 and table B.41:

Table B.42. Porous case 12 ANSYS geometrical settings

Case Number	**L6 [m]**	**A7 [°]**	**V10 [m]**
12	0.231303395	159.1078858	0.022804491

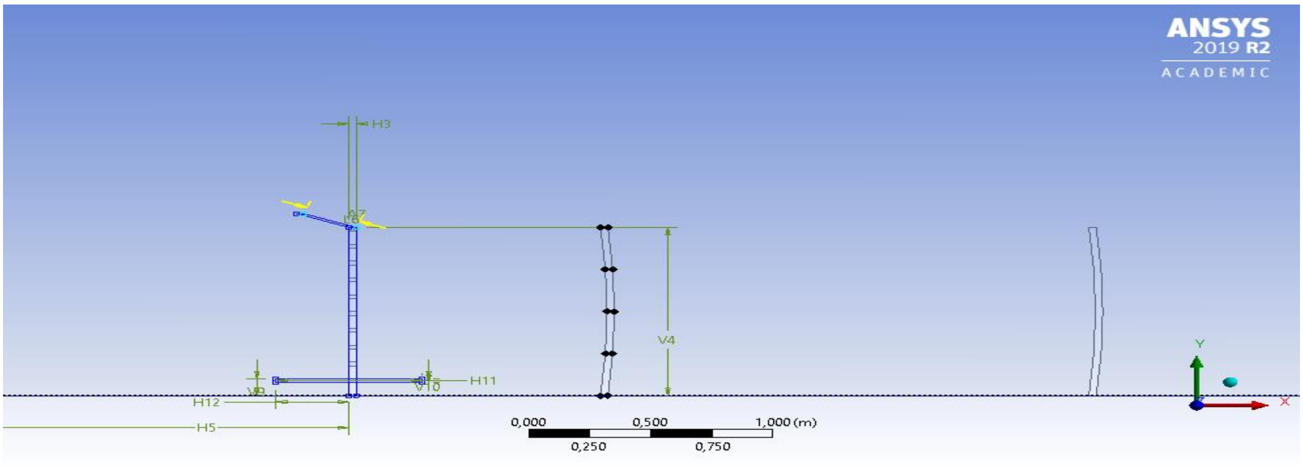

Figure B.41. Porous case 12 geometrical settings

B.12.2. MESH SETTING

The mesh of this case was generated as explained in chapter 2 and the mesh information and quality can be shown in table B.43 and displayed in figure B.41.

Table B.43. Porous case 12 mesh statistics

Nodes	878131
Elements	875675
Mesh Metric Min -Element Quality	2,34e-002
Mesh Metric Max-Element Quality	0,99947
Mesh Metric Average-Element Quality	0,72048

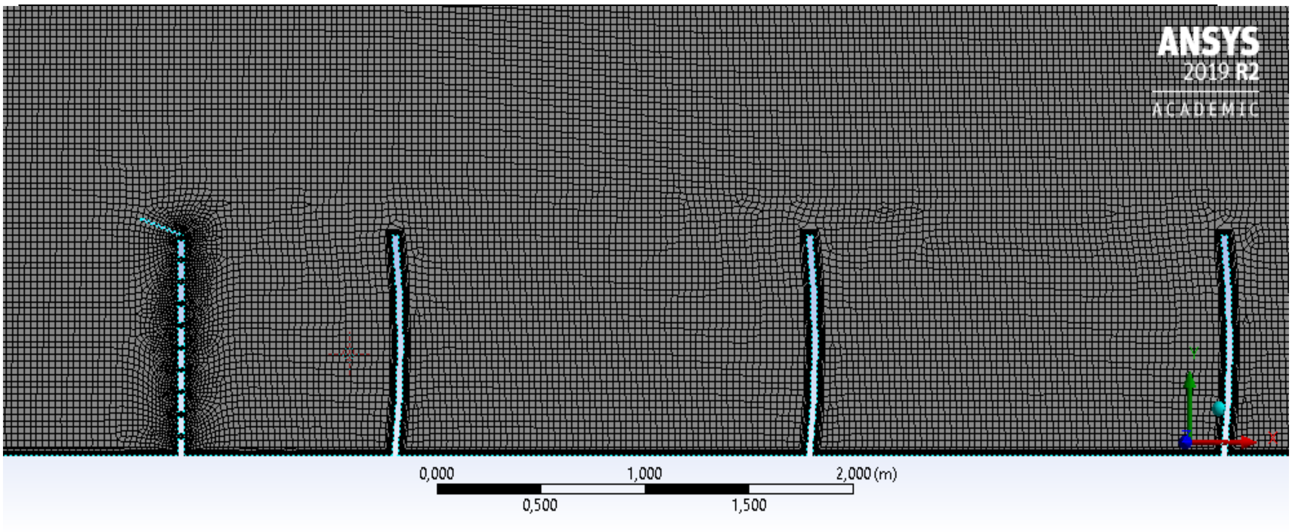

Figure B.42. Porous case 12 mesh settings

B.12.3. ANSYS-FLUENT SIMUALTION RESULTS

The ANSYS FLUENT settings were applied and the following results were obtained after solving for 2500 iterations:

i. Scaled Residuals: Convergence was achieved after 2500 iterations.

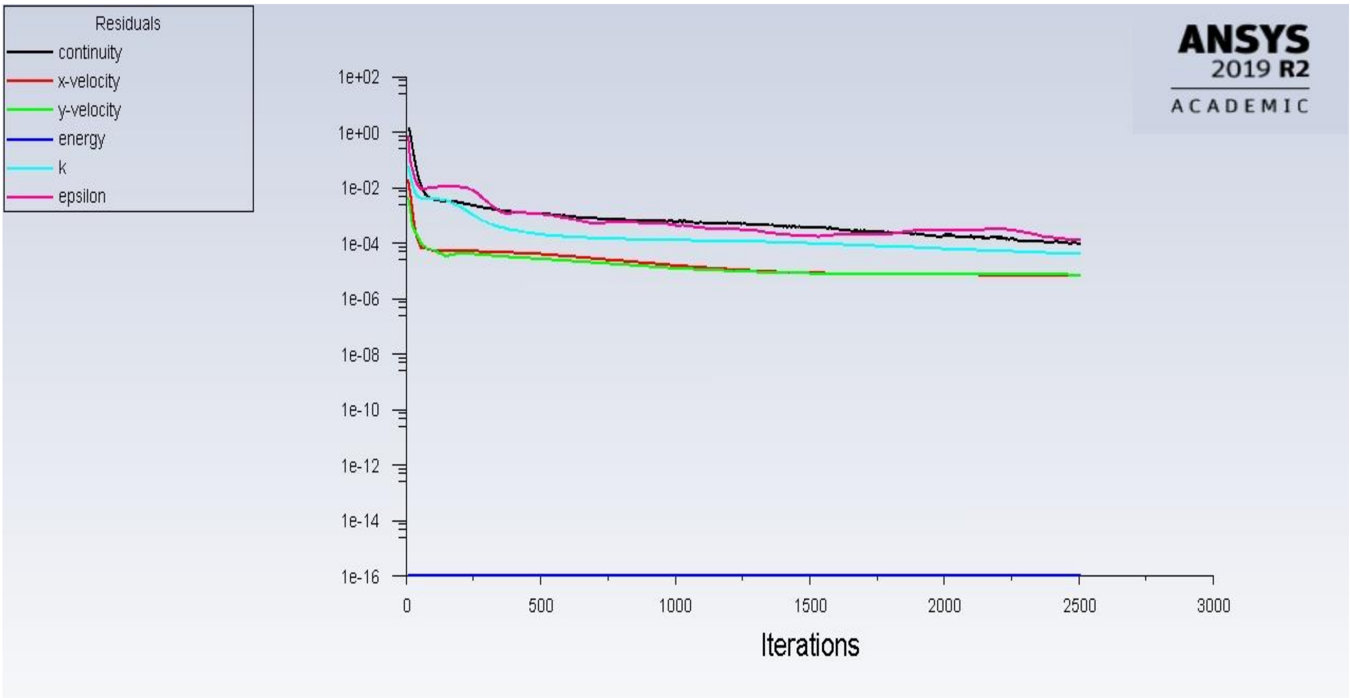

Figure B.43. Porous case 12 scaled residuals

ii. Particles tracked: 1 250 000 particles tracked.

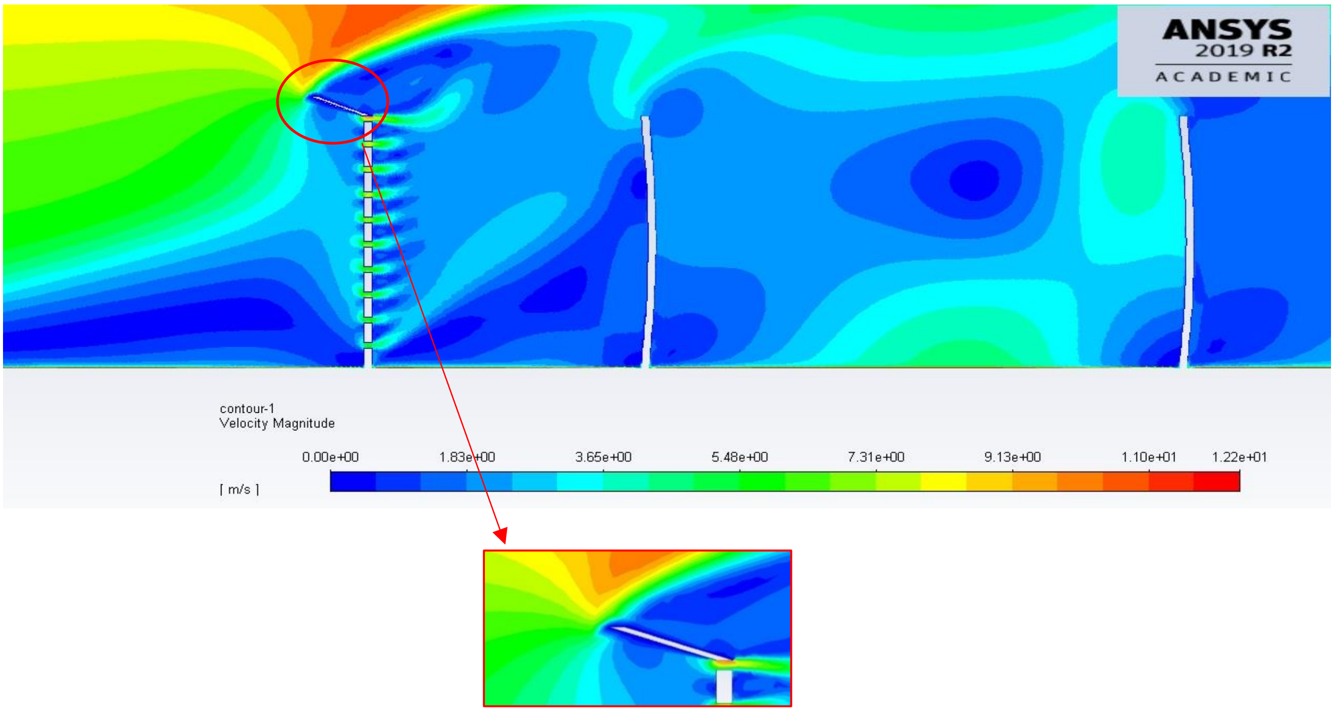

Figure B.44. Porous case 12 velocity contour magnitude

Table B.44. Porous case 12 particle fate

ANSY labelled Wall- ID zone	**Geometric Definition**	**Particles Trapped**	**Particles Escaped**
7	Outlet end side		328562
11	Ground distance of mirror pitch	50891	
12	Ground distance after mirror field	764631	
13	1st mirror front face	128	
14	2nd mirror front face	636	
15	3rd mirror front face	5089	
16	4th mirror front face	13995	
17	5th mirror front face	28308	
18	6th mirror front face	32443	
19	Wind Barrier front	15267	
20	Top and back sides of all mirrors	10178	
Soiling [Particles]		80599	

B.12. SIMULATED POROUS CASE 13

B.12.1. GEOMETRICAL SETTINGS

The thirteenth case assumes values as shown:

Table B.45. Porous case 13 variables

Case Number	**l_3 [m]**	**θ [°]**	**po [m]**
13	0.068696605	20.89211421	0.047195509

In ANSYS the geometrical settings were defined as shown in figure B.45 and table B.46:

Table B.46. Porous case 13 ANSYS geometrical settings

Case Number	**L6 [m]**	**A7 [°]**	**V10 [m]**
13	0.068696605	20.89211421	0.047195509

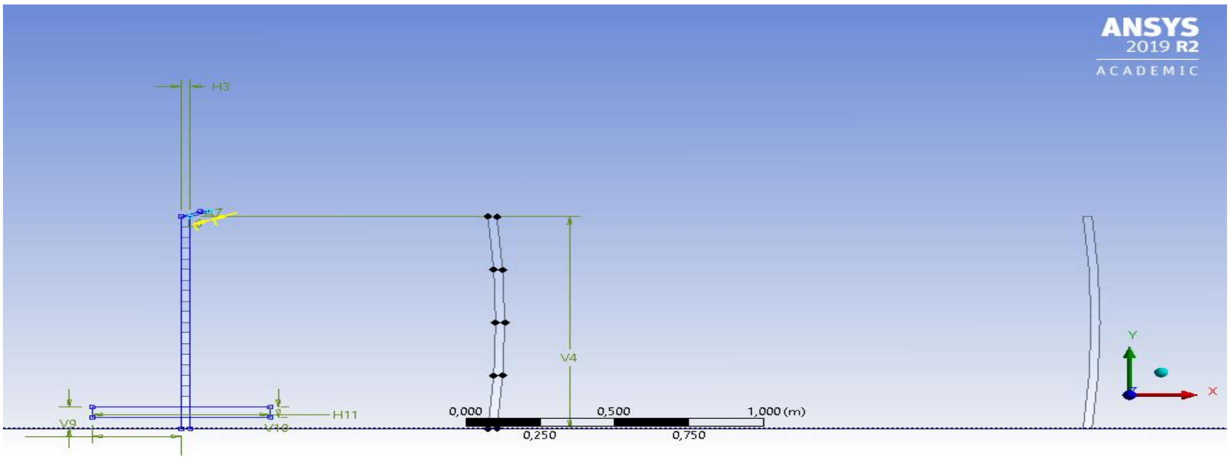

Figure B.45. Porous case 13 geometrical settings

B.12.2. MESH SETTING

The mesh of this case was generated as explained in chapter 2 and the mesh information and quality can be shown in table B.47 and displayed in figure B.46.

Table B.47. Porous case 13 mesh statistics

Nodes	874617
Elements	872401
Mesh Metric Min -Element Quality	3,7374e-002
Mesh Metric Max-Element Quality	0,99959
Mesh Metric Average-Element Quality	0,71753

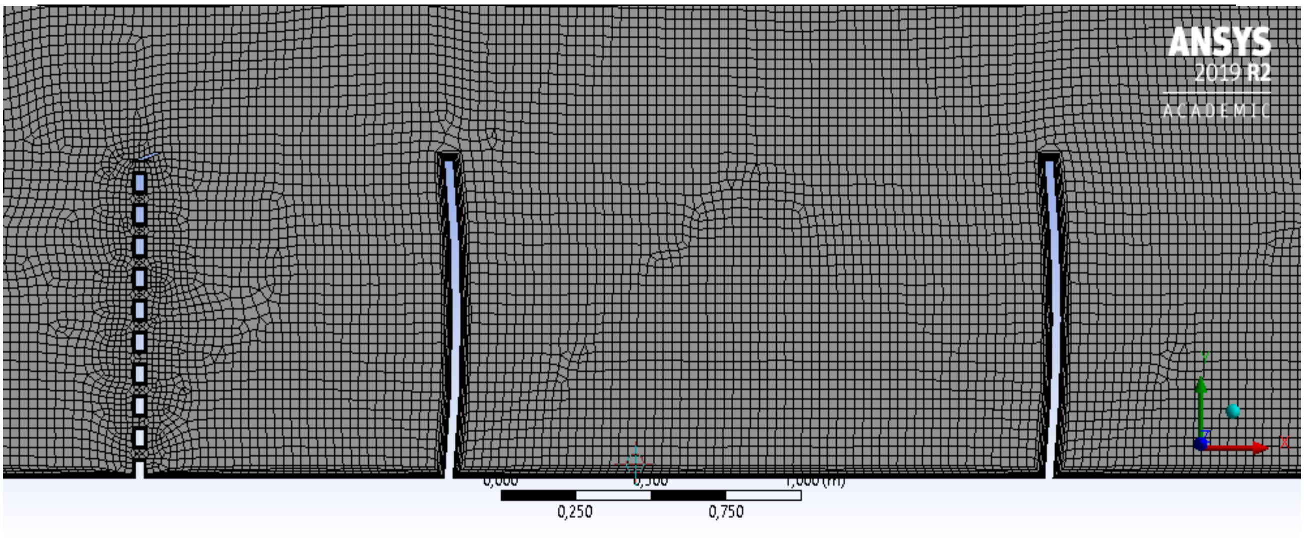

Figure B.46. Porous case 13 mesh settings

B.12.4. ANSYS-FLUENT SIMUALTION RESULTS

The ANSYS FLUENT settings were applied and the following results were obtained after solving for 2630 iterations:

i. Scaled Residuals: Convergence was achieved after 2630 iterations.

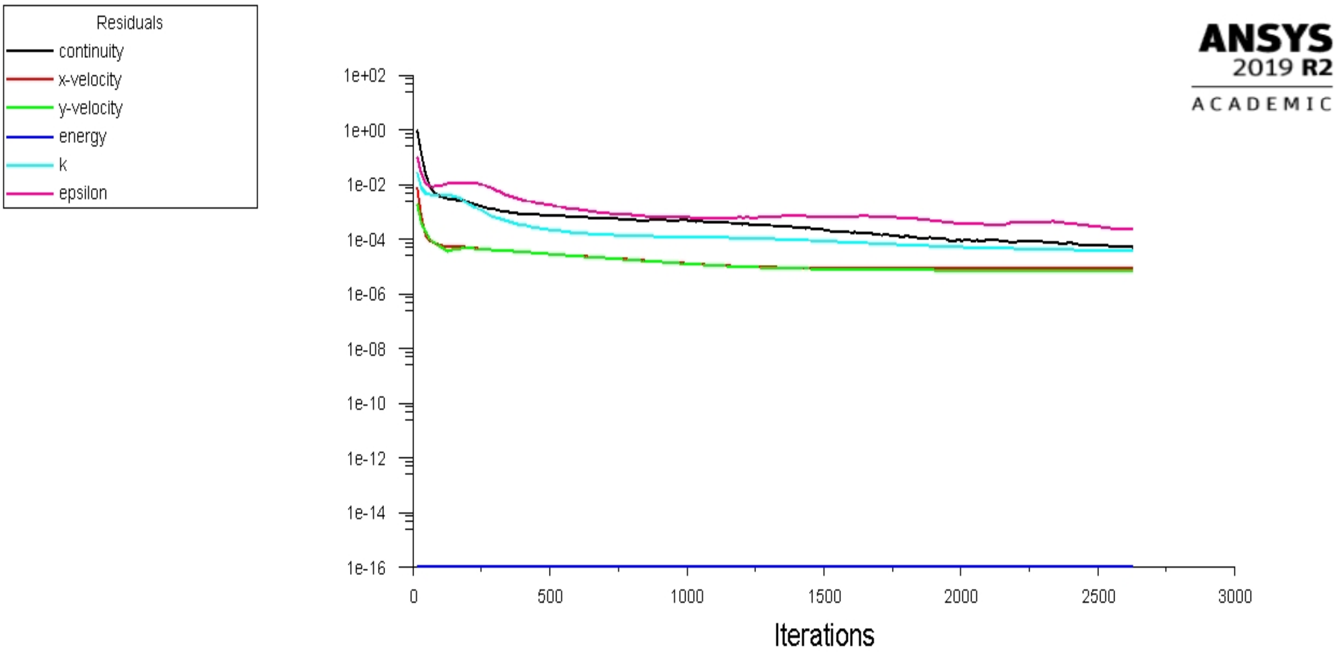

Figure B.47. Porous case 13 scaled residuals

ii. Particles tracked: 1 250 000 particles tracked.

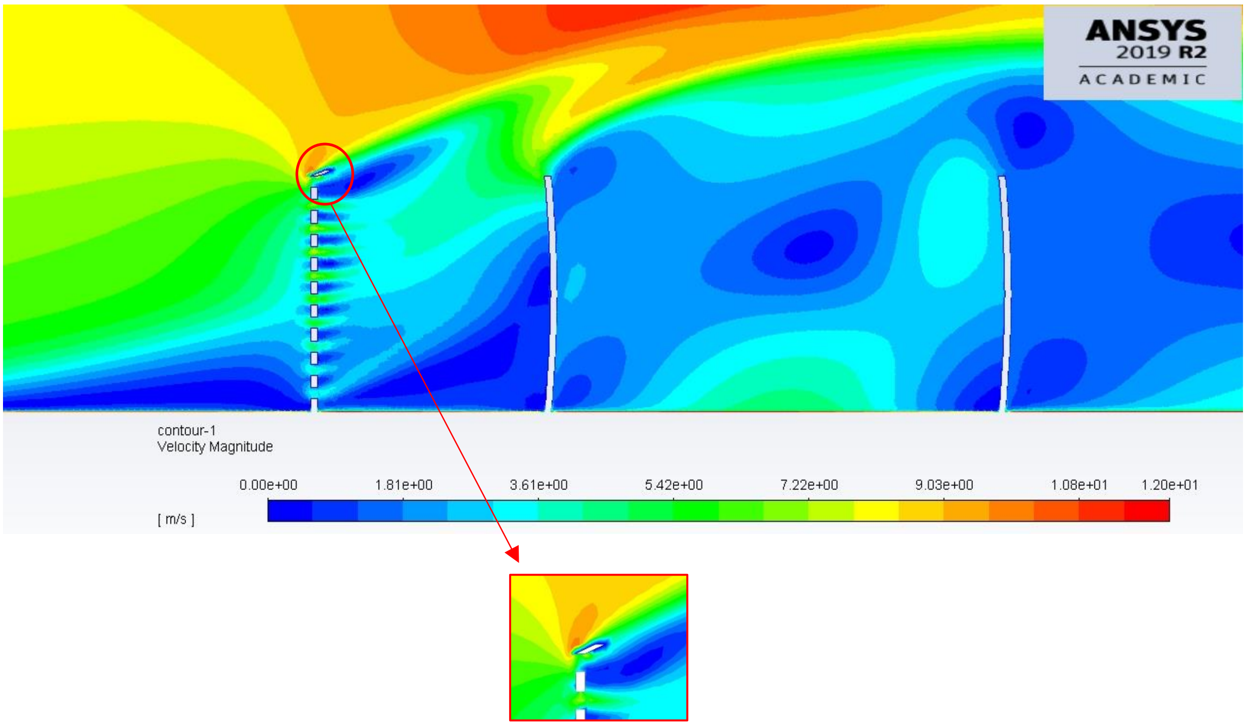

Figure B.48. Porous case 13 velocity contour magnitude

Table B.48. Porous case 13 particle fate

ANSY labelled Wall-ID zone	Geometric Definition	Particles Trapped	Particles Escaped
7	Outlet end side		328562
11	Ground distance of mirror pitch	44847	
12	Ground distance after mirror field	759542	
13	1st mirror front face	29	
14	2nd mirror front face	137	
15	3rd mirror front face	636	
16	4th mirror front face	7316	
17	5th mirror front face	21947	
18	6th mirror front face	31807	
19	Wind Barrier front	19084	
20	Top and back sides of all mirrors	5725	
Soiling [Particles]		61870	

B.13. SIMULATED POROUS CASE 14

B..13.1. GEOMETRICAL SETTINGS

The fourteenth case assumes values as shown:

Table B.49. Porous case 14 variables

Case Number	l_3 [m]	θ [°]	po [m]
14	0.231303395	20.89211421	0.047195509

In ANSYS the geometrical settings were defined as shown in figure B.49 and table B.50:

Table B.50. Porous case 14 ANSYS geometrical settings

Case Number	L6 [m]	A7 [°]	V10 [m]
14	0.231303395	20.89211421	0.047195509

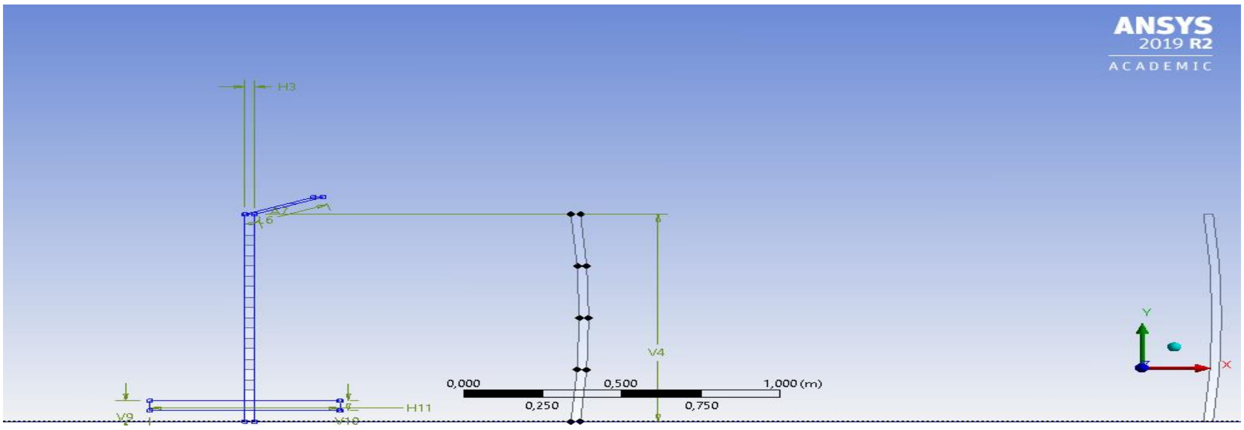

Figure B.49. Porous case 14 geometrical settings

B..13.2. MESH SETTING

The mesh of this case was generated as explained in chapter 2 and the mesh information and quality can be shown in table B.51 and displayed in figure B.50.

Table B.51. Porous case 14 mesh statistics

Nodes	874158
Elements	871825
Mesh Metric Min -Element Quality	3,7374e-002
Mesh Metric Max-Element Quality	0,99947
Mesh Metric Average-Element Quality	0,7197

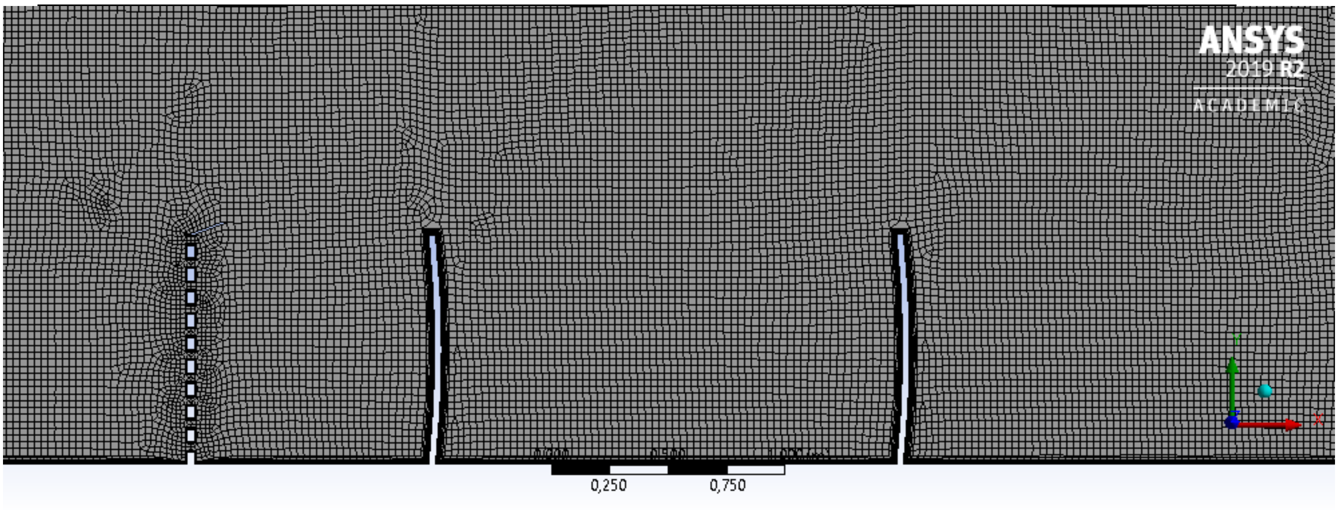

Figure B.50. Porous case 14 mesh settings

B..13.3. ANSYS-FLUENT SIMUALTION RESULTS

The ANSYS FLUENT settings were applied and the following results were obtained after solving for 2500 iterations:

i. Scaled Residuals: Convergence was achieved after 2500 iterations.

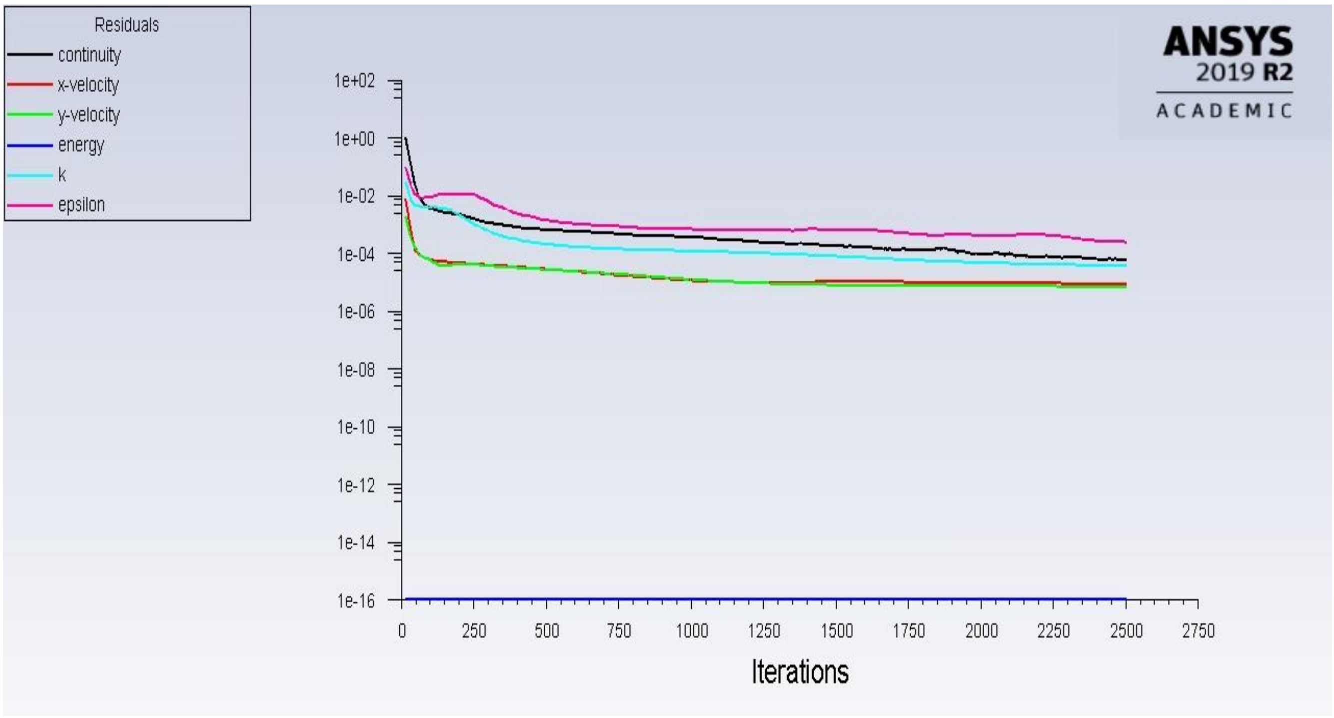

Figure B.51. Porous case 14 scaled residuals

ii. Particles tracked: 1 250 000 particles tracked.

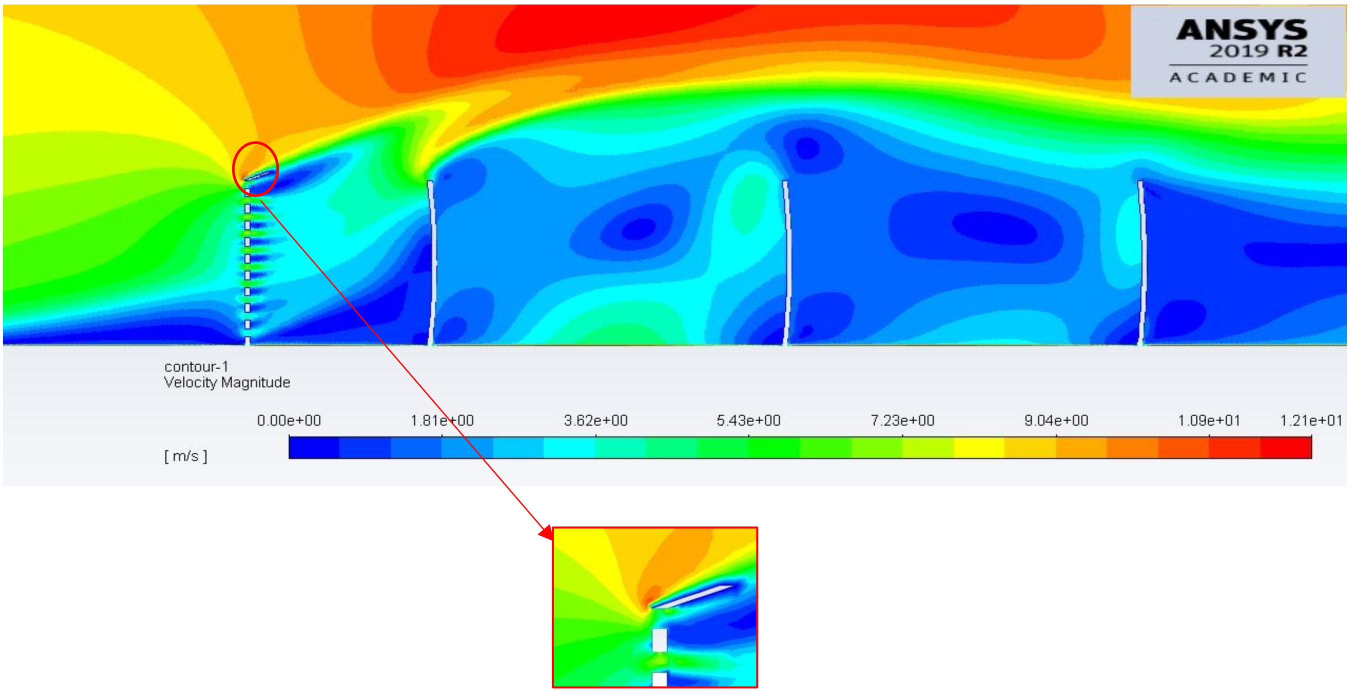

Figure B.52. Porous case 14 velocity contour magnitude

Table B.52. Porous case 14 particle fate

ANSY labelled Wall- ID zone	**Geometric Definition**	**Particles Trapped**	**Particles Escaped**
7	Outlet end side		359415
11	Ground distance of mirror pitch	40076	
12	Ground distance after mirror field	767176	
13	1st mirror front face	102	
14	2nd mirror front face	636	
15	3rd mirror front face	636	
16	4th mirror front face	8270	
17	5th mirror front face	21947	
18	6th mirror front face	21947	
19	Wind Barrier front	14949	
20	Top and back sides of all mirrors	8588	
Soiling [Particles]		53537	

B.14. SIMULATED POROUS CASE 15

B.14.1. GEOMETRICAL SETTINGS

The fifteenth case assumes values as shown:

Table B.53. Porous case 15 variables

Case Number	l_3 [m]	θ [°]	po [m]
15	0.068696605	159.1078858	0.047195509

In ANSYS the geometrical settings were defined as shown in figure B.53 and table B.54:

Table B.54. Porous case 15 ANSYS geometrical settings

Case Number	L6 [m]	A7 [°]	V10 [m]
15	0.068696605	159.1078858	0.047195509

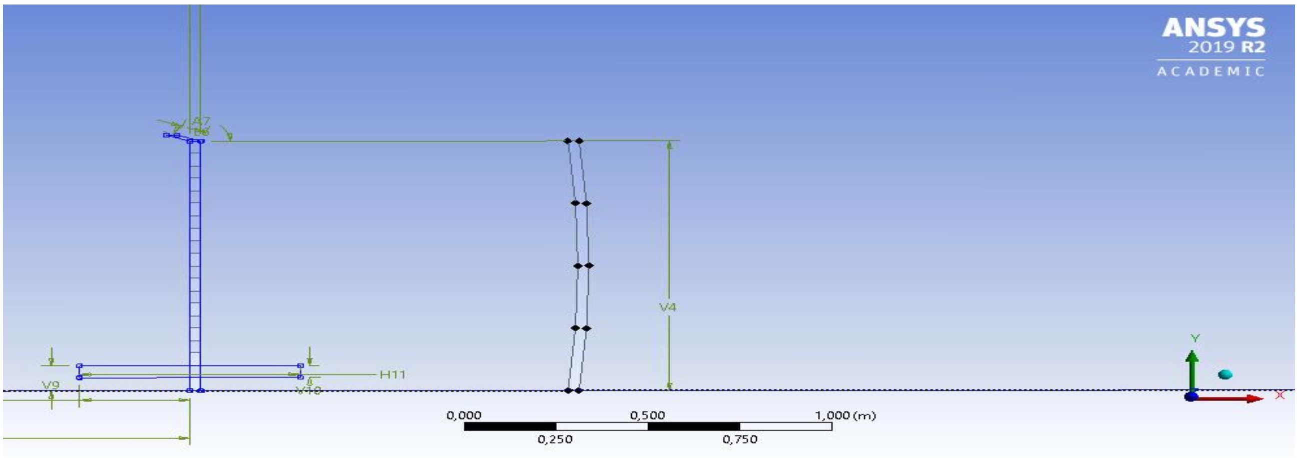

Figure B.53. Porous case 15 geometrical settings

B.14.2. MESH SETTING

The mesh of this case was generated as explained in chapter 2 and the mesh information and quality can be shown in table B.55 and displayed in figure B.54.

Table B.55. Porous case 15 mesh statistics

Nodes	874503
Elements	872221
Mesh Metric Min -Element Quality	3,7374e-002
Mesh Metric Max-Element Quality	0,9997
Mesh Metric Average-Element Quality	0,7197

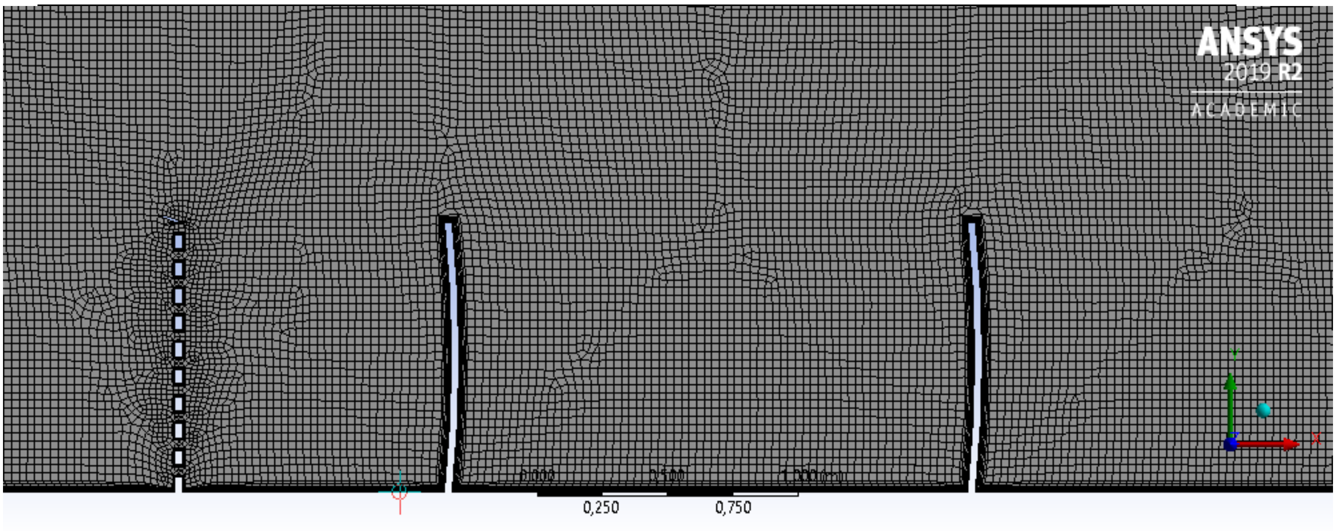

Figure B.54. Porous case 15 mesh settings

B.14.3. ANSYS-FLUENT SIMUALTION RESULTS

The ANSYS FLUENT settings were applied and the following results were obtained after solving for 2610 iterations:

i. Scaled Residuals: Convergence was achieved after 2610 iterations.

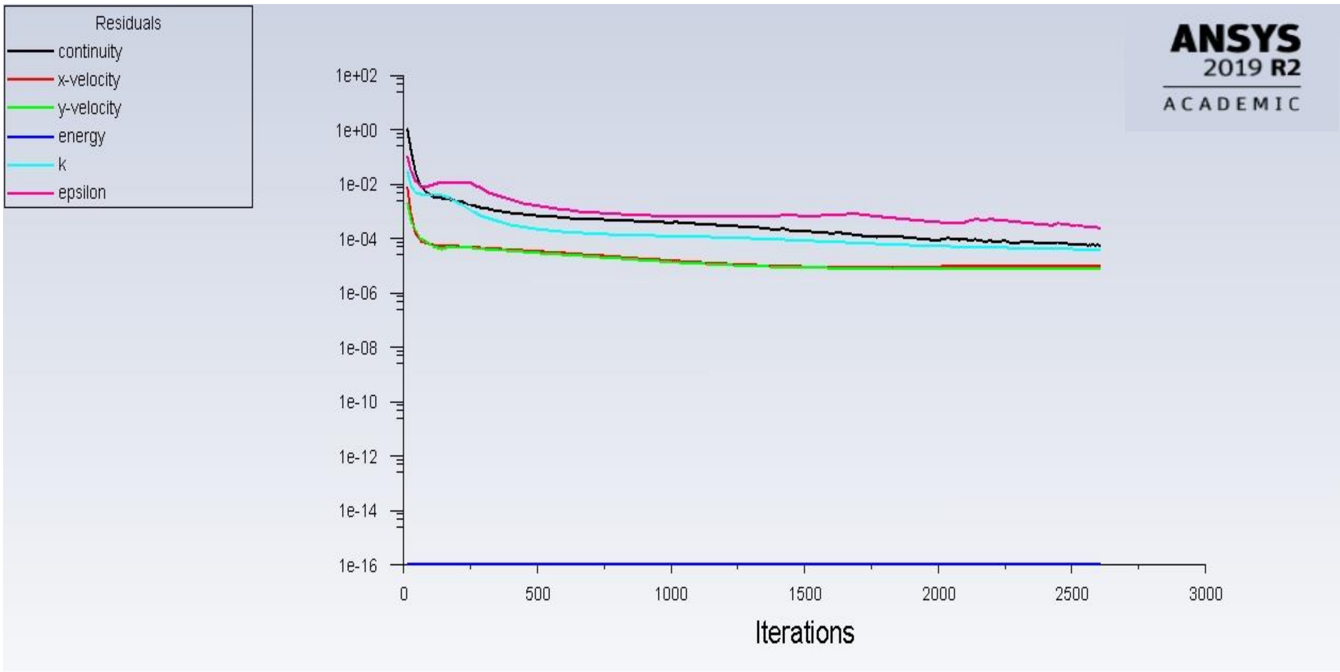

Figure B.55. Porous case 15 scaled residuals

ii. Particles tracked: 1 250 000 particles tracked.

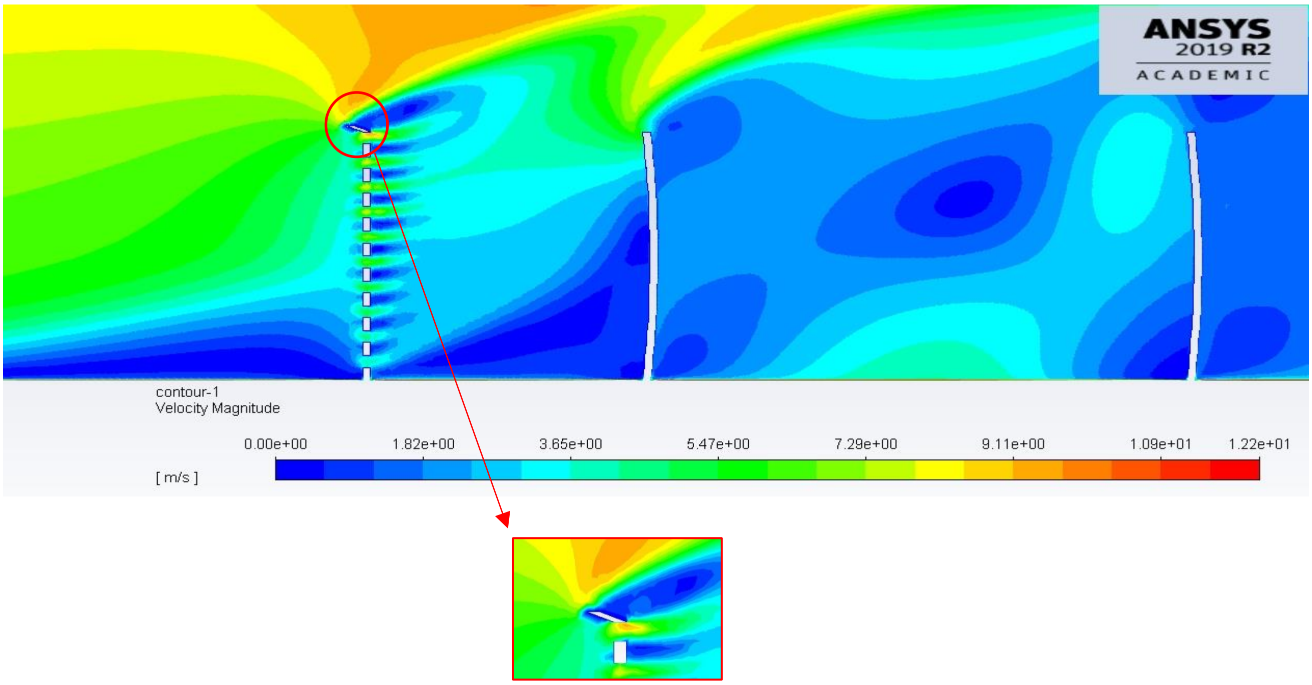

Figure B.56. Porous case 15 velocity contour magnitude

Table B.56. Porous case 15 particle fate

ANSY labelled Wall- ID zone	**Geometric Definition**	**Particles Trapped**	**Particles Escaped**
7	Outlet end side		363232
11	Ground distance of mirror pitch	41667	
12	Ground distance after mirror field	763359	
13	1st mirror front face	318	
14	2nd mirror front face	318	
15	3rd mirror front face	636	
16	4th mirror front face	7316	
17	5th mirror front face	20356	
18	6th mirror front face	28626	
19	Wind Barrier front	16539	
20	Top and back sides of all mirrors	7634	
Soiling [Particles]		57570	

B.15. SIMULATED POROUS CASE 16

B.15.1. GEOMETRICAL SETTINGS

The final porous case assumes values as shown:

Table B.57. Porous case 16 variables

Case Number	l_3 [m]	θ [°]	po [m]
16	0.231303395	159.1078858	0.047195509

In ANSYS the geometrical settings were defined as shown in figure B.57 and table B.58:

Table B.58. Porous case 16 ANSYS geometrical settings

Case Number	L6 [m]	A7 [°]	V10 [m]
16	0.231303395	159.1078858	0.047195509

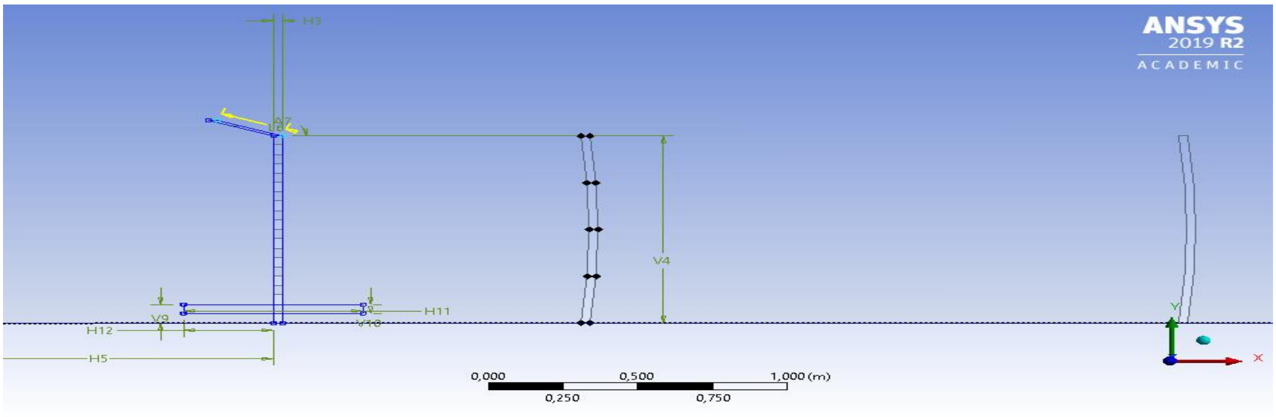

Figure B.57. Porous case 16 geometrical settings

B.15.2. MESH SETTING

The mesh of this case was generated as explained in chapter 2 and the mesh information and quality can be shown in table B.59 and displayed in figure B.58.

Table B.59. Porous case 16 mesh statistics

Nodes	873873
Elements	871506
Mesh Metric Min -Element Quality	3,7374e-002
Mesh Metric Max-Element Quality	0,99947
Mesh Metric Average-Element Quality	0,7203

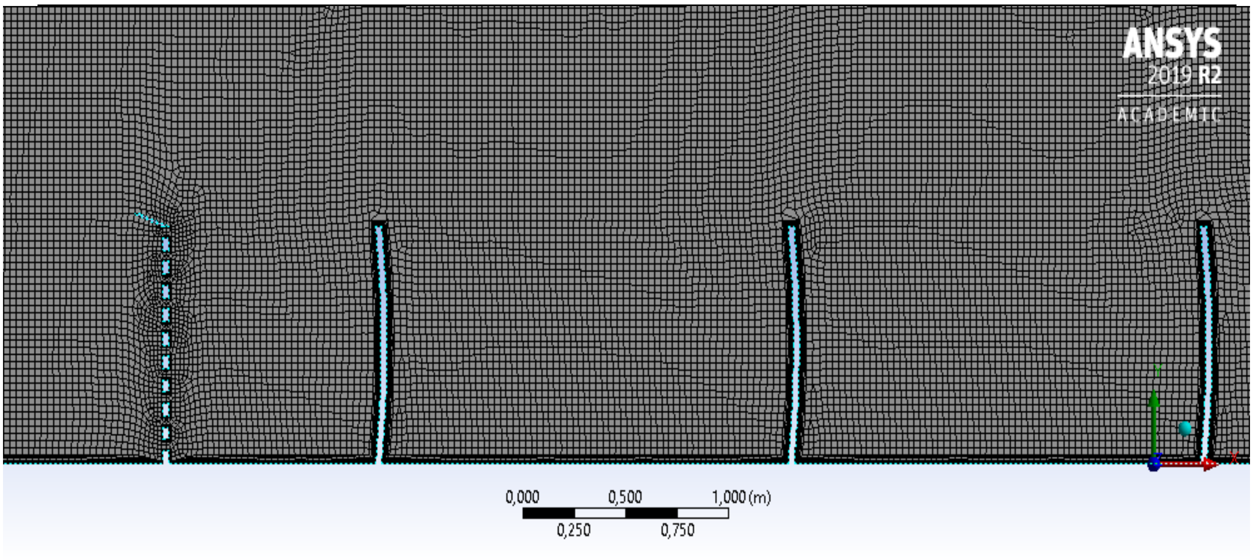

Figure B.58. Porous case 16 mesh settings

B.15.3. ANSYS-FLUENT SIMUALTION RESULTS

The ANSYS FLUENT settings were applied and the following results were obtained after solving for 2500 iterations:

i. Scaled Residuals: Convergence was achieved after 2500 iterations.

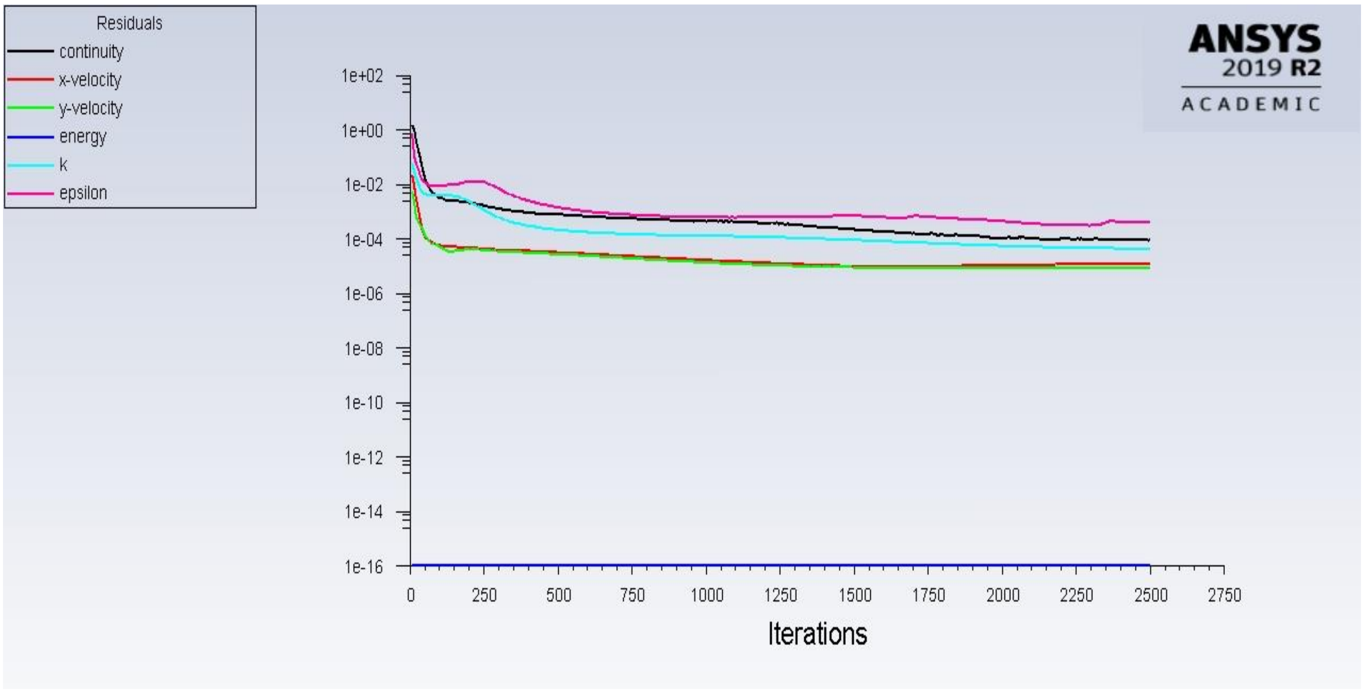

Figure B.59. Porous case 16 scaled residuals

ii. Particles tracked: 1 250 000 particles tracked.

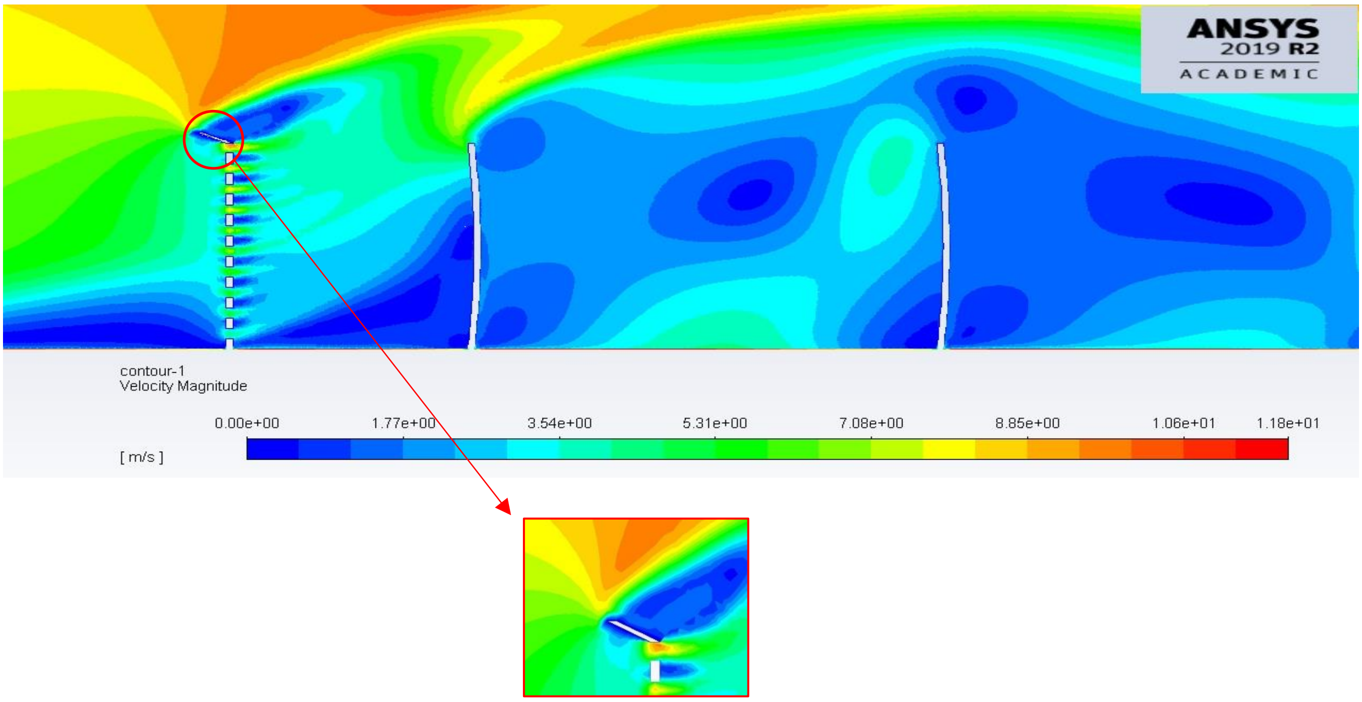

Figure B.60. Porous case 16 velocity contour magnitude

Table B.60. porous case 16 particle fate

ANSY labelled Wall- ID zone	**Geometric Definition**	**Particles Trapped**	**Particles Escaped**
7	Outlet end side		346056
11	Ground distance of mirror pitch	47710	
12	Ground distance after mirror field	779580	
13	1st mirror front face	6	
14	2nd mirror front face	13	
15	3rd mirror front face	636	
16	4th mirror front face	6043	
17	5th mirror front face	17812	
18	6th mirror front face	26718	
19	Wind Barrier front	18766	
20	Top and back sides of all mirrors	6679	
Soiling [Particles]		51228	

B.16. SIMULATED NON-POROUS CASE 1

B.16.1. GEOMETRICAL SETTINGS

The first non-porous case assumes values as shown:

Table B.61. Non-porous case 1 variables

Case Number	l_3 [m]	θ [°]	po [m]
1	0.15	90	0

In ANSYS the geometrical settings were defined as shown in figure 111 and table 74:

Table B.62. Non-porous case 1 ANSYS geometrical settings

Case Number	L6 [m]	A7 [°]	V10 [m]
1	0.15	90	0

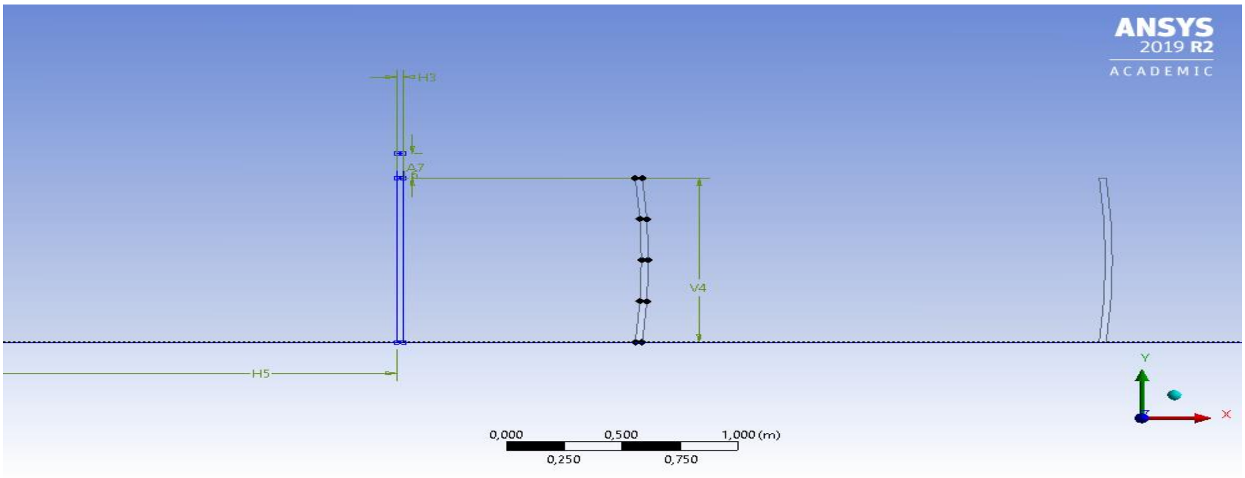

Figure B.61. Non-porous case 1 geometrical settings

B.16.2. MESH SETTING

The mesh of this case was generated as explained in chapter 2 and the mesh information and quality can be shown in table B.63 and displayed in figure B.62.

Table B.63. Non-porous case 1 mesh statistics

Nodes	195750
Elements	194441
Mesh Metric Min -Element Quality	4,3955e-003
Mesh Metric Max-Element Quality	0,99974
Mesh Metric Average-Element Quality	0,78083

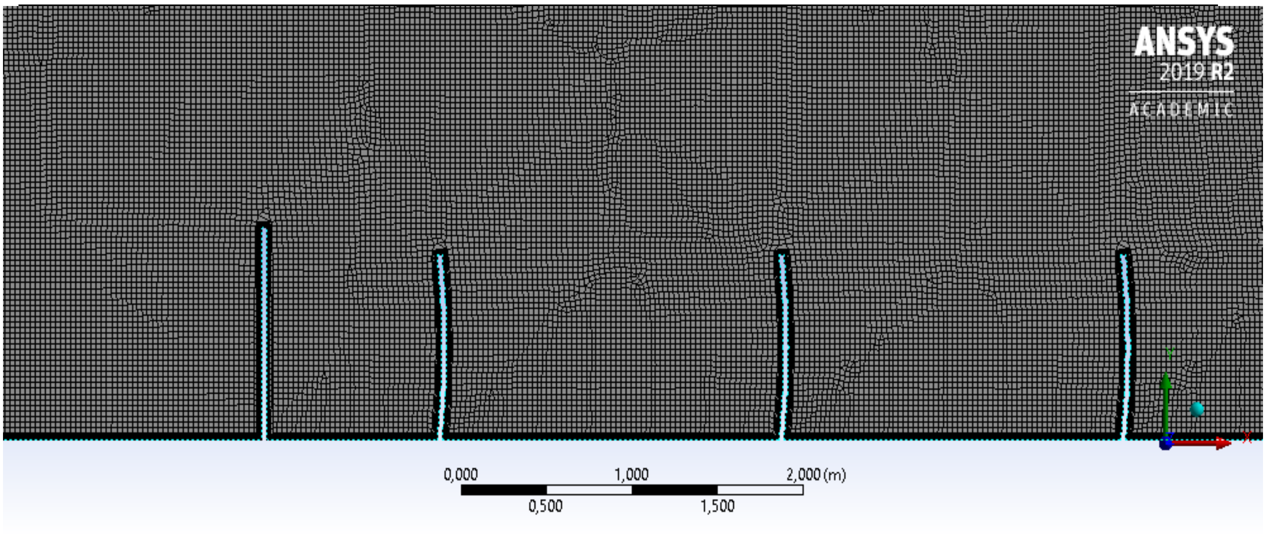

Figure B.62. Non-porous case 1 mesh settings

B.16.3. ANSYS-FLUENT SIMUALTION RESULTS

The ANSYS FLUENT settings were applied and the following results were obtained after solving for 2900 iterations:

i. Scaled Residuals: Convergence was achieved after 2900 iterations.

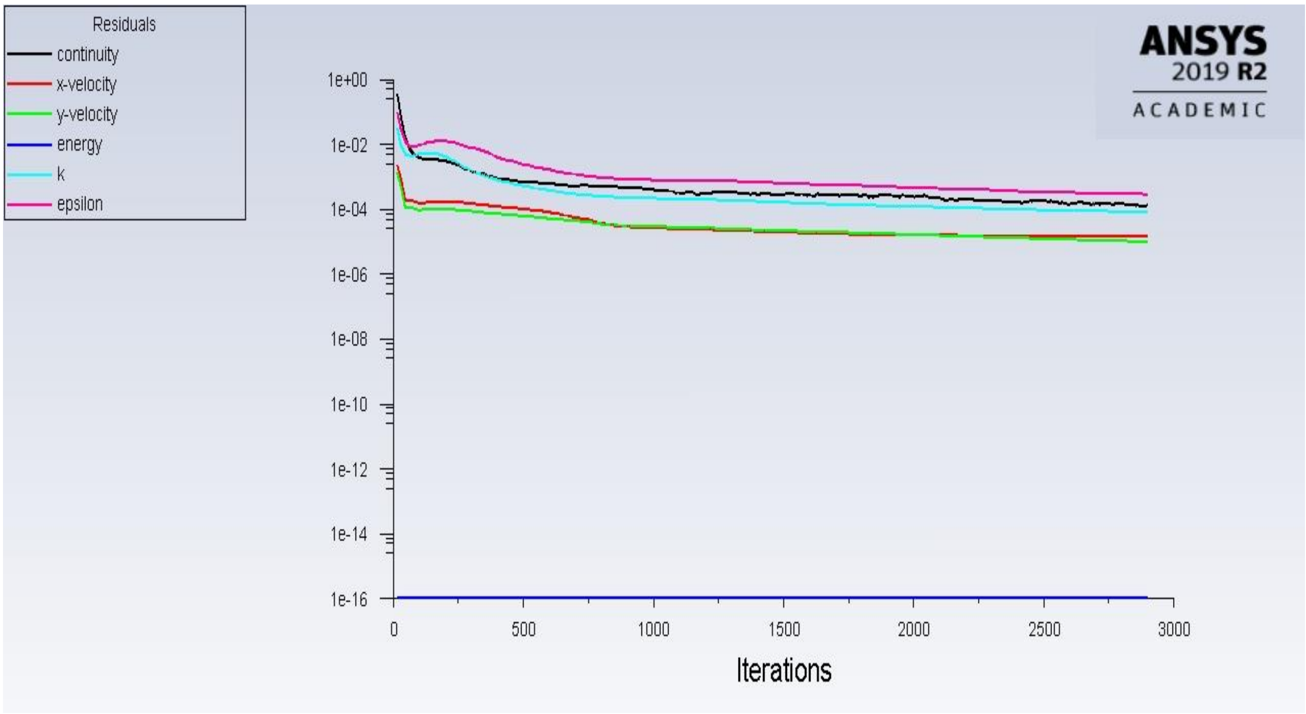

Figure B.63. Non-porous case 1 scaled residuals

ii. Particles tracked: 1 250 000 particles tracked.

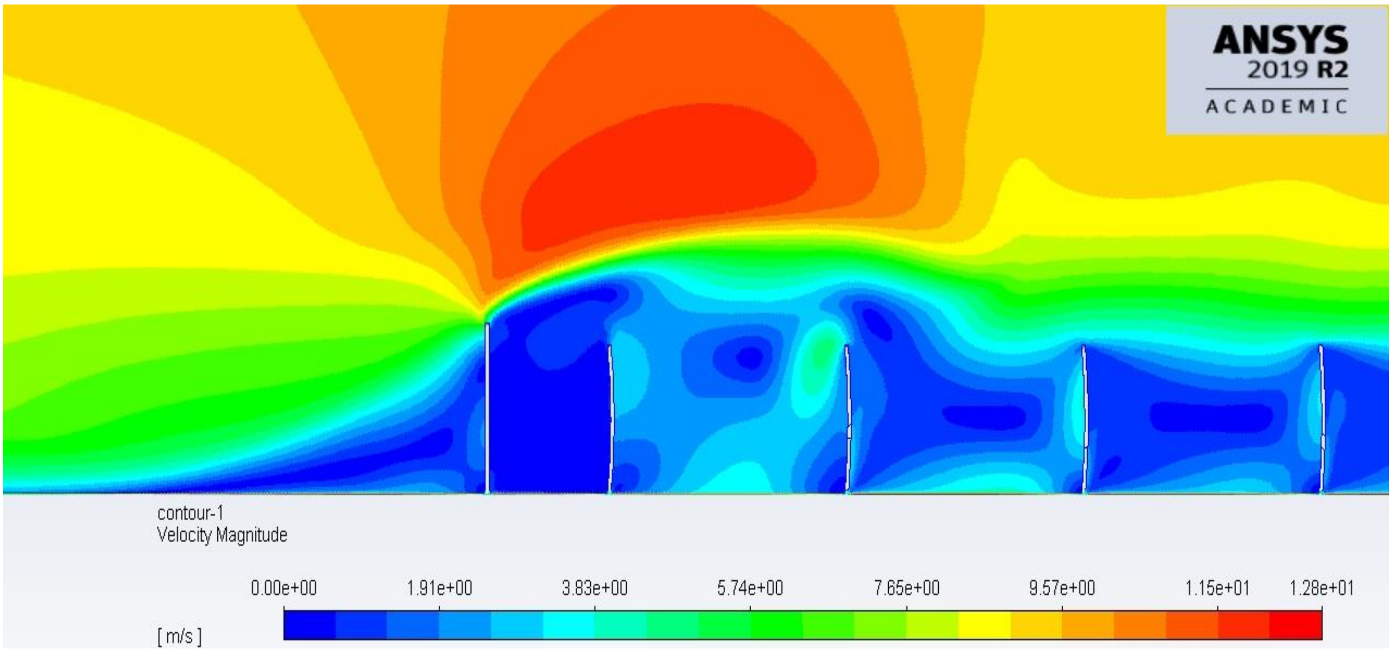

Figure B.64. Non-porous case 1 velocity contour

Table B.64. Non- porous case 1 particle fate

ANSY labelled Wall- ID zone	**Geometric Definition**	**Particles Trapped**	**Particles Escaped**
7	Outlet end side		349873
11	Ground distance of mirror pitch	65840	
12	Ground distance after mirror field	743639	
13	1st mirror front face	318	
14	2nd mirror front face	954	
15	3rd mirror front face	6361	
16	4th mirror front face	18130	
17	5th mirror front face	25763	
18	6th mirror front face	27036	
19	Wind Barrier front	954	
20	Top and back sides of all mirrors	10496	
Soiling [Particles]		78562	

B.17. SIMULATED NON-POROUS CASE 2

B.17.1. GEOMETRICAL SETTINGS

The second non-porous case assumes values as shown:

Table B.65. Non-porous case 1 variables

Case Number	l_3 [m]	θ [°]	po [m]
2	0.05	90	0

In ANSYS the geometrical settings were defined as shown in figure B.65 and table B.66:

Table B.66. Non-porous case 1 ANSYS geometrical settings

Case Number	L6 [m]	A7 [°]	V10 [m]
2	0.05	90	0

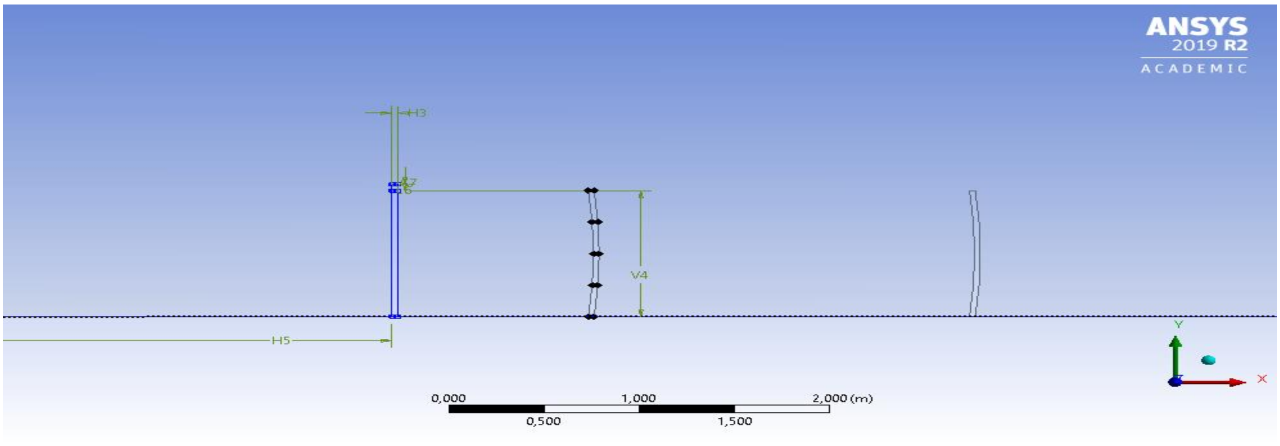

Figure B.65. Non-porous case 2 geometrical settings

B.17.2. MESH SETTING

The mesh of this case was generated as explained in chapter 2 and the mesh information and quality can be shown in table B.67 and displayed in figure B.66.

Table B.67. Non-porous case 1 mesh statistics

Nodes	873636
Elements	871333
Mesh Metric Min -Element Quality	3,7374e-002
Mesh Metric Max-Element Quality	0,99957
Mesh Metric Average-Element Quality	0,71888

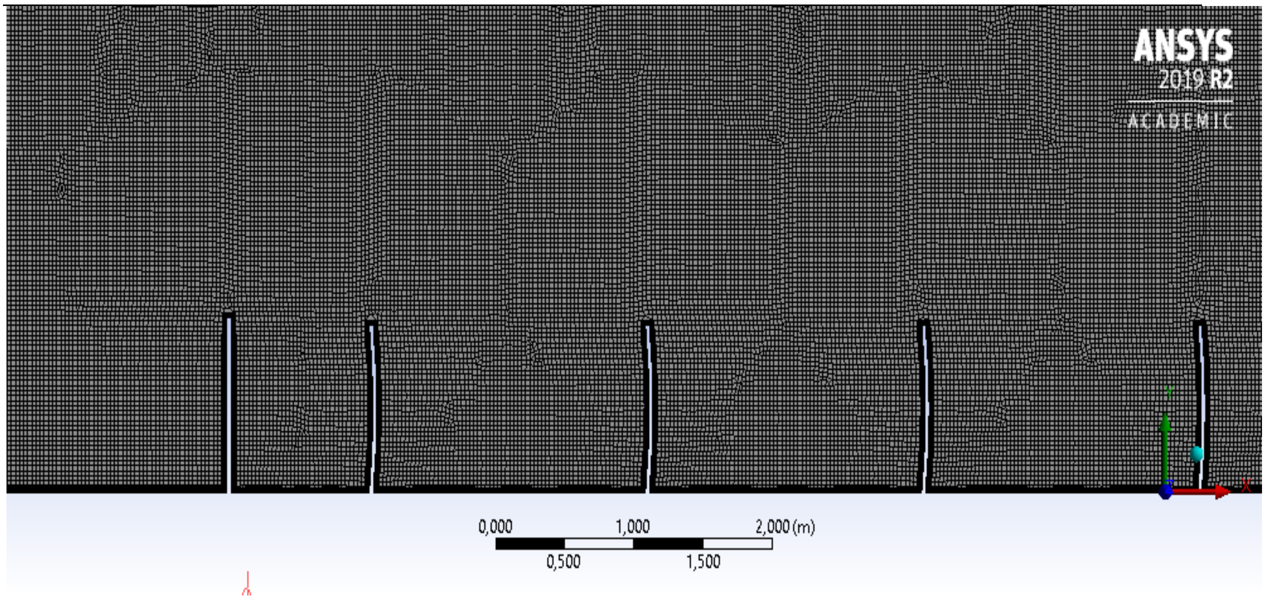

Figure B.66. Non-porous case 2 mesh settings

B.17.3. ANSYS-FLUENT SIMUALTION RESULTS

The ANSYS FLUENT settings were applied and the following results were obtained after solving for 2500 iterations:

i. Scaled Residuals: Convergence was achieved after 2500 iterations.

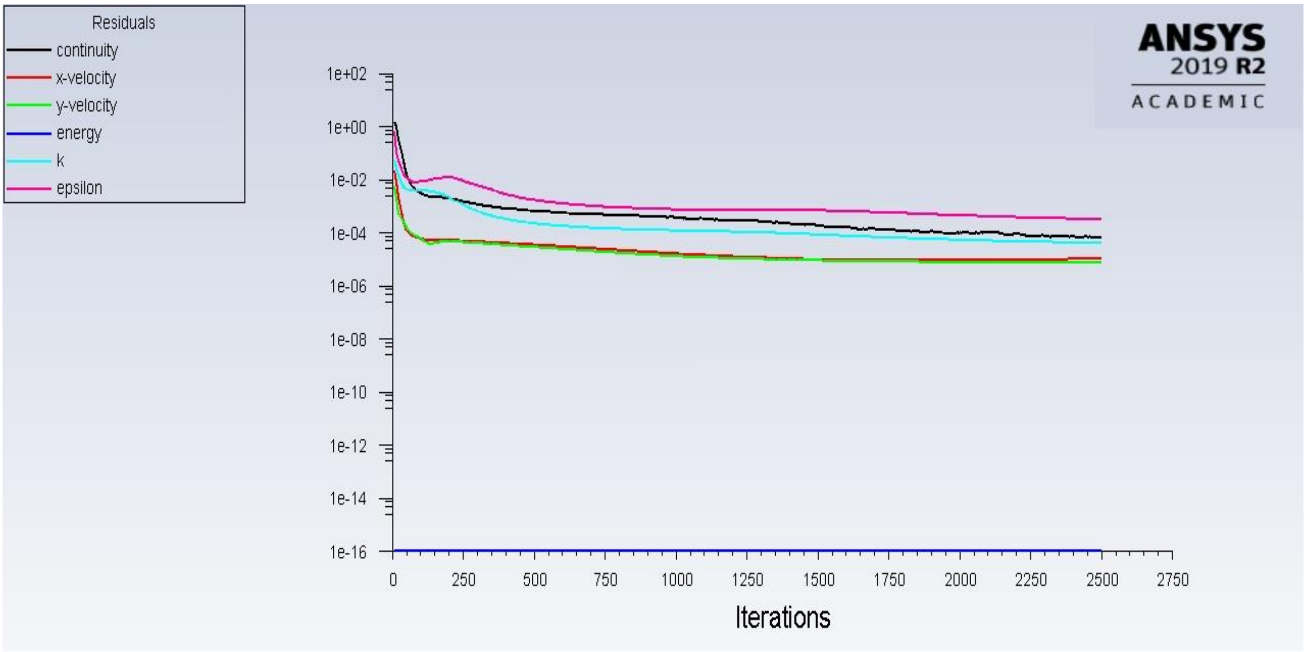

Figure B.67. Non-porous case 1 scaled residuals

ii. Particles tracked: 1 250 000 particles tracked.

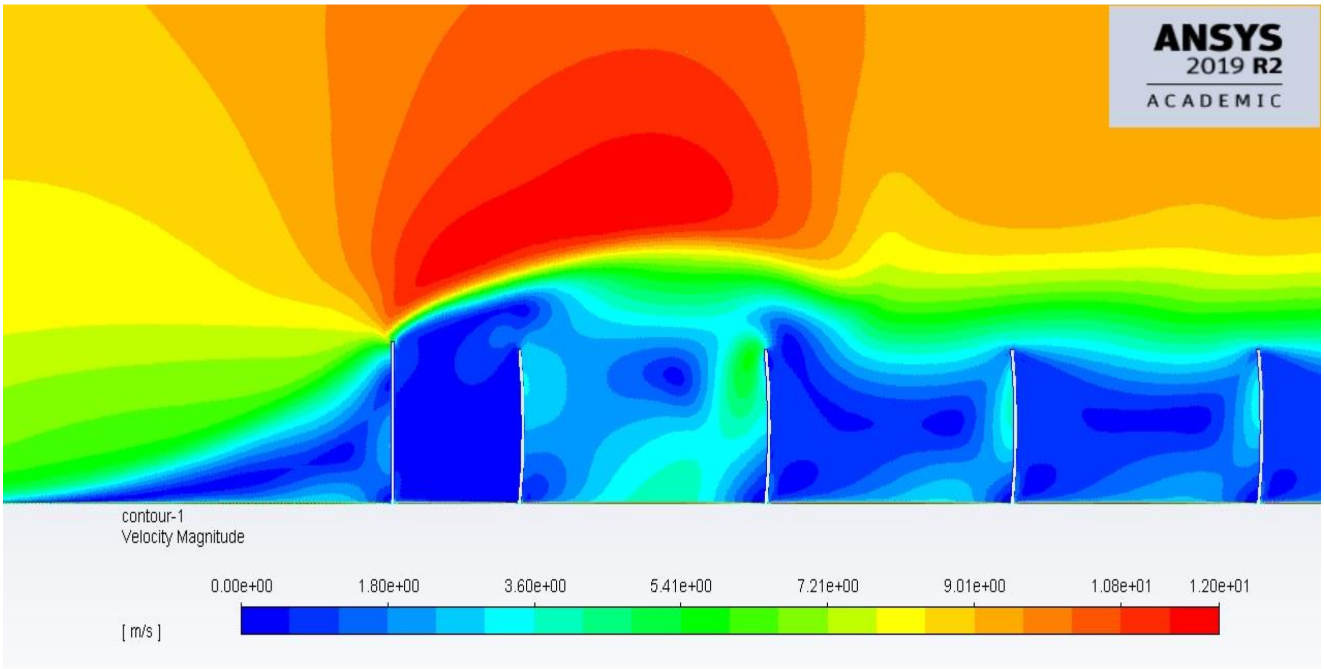

Figure B.68. Non-porous case 2 velocity contour

Table B.68. Non- porous case 2 particle fate

ANSY labelled Wall- ID zone	**Geometric Definition**	**Particles Trapped**	**Particles Escaped**
7	Outlet end side		349237
11	Ground distance of mirror pitch	67112	
12	Ground distance after mirror field	746183	
13	1st mirror front face	138	
14	2nd mirror front face	1272	
15	3rd mirror front face	9542	
16	4th mirror front face	17176	
17	5th mirror front face	24173	
18	6th mirror front face	22583	
19	Wind Barrier front	636	
20	Top and back sides of all mirrors	12405	
Soiling [Particles]		74884	

B.18. SIMULATED NON-POROUS CASE 3

B.18.1. GEOMETRICAL SETTINGS

According to table 8, the third non-porous case assumes values as shown:

Table B.69. Non-porous case 3 variables

Case Number	**l_3 [m]**	**θ [°]**	**po [m]**
3	0.25	90	0

In ANSYS the geometrical settings were defined as shown in figure B.69 and table B.70:

Table B.70. Non-porous case 3 ANSYS geometrical settings

Case Number	**L6 [m]**	**A7 [°]**	**V10 [m]**
3	0.25	90	0

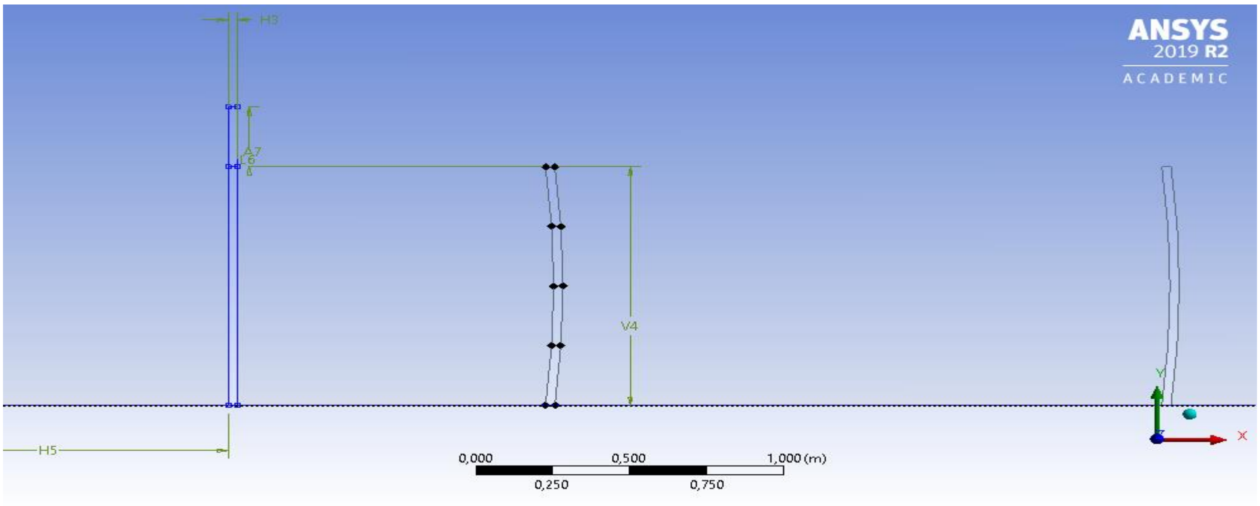

Figure B.69. Non-porous case 3 geometrical settings

B.18.2. MESH SETTING

The mesh of this case was generated as explained in chapter 2 and the mesh information and quality can be shown in table B.71 and displayed in figure B.70.

Table B.71. Non-porous case 3 mesh statistics

Nodes	873854
Elements	871533
Mesh Metric Min -Element Quality	3,7374e-002
Mesh Metric Max-Element Quality	0,99947
Mesh Metric Average-Element Quality	0,7195

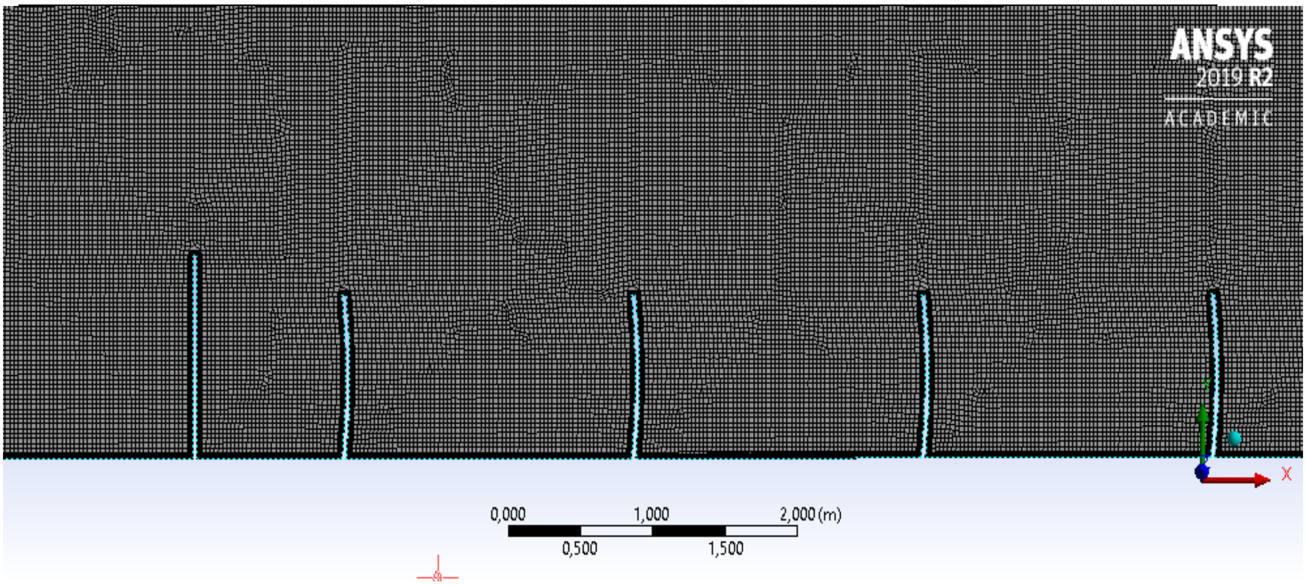

Figure B.70. Non-porous case 3 mesh settings

B.18.3. ANSYS-FLUENT SIMUALTION RESULTS

The ANSYS FLUENT settings were applied and the following results were obtained after solving for 2600 iterations:

i. Scaled Residuals: Convergence was achieved after 2600 iterations

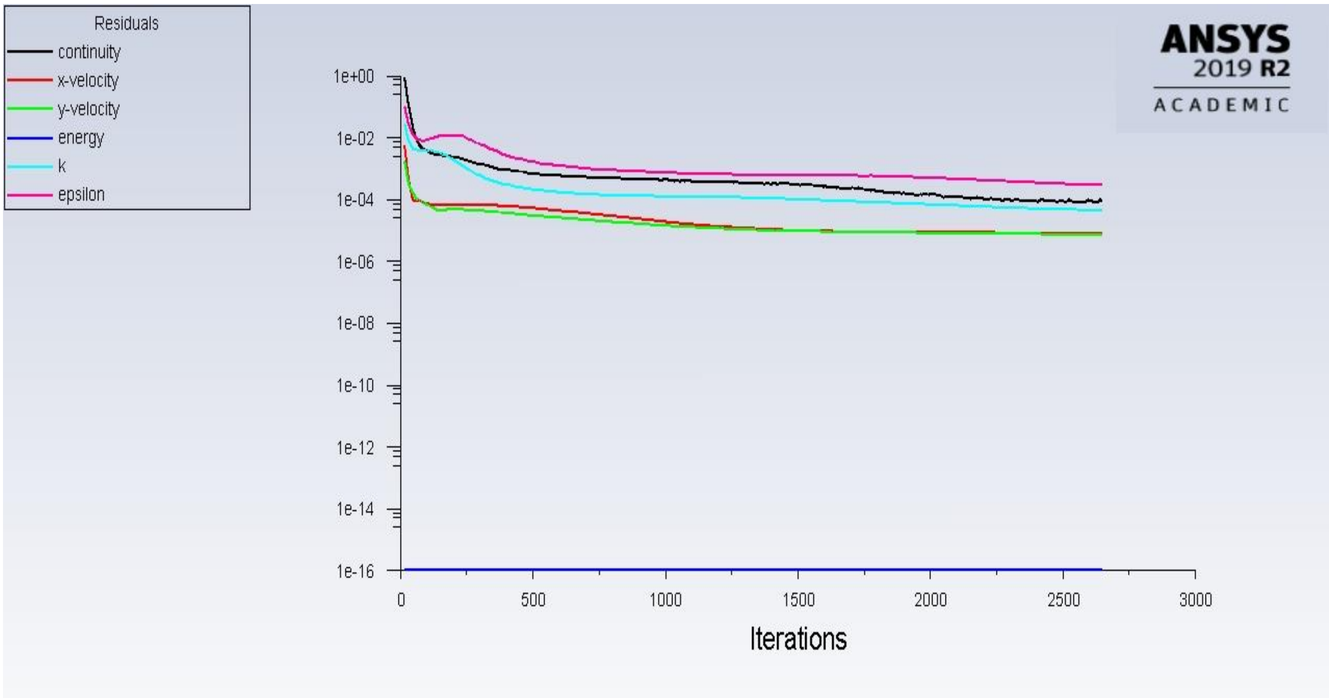

Figure B.71. Non-porous case 3 scaled residuals

ii. Particles tracked: 1 250 000 particles tracked.

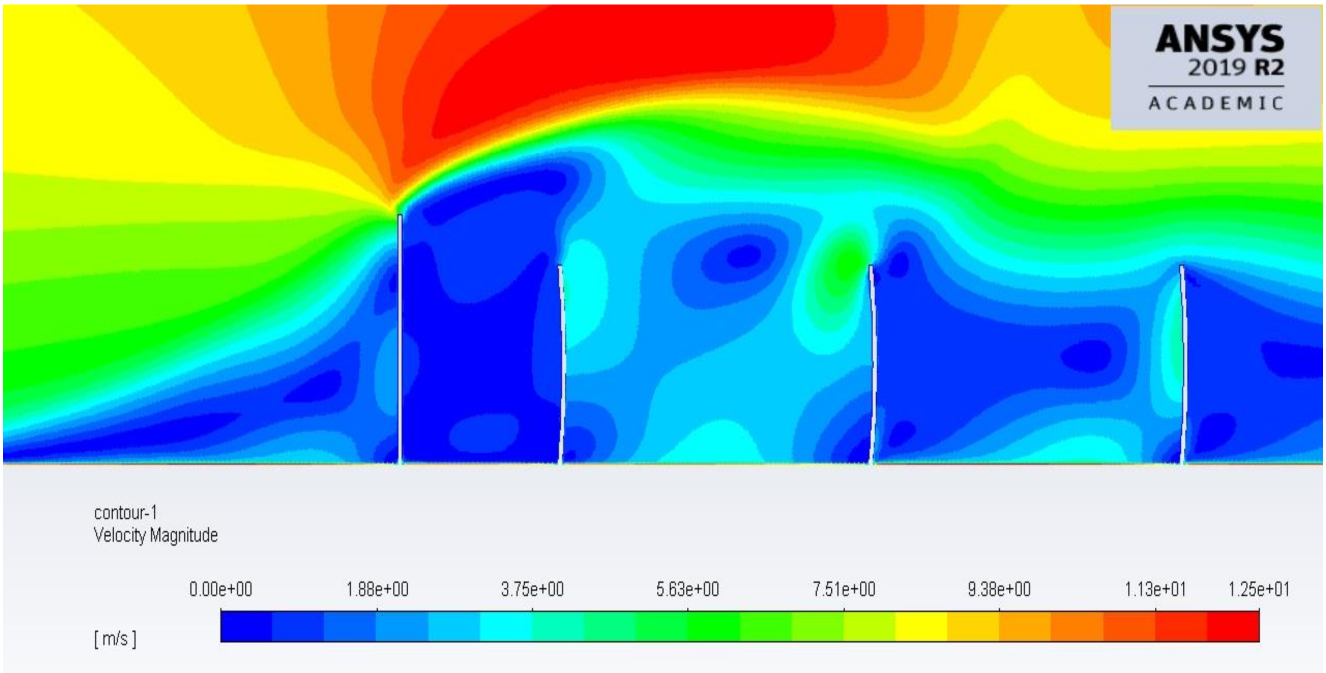

Figure B.72. Non-porous case 3 velocity contour

Table B.72. Non-porous case 3 particle fate

ANSY labelled Wall- ID zone	**Geometric Definition**	**Particles Trapped**	**Particles Escaped**
7	Outlet end side		356234
11	Ground distance of mirror pitch	65522	
12	Ground distance after mirror field	736959	
13	1st mirror front face	318	
14	2nd mirror front face	1272	
15	3rd mirror front face	10496	
16	4th mirror front face	15585	
17	5th mirror front face	21629	
18	6th mirror front face	25127	
19	Wind Barrier front	3181	
20	Top and back sides of all mirrors	13677	
Soiling [Particles]		74427	

B.19. SIMULATED NON-POROUS CASE 4

B.19.1. GEOMETRICAL SETTINGS

The fourth non-porous case assumes values as shown:

Table B.73. Non-porous case 4 variables

Case Number	**l_3 [m]**	**θ [°]**	**po [m]**
4	0.15	5	0

In ANSYS the geometrical settings were defined as shown in figure B.73 and table B.74:

Table B.74. Non-porous case 4 ANSYS geometrical settings

Case Number	**L6 [m]**	**A7 [°]**	**V10 [m]**
4	0.15	5	0

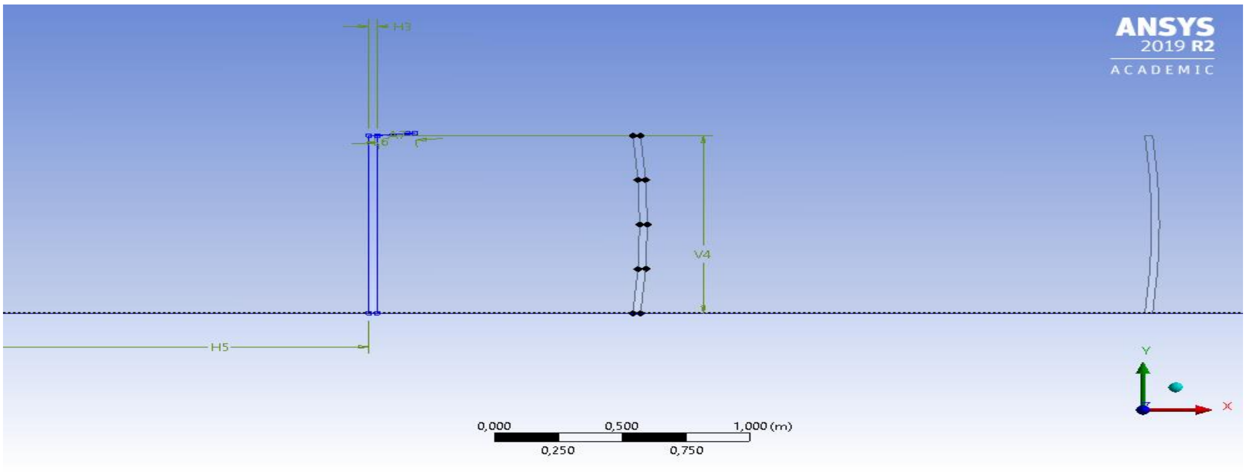

Figure B.73. Non-porous case 4 geometrical settings

B.19.2. MESH SETTING

The mesh of this case was generated as explained in chapter 2 and the mesh information and quality can be shown in table B.75 and displayed in figure B.74.

Table B.75. Non-porous case 3 mesh statistics

Nodes	873854
Elements	871533
Mesh Metric Min -Element Quality	3,7374e-002
Mesh Metric Max-Element Quality	0,99947
Mesh Metric Average-Element Quality	0,7195

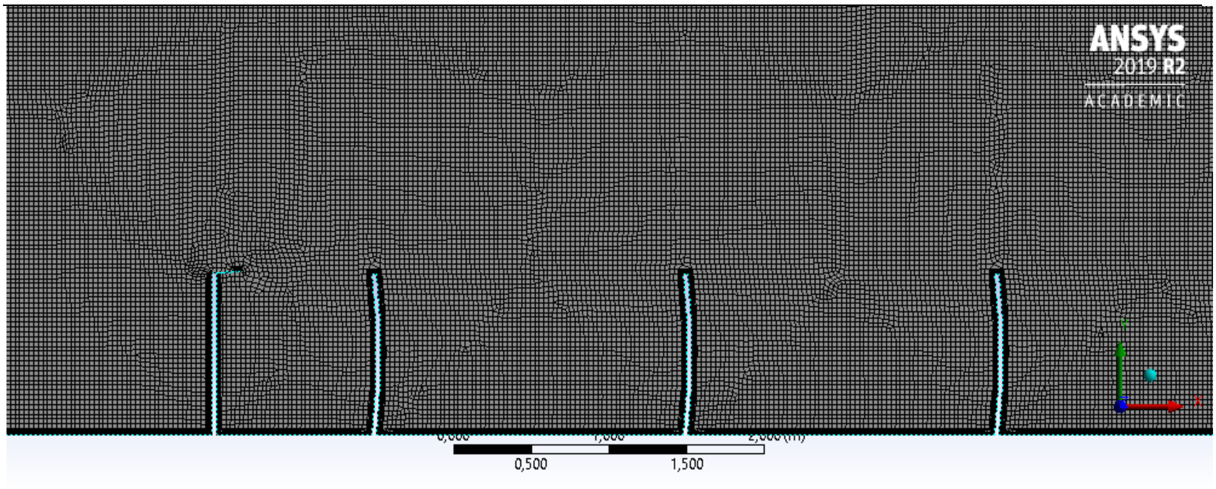

Figure B.74. Non-porous case 4 mesh settings

B.19.3. ANSYS-FLUENT SIMUALTION RESULTS

The ANSYS FLUENT settings were applied and the following results were obtained after solving for 2500 iterations:

i. Scaled Residuals: Convergence was achieved after 2500 iterations

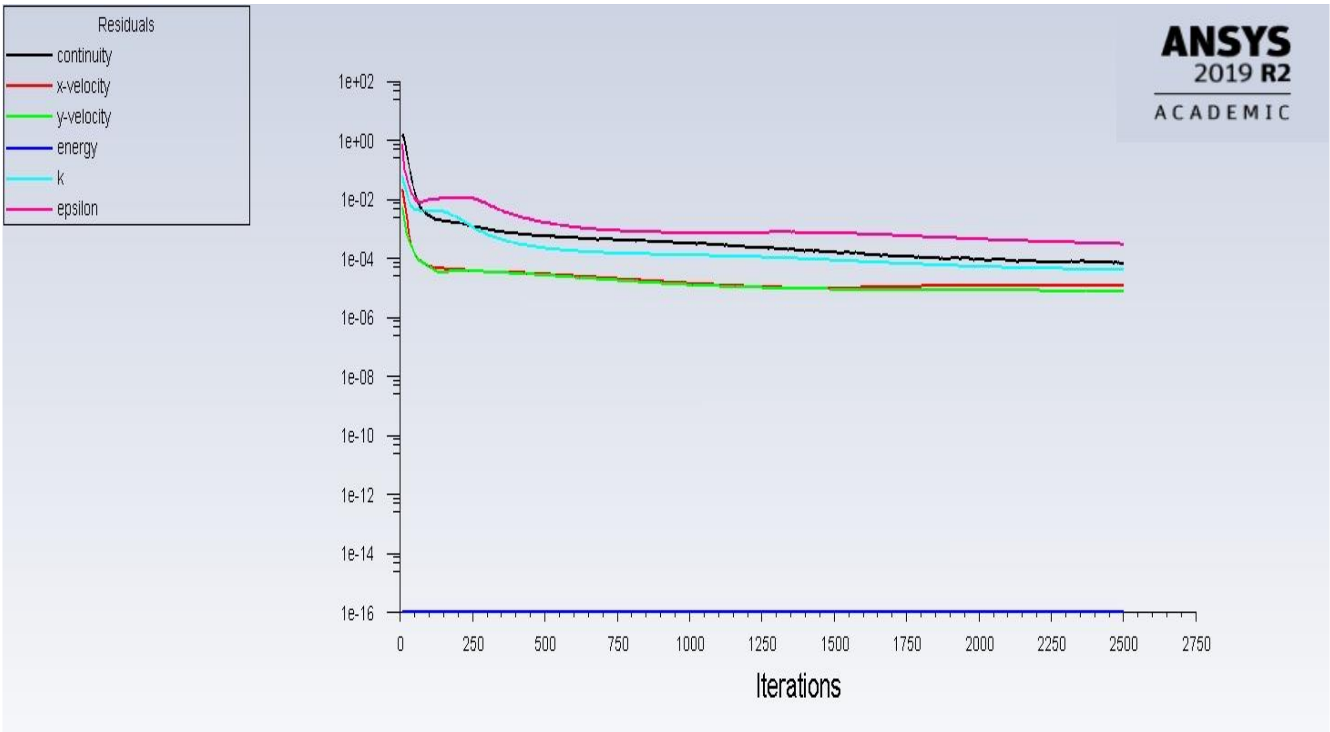

Figure B.75. Non-porous case 4 scaled residuals

iii. Particles tracked: 1 250 000 particles tracked.

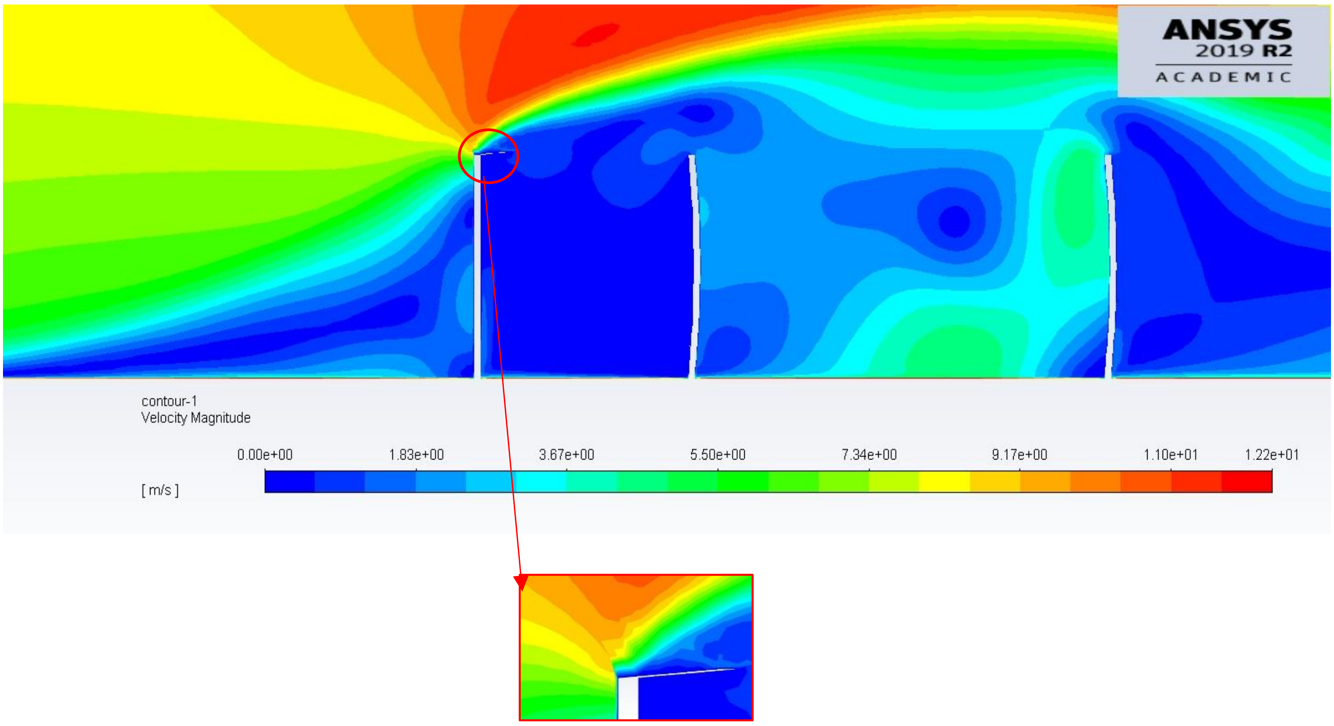

Figure B.76. Non-porous case 4 velocity contour

Table B.76. Non- porous case 3 particle fate

ANSY labelled Wall- ID zone	Geometric Definition	Particles Trapped	Particles Escaped
7	Outlet end side		354644
11	Ground distance of mirror pitch	64249	
12	Ground distance after mirror field	740458	
13	1st mirror front face	636	
14	2nd mirror front face	1908	
15	3rd mirror front face	6361	
16	4th mirror front face	11768	
17	5th mirror front face	24491	
18	6th mirror front face	33079	
19	Wind Barrier front	636	
20	Top and back sides of all mirrors	12405	
Soiling [Particles]		78244	

B.20. SIMULATED NON-POROUS CASE 5

B.20.1. GEOMETRICAL SETTINGS

According to table 8, the fifth non-porous case assumes values as shown:

Table B.77. Non-porous case 5 variables

Case Number	**l_3 [m]**	**θ [°]**	**po [m]**
5	0.15	175	0

In ANSYS the geometrical settings were defined as shown in figure B.77 and table B.78:

Table B.78. Non-porous case 5 ANSYS geometrical settings

Case Number	**L6 [m]**	**A7 [°]**	**V10 [m]**
5	0.15	175	0

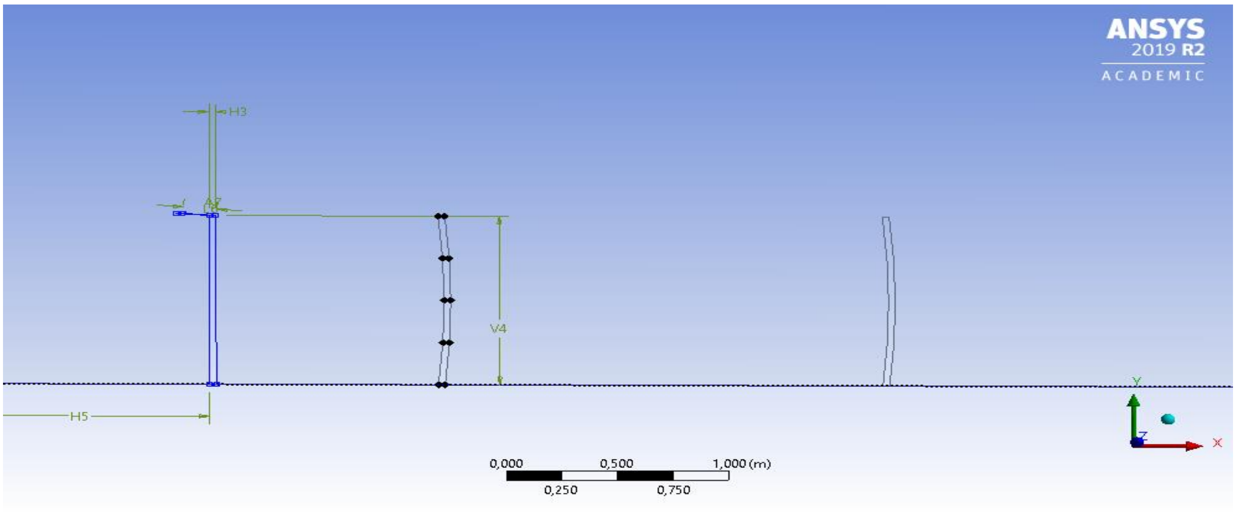

Figure B.77. Non-porous case 5 geometrical settings

B.20.2. MESH SETTING

The mesh of this case was generated as explained in chapter 2 and the mesh information and quality can be shown in table B.79 and displayed in figure B.78.

Table B.79. Non-porous case 5 mesh statistics

Nodes	874158
Elements	871827
Mesh Metric Min -Element Quality	3,7374e-002
Mesh Metric Max-Element Quality	0,99977
Mesh Metric Average-Element Quality	0,72029

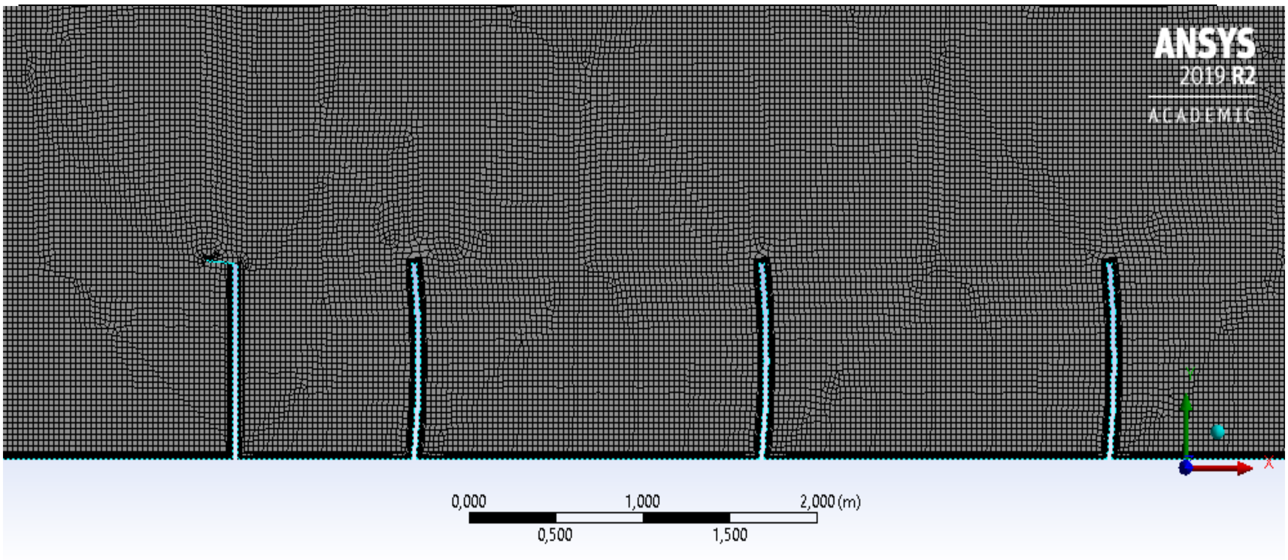

Figure B.78. Non-porous case 5 mesh settings

B.20.3. ANSYS-FLUENT SIMUALTION RESULTS

The ANSYS FLUENT settings were applied and the following results were obtained after solving for 2500 iterations:

i. Scaled Residuals: Convergence was achieved after 2500 iterations.

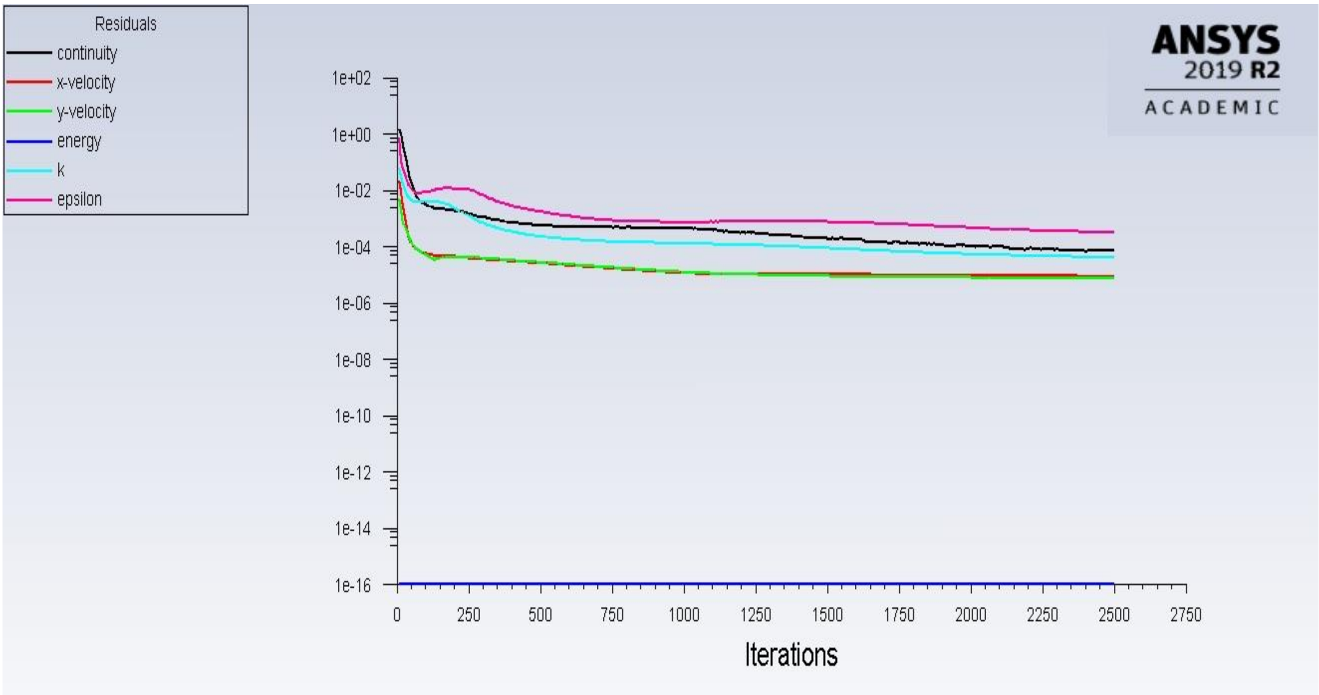

Figure B.79. Non-porous case 5 scaled residuals

ii. Particles tracked: 1 250 000 particles tracked.

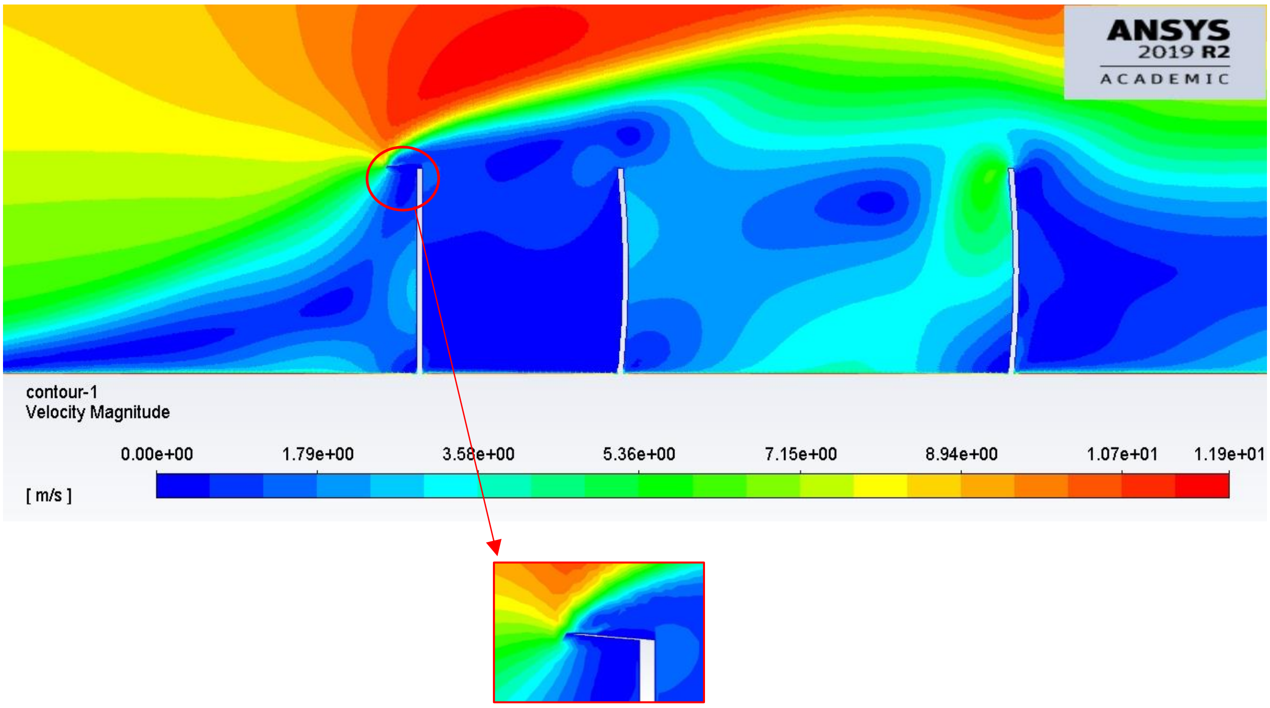

Figure B.80. Non-porous case 5 velocity contour

Table B.80. Non-porous case 5 particle fate

ANSY labelled Wall- ID zone	Geometric Definition	Particles Trapped	Particles Escaped
7	Outlet end side		343830
11	Ground distance of mirror pitch	68702	
12	Ground distance after mirror field	748410	
13	1st mirror front face	48	
14	2nd mirror front face	2863	
15	3rd mirror front face	8906	
16	4th mirror front face	16221	
17	5th mirror front face	22583	
18	6th mirror front face	26081	
19	Wind Barrier front	318	
20	Top and back sides of all mirrors	11768	
Soiling [Particles]		76702	

B.21. SIMULATED NON-POROUS CASE 6

B.21.1. GEOMETRICAL SETTINGS

The sixth non-porous case assumes values as shown:

Table B.81. Non-porous case 6 variables

Case Number	**l_3 [m]**	**θ [°]**	**po [m]**
6	0.05	5	0

In ANSYS the geometrical settings were defined as shown in figure B.81 and table B.82:

Table B.82. Non-porous case 6 ANSYS geometrical settings

Case Number	**L6 [m]**	**A7 [°]**	**V10 [m]**
6	0.05	5	0

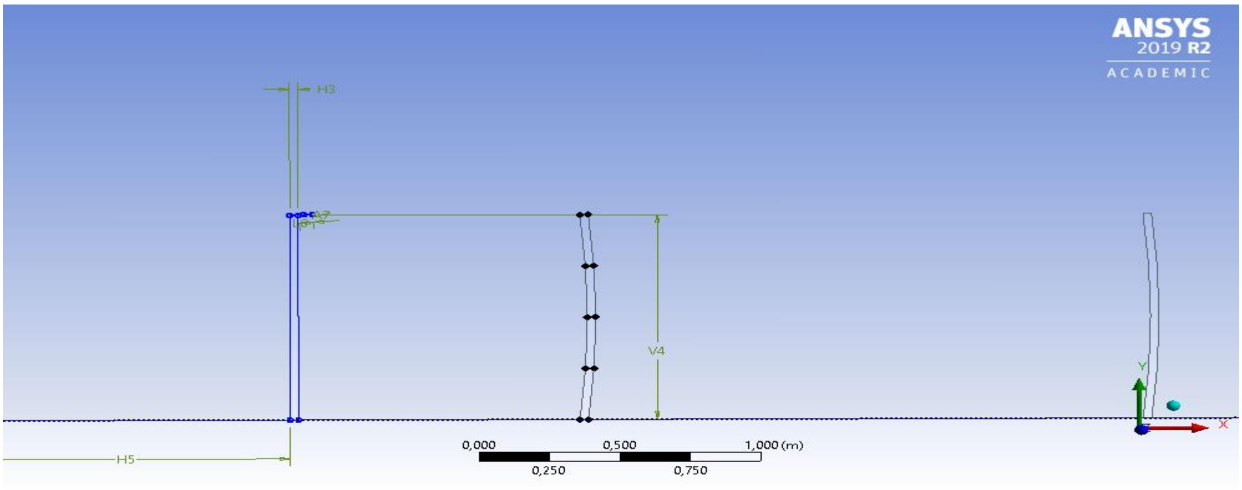

Figure B.81. Non-Porous Case 6 Geometrical Settings

B.21.2. MESH SETTING

The mesh of this case was generated as explained in chapter 2 and the mesh information and quality can be shown in table B.83 and displayed in figure B.82.

Table B.83. Non-porous case 6 mesh statistics

Nodes	873703
Elements	871384
Mesh Metric Min -Element Quality	3,7374e-002
Mesh Metric Max-Element Quality	0,99962
Mesh Metric Average-Element Quality	0,71932

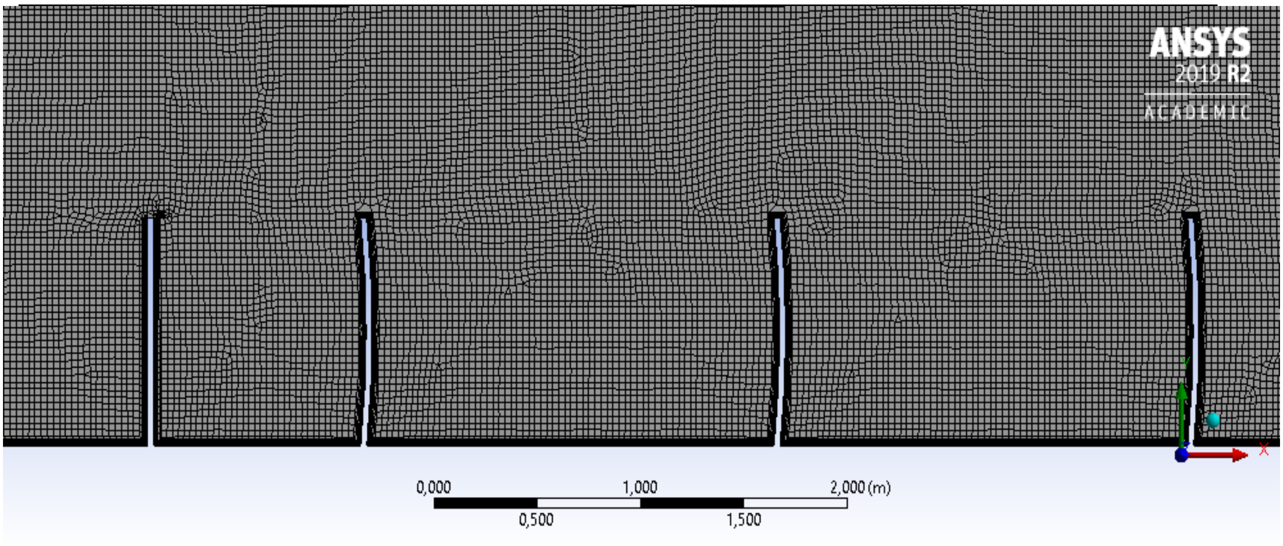

Figure B.82. Non-porous case 5 mesh settings

B.21.3. ANSYS-FLUENT SIMUALTION RESULTS

The ANSYS FLUENT settings were applied and the following results were obtained after solving for 2500 iterations:

i. Scaled Residuals: Convergence was achieved after 2500 iterations.

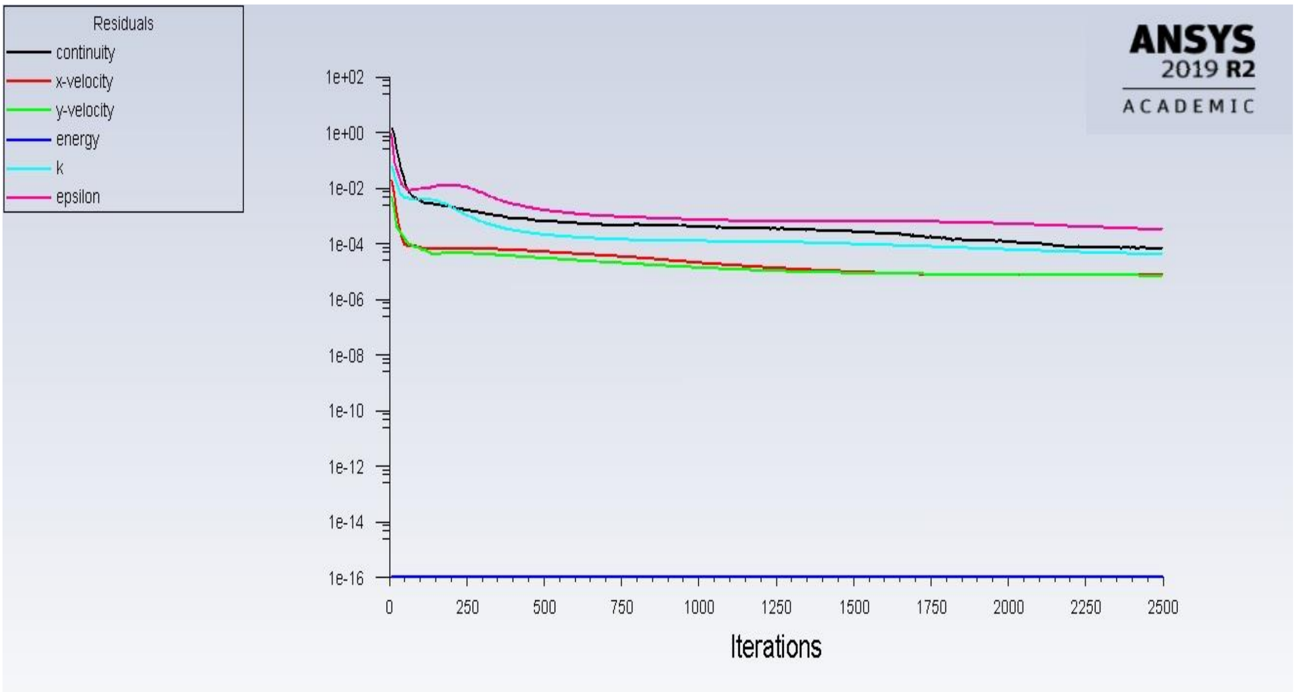

Figure B.83. Non-Porous Case 5 Scaled Residuals

ii. Particles tracked: 1 250 000 particles tracked.

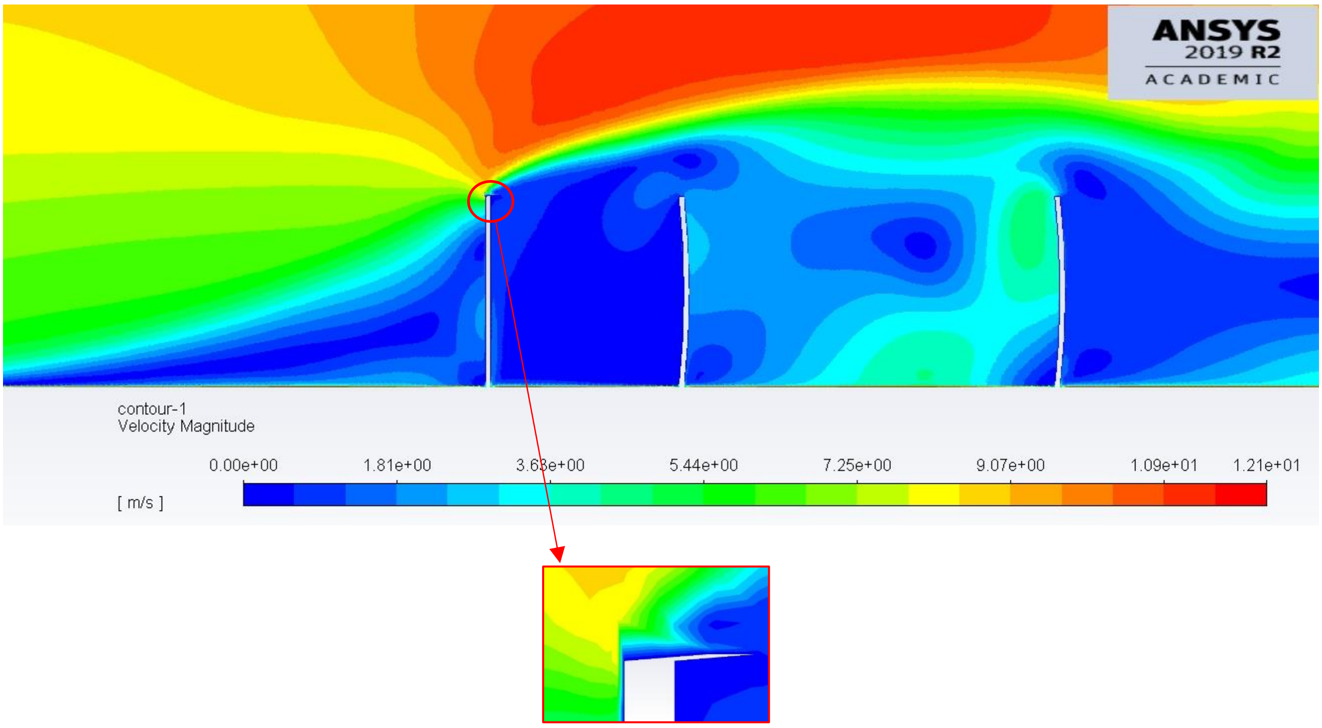

Figure B.84. Non-porous case 6 velocity contour

Table B.84. Non- porous case 6 particle fate

ANSY labelled Wall- ID zone	**Geometric Definition**	**Particles Trapped**	**Particles Escaped**
7	Outlet end side		343830
11	Ground distance of mirror pitch	68066	
12	Ground distance after mirror field	754453	
13	1st mirror front face	318	
14	2nd mirror front face	954	
15	3rd mirror front face	8906	
16	4th mirror front face	16221	
17	5th mirror front face	26081	
18	6th mirror front face	29898	
19	Wind Barrier front	318	
20	Top and back sides of all mirrors	17494	
Soiling [Particles]		82379	

B.22. SIMULATED NON-POROUS CASE 7

B.22.1. GEOMETRICAL SETTINGS

The seventh non-porous case assumes values as shown:

Table B.85. Non-porous case 7 variables

Case Number	l_3 [m]	θ [°]	po [m]
7	0.25	5	0

In ANSYS the geometrical settings were defined as shown in figure B.85 and table B.86:

Table B.86. Non-porous case 7 ansys geometrical settings

Case Number	L6 [m]	A7 [°]	V10 [m]
7	0.25	5	0

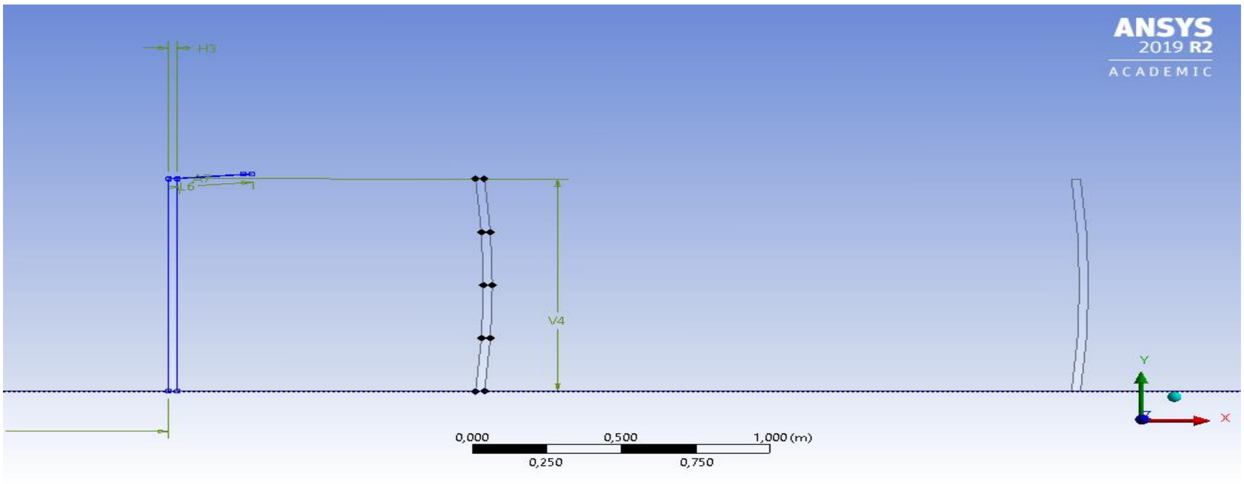

Figure B.85. Non-porous case 7 geometrical settings

B.22.2. MESH SETTING

The mesh of this case was generated as explained in chapter 2 and the mesh information and quality can be shown in table B.87 and displayed in figure B.86.

Table B.87. Non-porous case 7 mesh statistics

Nodes	873299
Elements	870991
Mesh Metric Min -Element Quality	3,7374e-002
Mesh Metric Max-Element Quality	0,9997
Mesh Metric Average-Element Quality	0,71877

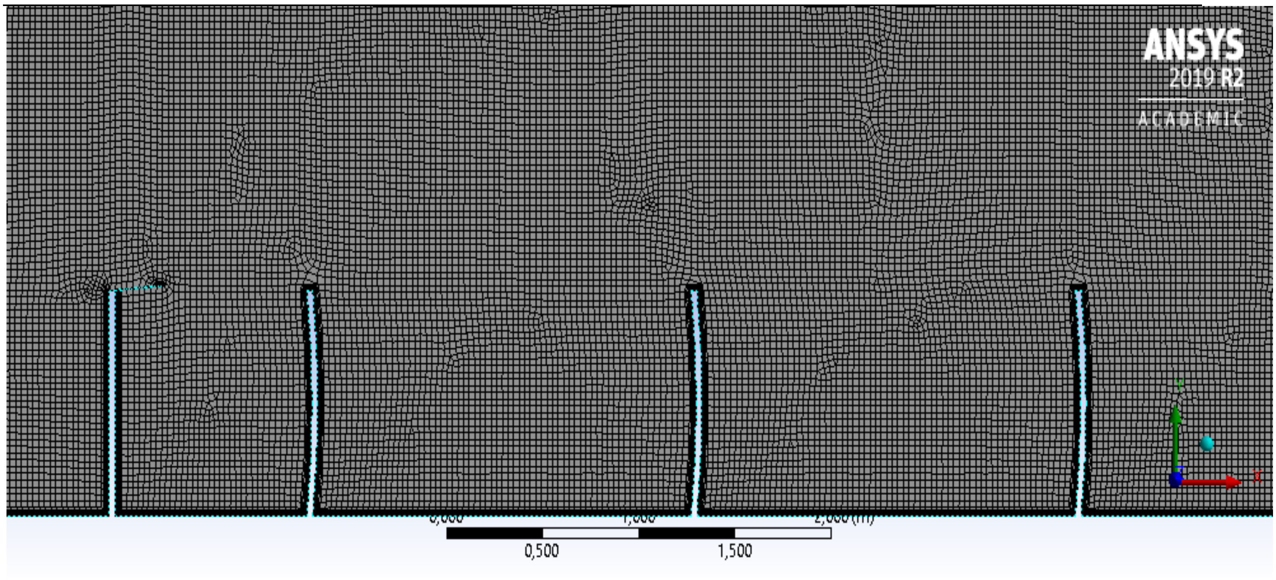

Figure B.86. Non-porous case 7 mesh settings

B.22.3. ANSYS-FLUENT SIMUALTION RESULTS

The ANSYS FLUENT settings were applied and the following results were obtained after solving for 2500 iterations:

i. Scaled Residuals: Convergence was achieved after 2500 iterations.

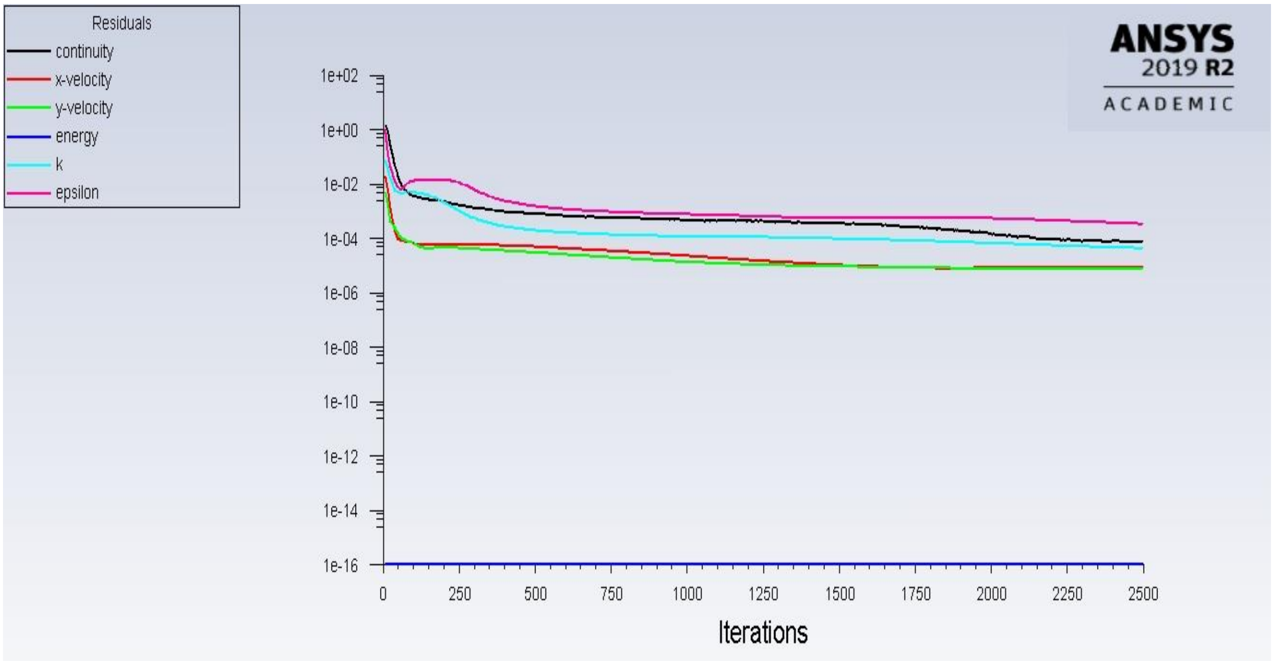

Figure B.87. Non-Porous Case 7 Scaled Residuals

ii. Particles tracked: 1 250 000 particles tracked.

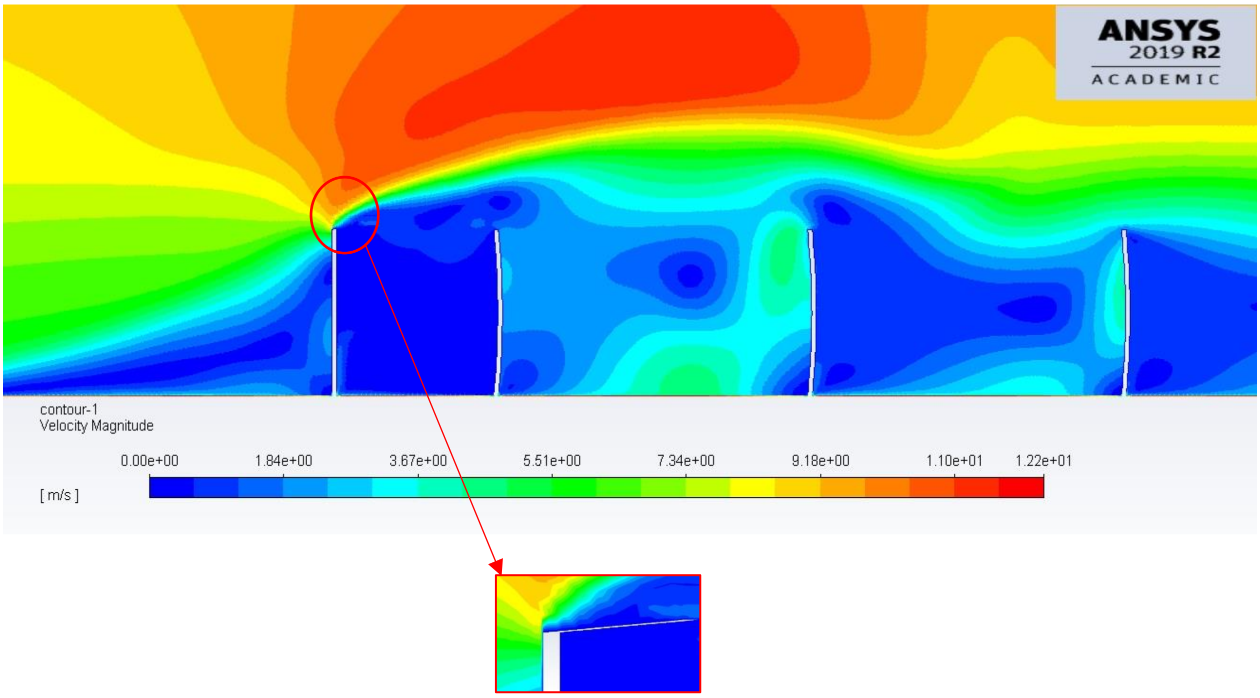

Figure B.88. Non-porous case 7 velocity contour

Table B.88. Non- porous case 7 particle fate

ANSY labelled Wall- ID zone	Geometric Definition	Particles Trapped	Particles Escaped
7	Outlet end side		350827
11	Ground distance of mirror pitch	71247	
12	Ground distance after mirror field	756043	
13	1st mirror front face	127	
14	2nd mirror front face	1590	
15	3rd mirror front face	6997	
16	4th mirror front face	20674	
17	5th mirror front face	27354	
18	6th mirror front face	30216	
19	Wind Barrier front	318	
20	Top and back sides of all mirrors	13359	
Soiling [Particles]		86959	

B.23. SIMULATED NON-POROUS CASE 8

B.23.1. GEOMETRICAL SETTINGS

The eighth non-porous case assumes values as shown:

Table B.89. Non-porous case 7 variables

Case Number	**l_3 [m]**	**θ [°]**	**po [m]**
8	0.05	175	0

In ANSYS, the geometrical settings were defined as shown in figure B.89 and table B.90:

Table B.90. Non-porous case 7 ANSYS geometrical settings

Case Number	**L6 [m]**	**A7 [°]**	**V10 [m]**
8	0.05	175	0

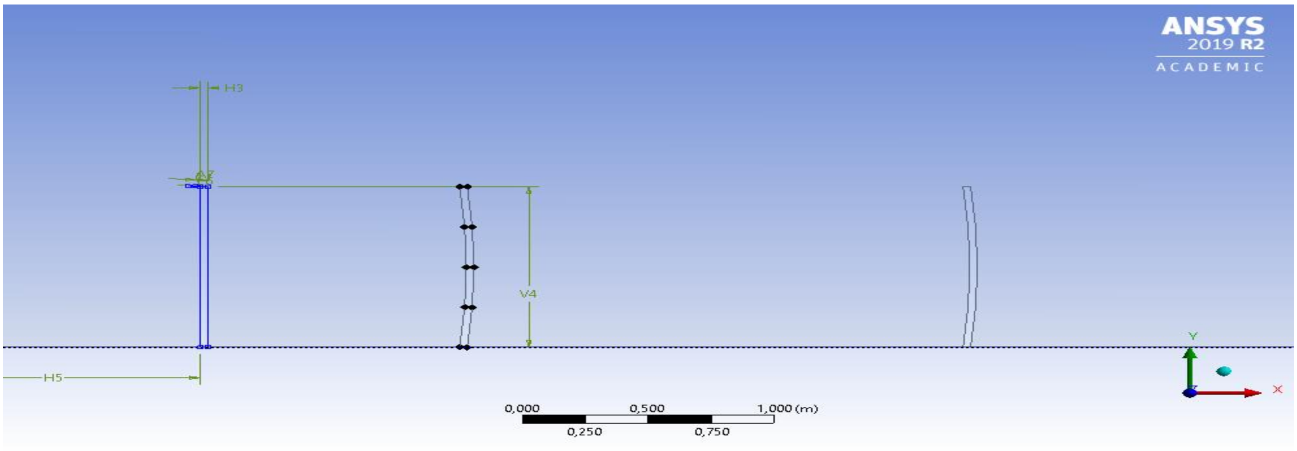

Figure B.89. Non-porous case 8 geometrical settings

B.23.2. MESH SETTING

The mesh of this case was generated as explained in chapter 2 and the mesh information and quality can be shown in table B.91and displayed in figure B.90.

Table B.91. Non-Porous Case 8 Mesh Statistics

Nodes	873720
Elements	871414
Mesh Metric Min -Element Quality	3,7374e-002
Mesh Metric Max-Element Quality	0,99988
Mesh Metric Average-Element Quality	0,71945

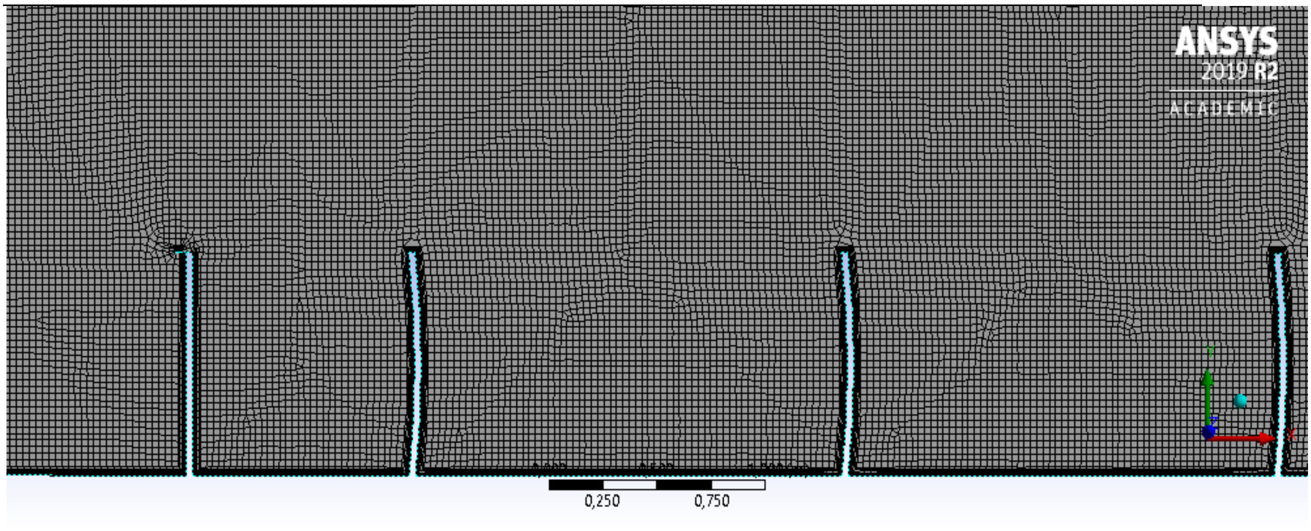

Figure B.90. Non-porous case 8 mesh settings

B.23.3. ANSYS-FLUENT SIMUALTION RESULTS

The ANSYS FLUENT settings were applied and the following results were obtained after solving for 2500 iterations:

i. Scaled Residuals: Convergence was achieved after 2500 iterations.

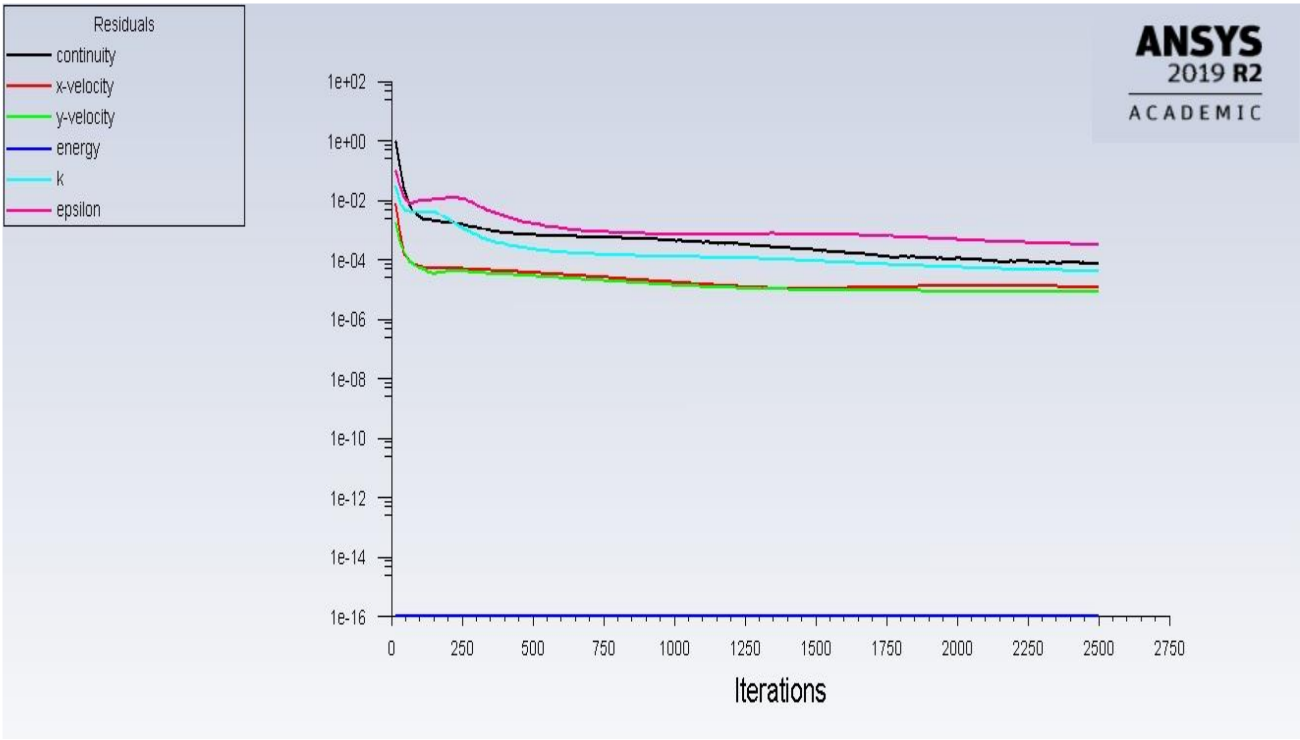

Figure B.91. Non-Porous Case 8 Scaled Residuals

ii. Particles tracked: 1 250 000 particles tracked.

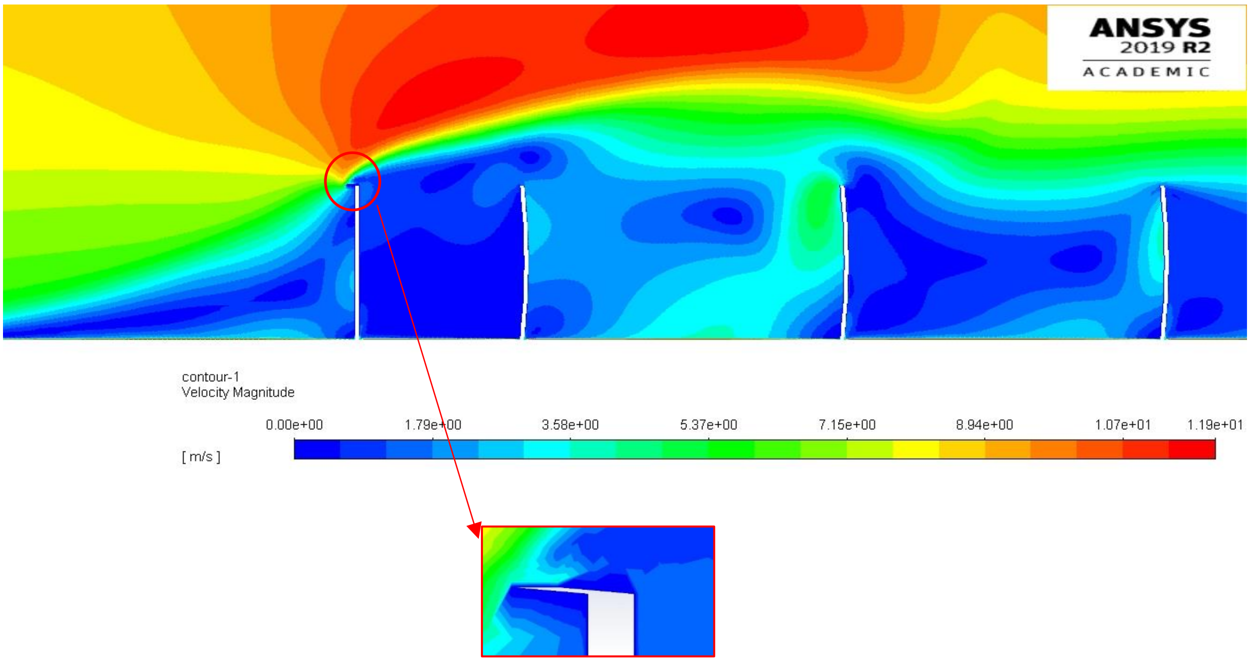

Figure B.92. Non-porous case 8 velocity contour

Table B.92. Non- porous case 8 particle fate

ANSY labelled Wall- ID zone	**Geometric Definition**	**Particles Trapped**	**Particles Escaped**
7	Outlet end side		344784
11	Ground distance of mirror pitch	69975	
12	Ground distance after mirror field	747138	
13	1st mirror front face	54	
14	2nd mirror front face	1908	
15	3rd mirror front face	6997	
16	4th mirror front face	16858	
17	5th mirror front face	23219	
18	6th mirror front face	25445	
19	Wind Barrier front	83	
20	Top and back sides of all mirrors	13041	
Soiling [Particles]		74482	

B.24. SIMULATED NON-POROUS CASE 9

B.24.1. GEOMETRICAL SETTINGS

The final non-porous case assumes values as shown:

Table B.93. Non-porous case 9 variables

Case Number	l_3 [m]	θ [°]	po [m]
9	0.25	175	0

In ANSYS, the geometrical settings were defined as shown in figure B.93 and table B.94:

Table B.94. Non-porous case 9 ANSYS geometrical settings

Case Number	L6 [m]	A7 [°]	V10 [m]
9	0.25	175	0

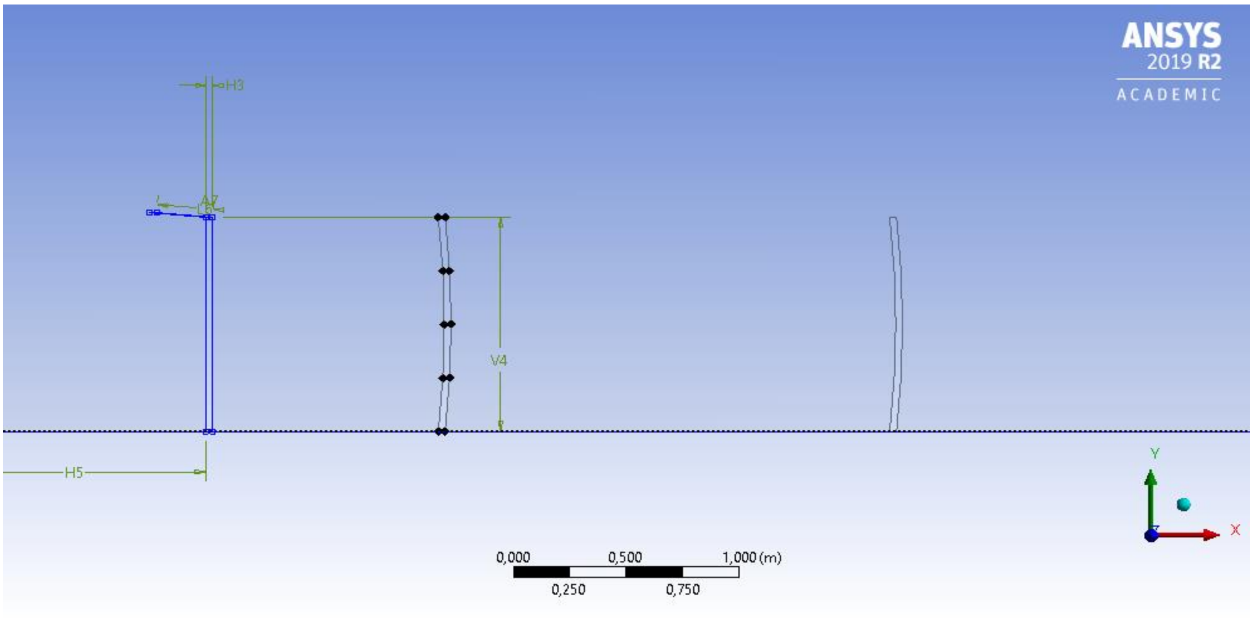

Figure B.93. Non-porous case 9 geometrical settings

B.24.2. MESH SETTING

The mesh of this case was generated as explained in chapter 2 and the mesh information and quality can be shown in table B.95 and displayed in figure B.94.

Table B.95. Non-porous case 9 mesh statistics

Nodes	873720
Elements	871414
Mesh Metric Min -Element Quality	3,7374e-002
Mesh Metric Max-Element Quality	0,99988
Mesh Metric Average-Element Quality	0,71945

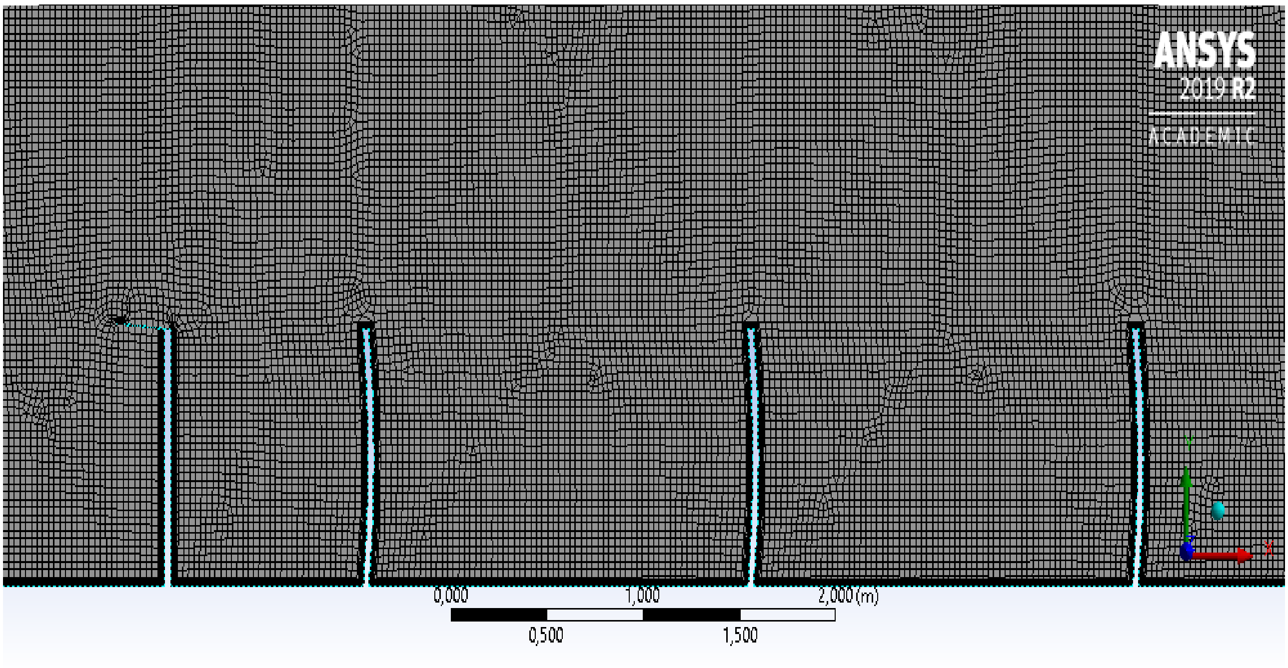

Figure B.94. Non-porous case 8 mesh settings

B.24.3. ANSYS-FLUENT SIMUALTION RESULTS

The ANSYS FLUENT settings were applied and the following results were obtained after solving for 2500 iterations:

i. Scaled Residuals: Convergence was achieved after 2500 iterations.

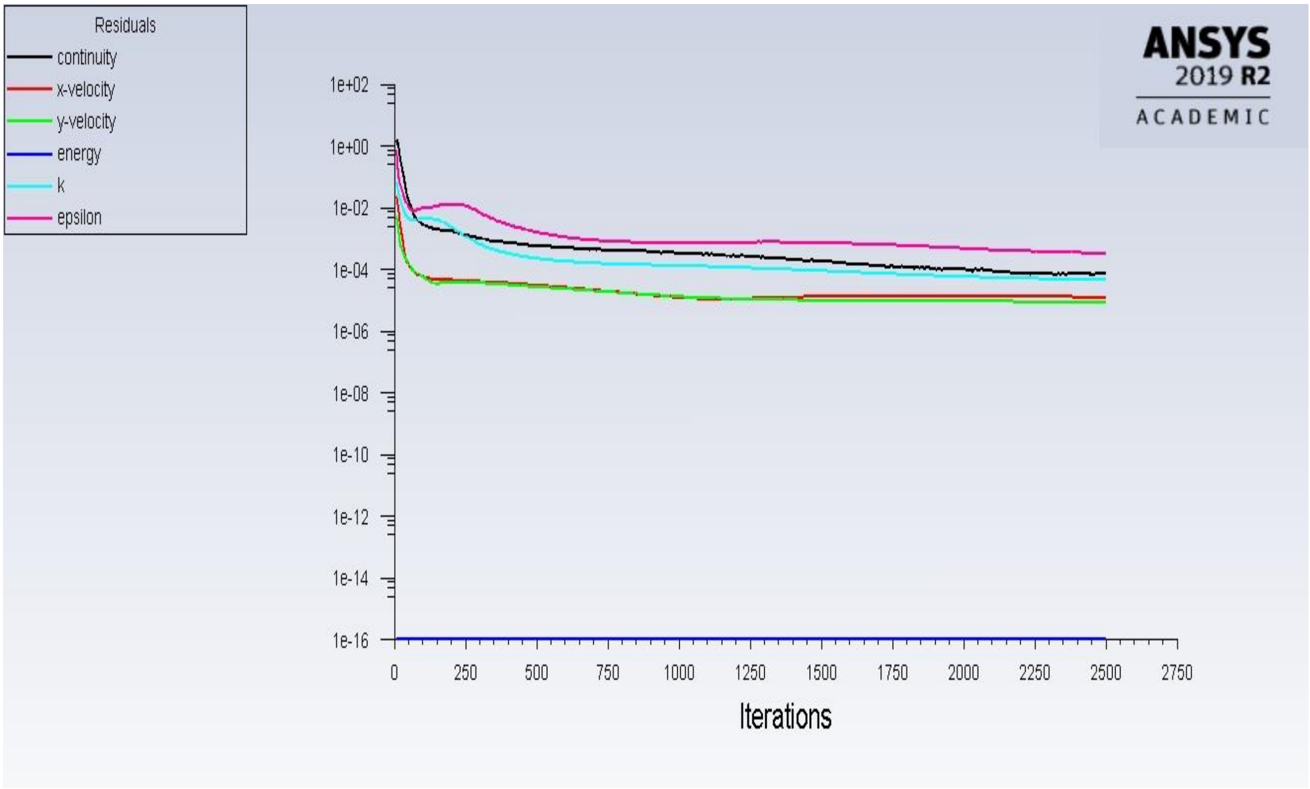

Figure B.95. Non-porous case 9 scaled residuals

iii. Particles tracked: 1 250 000 particles tracked.

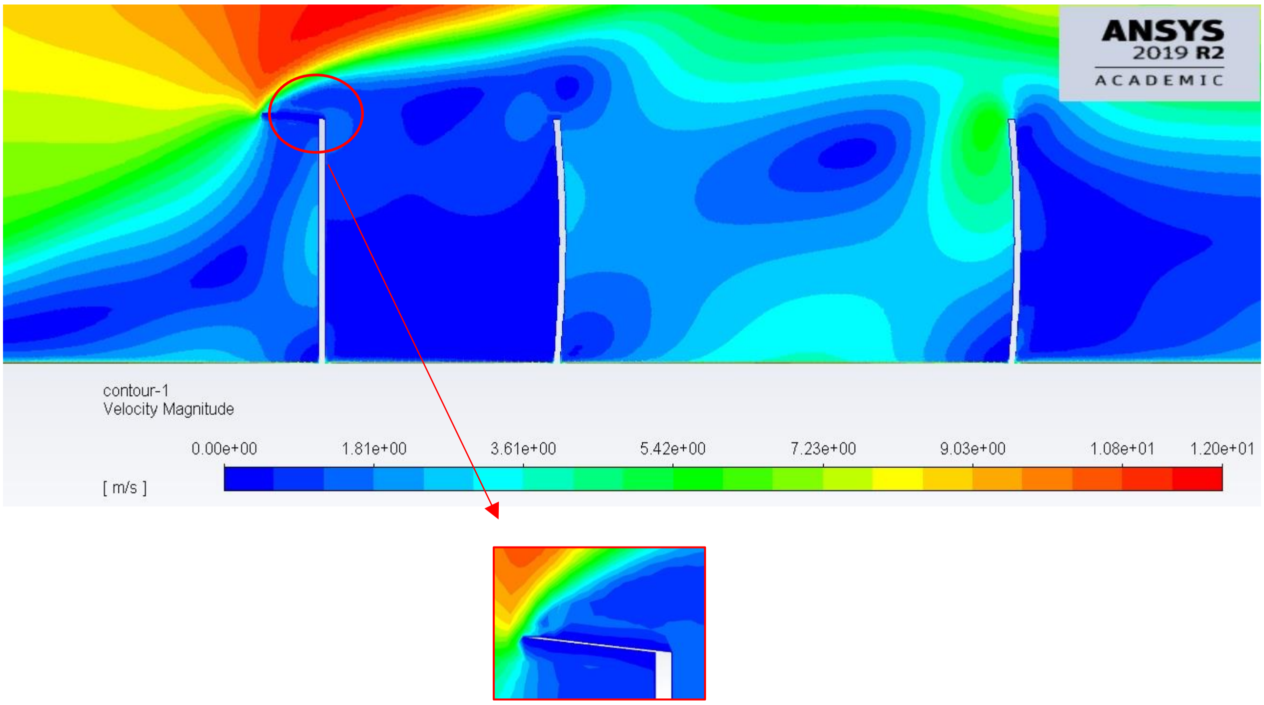

Figure B.96. Non-porous case 9 velocity contour

Table B.96. Non- porous case9 particle fate

ANSY labelled Wall- ID zone	**Geometric Definition**	**Particles Trapped**	**Particles Escaped**
7	Outlet end side		344784
11	Ground distance of mirror pitch	69020	
12	Ground distance after mirror field	746183	
13	1st mirror front face	15	
14	2nd mirror front face	2863	
15	3rd mirror front face	9860	
16	4th mirror front face	12087	
17	5th mirror front face	21629	
18	6th mirror front face	27990	
19	Wind Barrier front	954	
20	Top and back sides of all mirrors	14313	
Soiling [Particles]		74442	